The Magnetic Microbolometer: A Novel Cryogenic Detector for Cosmology

Zur Erlangung des akademischen Grades eines

DOKTORS DER INGENIEURWISSENSCHAFTEN (Dr.-Ing)

von der KIT-Fakultät für Elektrotechnik und Informationstechnik des Karlsruher Instituts für Technologie (KIT)

angenommene

DISSERTATION

von

Dipl.-Ing. Juan Manuel Geria

geboren in: Buenos Aires, Argentinien

Tag der mündlichen Prüfung:	28.10.2025
Hauptreferent:	Prof. Dr. Sebastian Kempf
Korreferent:	Dr.-Ing Matias Rolf Hampel

Karlsruher Institut für Technologie

UNSAM

The Magnetic Microbolometer: A Novel Cryogenic Detector for Cosmology

Para obtener el título académico de

DOCTOR EN CIENCIAS APLICADAS Y DE LA INGENIERÍA

de la Escuela de Ciencia y Tecnología de la
Universidad Nacional de San Martín (UNSAM)

versión aprobada

DISERTACIÓN

de

Ing. Juan Manuel Geria

nacido en: Buenos Aires, Argentina

Fecha de la defensa oral:	28.10.2025
Director por UNSAM:	Dr.-Ing. Matias Rolf Hampel
Director por KIT:	Prof. Dr. Sebastian Kempf

Karlsruher Institut für Technologie

UNSAM

Abstract

This thesis presents the foundational work in the development of a Magnetic Microbolometer (MMB), a novel cryogenic detector concept designed for polarization measurements in Cosmic Microwave Background (CMB) surveys with unprecedented precision. The MMB builds on the principles of Magnetic Microcalorimeters (MMC), adapting this class of paramagnetic sensors for use as highly sensitive cryogenic bolometers, thereby extending MMC technology into the domain of observational cosmology.

The detector requirements used in this work are derived from the Q & U Bolometric Interferometer for Cosmology (QUBIC) instrument. It is designed to observe the polarization of the CMB at large angular scales in the search for primordial B-modes in the polarization spectrum of the CMB. QUBIC contributes to the global effort to test predictions of the theory of cosmic inflation. While the MMB design is evaluated within the context of QUBIC, the concept is inherently versatile and can be adapted to meet the needs of a wide range of cryogenic instrumentation beyond this specific experiment.

This thesis spans a wide spectrum from theoretical modeling to experimental realization. The theoretical analysis of the MMB concept is presented starting from the underlying physical principles to obtain estimations of the signal response and noise characteristics. The suitability of the MMB for its applicability to the demanding requirements of ground-based CMB polarization experiments is also shown. Based on these findings, a fabrication pathway to implement the MMB detector technology was developed, including the optimization of microfabrication techniques and material processes necessary to produce functional MMB prototypes. This development also included the construction of a xenon difluoride (XeF_2) etching system that is required to fully materialize the MMB detector concept. Finally, the experimental characterization of the fabricated detector prototypes is presented. A dedicated cryogenic setup was assembled to perform low-temperature measurements of the first prototypes in a ^{3}He/^{4}He dilution refrigerator cryostat.

Altogether, this work establishes the theoretical and experimental foundations of the MMB detector, identifies key fabrication challenges, and defines a clear path for further refinement. It contributes both to the advancement of cryogenic detector technologies and to the broader effort of enabling next-generation measurements of the CMB by introducing a new detector technology aimed at probing the birth of the Universe.

Zusammenfassung

Diese Dissertation präsentiert die grundlegende Arbeit zur Entwicklung eines Magnetischen Mikrobolometers (MMB), eines neuartigen kryogenen Detektorkonzepts für Polarisationsmessungen der Kosmischen Mikrowellenhintergrundstrahlung (CMB) mit bisher unerreichter Präzision. Das MMB baut auf den Prinzipien eines Magnetischen Mikrokalorimeters (MMC) auf und passt diese Klasse von paramagnetischen Sensoren für den Einsatz als hochsensitive kryogene Bolometer an, wodurch die MMC-Technologie in den Bereich der Beobachtungskosmologie erweitert wird.

Die dieser Arbeit zugrunde gelegten Detektoranforderungen stammen aus dem Q&U Bolometric Interferometer for Cosmology (QUBIC). Dieses Instrument ist dafür konzipiert, die Polarisation der CMB auf großen Winkelskalen zu beobachten, um nach primordialen B-Moden im Polarisationsspektrum der CMB zu suchen. QUBIC trägt zu den weltweiten Bemühungen bei, die Vorhersagen der Theorie der kosmischen Inflation zu überprüfen. Obwohl die MMB-Technologie im Kontext von QUBIC untersucht wird, ist das Konzept grundsätzlich vielseitig und kann an die Anforderungen einer breiten Palette kryogener Anwendungen über dieses spezifische Experiment hinaus angepasst werden.

Diese Dissertation umfasst ein breites Spektrum von der theoretischen Modellierung bis zur experimentellen Umsetzung. Die theoretische Analyse des MMB-Konzepts beginnt bei den zugrunde liegenden physikalischen Prinzipien und führt zu Abschätzungen der Signalantwort und der Rauschcharakteristika. Zudem wird die Eignung des MMB zur Erfüllung der anspruchsvollen Anforderungen bodengebundener CMB-Polarisationsexperimente gezeigt. Auf Grundlage dieser Ergebnisse wurde ein Herstellungsprozess zur Umsetzung der MMB-Detektortechnologie entwickelt, einschließlich der Optimierung von Mikrostrukturierungstechniken und Materialprozessen, die für die Herstellung funktionaler MMB-Prototypen erforderlich sind. Diese Entwicklung umfasste auch den Entwurf und den Aufbau einer Ätzanlage für den Einsatz von Xenondifluorid (XeF_2) als Prozessgas, die notwendig ist, um das MMB-Detektorkonzept vollständig zu realisieren. Schließlich wird die experimentelle Charakterisierung der gefertigten Detektorprototypen vorgestellt. Hierzu wurde ein spezieller kryogener Versuchsaufbau realisiert, um Tieftemperaturmessungen der ersten Prototypen in einem ^{3}He/^{4}He-Verdünnungskryostaten durchzuführen.

Insgesamt etabliert diese Arbeit die theoretischen und experimentellen Grundlagen des MMB-Detektors, identifiziert zentrale Herausforderungen in der Fertigung und definiert einen klaren Weg zur weiteren Optimierung. Sie leistet sowohl einen Beitrag zur Weiterentwicklung kryogener Detektortechnologien als auch zu den umfassenderen Bemühungen, durch die Einführung einer neuartigen Detektortechnologie Messungen der nächsten Generation des CMB zu ermöglichen, die auf die Erforschung des Ursprungs des Universums abzielen.

Resumen

Esta tesis presenta la propuesta y el desarrollo de un Microbolómetro Magnético (MMB), un novedoso detector criogénico diseñado para mediciones de polarización en estudios de la Radiación Cósmica de Fondo (CMB, por sus siglas en inglés) con una precisión sin precedentes. El MMB se basa en los principios de los Microcalorímetros Magnéticos (MMC), adaptando esta clase de sensores paramagnéticos para su uso como bolómetros criogénicos de alta sensibilidad, extendiendo así la tecnología MMC al ámbito de la cosmología observacional.

Los requisitos del detector utilizados en este trabajo se derivan del instrumento Q & U Bolometric Interferometer for Cosmology (QUBIC). Este instrumento está diseñado para observar la polarización del CMB a grandes escalas angulares en la búsqueda de modos-B primordiales en su espectro de polarización. QUBIC contribuye al esfuerzo global por poner a prueba las predicciones de la teoría de la inflación cósmica. Si bien el diseño del MMB se evalúa en el contexto de QUBIC, el concepto es intrínsecamente versátil y puede adaptarse a las necesidades de una amplia gama de instrumentación criogénica más allá de este experimento específico.

Esta tesis abarca un amplio espectro que va desde el modelado teórico hasta la realización experimental. El análisis teórico del MMB se presenta partiendo de los principios físicos fundamentales para obtener estimaciones de la respuesta de señal y las características de ruido. Asimismo, se demuestra la idoneidad del MMB para cumplir con los exigentes requisitos de los experimentos terrestres para medir el espectro de polarización del CMB. A partir de estos resultados, se desarrolló una ruta de fabricación para implementar la tecnología del detector MMB, que incluye la optimización de técnicas de microfabricación y procesos de materiales necesarios para producir prototipos funcionales. Este desarrollo también comprendió la construcción de un sistema de grabado con difluoruro de xenón (XeF_2), requerido para materializar plenamente el concepto del detector. Finalmente, se presenta la caracterización experimental de los prototipos fabricados. Para ello se ensambló un sistema criogénico dedicado a realizar mediciones a baja temperatura de los primeros prototipos en un criostato de dilución de $^3He/^4He$.

En conjunto, este trabajo establece las bases teóricas y experimentales del detector MMB, identifica los principales desafíos de fabricación y define un camino claro para su perfeccionamiento futuro. Contribuye tanto al avance de las tecnologías de detectores criogénicos como al esfuerzo más amplio de habilitar mediciones de próxima generación del CMB, al introducir una nueva tecnología de detección orientada a observar el nacimiento del Universo.

Acknowledgments
Danksagung
Agradecimientos

This dissertation represents for me not only an academic process but also a personal journey of growth — a timeless human experience in which I had the chance to meet, learn from, and laugh with wonderful people all around the world. I would like to honor and thank them here for the many ways they have enriched this path.

I am grateful to ITeDA and IMS for supporting me and providing the tools to pursue a career in Engineering Sciences. These top-level international research institutes have allowed me to build a profound and diverse background. I also wish to thank the broader institutions on which they depend — CNEA, CONICET, UNSAM, and KIT — for organizing and managing the resources that enable scientific research, as well as the taxpayers who ultimately make all of this possible.

I am forever indebted to my supervisors, Matías Hampel and Prof. Sebastian Kempf, for their guidance, patience, and belief in my work. Their advice has been invaluable, and their confidence in me was always a source of motivation, especially during challenging times. I am grateful for the freedom they gave me to explore my own ideas, while always providing the right guidance to stay on track.

To my colleagues in Argentina — Juan Bonaparte, Jesús Bonilla, Nahuel Müller, Juan Manuel Salum, Luciano Ferreyro, Alejandro Almela, Manuel García, Alan Fuster, and Manuel Platino — for the many enriching technical discussions we shared throughout this journey, as well as for their friendship and countless moments of laughter that made even the most demanding days more enjoyable. I also thank Lucía Sucunza, with whom I had the pleasure to collaborate on the development of a key piece of equipment, which was central to this work. I am further indebted to the whole team — Pablo Strazzeri, Carlos Varela, Diego Silva, Néstor del Castillo, Adrián Riello, Adrián Sedosky, Luciana Rosellini, Leonardo Paolucci, Gustavo Dominguez, Abigail Gonzalez, Daniel Gorbeña, Gabriel de Innocenti, Carlos Pyñero, and Andrés Pantarotto — for their dedication, professionalism, and invaluable support in building and providing the many tools required for this thesis, as well as for the good humor and companionship that lightened long working hours.

To my colleagues in Germany — Mathias Wegner, Constantin Schuster, Michael Müller, Martin Neidig, Fabienne Adam, Lena Hauswald, Nik Ardlt, and Friedrich Wagner — for welcoming me and for their unwavering support during my time abroad. Beyond

the scientific collaboration, I am deeply grateful for the warmth, kindness, and personal moments we shared, which made my stay in Germany an unforgettable experience. I also owe special thanks to Konstantin Il'in for his insightful lectures and discussions on superconducting thin films, which provided valuable input for understanding several phenomena relevant to this research.

I extend my gratitude to the many collaborators from other institutes who generously shared their expertise and resources, which proved fundamental to the success of this thesis. Prof. Christian Enss, Andreas Fleischmann, Andreas Reifenberger, and Thomas Wolf from KIP Heidelberg welcomed my colleagues and me to their institute for the preparation of specialized materials required for the detectors developed in this work. Jörn Beyer from PTB kindly lent a sputtering target to IMS, enabling the production of detector prototypes while our own was being prepared. Benjamin Westbrook from UC Berkeley provided essential advice and contributed specialized silicon wafers required for the realization of this thesis. My heartfelt thanks go to all of them for their generous and selfless contributions.

Finally, I wish to express my deepest gratitude to my nearest and dearest for their unconditional support, and encouragement throughout my life. To my parents, Nelsy and Uchi, who always placed my education and well-being above all else and taught me perseverance and resilience in the face of challenges; to my brother José, for his constant presence, generosity, and strength; and to Denise, who has shown me what love truly feels like. Without their belief in me, this journey would not have been possible.

Contents

Abstract **i**

Acknowledgments **iii**

1 Introduction **1**
1.1 The Cosmic Microwave Background (CMB) 1
1.2 CMB polarization survey 3
1.3 The QUBIC Instrument 5
1.4 The Magnetic Microbolometer (MMB) 7
1.5 Outline 8

2 Radiation Coupling **11**
2.1 Electromagnetic simulations with superconductors 11
2.2 Dielectric losses at cryogenic temperatures 13
2.3 Antenna geometries 14
2.4 Silicon lenses 15
2.5 Antenna impedance 18
2.6 Matching network 20
2.7 Band-defining filters 23
2.8 Optical efficiency analysis 30
2.9 Photon noise equivalent power (NEP_γ) 32

3 The Magnetic Microbolometer (MMB) **37**
3.1 Detection principle 37
3.2 Thermal response 38
3.3 Sensor material 40
3.4 Magnetic bias field and signal readout 46
3.5 Noise contributions 51
3.6 Optimization of an MMB for QUBIC 53
3.7 Optimization of an MMB for other experiments 58
3.8 The MMB Technical Demonstrator (MMB-TD) 59

4 Fabrication Methods **63**
4.1 Active Detector Components 63
4.1.1 Pickup coil 65

4.1.2 Persistent current switch 80
4.1.3 Sensor material 81
4.2 Release of Detector Structures 83
4.2.1 KOH-based wet-etching technique 83
4.2.2 XeF_2-based dry-etching technique 89

5 Characterization Methods **99**
5.1 Cryogenics 99
5.1.1 Pulse-tube cryocooler (PTC) 100
5.1.2 $^3He/^4He$ dilution refrigerator 101
5.2 Superconducting QUantum Interference Device (SQUID) 101
5.3 The two-stage SQUID-based amplifier 103
5.3.1 Frequency response 104
5.3.2 dc-SQUID characterization 106
5.3.3 Noise performance and bandwidth 106

6 Experimental Results **111**
6.1 Measurement setup 111
6.2 Inductance measurements 113
6.3 Bias field injection 116
6.4 Thermally-induced detachment of the Au:Er sensor 117
6.5 Thermal runaway breakdown 118
6.6 Sensor magnetization measurement 119
6.7 Released Au:Er sensor in the MMB-TD 125

7 Summary and Outlook **129**

List of Figures **131**

List of Tables **143**

List of Acronyms **145**

List of Publications **147**

Bibliography **151**

Chapter 1

Introduction

This chapter outlines the scientific motivation for the development of magnetic microbolometers. It begins with a brief description of the Cosmic Microwave Background (CMB) and its relation to cosmology, followed by an overview of the key requirements that ongoing surveys must meet. The Q & U Bolometric Interferometer for Cosmology (QUBIC) instrument is introduced as the project that served as the starting point for the magnetic microbolometer technology developed in this thesis.

1.1 The Cosmic Microwave Background (CMB)

The CMB was first measured serendipitously by Penzias and Wilson in 1964 [1]. They used a large horn antenna, originally designed for satellite communication experiments, to conduct radio astronomy observations of the Milky way and other celestial sources. The signal was detected as a persistent noise that interfered with their measurements coming from every direction, and the spectra matched a 3.5 K blackbody radiation. Upon closer examination, it was determined that it was in fact an ancient remnant of the violent origin of the Universe, first proposed in a series of papers published in the 1940s by Gamow, Alpher, and Hernan [2, 3]. Its emission was traced to about 380.000 years after the Big Bang. Prior to which, no light could propagate due to the constant scattering of photons with charged particles that covered the entirety of the recently born Universe. It was at the recombination epoch, that the last scattering of this primordial light occurred.

Nowadays, after approximately 13.8 billion years of accelerated expansion of the Universe, we can observe the CMB as a highly redshifted blackbody radiation that peaks at a frequency of around 150 GHz. A recent and accurate measurement comes from the Far-Infrared Absolute Spectrophotometer (FIRAS) instrument on board the COsmic Background Explorer (COBE) [4] recalibrated with the Wilkinson Microwave Anisotropy Probe (WMAP) [5], a temperature of (2.72550 ± 0.00085) K was reported [6]. Relative temperature variations across the sky in the order of 10^{-5} correspond to the conditions in the Universe at the recombination epoch (primary anisotropies) plus distortions experienced by CMB radiation as it travels through the Universe (secondary anisotropies).

A Mollweide projection aligned with the Milky Way Galaxy plane is built to show

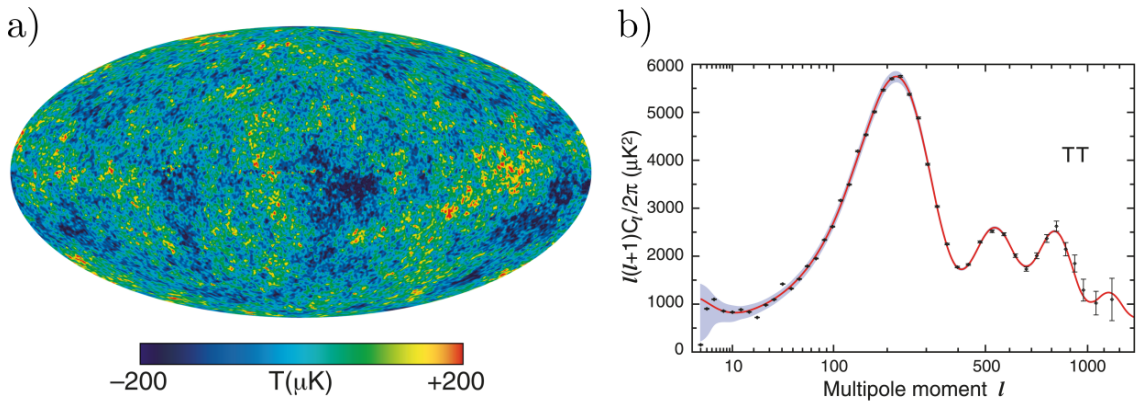

Figure 1.1: a) ILC map of the CMB produced by the WMAP survey with a nine-year observation dataset. **b)** CMB temperature auto-correlation power spectrum expressed as $\ell(\ell+1)C_\ell^{\mathrm{TT}}/2\pi$ obtained from the ILC CMB map. The plot also includes error bars in black and a best-model fit in red [7].

the CMB temperature anisotropy distribution in the sky. Figure 1.1 (a) shows a CMB anisotropy map which consists of an Internal Linear Combination (ILC) of a nine-year observation dataset from WMAP [7].

The relative temperature variations or anisotropies ($\Delta T(\hat{n})$) are measured with respect to angular scale and quantified by the temperature auto-correlation power spectrum C_ℓ^{TT} with respect to the multipole moment ℓ (inverse of the angular scale, analogous to frequency). It is calculated by expanding the temperature anisotropies in spherical harmonics:

$$\Delta T(\hat{n}) = \sum_{\ell=0}^{\infty} \sum_{m=-\ell}^{\ell} a_{\ell m} \cdot Y_{\ell m}(\hat{n}). \tag{1.1}$$

Here, $\hat{n}$ is the unit vector in spherical coordinates representing a point on the surface of a sphere, and $Y_{\ell m}(\hat{n})$ are the spherical harmonic functions or moments into which the temperature auto-correlation function is decomposed, the number m refers to the orientation of each spherical harmonic component. As a result, the multipole coefficients $a_{\ell m}$ characterize the temperature fluctuation distribution in the multipolar moment space. The temperature auto-correlation power spectrum C_ℓ^{TT} is ultimately obtained by averaging the power of $a_{\ell m}$ with respect to m:

$$C_\ell^{\mathrm{TT}} = \langle |a_{\ell m}|^2 \rangle_m. \tag{1.2}$$

The quantity $\ell(\ell+1)C_\ell^{\mathrm{TT}}/2\pi$ is plotted in Figure 1.1 (b) [7]. The best-fit model, shown as a red trace in the same plot, was constructed from theoretical expectations framed within the Lambda Cold Dark Matter Model (ΛCDM). Such model fits are used to constrain the cosmological constants of the Universe [8, 9].

The proposed solution and leading paradigm to solve the Horizon and Flatness problems [10, 11] within the ΛCDM model is the Theory of Cosmic Inflation [12], proposed by Guth in the early 1980s. It suggests an inflationary phase in which an exponential

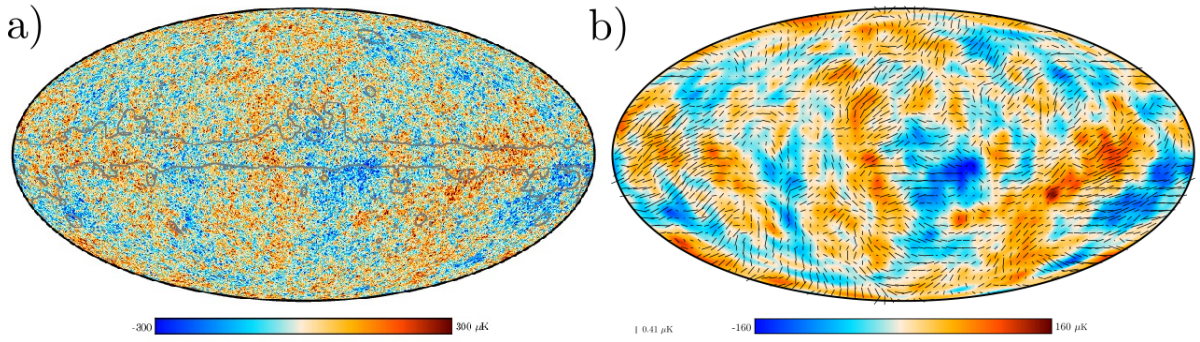

Figure 1.2: a) Temperature anisotropy map of the CMB. **b)** Polarization field superimposed on the temperature map smoothed for visibility purposes. Both maps were extracted and published by the Planck Collaboration [14].

expansion takes place 10^{-32} seconds after the Big Bang. During this very short time period, the horizon size of the Universe would have rapidly increased by several orders of magnitude.

1.2 CMB polarization survey

A fraction of the CMB radiation is linearly polarized due to Thomson scattering of photons during decoupling of matter from radiation [13]. Figure 1.2 shows the anisotropy and polarization maps published by the Planck Collaboration [14]. Cosmic Inflation would have produced primordial gravitational waves that translate to a particular polarization pattern in the CMB [15]. CMB polarization maps are therefore an additional probe to the early Universe and can even offer insights into the quantum nature of gravity [16].

Linear polarization can be represented by the Stokes parameters Q and U. These parameters are not scalars, but rank-2 tensors and thus vary according to the orientation of the coordinate system [13]. To overcome this, a tensorial spherical harmonic expansion is used [17] similar to Equation 1.1:

$$\vec{\Delta \mathrm{T}}(\hat{n}) = \sum_{\ell=2}^{\infty} \sum_{m=-\ell}^{\ell} \left[a^{E}_{\ell m} \cdot \mathfrak{Y}^{E}_{\ell m}(\hat{n}) + a^{B}_{\ell m} \cdot \mathfrak{Y}^{B}_{\ell m}(\hat{n}) \right], \tag{1.3}$$

with this expansion, two more auto-correlation and three cross-correlation spectra, (totaling six including C_ℓ^{TT}) are identified. The E-mode auto-correlation power spectrum,

$$C_\ell^{\mathrm{EE}} = \langle |a^{\mathrm{E}}_{\ell m}|^2 \rangle_m, \tag{1.4}$$

the B-mode auto-correlation power spectrum,

$$C_\ell^{\mathrm{BB}} = \langle |a^{\mathrm{B}}_{\ell m}|^2 \rangle_m, \tag{1.5}$$

and cross-correlation spectra, C_ℓ^{TE}, C_ℓ^{TB} and C_ℓ^{EB}. The decomposition of the CMB polarization into E-mode and B-mode spectra is analogous to the separation of a vector field

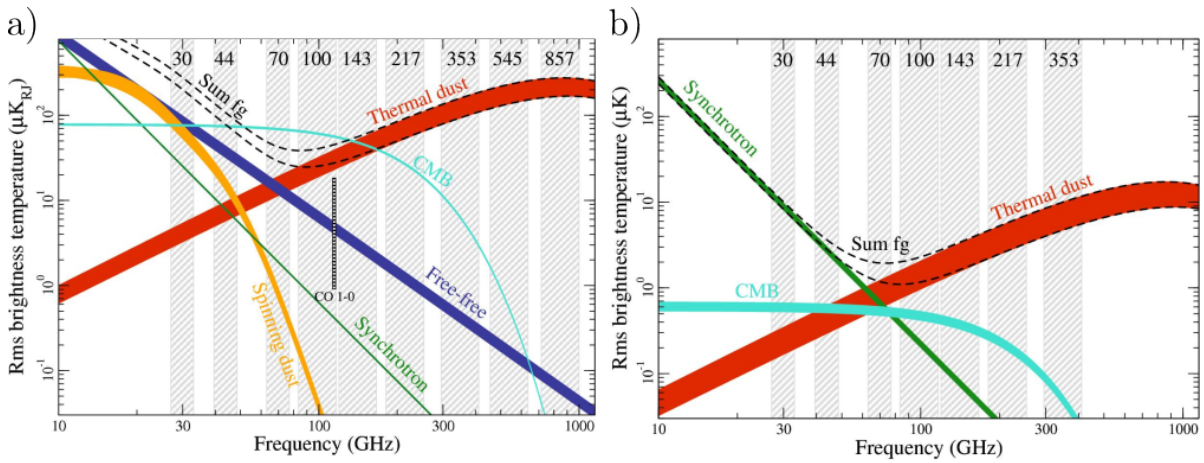

Figure 1.3: Rms Brightness temperature as a function of frequency of the CMB and foreground contribution signals for temperature (**a**) and polarization (**b**). The gray-shaded regions correspond to the multiple spectral bands observed by the Planck Satellite Mission (PLANCK) to perform foreground extraction [27].

into curl-less and divergence-less components. Cosmological perturbations can be scalar (energy density perturbations) producing only curl-less type polarization (E-modes) or they can also be tensorial (gravitational waves) producing divergence-less type polarization (B-modes) [18].

E-mode content is predominant in the CMB polarization and has been measured by multiple experiments such as WMAP [7, 19, 20], the Planck Satellite Mission (PLANCK) [14, 21] and the BICEP2+KeckArray [22, 23]. Cosmic Inflation, however, predicts B-mode content is also imprinted in the CMB. These are the so-called primordial B-modes, and their detection has not yet been confirmed.

The strength of the primordial B-mode spectrum is described in relation to the strength of the E-mode spectrum, this relationship is determined by the tensor-to-scalar ratio r, and it is estimated to be in the range of a few per mil or maybe even less [24]. The detection of primordial B-modes poses a significant challenge due to two primary factors: instrumental systematic errors and foreground anisotropies. The main identified sources of foreground anisotropies are thermal emission from galactic dust grains, synchrotron emission from electrons spiraling in magnetic fields within the galaxy, free-free radiation (also known as Bremsstrahlung) [25], atmospheric opacity and emission lines, and gravitational lensing [26].

The CMB and foreground anisotropies can be observed as a function of frequency in the plots shown in Figure 1.3 [27]. Foregrounds have well-defined frequency distributions, and thus, CMB experiments measure the sky in multiple spectral bands to perform foreground extraction through detailed data analysis.

A great number of CMB observatories, deployed at different sites around the world, aim to measure the B-mode power spectrum in the search for primordial B-modes. Their location is selected to minimize electromagnetic interference and feature a dry atmosphere as well as high altitude, making isolated and dry mountainous regions ideal

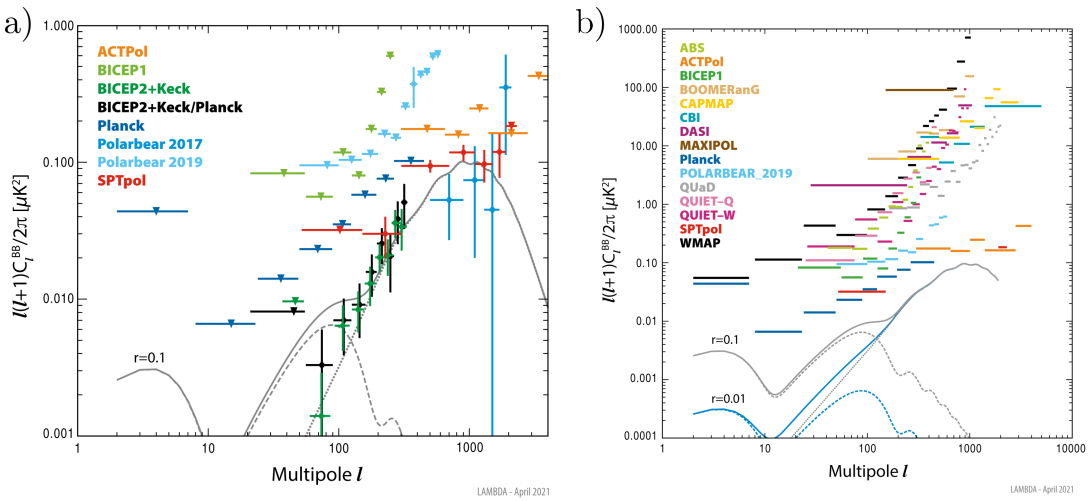

Figure 1.4: **a)** Observed B-mode power spectrum reported by finished CMB experiments. **b)** Current bounds of the B-mode signal. The plots contain dashed traces showing the theoretical curves for a ΛCDM model with $r = 0.1$ (black) and $r = 0.01$ (blue) as well as the lensing B-mode spectrum, the sum of both spectra is shown in solid trace [28].

for ground-based observations. A selection of results obtained by finished experiments are shown in Figure 1.4, these results are compiled by the NASA/LAMBDA [28] archive team and contain reported results from ACTPol [29], BICEP1 [30], BICEP2 [31], BICEP2+KeckArray [32], BICEP2+KeckArray/PLANCK [22], BOOMERANG [33], CAPMAP [34], CBI [35], DASI [36], MAXIPOL [37], POLARBEAR [38, 39], QUaD [40], QUIET-Q [41], QUIET-W [42], SPTPol [43] and WMAP [7, 44].

The current bounds on the primordial B-mode spectrum (Figure 1.4 (b)) do not reach the required level of sensitivity at low ℓ to verify the Theory of Cosmic Inflation. There are ongoing efforts in this endeavor utilizing telescopes with high-quality optics and increasingly sensitive detector arrays combined with smart observation strategies to tackle this challenge. Among these we find QUBIC [45], CLASS [46], POLARBEAR2 + SimonsArray [47–49], AdvACT [50], BICEP3/KeckArray [51] and AliCPT [52]. Other experiments are in the planning phase, such as the Simons Observatory [53], PIPER [54], LSPE [55], CMB-S4 [56], LiteBIRD [57] and PICO [58].

1.3 The QUBIC Instrument

The Q & U Bolometric Interferometer for Cosmology (QUBIC) [45] is a ground-based experiment deployed in the Northwestern region of Argentina. It is located in Alto Chorrillos at a height of approximately, 4900 meters above mean sea level.

It is a large-angular-scale (low ℓ) radiotelescope that incorporates a powerful technique called bolometric interferometry [59]. The interferometer consists of an array of back-to-back horn antennas that individually couple and re-emit the incoming radiation. These antennas act as a set of pupils in a Fizeau-like interferometer, each pair of pupils

contributes with an interference fringe on the focal plane. The beams are summed by a compensated off-axis Gregorian combiner that coherently focuses the synthesized beam (dirty image) onto the focal plane of the instrument.

The horns in the interferometer can be switched on and off via RF mechanical shutters [60], meaning that the resulting complex interference pattern can be tuned. By observing a polarized artificial point source using a sequence of paired open horns, no variation in the resulting signal should occur if the instrument is free from systematic errors and the distance between the opened horns is the same. Any discrepancies in the measured signals can be attributed to instrumental systematic errors, which can be identified and corrected to refine the data appropriately. This form of self-calibration, which is commonly used in traditional aperture synthesis, is also applied to bolometric interferometry and represents one of QUBIC's key advantages [61].

In the QUBIC Full Instrument the synthesized beam will be formed by an array of 400 horns, achieving an angular resolution of 23.5 arcminutes at 150 GHz [62]. It differs substantially from a classical imager radiotelescope as it will exhibit multiple peaks for a point-like source in the focal plane. The distance between peaks depends on the ratio of the source wavelength to the maximal distance between pupils. Thus, the synthesized beam varies with frequency, enabling spectral imaging capabilities [63].

Map-making with the QUBIC instrument is more complex compared to a classical imager as it involves partial deconvolution to disentangle the small contamination by the secondary peaks. However, recovery of the input maps was demonstrated with specific map-making algorithms using the inverse problem approach [64] provided that a sufficient number of polarization angles can be produced.

The observation bands of the instrument are centered at 150 GHz and 220 GHz, each with a fractional bandwidth of approximately 25 %. These bands are typical for CMB experiments. The 150 GHz band sits in a favorable atmospheric window (low precipitable-water-vapour attenuation) for ground-based observation and CMB anisotropy also peaks near 150 GHz in brightness temperature. Polarized galactic dust foreground increases with frequency seemingly as a modified blackbody (see Figure 1.3 (b)), thus, the additional 220 GHz band provides leverage to separate CMB polarization from this foreground contribution.

To define the observation bands, the initial plan was to employ a dichroic mirror placed in front of the focal plane. This mirror acts as a band-pass filter for the 150 GHz band while selectively reflecting the 220 GHz band at a specific angle [65]. As a result, two different focal planes are illuminated to measure the incoming radiation within each band.

QUBIC as well as other CMB experiments utilize large arrays of cryogenic bolometers for detection placed at the telescope's focal plane. A cryogenic bolometer [66] is a thermal radiation detector that can be designed to measure power flux of electromagnetic waves over a wide range of wavelengths with unmatched sensitivity. They turn out to be particularly well suited for sub-millimeter and millimeter-wave applications, where they are presently the most sensitive broadband detectors available [67].

The current bolometer array in the technical demonstrator instrument of QUBIC [68] consists of 256 superconducting Transition Edge Sensor (TES) [69] with a Time-Division

Multiplexing (TDM) readout [70]. Each TES is thermally coupled to a normal-conducting metal mesh and monitors its temperature; the mesh or membrane is mechanically supported by a backing dielectric membrane anchored to the detector wafer with thin legs and thus presents a low thermal conductivity to the cryostat heat bath. The metal mesh is heated when illuminated with incoming radiation. The surface resistivity and geometry of the metal mesh is adjusted to maximize absorption considering the impedance of free space, the refractive index of the backing membrane [71] and the use of back-short cavities [72].

TES are superconducting detectors, consisting of thin-film metal resistors that are operated at the transition point between their normal and superconducting states. At this transition, they exhibit a sharp variation in resistance with temperature. The resistance variation at the edge of the superconducting transition is used as a sensitive thermometer that can monitor the metal mesh temperature by transforming it into an electrical signal [73].

TES bolometers, when operated at a stable temperature and operating point, detect incoming radiation through a process known as DC power substitution. The DC bias power heats the TES to a fixed, stable temperature, and upon exposure to radiation, part of the DC bias power is reduced to maintain this temperature fixed through negative Electro-Thermal Feedback (ETF) [74]. The absorbed radiation effectively substitutes the reduced bias power, maintaining thermal equilibrium. Therefore, there is an inherent limit to the amount of power they can measure, which is the DC bias power. It is determined by the transition temperature of the superconductor, the base temperature of the cryostat and the thermal conductivity of the detector [75]. If the radiation incident on the TES exceeds the bias power, the ETF mechanism is disrupted, and the detector becomes saturated. This behavior can be managed to some extent by reducing the sensitivity of the TES. Because of this, TES have a fixed dynamic range, which represents the balance between their sensitivity and saturation power.

In CMB experiments, the DC bias power is adjusted to be double or triple the predicted optical power load illuminating the focal plane for ample overhead. However, there is considerable variation in the incoming power, influenced by the observed sky position, such as the difference between the zenith and horizon, and also laboratory characterization that is performed with sources that can easily saturate the TES. This variability has sometimes required the implementation of dual TES detectors, featuring two TES per pixel, as seen in the BICEP2, the KeckArray, and SPIDER [76], along with the POLARBEAR focal plane [77]. This strategy facilitates the management of a wide spectrum of incoming power while maintaining high sensitivity for lower power levels.

1.4 The Magnetic Microbolometer (MMB)

In this thesis, a novel type of bolometric detector is presented: the Magnetic Microbolometer (MMB) [78]. The detector utilizes the paramagnetic behavior of rare earth-doped metals like gold erbium (Au:Er) and silver erbium (Ag:Er). The detection concept is inspired by the widely-known and successful Magnetic Microcalorimeter (MMC) [79, 80]

used in cryogenic particle detection for over two decades. The MMB not only lacks power dissipation but also does not require a fixed operating temperature. Both Au:Er and Ag:Er are paramagnetic, displaying a broad and smooth variation in magnetization with temperature, which can be exploited to function as a precise cryogenic bolometer with minimal intrinsic noise. Even though these bolometric detectors lack an ETF mechanism to establish a set operating point, the response curve can be precisely characterized, and a calibration curve is sufficient for their use. The MMB offers an exceptionally high dynamic range without encountering saturation power within the power levels handled for CMB polarimetry.

To perform measurements of the CMB with cryogenic bolometers such as the MMB, incoming power, in the form of millimeter-wave radiation, needs to be efficiently coupled to the detector. Different types of antenna coupling architectures have been implemented for CMB detectors [81] and are currently considered state-of-the-art. RF detectors can be placed directly to one end of the antenna, or microwave circuitry can be used to perform on-chip signal processing.

Planar antenna coupled detectors are the main focus of the present thesis. They are fabricated in the same process as the RF circuitry and detectors. This approach enables to develop a multi-band or multi-chroic pixel. Antennas derived from logarithmic periodic structures are sensitive to large bandwidths [82]. Complemented with in-line band defining filters, they can be used to measure optical power in all required observation bands using one focal plane array. This is an attractive approach when the space inside the cryostat of a radiotelescope is either restricted in volume or shared between different experiments and surveys. The pixel design architecture is shown in Figure 1.5.

1.5 Outline

The goal of this thesis was twofold. First, to propose and study the suitability of the MMB as a new detector technology for CMB polarization survey and secondly, the design, fabrication and experimental analysis of a first prototype.

The suitability of the MMB is presented in Chapters 2 and 3. In Chapter 2, an appropriate radiation coupling circuit is defined. The chapter centers on an antenna coupling scheme for magnetic microbolometers, focusing on two types of planar broadband antennas: the sinuous antenna and the logarithmic spiral antenna. The total incoming power to the detector with its respective background noise is calculated considering the optics design of the QUBIC instrument. In Chapter 3, the theoretical background behind the MMB is presented. The work includes the development of multiple simulation tools to evaluate the applicability of this technology, analyzing the sensitivity by taking into account its known noise contributions. Main design parameters are also identified that can be adjusted to achieve Background Limited Photometry (BLIP) under given conditions.

Chapter 4 illustrates the path towards a working MMB prototype. Among all the required microfabrication processes, this path also included the development of a specialized machine used for bulk silicon etching based on xenon difluoride (XeF_2) designed and built during this thesis to enable the successful release of the finished devices. The release

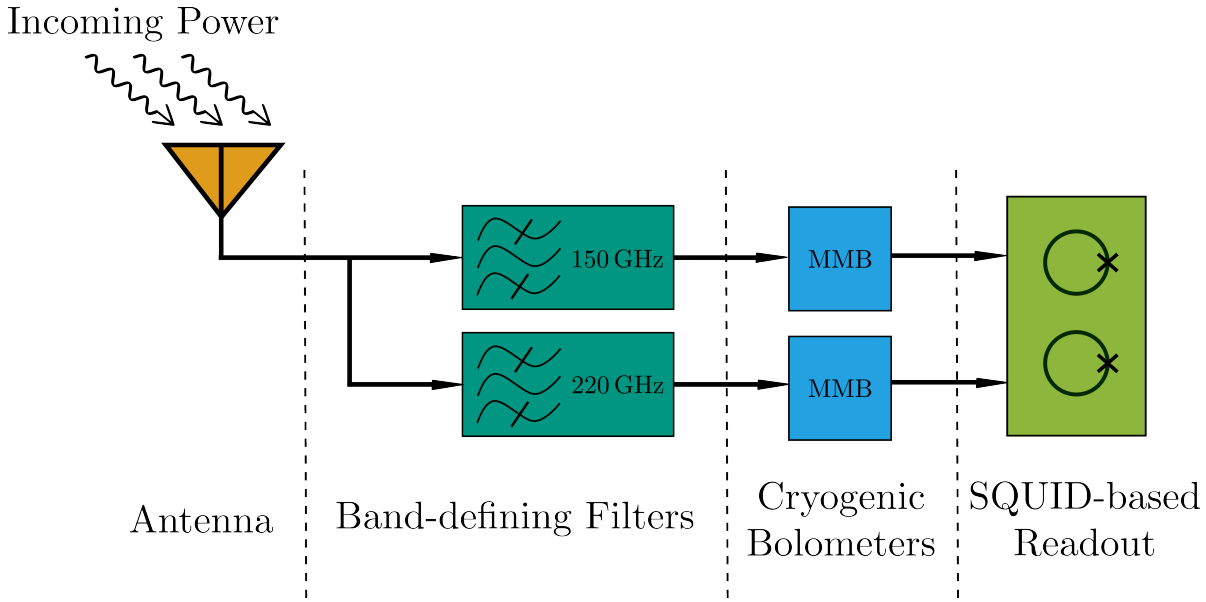

Figure 1.5: Antenna-coupled bolometer architecture investigated in this thesis for the development of the MMB detector concept. Incoming radiation is coupled to a broadband antenna, in-line band-pass filters define the observation bands of the instrument and the filtered signals are measured with MMB detectors. The detectors are readout by a SQUID-based readout system.

process is a key step in the fabrication of leg-isolated bolometers for CMB photometry in general.

Chapter 5 describes the experimental methods employed in the analysis of the fabricated MMB technical demonstrator. The cryogenic equipment and measurement tools based on the Superconducting Quantum Interference Device (SQUID) are presented.

Chapter 6 shows all relevant results extracted during characterization using a specialized measurement setup. The experience gained through the development and evaluation of this prototype establishes the foundational basis upon which the MMB detector technology is built.

Chapter 7 concludes the thesis by summarizing the potential impact of this technology on future bolometric measurements of the CMB. It highlights the further steps needed to advance the development of these promising detectors, building on the knowledge gained throughout this work.

Chapter 2

Radiation Coupling

In this chapter, the radiation coupling circuit for MMB detectors is discussed. The circuit is composed of the first two elements in Figure 1.5. Two types of planar antennas were investigated for this purpose, the sinuous antenna and the planar logarithmic spiral antenna, for polarimetric and non-polarimetric detectors respectively. Impedance matching network and in-line band defining filter design is also shown, and the optimization for multichroic pixels using both types of antennas is described in detail. Finally, the noise equivalent power for suitability study is determined, using the QUBIC instrument [45] as reference.

2.1 Electromagnetic simulations with superconductors

The MMB detectors developed within this thesis are fabricated using thin-film deposition techniques of elemental superconductors (mostly niobium) on silicon wafers. The design and simulation of the active structures of the detector must hence account for the behavior of Electromagnetic (EM) fields and waves in superconducting circuits. Using the skin effect as a starting point to consider propagation of EM waves in imperfect real conductors we can arrive to the following expression for the impedance experienced by a wave propagating along the surface of a normal metal [83]:

$$Z_s(f) = (1+j)\sqrt{\frac{\pi\mu}{\sigma}f}. \tag{2.1}$$

where μ is the magnetic permeability and σ is the surface conductivity and f is frequency. When examining metals operating at low temperatures or high frequencies, the concept of the anomalous skin effect [84] should be considered. Equation 2.1 assumes that Ohm's law applies, with current density at any location being determined exclusively by the electric field at that specific location, which is the local limit. This assumption holds true when the skin depth ($\delta(f) = \sqrt{(\pi f \mu \sigma)^{-1}}$) is significantly greater than the mean-free path (l) of electrons, $\delta \gg l$. As metals are cooled, the reduction in lattice vibrations (phonons) leads to an increase in the mean-free path. Conversely, high frequencies lead to a decrease in δ. In both scenarios, a threshold where $\delta < l$ can be reached, causing electrons to encounter changes in electric field between scattering occurrences. In

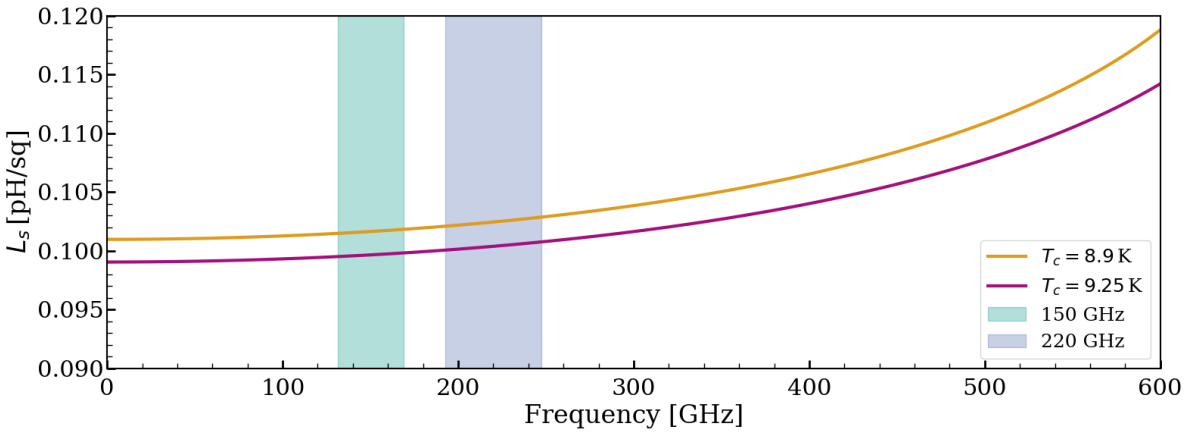

Figure 2.1: Surface inductance of superconducting niobium at $T = 300\,\mathrm{mK}$. The superconducting properties used to create the plot are $\Delta(0) = 1.76\,k_B\,T_\mathrm{c}$, $\xi_0 = 39\,\mathrm{nm}$, and $l = 33\,\mathrm{nm}$ [88]. The critical temperature (T_c) was set to 8.9 K (orange) and 9.25 K (purple), to account for sample variability during fabrication. The shaded regions in the plot correspond to the observation bands considered in the pixel design for the QUBIC instrument.

1958, Mattis and Bardeen developed equations concerning the anomalous skin effect as it pertains to superconductors [85]. They introduced the concept of complex conductivity under the extreme anomalous condition which implies that σ must have both a real and imaginary component. The imaginary part of the complex conductivity of superconductors (σ_SC) can be understood as kinetic inductance arising from the non-negligible inertia of electrons when they experience zero resistivity and must be accelerated by the EM wave propagating through the superconductor. The result is an apparent current lag following an electric field variation (inductive behavior). When σ_SC is introduced in Equation 2.1, a complex surface impedance is obtained. For a quick approximation, the surface impedance can be simplified by assuming a surface inductance $L_\mathrm{s} \approx 0.1\,\mathrm{pH/sq}$ [86].

In this thesis, Zimmermann equations of the complex conductivity [87] were used to calculate the surface impedance of the simulated superconductors. Efficient algorithms to calculate the complex surface impedance of superconductors are available in literature [86, 88]. These algorithms take the superconducting transition temperature (T_c), energy gap ($\Delta(0)$,) electron mean-free-path (l), and intrinsic coherence length (ξ_0), as inputs and outputs the resulting the complex conductivity of the superconductor (σ_SC). In Figure 2.1, the resulting surface inductance L_s value for a niobium (Nb) sample at $T = 300\,\mathrm{mK}$ as a function of frequency is shown.

The calculated Z_s is utilized in 3D EM simulation software, such as CST Microwave Studio[1] and Ansys HFSS[2], to model antenna structures and millimeter-wave circuit components. This calculation of Z_s also accounts for the finite sheet resistance that arises and accounts for conductor losses at milimeter wave frequencies associated with the used

[1] CST Microwave Studio. CST Studio Suite. CST-Computer Simulation Technology.
[2] Ansys hfss, https://www.ansys.com/

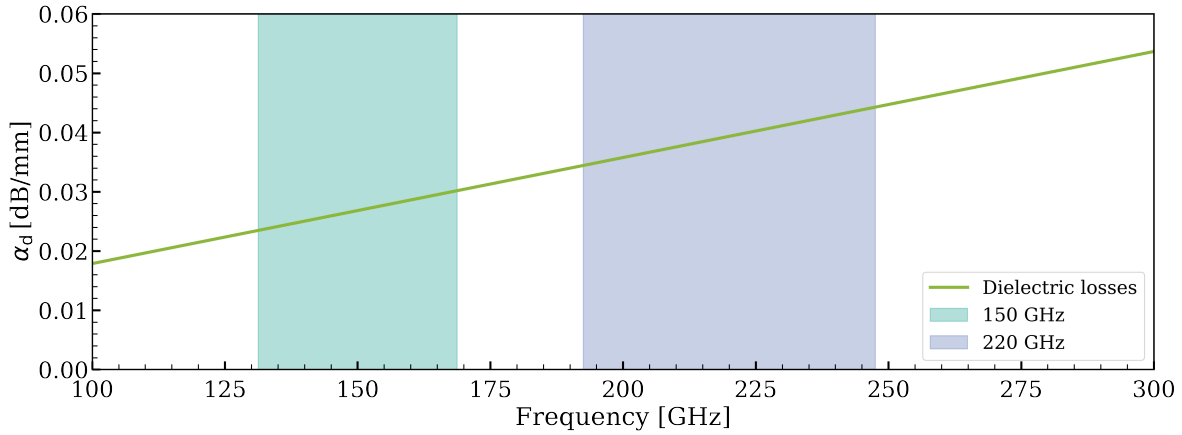

Figure 2.2: Estimated attenuation term associated with dielectric losses for our $Nb/SiO_2/Nb$ microstrip transmission lines as a function of frequency assuming $\tan\delta = 1 \times 10^{-3}$. Green and blue shaded regions represent QUBIC observation bands.

superconductor. For in-line band-defining filters, the 2.5D EM simulator SONNET[3] is employed. This software is particularly suited for simulating superconductors, as much of the formulation is handled internally based on the London theory [89].

2.2 Dielectric losses at cryogenic temperatures

Most dielectrics used in superconducting circuits, present loss tangent ($\tan\delta$) values that drop dramatically at cryogenic temperatures because phonon-mediated relaxation processes freeze out. Thus, dielectric losses associated with the silicon (Si) substrate and low silicon nitride films (LSiN) are considered negligible compared to losses arising from imperfect matching, or scattering from lithographic features. However, measurements of dielectric losses on amorphous dielectrics used in transmission lines and band-defining filters such as silicon dioxide (SiO_2) show relatively large cryogenic microwave loss tangents [90]. These losses are often explained in terms of a two-level state defect model. Values reported are in the range of $\tan\delta \approx \times 10^{-3}$ [91, 92] at frequencies of a few GHz. To a first approximation, we can assume this value to calculate the attenuation term in the propagation constant associated with dielectric losses in our transmission lines as [83]

$$\alpha_d = \frac{\pi f}{c}\sqrt{\epsilon_r}\tan\delta, \tag{2.2}$$

where f is frequency, ϵ_{eff} is the effective dielectric constant of the transmission line and c is the speed of light. Microstrip transmission lines in our pixel design have a simulated $\epsilon_{eff} \approx 3.87$. Figure 2.2 illustrates the attenuation term for a Nb microstrip transmission line as a function of frequency. The estimated attenuation is in the range of 0.02...0.05 dB/mm within QUBIC observation bands.

[3] SONNET® Precision Electromagnetics https://www.sonnetsoftware.com/

2.3 Antenna geometries

Two types of planar antennas have been investigated for the design of the multichroic pixel. These are the sinuous antenna and the logarithmic spiral (or log-spiral) antenna.

The sinuous antenna (Figure 2.3 (a)) is polarization sensitive and has been extensively used in CMB experiments [93, 94]. It offers a design improvement over other log-periodic antennas with regard to the reduced polarization wobble that is kept within an acceptable level for polarimetry in radioastronomy. A polar sinusoidal shaped cell is repeated outwards from the center with exponentially increasing size. The defining equation of the antenna, expressed in polar coordinates (ρ and ϕ), is

$$\phi(\rho) = \alpha \cdot \sin\left(\frac{\pi \cdot \ln(\rho/R_{\text{in}})}{\ln(\tau)}\right) \pm \delta, \tag{2.3}$$

with $R_{\text{in}} < \rho < R_{\text{out}} = R_{\text{in}} \cdot \tau^N$, where α is the angular amplitude of the switchback arms, R_{in} being the inner radius of the antenna, τ being the growth rate of the active regions, δ being the angular width of the traces, and N being the number of repeating cells in the antenna, and R_{out} being the outer radius of the antenna. The inner and outer radii are selected according to the required detector bandwidth:

$$R_{\text{in}} = \frac{\lambda_{\text{high}}}{8(\alpha+\delta)}, \text{ and, } R_{\text{out}} = \frac{\lambda_{\text{low}}}{4(\alpha+\delta)}, \tag{2.4}$$

where λ_{low} and λ_{high} are the wavelengths at the lowest and highest frequency, respectively. To couple both linear polarizations, two pairs of opposing arms are constructed. The resulting geometry consists of four sinuous arms that are rotated 90 ° with respect to each other. In this configuration, and when choosing $\alpha = \pi/4$ and $\delta = \pi/8$, a self-complementary design is achieved, meaning that both the blank and filled areas of the pattern are identical within the inner and outer radii, as can be seen in Figure 2.3 (a).

Each polarization is measured with a dedicated detector, requiring two detectors per observation band. For instruments such as QUBIC, where a polarizing grid and rotating half-wave plate are used for polarimetry, both detectors should be summed to measure the total incoming power in dual-polarization mode. An alternative geometry is the log-spiral antenna [82]. This antenna (Figure 2.3 (b)) is circularly polarized and can be used to couple linearly polarized radiation in any orientation. To avoid penalizing the optical throughput, a geometrical conversion from linear to circular polarization is needed. This is achieved by means of a quarter-wave plate at 45 degree angle with respect to the polarizing grid. This approach only requires one detector per band at the expense of an additional quarter-wave plate in the optical system.

The geometry of a log-spiral antenna consists of two opposing arms that are defined by

$$\rho(\phi) = R_{\text{in}} \cdot e^{\tau(\phi \pm \delta)}, \tag{2.5}$$

with $0 < \phi < 2\pi N$, and $\tau = \frac{\ln(R_{\text{out}}/R_{\text{in}})}{2\pi N}$, where R_{in} is the inner radius of the antenna, τ is the growth rate of the active regions, δ is the angular width of the traces, and N is

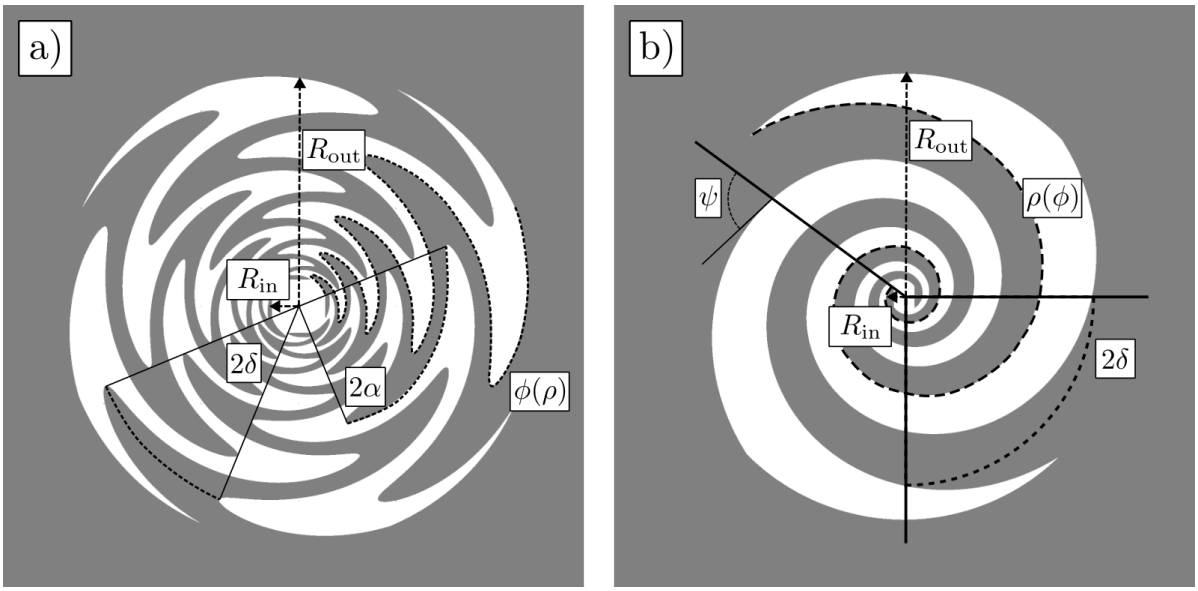

Figure 2.3: Antenna geometries designed for the multichroic detector pixel with their respective design parameters. **a)**: Sinuous antenna with a self-complimentary design ($\alpha = \pi/4$ and $\delta = \pi/8$). **b)**: Logarithmic spiral antenna also with a self-complimentary design ($\delta = \pi/8$).

the number of full rotations for each arm. With this antenna design, the inner and outer radii are defined as

$$R_{\text{in}} = \frac{\lambda_{\text{high}}}{4}, \text{ and, } R_{\text{out}} = \frac{\lambda_{\text{low}}}{2\pi}. \tag{2.6}$$

2.4 Silicon lenses

The thickness of the wafer is small with respect to the far-field region, and when combined with a silicon-vacuum interface (representing a step-like refractive index variation), it yields a non-optimal radiation lobe, which in some cases can even present zero forward gain on boresight. The angular width and forward gain of the antenna's radiation pattern can be enhanced by the use of lenses. The material used for such lenses is required to match the refractive index of the silicon substrate to avoid reflections at the substrate-lens interface. In addition, the lenses' surface is coated with multiple layers of anti-reflection coatings to further minimize reflections at the silicon-vacuum interface. The permittivity of silicon is relatively high $\epsilon_{\text{Si}} \approx 11.75$ [95] and a refractive index, $n_{\text{Si}} = \sqrt{\epsilon_{Si}} \approx 3.43$. By the addition of the lens, the antenna can be considered to sit in between two well-defined media, a vacuum media ($\epsilon = 1$) to one side and a silicon media to the other side. Electromagnetic radiation propagates preferentially into high-permittivity media, suppressing back lobe radiation and rendering the antenna unidirectional.

The optimal shape for the lens is an ellipse with eccentricity equal to the inverse of the refractive index. However, fabrication of these type of lenses with an elliptical shape is challenging to achieve in the small scales required. The most popular approach is the

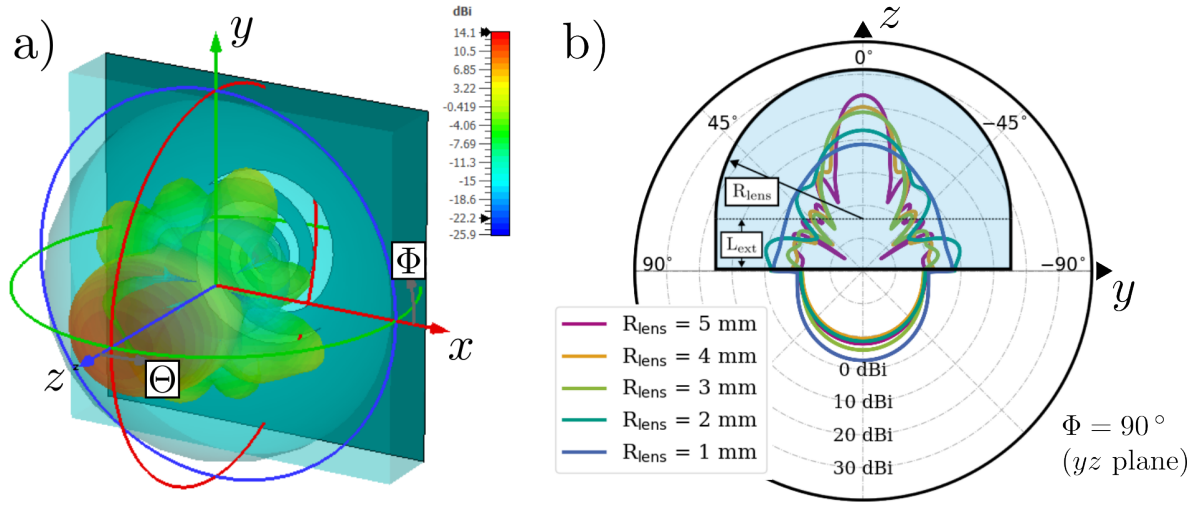

Figure 2.4: a) Simulated radiation lobe of the log-spiral antenna, including the extended hemispherical lens. **b)** Side-view sketch of the resulting structure with the radiation lobes for various lens radii (R_{lens}).

use of the extended hemispherical lens that consists of a half sphere with a cylindrical extension length, L_{ext}. Increasing the value of L_{ext} has been demonstrated to increase the antenna's directivity until the diffraction-limited condition is met at the elliptical point, this occurs at $L_{\text{ext}} = 0.38 R_{\text{lens}}$ [96, 97]. Placing the extended hemispherical lens on the backside of the detector wafer can be used to efficiently couple the detector to the radio telescope as well as to prevent substrate and surface modes from propagating [77, 98].

Radiation lobe simulations of the log-spiral antenna including hemi-spherical silicon lenses are shown in Figure 2.4, considering multiple lenses with varying R_{lens} and appropriate L_{ext} for each case. Increasing R_{lens} increases the antenna gain on boresight, which also translates to narrower and more directional beam shapes. The adequate directivity is ultimately given by the telescope f/D ratio.

The efficiency associated with the lens was also explored. As radiation propagates through different media, the signal can be transmitted, absorbed, or reflected. Absorption can be neglected, as dielectric and semiconductor materials at very low temperatures can be regarded as lossless media. However, at the interface between the vacuum and the silicon lens, the traveling wave encounters a significant change in refractive index. This produces a mismatch in wave impedance between the lens interior and exterior that leads to almost a third of incoming radiation being reflected and not reaching the detector. We can calculate the reflection losses for normal incidence (R) using the Fresnel equation [99] that relates the refractive index of both media ($n_{\text{air}} = 1$ and $n_{\text{Si}} = 3.43$).

$$R = \left(\frac{n_{\text{Si}} - n_{\text{air}}}{n_{\text{Si}} + n_{\text{air}}} \right)^2 = 0.298, \tag{2.7}$$

meaning that 29.8 % of the incoming radiation is reflected at the silicon-vacuum interface, resulting in substantial signal loss. To mitigate this losses, a series of Anti-Reflection (AR) coatings can be applied to the surface of the silicon lens. By introducing layers with

intermediate wave impedance, the total reflected portion of the incoming radiation can be substantially reduced. In the case of a single layer, a refractive index equal to the geometric mean between both media, $n_{\mathrm{AR}} = \sqrt{n_{\mathrm{air}} \cdot n_{\mathrm{Si}}} = 1.84$ and length equal to a quarter-wavelength is the optimal solution. The reflection R as a function of frequency can be calculated for an arbitrary number of AR coating layers, thicknesses, and angles of incidence. Assuming normal incidence of radiation, we can define the characteristic matrix of an assembly of N thin film coatings as [100]

$$\begin{bmatrix} B \\ C \end{bmatrix} = \prod_{i=1}^{N} \begin{bmatrix} \cos(\delta_i) & j\,\sin(\delta_i)/n_i \\ j\,n_i \sin(\delta_i) & \cos(\delta_i) \end{bmatrix} \cdot \begin{bmatrix} 1 \\ n_{\mathrm{s}} \end{bmatrix}, \text{ with, } \delta_i = \frac{n_i d_i f}{c}, \tag{2.8}$$

where n_i is the refractive index of the AR coating layer, d_i is the layer thickness, and n_s is the refractive index of the substrate (n_{Si}). Then, the reflectance of the system is given by $\Upsilon(f) = C/B$. The total reflection of the coated lenses is estimated using the Fresnel equation

$$R(f) = \left| \frac{n_{\mathrm{air}} - \Upsilon(f)}{n_{\mathrm{air}} + \Upsilon(f)} \right|^2. \tag{2.9}$$

The combined effect of these layers significantly reduces total reflection and enhances the efficiency of the optical coupling. The layers are optimized for an intermediate frequency between the 150 GHz and 220 GHz bands. For configurations with two or more layers, the refractive indices are selected to match the wave impedance of Chebyshev multisection transformers [83]. Increasing the number of layers allows for low reflection over a broader bandwidth. However, achieving these results requires precise control of the refractive indices and exact quarter-wave layer thicknesses. In practical implementations, efficiency may be constrained by material availability and fabrication tolerances. A cost-effective and scalable approach using polytetrafluoroethylene (PTFE) materials with intermediate low density polyethilene (LDPE) bonding layers to fabricate three-layer AR coatings has been demonstrated [101]. The methods proved high optical efficiencies, with reported measurements reaching up to 99.4 % for the 150 GHz band. The AR coatings were designed for the SPT-3G focal plane installed in the South Pole Telescope [102].

Table 2.1 specifies the ideal refractive index of each AR coating layer with their target thicknesses and also values for commercially available PTFE-based AR solutions developed for the SPT-3G camera. The resulting reflection R in percentage as a function of frequency is shown in Figure 2.5.

For the development of the MMB as a CMB detector pixel, the addition of contacting lenses is a requirement. Appropriate AR coatings enhance the optical efficiency, as they reduce the signal losses due to reflection at the vacuum-lens interface. For the suitability analysis that will follow in Chapter 3, the coupled signal, assuming an extended hemispherical lens with and without AR coatings, is considered to assess the full potential realization of this detector concept in CMB surveys.

Layer	1 AR coating	2 AR coatings	3 AR coatings	SPT-3G
1 n_1 (d_1)	1.84 (220 μm)	1.38 (294 μm)	1.24 (327 μm)	PM-23J: 1.32 (307 μm)
2 n_2 (d_2)	-	2.44 (166 μm)	1.84 (220 μm)	RO3035: 1.87 (217 μm)
3 n_3 (d_3)	-	-	2.74 (148 μm)	RO3006: 2.56 (158 μm)

Table 2.1: Refractive indices for the AR coatings with their respective thicknesses in brackets for ideal transmission and values using custom materials published for SPT-3G [101].

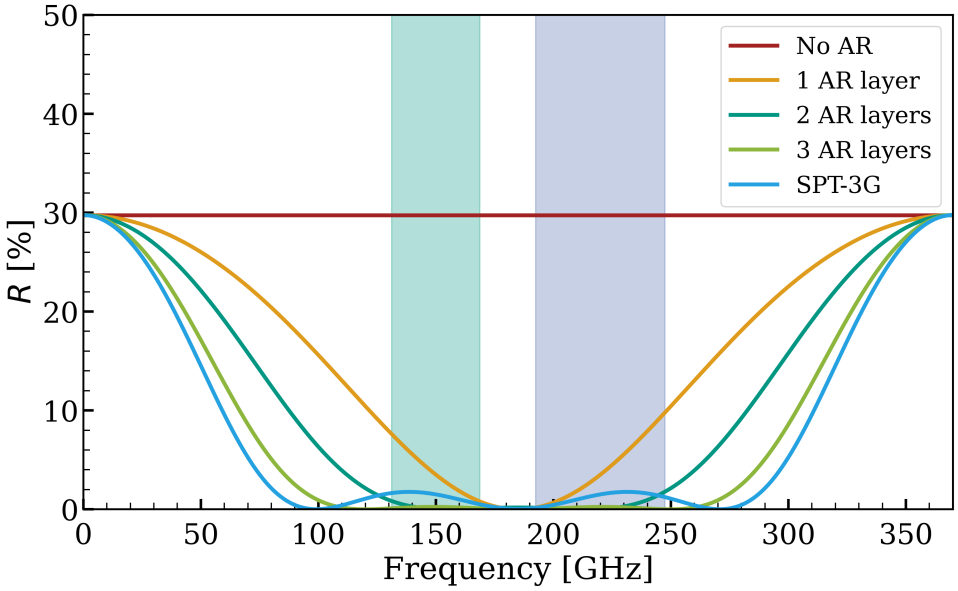

Figure 2.5: Relectance at the vacuum-silicon interface of the coupling lenses with increasing number of anti reflection coatings. The reflection considering the AR coatings with the materials used in SPT-3G [101] focal plane are also shown. The observation bands at 150 GHz and 220 GHz with 25 % fractional bandwidth are also shown in green and blue shaded regions, respectively.

2.5 Antenna impedance

The Booker-Babinet principle [103] states that the input impedance (Z_{in}) of a two-port infinite antenna and its complement satisfy

$$Z_{\text{in}} \cdot \overline{Z_{\text{in}}} = \left(\frac{\eta_0}{2}\right)^2,$$

where η_0 is the impedance of free space, and $\overline{Z_{\text{in}}}$ is the impedance of the antenna's complement. Both the sinuous and log-spiral antennas are designed as self-complementary structures. In these cases, both Z_{in} and $\overline{Z_{\text{in}}}$ and are equal to $\frac{\eta_0}{2} = 188.5\ \Omega$. In the case of the sinuous antenna, the equation must be modified because it is a four-port network. Deschamps generalization of the Booker-Babinet principle [104] allows calculating the

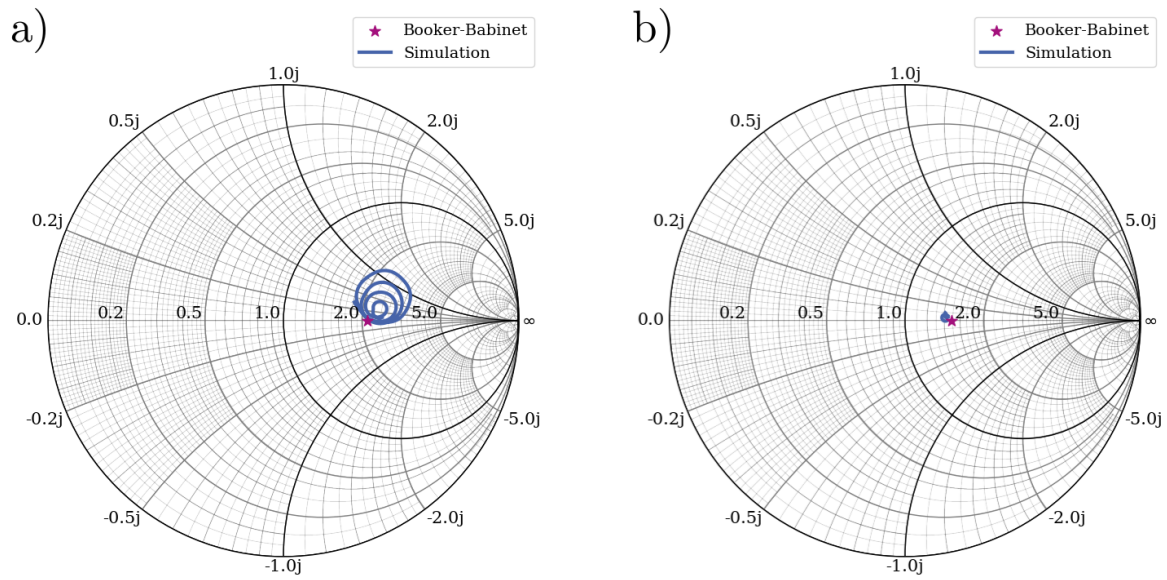

Figure 2.6: Smith charts displaying simulated Γ curves of **a)** the sinuous antenna and **b)** the log-spiral antenna. Both Smith charts are normalized to an impedance $Z_0 = 50\,\Omega$. Γ is shown as a solid blue trace within the bandwidth of interest. The frequency-independent values of Γ for each antenna calculated with the Booker-Babinet equations are also displayed with a purple star.

impedance for N-port infinite antennas as

$$Z_{\text{in}}^{m} \cdot \overline{Z_{\text{in}}^{m}} = \frac{\left(\frac{\eta_0}{4}\right)^2}{\sin^2\left(\frac{m\pi}{N}\right)},$$

where m stands for one of the N eigenmodes, $m = \{0, 1, 2, ..., N-1\}$. In this case, $N = 4$, modes $m = 0$ and $m = 2$ are phase shifted by 180° between opposing arms so the radiation of these modes cancel on boresight, the only useful modes are $m = 1$ and $m = 3$,

$$Z_{\text{in}}^{1} = Z_{\text{in}}^{3} = \frac{\eta_0}{2\sqrt{2}} = 133.28\,\Omega,$$

and the total impedance between pairs of opposing arms is

$$Z_{in} = \frac{\eta_0}{\sqrt{2}} = 266.57\ \Omega.$$

The structures are fabricated on silicon substrates and silicon lenses are used to enhance the beam shape. Effectively, an infinite half space of silicon is formed. The value of η_0 is replaced considering an equivalent dielectric constant, assuming a homogeneous space by averaging the dielectric constants of the vaccuum ($\epsilon_0 = 1$) and silicon ($\epsilon_{Si} = 11.75$) half spaces the impedances for the log-spiral (Z_{spiral}) and sinuous (Z_{sinuous}) antennas are

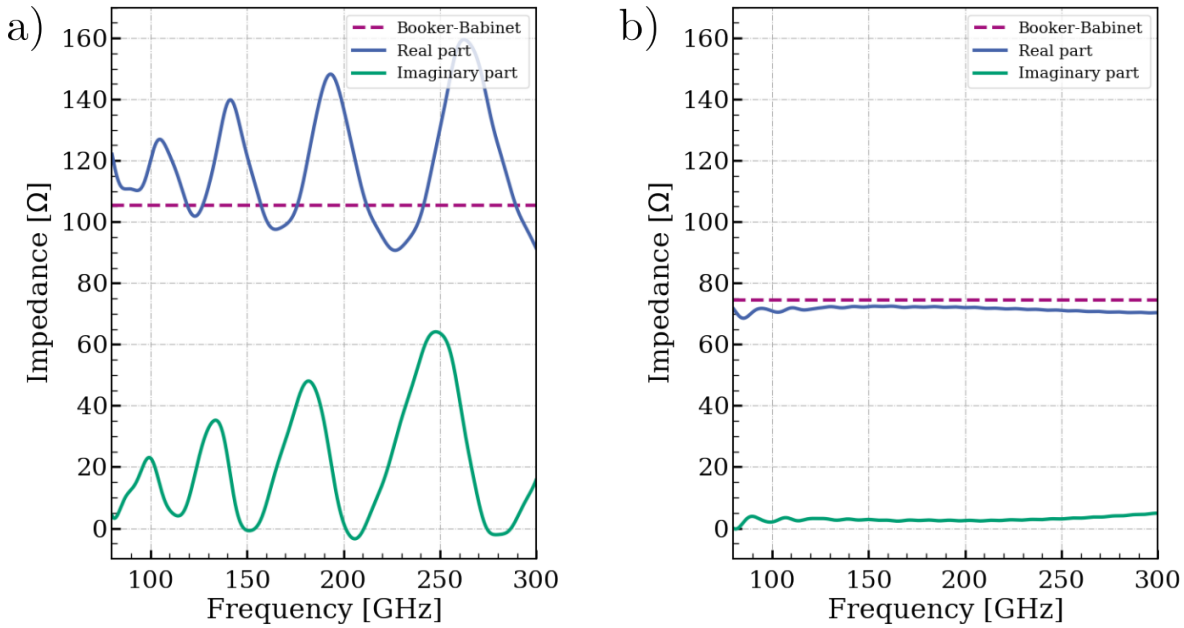

Figure 2.7: Simulated Z_{in} of **a)** the sinuous antenna and **b)** the log-spiral antenna. The real (blue) and imaginary (green) parts of Z_{in} are displayed. The frequency-independent value calculated with Booker-Babinet equations is also shown for each antenna with dashed purple traces.

$$Z_{\text{spiral}} = \frac{\eta_0}{2 \cdot \sqrt{6.4}} = 74.51\,\Omega, \tag{2.10}$$

$$Z_{\text{sinuous}} = \frac{\eta_0}{\sqrt{2} \cdot \sqrt{6.4}} = 105.37\,\Omega. \tag{2.11}$$

The antennas are not truly self-complimentary due to the high permitivity silicon substrate. To transform it to its compliment we must exchange high-permittivity materials with high-permeability materials. This makes the antenna's impedance dependent on frequency and also presents an added reactance. Figures 2.6 and 2.7 display the simulated reflection coefficient (Γ) and input impedance (Z_{in}), respectively, for (a) the sinuous antenna and (b) the spiral antenna. The calculated Z_{in} using the Booker-Babinet equations is also marked and displayed for comparison.

Both antennas exhibit an inductive reactance that is attributed to the inhomogeneous propagation media described. The sinuous antenna in particular shows a large variation in the impedance with respect to frequency. This large variation can be lowered by choosing τ values closer to unity [96].

2.6 Matching network

Microstrip transmission lines are employed to guide the coupled signal from the antenna to the cryogenic bolometers (third components in Figure 1.5). To achieve high impedances,

such as Z_{sinuous}, with a 500 nm thick SiO_2 dielectric layer, a line width below 1 μm is required. Microfabrication facilities available cannot reliably produce millimeter-wave circuits with submicron tracks at an acceptable yield. As a result, a wider microstrip line, around 10 μm, is preferred. For this implementation, a line impedance of 10 Ω was chosen, corresponding to a width of 8.4 μm.

To match the antenna impedance, a multisection matching transformer or tapered line was designed using a specific impedance profile $Z_0(x)$, where x is the position along the line. This profile can take many shapes according to the specific application. A linear taper, for example, consists of a linearly increasing or decreasing impedance from the source Z_1 to the load Z_2,

$$Z_0(x) = Z_1 + \frac{Z_2 - Z_1}{L} \cdot x, \tag{2.12}$$

where L is the length of the taper and $0 \leq x < L$. The band-pass characteristics of such a taper, however, are not ideal. Exponential tapers such as

$$Z_0(x) = Z_1 e^{\frac{1}{L}\ln(Z_2/Z_1)\cdot x} \tag{2.13}$$

are another option that can moderately improve the response at lower frequencies but can still be further optimized. Superior techniques involve Chebyshev polynomials introduced in the calculation of $Z_0(x)$ to optimize bandwidth at the expense of band-pass ripple [83]. Examples of highly efficient and commonly used profiles are Dolph-Chebyshev [105] and Klopfenstein [106].

A Dolph-Chevyshev taper has a position-dependent impedance following,

$$\ln[Z_0(x)] = \ln(Z_1) + \frac{1}{2}\ln\left(\frac{Z_2}{Z_1}\right) \cdot \sin\left[\pi\left(\frac{x}{L} - \frac{1}{2}\right) + 1\right]. \tag{2.14}$$

Here, the taper length determines the low cutoff frequency when L equals half the wavelength. The Klopfenstein taper is calculated as

$$\ln(Z_0(x)) = \begin{cases} \frac{1}{2}\ln(Z_1 Z_2) + \frac{\rho_0}{cosh(A)} \cdot \left[A^2\phi(2x/L, A) + U(x - L/2) + U(x + L/2)\right], & |x| \leq L/2, \\ \ln(Z_2), \quad x > L/2, \\ \ln(Z_1), \quad x < L/2, \end{cases} \tag{2.15}$$

where $U(x)$ is the heaviside step function,

$$U(x) = \begin{cases} 0, & x < 0, \\ 1, & x > 0, \end{cases} \tag{2.16}$$

and the ϕ function is defined as

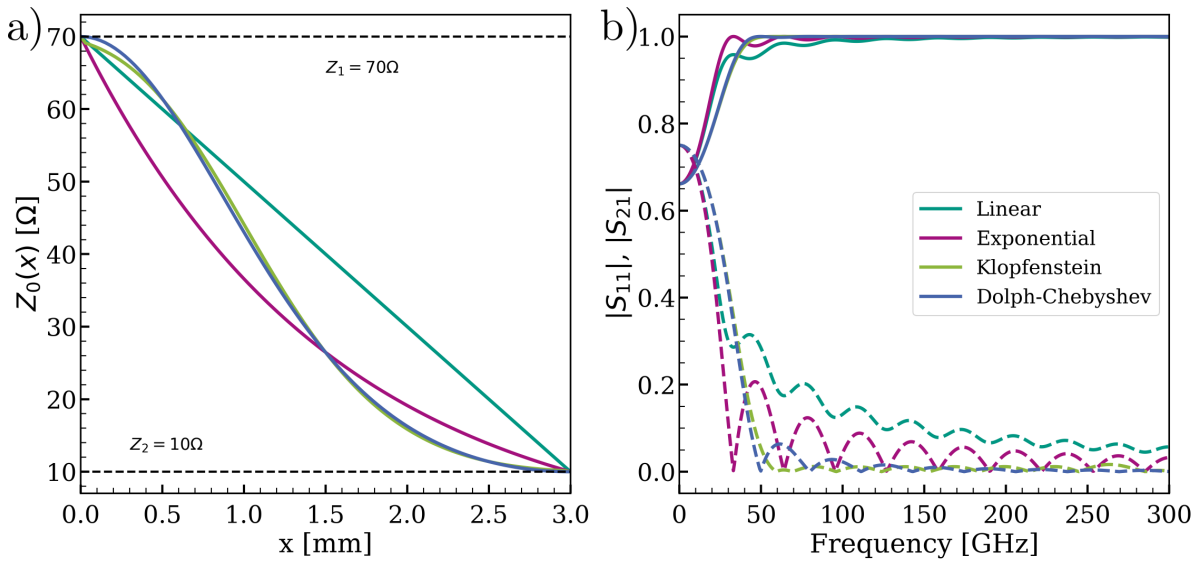

Figure 2.8: a) Different impedance profiles following linear, exponential, Klopfenstein and Dolph-Chebyshev profiles used to compute the impedance of the short line sections in the theoretical taper model. **b)** The modulus of the resulting transmission coefficient $|S_{21}|$ and reflection coefficient $|S_{11}|$ are shown in solid and dashed traces, respectively.

$$\phi(z, A) = -\phi(-z, A) = \int_0^z \frac{I_1(A\sqrt{1-y^2})}{A\sqrt{1-y^2}} dy, \quad |z| \leq 1. \tag{2.17}$$

with $I_1(x)$ that is the Bessel function of the first order and $A = \operatorname{arccosh}(\frac{\ln(Z_2/Z_1)}{2R_P})$, where R_P is the maximum ripple admissible within the taper bandwidth.

To compare the performance of each described taper, a transmission line composed of a large number of short line sections of length Δx and impedance $Z_0 = Z_0(x)$ according to the impedance profiles was studied. The scattering matrix is calculated by equating all chained sections. It is important to note that for the theoretical analysis, the scattering matrix of the taper has different normalization impedances for input and output ports equal to the source and load impedances, respectively. For this analysis a $Z_1 = 70\,\Omega$, $Z_2 = 10\,\Omega$ and $L = 3\,\text{mm}$ was assumed.

In Figure 2.8, the four impedance profiles as a function of x, and calculated $|S_{11}|$ and $|S_{21}|$ parameters for each profile are shown. The cutoff frequency (f_c) observed in the scattering parameters is consistent with $\lambda_c = c/\sqrt{\epsilon_r} f_c = 2L$, a permittivity of $\epsilon_r = 3.9$ was specified as a preliminary estimation for the transmission lines resulting in $f_c \approx 25.3\,\text{GHz}$.

The linear taper shows the highest reflection coefficient within the bandwidth of the taper. The exponential taper reflection remains below that of the linear taper but still presents a substantial ripple. It can be seen how Dolph-Chebyshev and Klopfenstein tapers achieve a very low reflection coefficient as opposed to the previous methods. The Klopfenstein taper yields a stable and constant low ripple along the entire bandwidth that is below that of the Dolph-Chebyshev for the lower frequencies. For higher frequencies, the Dolph-Chebyshev taper becomes superior. In practice, as can be seen in Figure 2.8

(a), the impedance profiles of these two alternatives are very similar, and when considering the technological aspects of the fabrication of these matching networks, it can be argued that there is no clear advantage of one with respect to the other. Both achieve a stable and flat broadband transmission that meets the application requirements. In the end, a Dolph-Chebyshev profile is chosen within this thesis because of the reduced complexity in the calculation of the impedance profile.

To synthesize the taper, even though there exist empirical expressions that relate the microstrip width w, substrate height h and dielectric constant ϵ to the characteristic impedance Z_0, there is no closed-form inverse expression that allows to calculate $w(x)$ as a function of Z_0. For this reason, the width profile is determined numerically by calculating $w(x_0)$ for each $Z_0(x_0)$, where $0 < x_0 < L$, and a polynomial fit of the resulting discrete $w(x_0)$ values is then used for interpolation. As a final step, the optimized width profile $w(x)$ is adjusted to match the antenna's arms. This process involves numerically sampling the antenna's defining equation and assigning the corresponding width at each coordinate. The line integral of the antenna's defining equation determines L and, in consequence, the cutoff frequency of the taper.

In Figure 2.9 the impedance and approximated width profile design are shown together with the taper design for a sinuous antenna using the methods described. Simulations of a straight and sinuous taper using 3D EM simulation software are compared with the theoretical curve obtained with the simplified numerical analysis. The quality of the taper response is impaired by the designed implementation, in principle because of subtle differences in the resulting impedance profile and, in the case of the sinuous taper, the switchbacks visible at each logarithmic cell. The slight difference in the cutoff frequency, can be attributed to the discrepancies in the utilized effective permittivity for the width calculation compared to that of the more precise values determined by the EM simulations. In this example, a source impedance of $Z_1 = 70\,\Omega$ and load impedance of $Z_2 = 10\,\Omega$ is used, to showcase the results of the taper design process. Any two real source and load impedances can, in principle, be matched with this technique while keeping in mind the Bode-Fano criterion [107], with which the minimum achievable ripple in the pass-band of a matching network of these characteristics can be foreseen.

2.7 Band-defining filters

Observation bands in the pixel architecture shown in Figure 1.5 are determined using in-line band-pass filters that shape the pixel response for each bolometer. Ground-based observations necessitate a broad band-pass to capture sufficient integrated power while maintaining a sharp roll-off to suppress atmospheric emission lines. The filtered bands are centered at 150 GHz and 220 GHz, each with a fractional bandwidth of 25 %. For this application, Chebyshev filters are preferred due to their controlled passband ripple and steep roll-off characteristics. The close spacing of the observation bands requires high stop-band rejection to minimize crosstalk between channels. To meet these requirements, 5^{th}-order Chebyshev filters were chosen. These filters provide the desired performance characteristics and can be fabricated within the small dimensions suitable for the pixel

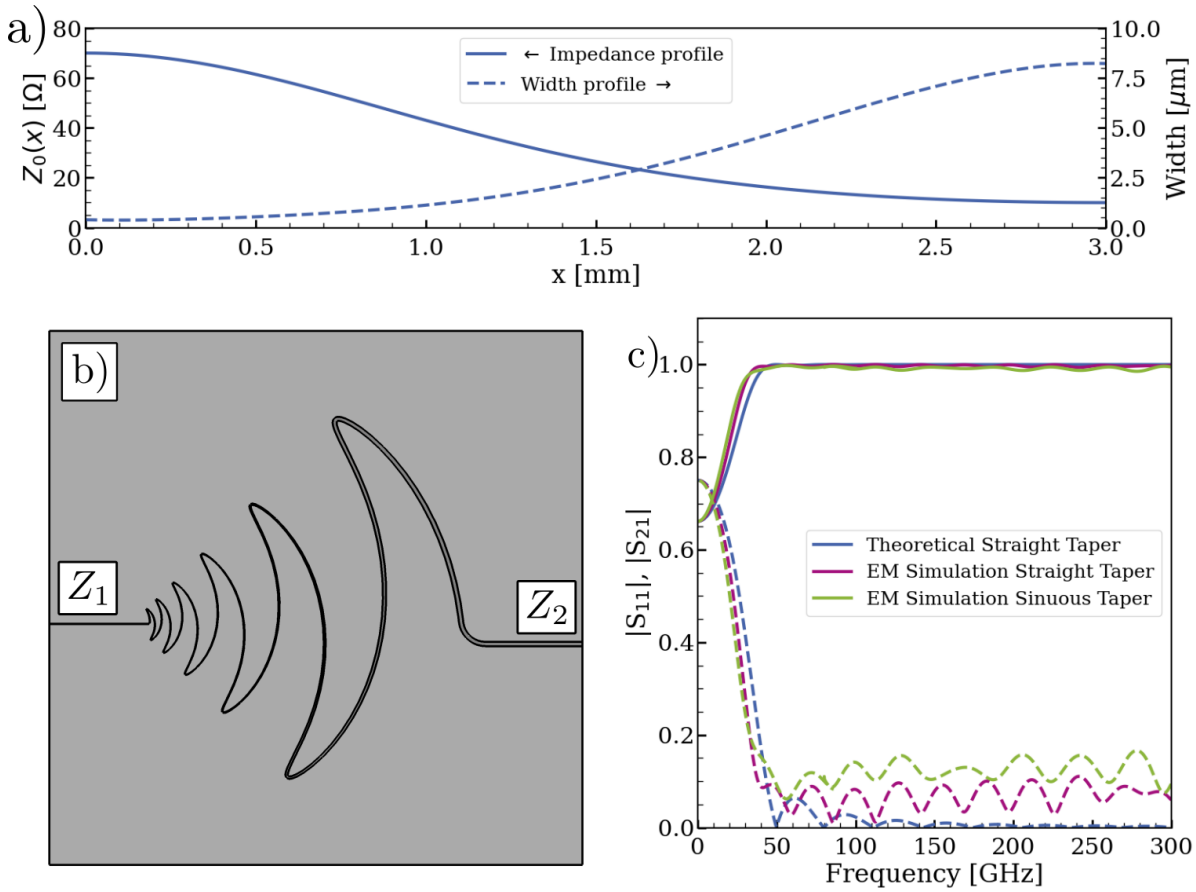

Figure 2.9: a) Impedance and width profiles for the Dolph-Chevyshev taper design. **b)** Design of the taper for the sinuous antenna, the path of the taper is designed to follow the antenna's arms. **c)** Comparison of the theoretical analysis of the taper and EM simulations for the basic straight and final sinuous design. The resulting transmission coefficient S_{21} is shown in solid trace and reflection coefficient S_{11} in dashed traces for each case.

design.

The filters are implemented from their component values, following fundamental circuit theory [83]. Subsequent circuit transformations [108] are applied to achieve a tubular band-pass topology, shown in Figure 2.10. The filter template is selected to present a ripple below 0.5 dB in addition to the 25 % fractional bandwidth specified.

The filter circuits are symmetric and reciprocal, resulting in the following relations $L = L_1 = L_2 = L_3 = L_4 = L_5$, $C_{11} = C_{42}$, $C_{12} = C_{41}$, $C_{13} = C_{43}$, $C_{21} = C_{32}$, $C_{22} = C_{31}$ and $C_{23} = C_{33}$. In Table 2.7, the values determined for each component of the tubular filters are shown.

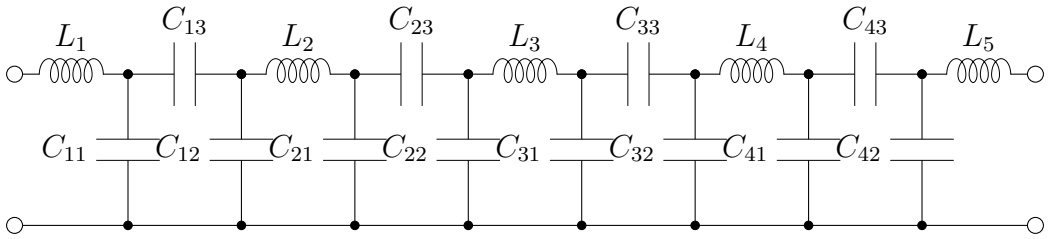

Figure 2.10: Tubular circuit topology implemented for the in-line band-defining filters.

Element	150 GHz BPF	220 GHz BPF
L	60.33 pH	49.36 pH
C_{11}	12.22 fF	7.486 fF
C_{12}	31.10 fF	18.06 fF
C_{13}	8.124 fF	3.768 fF
C_{21}	29.09 fF	17.11 fF
C_{22}	27.45 fF	16.37 fF
C_{23}	14.95 fF	6.749 fF

Table 2.2: Element values calculated for the 5$^{\text{th}}$-order Chebyshev in-line band-defining filters.

A lumped-element method is used to implement the filters. Impedance steps are strategically introduced in the transmission line to resemble lumped components and build the circuit shown in Figure 2.10. To ensure each line section behaves as a lumped element, its length must be limited to be less than $\lambda/8$ [109]. High-impedance sections of the transmission lines are used to synthesize series inductors, while low-impedance sections create shunt capacitors. Series capacitors are formed by introducing interruptions in the lines with floating ground planes to increase the capacitance.

The following equation is used to estimate the required line lengths l_{ind} for a series inductor of value L [109]:

$$l_{\text{ind}} = \frac{\lambda_L}{2\pi} \sin^{-1}\left(\frac{2\pi f_0 \cdot L}{Z_{0L}}\right). \tag{2.18}$$

Here, f_0 is the operating frequency, and Z_{0L} and λ_L are the line impedance and wavelength of the inductor section, respectively. Z_{0L} is adjusted by reducing the width (w) of the line to ensure a section length well below the $\lambda/8$ limit. Later, 2.5D EM simulations were performed to further adjust the lengths of each line section.

Microstrip lines in this configuration cannot achieve arbitrarily high impedance levels. To address this, an opening is introduced in the ground plane of the line, transforming it into a coplanar waveguide (CPW). By adjusting the gap (g) on either side of the main line with a narrower width, the impedance can be increased to relatively high values, reducing l_{ind} as needed to achieve a lumped-element behavior. The resulting schematic and physical implementation of the inductor are shown in Figure 2.11, respectively. The inductive CPW lines have $w = 4\,\mu$m and, $g = 20\,\mu$m. The length of the inductors was adjusted to present the required inductance values, these results are also shown in Figure 2.11 (c).

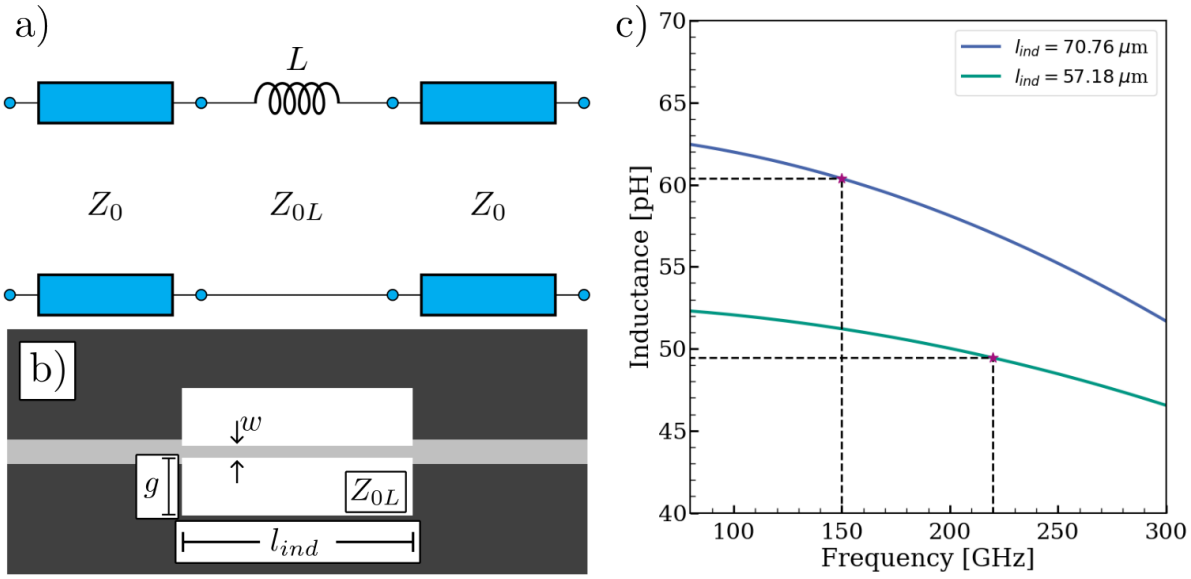

Figure 2.11: a) Schematic of the inductive CPW line. **b)** Design layout design for the inductor, the dark gray sections represent the groundplane while the lighter gray areas represent the stepped-impedance transmission lines. **c)** Optimized length values for the inductors appearing in the band-pass filters for the 150 GHz and 220 GHz bands at their respective central frequencies.

In the case of the capacitor π-network, a lower impedance section in the microstrip line is regarded as a shunt capacitor and can be produced by increasing w. An interruption in the transmission line produces a series capacitor, this interruption can be as small as fabrication tolerances allow. For a conservative approach, a 4 μm gap is selected, and therefore the series capacitance value is fixed to a relatively low value. The series capacitance is increased by cutting a rectangular section in the ground plane below the opening to increase the effective area. The schematic circuit of the π-network, its implementation, and the optimization results are shown in Figure 2.12.

With the optimized dimensions for each filter component, the tubular circuit topology is built. The simulated response of the filters does not perfectly match the theoretical response due to the frequency-dependent behavior of the components. As illustrated in Figures 2.11 and 2.12, the target values for these components can only be achieved at a specific frequency, which is selected as the center frequency for each filter. To address these discrepancies, each filter is individually optimized, leaving free parameters to compensate for the variations. Figure 2.13 presents the simulated S_{21} parameter for the 150 GHz and 220 GHz filters. To fully implement the diplexer circuit, the two filters must be connected as a three-port network. While each filter is optimized to function individually, connecting them into a single circuit introduces interference between their responses. Therefore, an additional EM optimization step was carried out on the final diplexer. This optimization focused primarily on the first inductor and capacitor π-network to accommodate the responses of both filters and ensure the diplexer splits the observation bands efficiently.

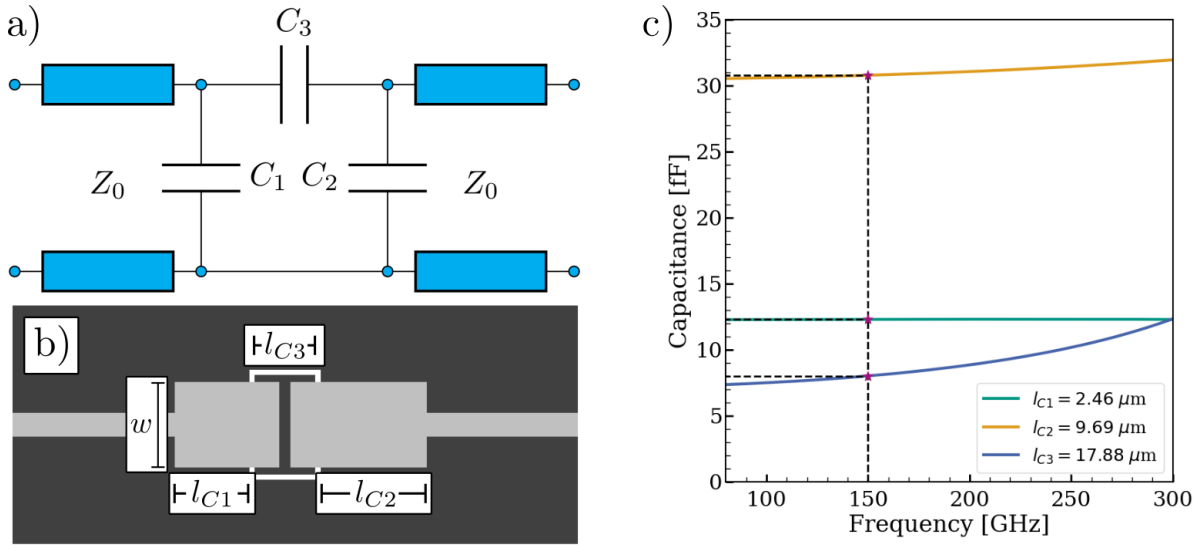

Figure 2.12: **a)** Schematic of the capacitive π-network. **b)** Design layout of capacitive π-network, the dark gray sections represent the groundplane while the lighter gray areas represent the stepped-impedance transmission lines. **c)** Capacitor length values adjusted for the 150 GHz and 220 GHz bands at their respective central frequencies.

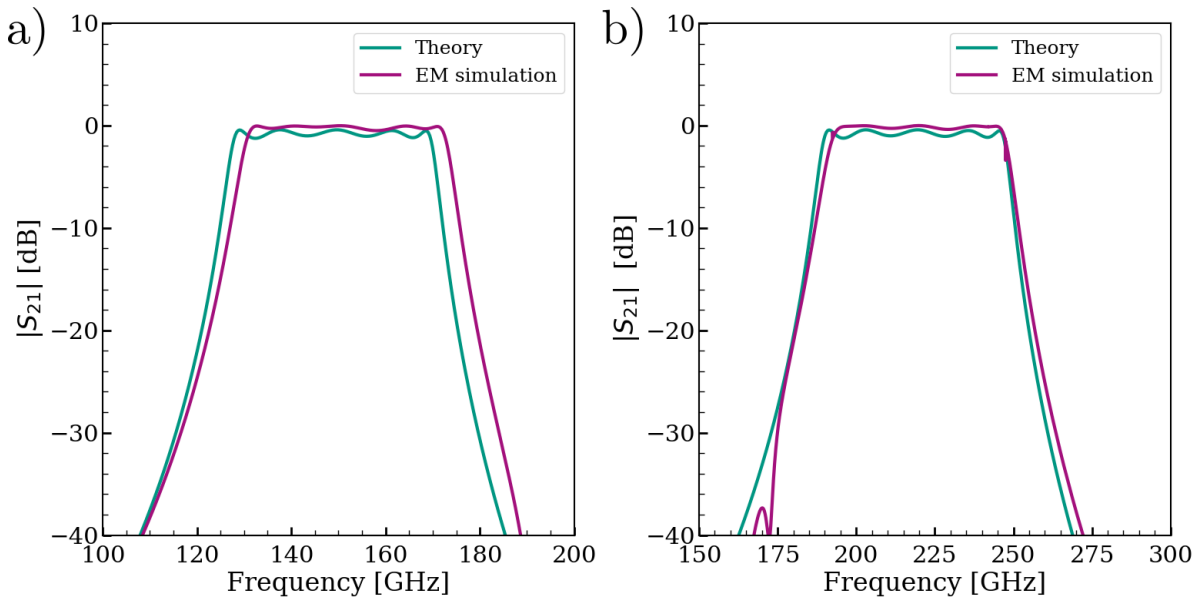

Figure 2.13: $|S_{21}|$ parameter of the 150 GHz (**a**) and 220 GHz (**b**) band-pass filters. The green trace represents the theoretical response of the filters, as calculated using discrete circuit components in LTSpice. The purple trace corresponds to the EM simulations performed with SONNET® after optimization.

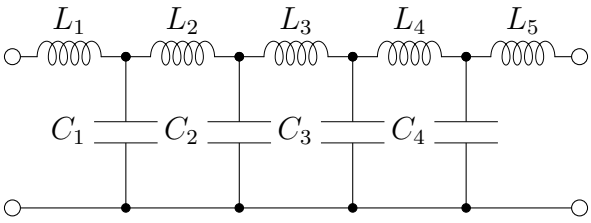

Figure 2.14: Ladder-type circuit implemented in the physical realization of the 300 GHz low-pass filters.

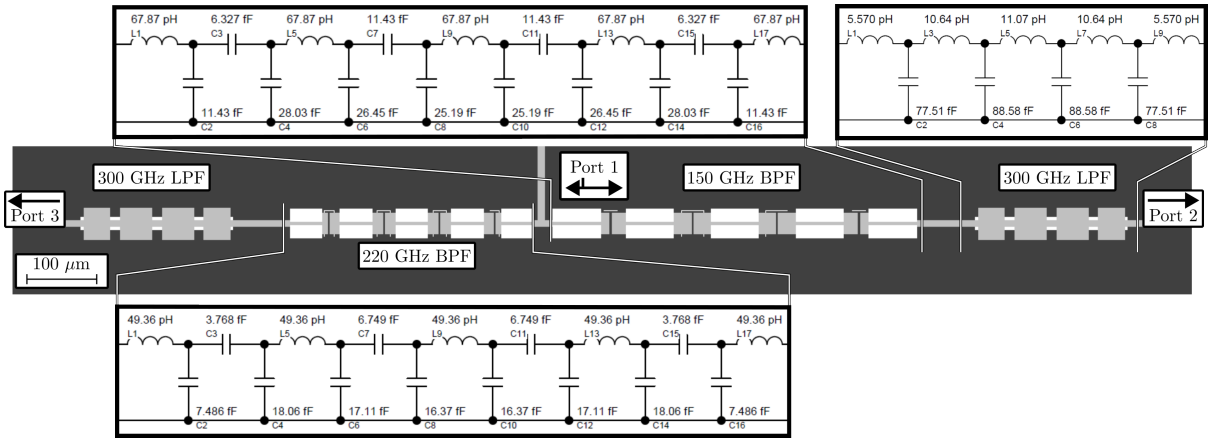

Figure 2.15: Diplexer network design including low-pass filters for off-band resonance attenuation. The physical design and equivalent circuits are shown.

Superconducting niobium exhibits an energy gap 2Δ of 2.8 meV which corresponds to a gap frequency of $f_{\text{gap}} = 2\Delta/h \approx 680\,\text{GHz}$ setting a maximum frequency limit. High-frequency resonances derived from excitations of higher order modes in the the filter structures appear below f_{gap}. 9^{th}-order Butterworth low-pass filters are included after each band-pass filter to mitigate their effect. Spectral analysis of the diplexer network is limited to frequencies below f_{gap}, since suppression of superconductivity in niobium beyond this point naturally acts as a low-pass filter [110].

The low-pass filters are designed with the same lumped-element method, the circuit is shown in Figure 2.14. The low-pass filters are symmetric and reciprocal, and the component values are: $L_1 = L_5 = 5.57\,\text{nH}$, $L_2 = L_4 = 10.64\,\text{nH}$, $L_3 = 11.07\,\text{nH}$, $C_1 = C_4 = 77.51\,\text{fF}$ and $C_2 = C_3 = 88.58\,\text{fF}$. These component values produce a Butterworth response with a cutoff frequency of 300 GHz and band-pass attenuation of 0.5 dB.

Figure 2.15 illustrates the implementation of the complete diplexer network. The designed layout and the target circuit for each filter are displayed. Figure 2.16 depicts the response of the diplexer network, with the atmospheric opacity calculated using the *am* Atmospheric Model [111]. The green and blue shaded regions represent the target observation bands of 150 GHz and 220 GHz, respectively. In dashed trace, the scattering parameters of the diplexer without these filters is visible, showcasing an undesired spurious response above 450 GHz. In solid trace, it can be seen how these filters help mitigate

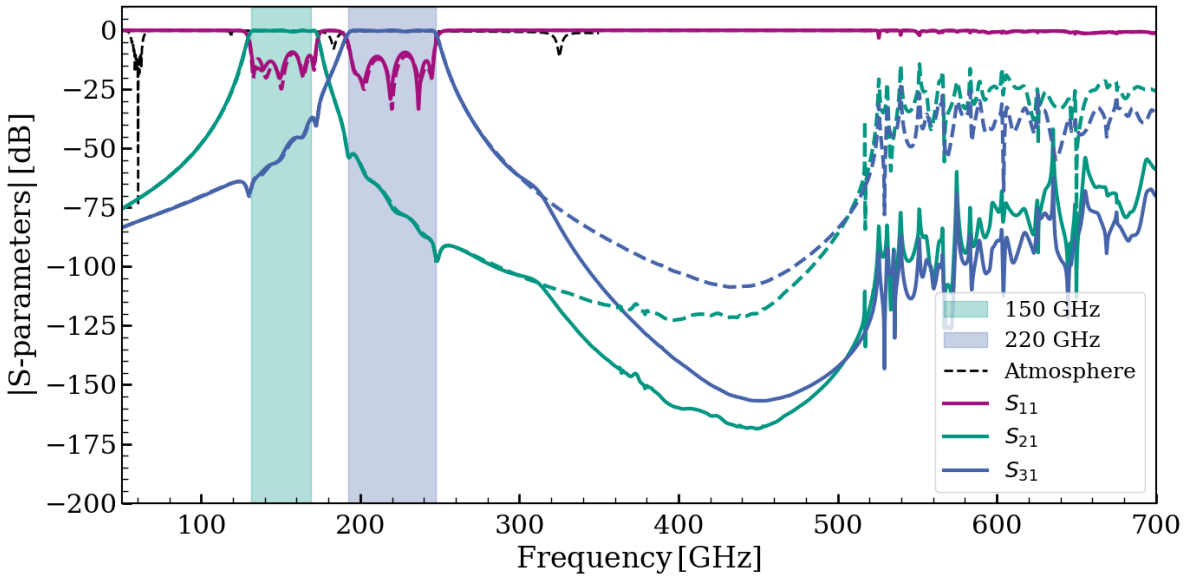

Figure 2.16: Diplexer scattering parameters illustrating the response of the diplexer network. The scattering parameters of the diplexer are depicted in dashed traces, and the scattering parameters accounting for the inclusion of the low-pass filters is shown in solid traces. Additionally, the atmospheric opacity calculated for the conditions at the QUBIC site is displayed.

these spurious signals, lowering their contribution to the transmission by approximately 40 to 50 dB.

The quality of the diplexer can be quantitatively assessed by analyzing the averaged simulated scattering parameters. Assuming perfectly matched source and load, we can calculate the following quality factors:

- **Insertion Loss** (IL): Calculated from the S_{21} and S_{31} parameters, representing the average signal loss within the observation band.
- **Return Loss** (RL): Obtained from the S_{11} parameter, which indicates the average reflection of the signal back towards the source.
- **Isolation** (I): Determined using the S_{23} and S_{32} parameters, reflecting the level of separation between the two bands.
- **Crosstalk** (X): Extracted in a manner similar to IL, but integrated over the bandwidth of the other channel, quantifying the signal leakage between bands.

The scattering parameters within the defined bandwidth are averaged as:

$$\langle S_{ij} \rangle = \frac{1}{\Delta f} \int_{\Delta f} |S_{ij}(f)|\, df \tag{2.19}$$

where Δf is the frequency band considered. The quality factors are calculated as

$$IL_{\mathrm{dB}} = \begin{cases} -20 \log_{10} \langle S_{21} \rangle, & \text{for 150 GHz band,} \\ -20 \log_{10} \langle S_{31} \rangle, & \text{for 220 GHz band,} \end{cases} \tag{2.20}$$

$$X_{\mathrm{dB}} = \begin{cases} 20\log_{10}\langle S_{31}\rangle, & \text{for 150 GHz band,} \\ 20\log_{10}\langle S_{21}\rangle, & \text{for 220 GHz band,} \end{cases} \tag{2.21}$$

$$RL_{\mathrm{dB}} = -20\log_{10}\langle S_{11}\rangle, \tag{2.22}$$

and,

$$I_{\mathrm{dB}} = \begin{cases} -20\log_{10}\langle S_{23}\rangle, & \text{for 150 GHz band,} \\ -20\log_{10}\langle S_{32}\rangle, & \text{for 220 GHz band.} \end{cases} \tag{2.23}$$

The obtained results are detailed in Table 2.7. X and I are at levels that ensure minimal signal leakage between bands, with dynamic ranges of almost 50 dB or more for both filters. These results only account for the diplexer's performance. For an exhaustive analysis of the proposed radiation coupling, the pixel power transfer ratio is more appropriate, incorporating the simulated behavior of all millimeter-wave components.

	IL [dB]	RL [dB]	X [dB]	I [dB]
150 GHz	0.22	13.55	-65.04	50.47
220 GHz	0.22	14.07	-49.37	64.73

Table 2.3: Calculated quality factors from the diplexer network scattering parameters.

2.8 Optical efficiency analysis

The efficiency of the antenna coupling must combine the results of numerous simulation results, mainly scattering parameters obtained by different simulation software and, in some cases, different normalization impedances at each port. A flow diagram of the pixel architecture is shown in Figure 2.17. Flow diagrams illustrate the paths of traveling waves entering (a_i) and exiting (b_i) the i^{th}-network element at their respective nodes [112]. The net dissipated power of a one-port network (such as the termination resistors of each bolometer) can be calculated by the difference between their incident and reflected power which are the squared values of a_i and b_i respectively. To analyze the relationships between various nodes in the diagram and obtain transfer functions governing the power flow throughout the pixel network, Mason's gain formula [113] was applied. With these relationships, the power transfer ratio defined as the square of the transfer function $T(f)$ for each bolometer as a function of frequency is:

$$|T(f)|^2 = \frac{P_{\mathrm{bol}}}{P_{\mathrm{inc}}} = (1 - |\Gamma_{ant}|^2) \cdot \frac{|a_{\mathrm{bol}}|^2 - |b_{\mathrm{bol}}|^2}{|b_{\mathrm{ant}}|^2}. \tag{2.24}$$

Here, P_{bol} is the power dissipated in the termination resistor of each bolometer computed as the incident power wave ($|a_{bol}|^2$) minus the reflected power wave ($|b_{\mathrm{bol}}|^2$) in the corresponding reference plane in the graph, P_{inc} is the incident power coupled by the antenna

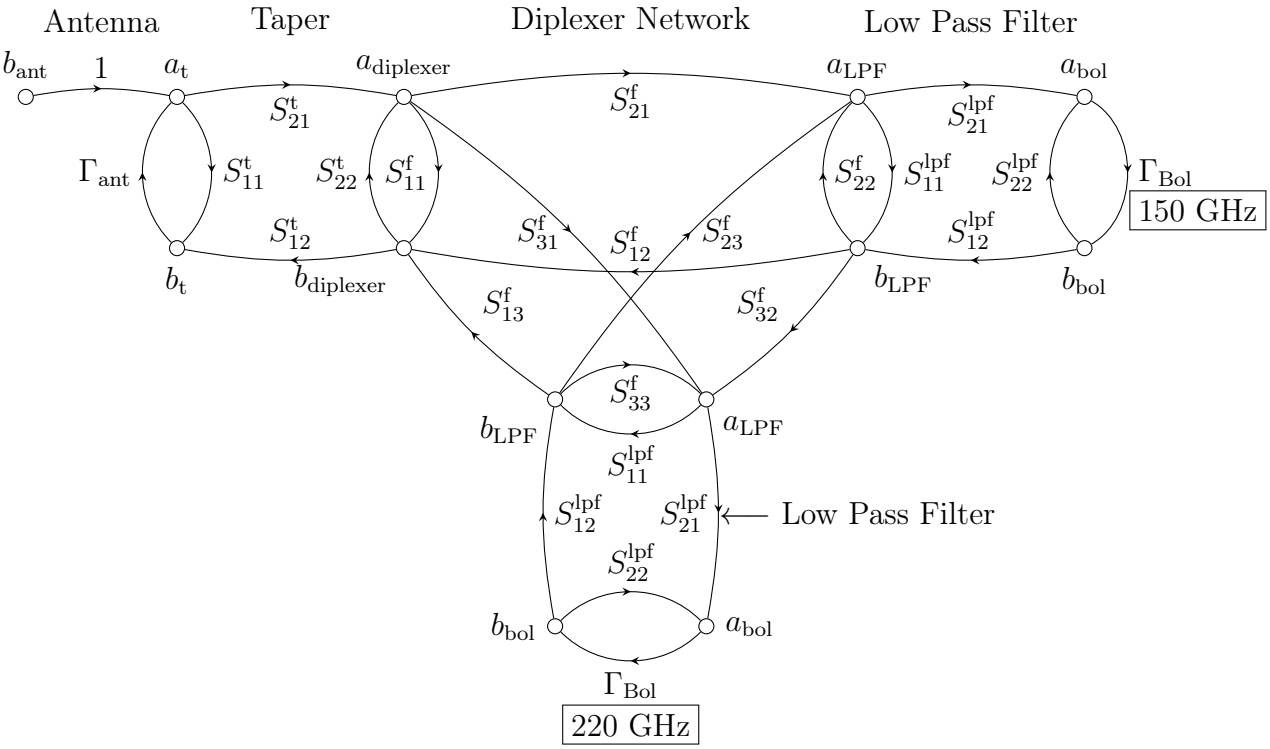

Figure 2.17: Signal flow graph illustrating the proposed dual-band radiation coupling, depicting the connections between the millimeter-wave components involved in the pixel.

that is computed as the available power that enters the system, $P_{\mathrm{inc}} = |b_{\mathrm{ant}}|^2/(1-|\Gamma_{\mathrm{ant}}|^2)$, where Γ_{ant} is the reflection coefficient of the antenna. The calculation of the power transfer ratios is too intricate, and impractical to perform manually. Alternatively, the transfer functions involved in Equation 2.24 were extracted using algorithms that interpret signal flow graphs, such as the one shown in Figure 2.17 and output a symbolic string which can be copied into a script for the numerical calculation. For reference, the line of code built from such algorithms to compute Equation 2.24 for a single bolometer is 51,624 characters long, exceeding that of this entire chapter. The attenuation of the transmission lines is incorporated into the model by multiplying the transfer function by an exponential decay term, $e^{-\alpha_{\mathrm{d}}\ell}$, where ℓ denotes the total length of the differential lines connecting the termination resistors.

By multiplying the pixel's power transfer function with the resulting optical reflection at the interface of the silicon lenses (both with and without AR coatings), the optical efficiency of the pixel is determined as

$$\mathfrak{O}_{\mathrm{eff}}(f) = (1 - R(f)) \cdot |T(f)|^2. \tag{2.25}$$

Figure 2.18 illustrates $\mathfrak{O}_{\mathrm{eff}}(f)$ for each bolometer, considering both antenna geometries. The total area under the curve is compared to that of the target observation band, and the corresponding percentage is provided for both antenna designs. The sinuous antenna

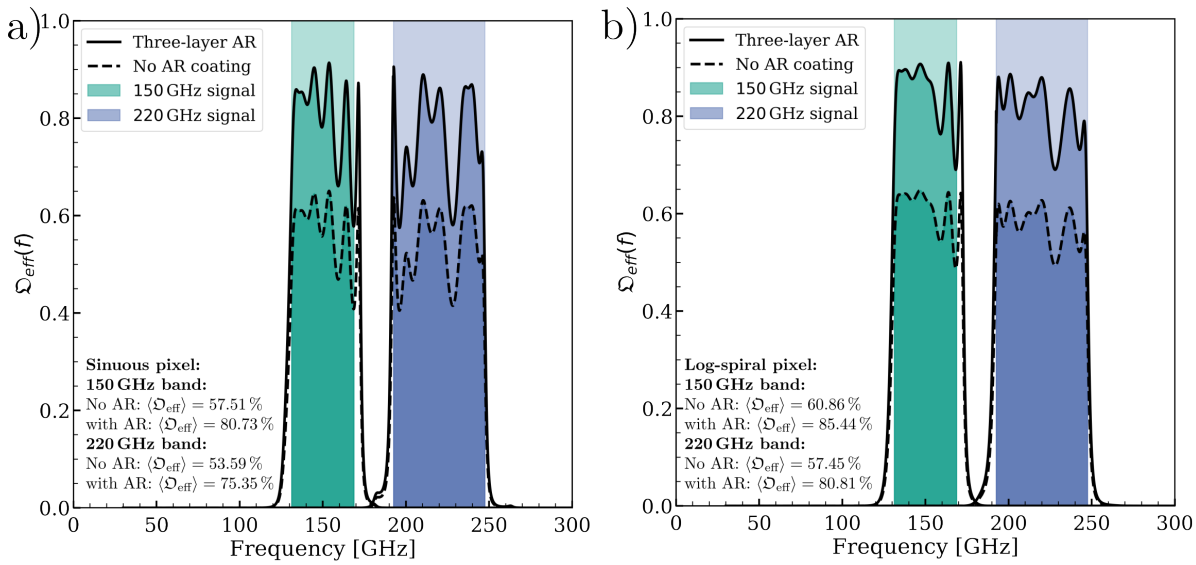

Figure 2.18: Optical efficiency results of the sinuous antenna pixel **(a)** and the log-spiral antenna pixel **(b)**. The analysis takes $\mathfrak{O}_{\text{eff}}(f)$ for the 150 GHz (green) and 220 GHz (blue) bands and compares it to the brick-wall-type ideal diplexer. The comparison, expressed as percentage for each case, represents the ratio between the intersecting area and the total target area for each band. The results are calculated for the case of no AR coatings and the three-layer AR coating developed for the SPT-3G focal plane [101].

variant exhibits lower optical efficiency compared to the log-spiral antenna, which can be attributed to the significant impedance variations shown in Figure 2.7 (a). Despite this, efficiencies of 75 % and higher can be achieved. The calculated averaged optical efficiency, $\langle\mathfrak{O}_{\text{eff}}\rangle$, within each band, shown in Figure 2.18, are summarized in Table 2.4.

Detector	without AR coatings	with AR coatings
Sinuous Pixel		
150 GHz band	$\langle\mathfrak{O}_{\text{eff}}\rangle = 57.51\,\%$	$\langle\mathfrak{O}_{\text{eff}}\rangle = 80.73\,\%$
220 GHz band	$\langle\mathfrak{O}_{\text{eff}}\rangle = 53.59\,\%$	$\langle\mathfrak{O}_{\text{eff}}\rangle = 75.35\,\%$
Spiral Pixel		
150 GHz band	$\langle\mathfrak{O}_{\text{eff}}\rangle = 60.86\,\%$	$\langle\mathfrak{O}_{\text{eff}}\rangle = 85.44\,\%$
220 GHz band	$\langle\mathfrak{O}_{\text{eff}}\rangle = 57.45\,\%$	$\langle\mathfrak{O}_{\text{eff}}\rangle = 80.81\,\%$

Table 2.4: Averaged optical efficiency results for each bolometer in both pixel designs

2.9 Photon noise equivalent power (NEP_γ)

The figure of merit used to characterize CMB detectors is the noise equivalent power (NEP) defined as the minimum required power spectral density at the input of the detector to achieve a signal-to-noise ratio (SNR) of one in one Hz of output bandwidth.

Component	T [K]	Emissivity (ϵ)	Efficiency (η)
5.6 cm Low Pass	0.3	0.02	0.98
6.2 cm Low Pass	0.3	0.02	0.98
7 cm Low Pass	0.3	0.02	0.98
Cold Stop + Low Pass	1	0.02	0.95
Beam Combiner	1	0.01	0.99
Horn Interferometer	6	0.05	0.99
Polarizing Grid	6	0.01	0.99
Half-Wave Plate	6	0.025	0.95
12 cm Low Pass	6	0.02	0.95
IR Block 6	6	0.01	0.98
IR Block 5	100	0.015	0.98
IR Block 4	100	0.01	0.98
IR Block 3	100	0.01	0.95
IR Block 2	250	0.013	0.98
IR Block 1	250	0.01	0.98
Window	250	0.01	0.98
Atmosphere	273	0.03	0.97
CMB	2.73	1	1

Table 2.5: Optical loading characteristics of the QUBIC instrument used to determine the incoming optical power on the focal plane [68].

Noise in bolometric measurements is composed of the random fluctuation in the arrival of photons to the detector referred to as photon noise (NEP_γ) and the intrinsic noise ($\mathrm{NEP}_{\mathrm{det}}$) of the detector itself. It is desirable to reduce $\mathrm{NEP}_{\mathrm{det}}$ as much as possible until NEP_γ is the dominant noise contribution. At this point, further reduction of $\mathrm{NEP}_{\mathrm{det}}$ does not account for better sensitivity of an individual detector and under this condition the detector is said to be background-limited. The sensitivity of a background-limited instrument can only be improved by increasing the integration time, either by planning longer experiments or increasing the number of detectors that measure simultaneously in the array. This is why it is generally required for CMB instruments to have both background-limited and scalable detector technology.

Using the QUBIC instrument as a reference, we can combine its optical characteristics with the calculated optical efficiency, of the pixel to determine the optical power P_{opt} incident on the bolometer. This calculation is performed by considering the emissivity (ϵ) and efficiency (η), of each optical component between the CMB and the detector. It is based on the optical characteristics detailed in Table 2.5, as specified in the QUBIC technical design report [68].

Each object emits blackbody radiation that can be calculated by knowing its temperature and emissivity, the blackbody radiation or brightness function can be calculated as:

Detector	P_{opt} [pW]	NEP_γ [aW/$\sqrt{\text{Hz}}$]
Sinuous Pixel		
150 GHz band	6.18 (4.40)	53.73 (41.41)
220 GHz band	7.14 (5.07)	61.64 (48.44)
Spiral Pixel		
150 GHz band	6.65 (5.03)	56.98 (45.80)
220 GHz band	8.56 (6.09)	70.08 (54.69)

Table 2.6: Estimated incoming optical power and photon noise equivalent power for both pixel designs within each observation band. The numbers are calculated using the optical efficiency accounting for the optimized three-layer AR coating and without any AR coating in brackets.

$$B(\epsilon, T, f) = \frac{\epsilon h f^3}{c^2(e^{hf/k_B T} - 1)} \tag{2.26}$$

where T, is the object's temperature, c is the speed of light and k_B is the Boltzmann constant. Knowing the frequency response of the detector, allows calculating the power spectral density $P_\delta(f)$ of the i-th component incident on the bolometer. This is done by considering the brightness function of each object, multiplied by the optical throughput for diffraction-limited single-mode detectors, $A\Omega = \lambda^2$, where λ is the wavelength of the radiation. Additionally, the accumulated efficiency of all optical elements between the source and the detector, as well as the frequency response $\mathfrak{O}_{\text{eff}}(f)$ obtained through the analysis presented in this chapter, are taken into account.

$$P_\delta(f)_i = \frac{1}{2}\left(\prod_{k=0}^{i} \eta_k\right) A\Omega \; (1 - R(f)) \, |T(f)|^2 \, B(\epsilon_i, T_i, f). \tag{2.27}$$

The 1/2 factor accounts for the fact that only half of the total incident power reaches the bolometer due to polarization sensitivity. The total power density $P_\delta(f)$ and integrated optical power P_{opt} are then

$$P_\delta(f) = \sum_{i=0}^{N-1} P_\delta(f)_i \tag{2.28}$$

and

$$P_{\text{opt}} = \int P_\delta(f) df. \tag{2.29}$$

From these results, we can estimate NEP_γ as [114]

$$\text{NEP}_\gamma^2 = \int_{\Delta f} 2hf \cdot P_\delta(f) df + \frac{2}{m} \int_{\Delta f} P_\delta(f)^2 df, \tag{2.30}$$

where $m = 1$ is the number of polarizations detected.

Table 2.6 presents the total integrated power reaching the bolometers for both pixel designs discussed. The assumed dielectric losses in the superconducting transmission lines are responsible for coupling degradation in the order of 5...10 %. The values in brackets correspond to calculations assuming no anti-reflection coatings on the surface of the silicon lenses, representing the worst-case scenario. These values establish the noise performance requirements that the cryogenic bolometer must satisfy to achieve a background-limited CMB detector.

Chapter 3

The Magnetic Microbolometer (MMB)

In this chapter, the Magnetic Microbolometer (MMB) is introduced. These detectors are connected to the output lines of the radiation coupling circuit described in Chapter 2 and are the third element in Figure 1.5. The MMB is an adaptation of the Magnetic Microcalorimeter (MMC) to work as a cryogenic bolometer and measure incoming optical power in the observation bands required for CMB survey. To the best of my knowledge, the use of MMC technology has never been proposed before for Cosmology experiments so an in-depth discussion with regard to the detection principle, sensor material, detector geometry, biasing, and readout is described first, and then the noise performance analysis and optimization process are presented to design an MMB for background-limited measurements of the CMB using the QUBIC instrument as reference.

3.1 Detection principle

An MMC is a cryogenic detector widely used in single particle detection [115]. It is typically operated at temperatures below 100 mK and is based on a metallic paramagnetic material to transduce the temperature rise due to the absorption of an energetic particle into a magnetic flux variation threading a closed superconducting loop. The paramagnetic material is mostly a noble-metal doped with a few hundred ppm of erbium. The magnetic flux variation can be measured with high precision using a Superconducting Quantum Interference Device (SQUID). The performance of MMC detectors has been optimized for numerous applications in the course of more than two decades [80]. The maturity of this technology and its success owing to the fast signal rise time and remarkable energy resolution motivated the efforts to apply metallic magnetic sensors to different fields of physics, namely observational cosmology.

The MMB operates at temperatures above 100 mK (typical in cryostats found in CMB instruments) and is coupled to incoming radiation by millimeter-wave circuitry as described in Chapter 2. Incoming radiation is thermalized by a thermal mass in tight thermal contact to the paramagnetic temperature sensor, which is biased with an externally applied magnetic field. The change in sensor magnetization, resulting from temperature changes, induces a magnetic flux change within a superconducting pickup

coil that is coupled to a SQUID, a precise magnetometer capable of converting a magnetic flux signal into a voltage signal reaching almost quantum-limited noise performance [116].

The responsivity or gain ($\mathfrak{R}_{\mathrm{MMB}}$) of the MMB is determined by the thermal response function ($\partial T/\partial P$) that describes how variations in incoming power (P) are converted into a variation in temperature (δT) as well as the magnetic response function ($\partial\Phi/\partial T$) of the paramagnetic thermometer that characterizes how the temperature change is transduced into a change of sensor magnetization (δM) or magnetic flux variation ($\delta\Phi$), respectively. In addition, there is a flux coupling term ($\partial\Phi_{\mathrm{SQ}}/\partial\Phi$) that specifies the change of magnetic flux ($\partial\Phi_{\mathrm{SQ}}$) within the SQUID loop due to a flux change ($\partial\Phi$) in the pickup coil. Considering the flux change in the SQUID loop ($\delta\Phi_{\mathrm{SQ}}$) as the actual measurement signal for incoming power variations (δP), the gain ($\mathfrak{R}_{\mathrm{MMB}}$) can be written as

$$\mathfrak{R}_{\mathrm{MMB}} = \frac{\partial\Phi_{\mathrm{SQ}}}{\partial P} = \frac{\partial\Phi_{\mathrm{SQ}}}{\partial\Phi}\frac{\partial\Phi}{\partial T}\frac{\partial T}{\partial P}. \tag{3.1}$$

3.2 Thermal response

The thermodynamic behavior of the MMB can be represented by an equivalent electrical circuit, following analogous system modeling [117]. Figure 3.1 shows the thermal model of the detector and the electrical circuit analog used. As incoming power is applied to the detector, the thermal response is governed by the thermal mass of the detector, which mostly consists of the metallic host with respective host heat capacity (C_{host}), and the heat capacity of the erbium ion subsystem (C_{Er}), the heat capacity of the termination resistor can also be included as part of C_{host}. The exchange energy between the metal host and the erbium ions can be represented by a heat conductance (G_{se}), representing electron-spin interactions within the alloy. The sensor is weakly anchored to a heat bath via a weak thermal conductance (G_{bath}). The associated thermal fluctuation noise in each thermal link produced by the random heat flow caused by temperature-dependent energy fluctuations are also considered in this model. The analog electrical circuit models thermal power as a current source and temperature as node voltages, establishing a direct correspondence between the thermal and electrical domain.

Using the state-space method [118], a linear approximation for $\partial T/\partial P$ was derived. The relationship between small variations of incoming optical power around a mean value ($P = \langle P_{\mathrm{opt}}\rangle + \delta P_{\mathrm{opt}}$) and the differential equations relating it to the temperatures of the metal host (T_{host}) and erbium subsystem (T_{Er}) is presented in matrix form,

$$\begin{bmatrix}\dot{T}_{\mathrm{host}}\\ \dot{T}_{\mathrm{Er}}\end{bmatrix} = \begin{bmatrix}-\frac{G_{\mathrm{bath}}+G_{\mathrm{se}}}{C_{\mathrm{host}}} & \frac{G_{\mathrm{se}}}{C_{\mathrm{host}}}\\ \frac{G_{\mathrm{se}}}{C_{\mathrm{Er}}} & -\frac{G_{\mathrm{se}}}{C_{\mathrm{Er}}}\end{bmatrix}\cdot\begin{bmatrix}T_{\mathrm{host}}\\ T_{\mathrm{Er}}\end{bmatrix} + \begin{bmatrix}\frac{1}{C_{\mathrm{host}}}\\ 0\end{bmatrix}\cdot(\langle P_{\mathrm{opt}}\rangle + \delta P_{\mathrm{opt}}), \tag{3.2}$$

where $\dot{T}_{\mathrm{host}}$ and $\dot{T}_{\mathrm{Er}}$ are the time derivatives of each respective temperature signal. Solving Equation 3.2 yields the following transfer function for T_{Er},

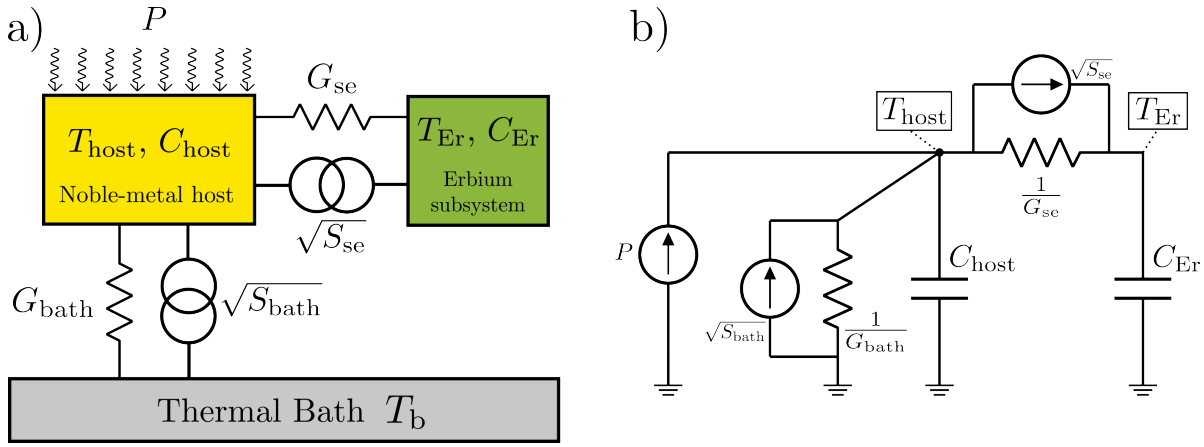

Figure 3.1: a) Thermal model of the MMB detector relating the thermal components described in the text. **b)** Electrical circuit analog used to describe the thermodynamic behavior of the detector. Noise sources representing thermodynamic energy fluctuations between different detector sub-systems are included in parallel to each thermal link.

$$\frac{\partial T}{\partial P} = \frac{\partial T_{\mathrm{Er}}}{\partial P} = \frac{T_{\mathrm{Er}}}{\langle P_{\mathrm{opt}} \rangle + \delta P_{\mathrm{opt}}} = \frac{1}{G_{\mathrm{bath}}} \left[1 - \frac{C_{\mathrm{host}} C_{\mathrm{Er}}}{G_{\mathrm{bath}} G_{\mathrm{se}}} \omega^2 + \frac{C_{\mathrm{host}} G_{\mathrm{se}} + C_{\mathrm{Er}} (G_{\mathrm{bath}} + G_{\mathrm{se}})}{G_{\mathrm{bath}} G_{\mathrm{se}}} j\omega \right]^{-1}, \tag{3.3}$$

with angular frequency, $\omega = 2\pi f$. The roots of the second-order polynomial in the variable ω give rise to two time constants (τ_0 and τ_1) that govern the time response. In the limit of $G_{\mathrm{se}} \to \infty$, where the thermal contact of the erbium ions to the metallic host is considered perfect, the thermal response reduces to

$$\frac{\partial T}{\partial P} \approx \frac{1}{G_{\mathrm{bath}}} \left[1 - \frac{C_{\mathrm{host}} + C_{\mathrm{Er}}}{G_{\mathrm{bath}}} j\omega \right]^{-1}. \tag{3.4}$$

The time constants τ_0 and τ_1 for perfect host-erbium thermal contact are given by

$$\tau_0 \approx \frac{C_{\mathrm{host}} + C_{\mathrm{Er}}}{G_{\mathrm{bath}}} \text{ and } \tau_1 \longrightarrow 0. \tag{3.5}$$

In this case, the detector speed is hence governed by a dominant time constant ($\tau_0 \gg \tau_1$) that depends on the total heat capacity of the detector and the thermal contact to the heat bath.

The thermal gain of the detector depends on the inverse of G_{bath}. Thus, to achieve a high thermal gain, G_{bath} must be as small as possible. This can be achieved by designing the MMB as a leg-isolated detector which has been the ubiquitous approach with CMB and sub-mm astronomy instruments for more than a decade. An expression for G_{bath} in leg-isolated detectors can be found using a similar linear analysis. Heat transport through suspending legs is dominated by longitudinal and transversal lattice vibrations (phonons) and remains in the diffusive limit at temperatures above 100 mK. In such a scenario [119],

$$P = A\frac{cl}{3L}\left(\frac{a}{2}(T^2 - T_{\text{bath}}^2) + \frac{b}{4}(T^4 - T_{\text{bath}}^4)\right), \tag{3.6}$$

where T_{bath} is the heat bath temperature, A is the cross-section area of the leg, c is the speed of sound in the material, l is the mean-free-path of phonons, and a and b are material constants related to its heat capacity that can be experimentally determined [119]. With small fluctuations in incoming power P, the heat conductance of a certain number (N) of low stress silicon nitride (LSiN) legs can be estimated from their length (L) as the derivative with respect to temperature (T) of the transported heat, resulting in

$$G_{\text{bath}} = \frac{\partial P}{\partial T} = N \cdot \frac{AlS}{3L} \cdot \left(a \cdot T + b \cdot T^3\right). \tag{3.7}$$

These expressions can be used to the extent to which linear approximations remain valid. Only weak variations in incoming optical power around a mean value that produce small variations in detector temperature at a fixed operating point can be analyzed. They are valid, for example, when analyzing noise performance and sensitivity, which is the purpose of this chapter.

3.3 Sensor material

The paramagnetic materials that serve as temperature sensors in the MMB are dilute alloys of erbium doping a noble-metal host such as gold or silver. The rare earth ions with unpaired electrons in the 4f shell contribute to a localized magnetic moment [115, 120]. The reason why metals are used for these detectors is that there exists a strong electron-spin coupling enabling fast relaxation times within the material in the order of or even below one microsecond described by the Korringa relation [121, 122], this is far superior to the relaxation times achieved solely through phonon-spin interactions occurring when using insulator hosts that are in the order of a few seconds. In dilute concentrations below ≈1.6%, erbium atoms substitute gold or silver atoms at regular face-centered cubic (fcc) lattice sites, giving three electrons to the conduction band of the host material [123]. The paramagnetic behavior of each erbium ion arises from the partially filled 4f shell and behave mostly as free ions due to the shielding effect of their filled outer 5s and 5p orbitals.

When a magnetic field is applied to such paramagnetic alloy, the magnetic moments align preferentially with the field direction. In the high temperature limit, for $T > 100\,\text{K}$, the thermal energy is so high that all multiplets are occupied and contribute equally, the crystal field effects can be ignored and the magnetic moment (μ) of each erbium ion can be approximated as [120],

$$\mu = -g\mu_{\text{B}}J, \tag{3.8}$$

where μ_{B} is the Bohr magneton and

$$g = 1 + \frac{J(J+1) + S(S+1) - L(L+1)}{2J(J+1)}, \tag{3.9}$$

with quantum numbers $L = 6$, $S = 3/2$, $J = 15/2$ resulting in a Landè factor $g = 6/5$ [124]. As the temperature is decreased and weak magnetic fields are applied, the higher multiplet states of the fcc crystal field are progressively depleted. At $T < 1.5\,\mathrm{K}$, the Γ_7 Kramers ground-state doublet represents the only available excited states and accounts for the paramagnetic behavior of the alloy [79]. As a consequence of this, the paramagentic behavior of Au:Er and Ag:Er is simplified and can be regarded as a system with effective spin $\hat{S} = 1/2$ and effective Landè factor $\hat{g} = 6.80 \pm 0.04$ in the case of Au:Er, and $\hat{g} = 6.84 \pm 0.05$ in the case of Ag:Er [125, 126].

The Γ_7 ground state doublet splits in the presence of external magnetic field, $\vec{B}$ with Zeeman splitting energy

$$E_\mathrm{z} = \hat{g}\mu_\mathrm{B}|\vec{B}|. \tag{3.10}$$

If we assume that the spins are isolated and don't interact with each other, we only consider E_z. The magnetization (M) of the paramagnetic alloy in such case is expressed as

$$M = n_\mathrm{Er}\hat{g}\mu_\mathrm{B}J \cdot \mathfrak{B}(h), \tag{3.11}$$

where n_Er is the number density of ions, and $\mathfrak{B}(h)$ is the Brillouin function, given by

$$\mathfrak{B}(h) = \frac{2J+1}{2J}\coth\left(\frac{h(2J+1)}{2J}\right) - \frac{1}{2J}\coth\left(\frac{h}{2J}\right), \tag{3.12}$$

h relates the magnetic and thermal energy ($k_\mathrm{B}T$) as,

$$h = \frac{g\mu_\mathrm{B}JB}{k_\mathrm{B}T}. \tag{3.13}$$

At low temperatures and/or high magnetic fields, $h \to \infty$, all moments are aligned with $\vec{B}$ and $\mathfrak{B}(h) = 1$. As temperature increases or the magnetic field is decreased, the Zeeman splitting becomes small with respect to $k_\mathrm{B}T$ and hence $h \to 0$. Approximating $\mathfrak{B}(h)$ with a first order Taylor expansion results in the well-known Curie law [120] that describes the susceptibility (χ) of paramagnetic substances in the high-temperature low-magnetic-field limit:

$$\chi = \frac{M}{H} = \frac{\mu_0 n_\mathrm{Er} g^2 J(J+1)\mu_B^2}{3k_\mathrm{B}T} \propto \frac{1}{T}. \tag{3.14}$$

The sensor heat capacity includes both the host and the erbium subsystem, $C_\mathrm{sen} = C_\mathrm{host} + C_\mathrm{Er}$. The heat capacity of the host material is calculated considering phononic and electronic excitations. At temperatures much lower than the Debye temperature ($T \ll \Theta_\mathrm{D}$) [127],

$$C_\mathrm{host} = \frac{V}{m_\mathrm{V}}\left(\gamma T + \beta T^3\right), \tag{3.15}$$

where V is the sensor volume, m_V is the molar volume of the host material, γ is the Sommerfeld constant (electronic contribution) and β is the Debye coefficient (phononic

contribution). Magnetic moments (erbium subsystem) contribute to the free energy and thus to the specific heat. This contribution is calculated as [127],

$$C_{\mathrm{Er}} = n_{\mathrm{Er}} k_B \left(\frac{E_z}{k_B T}\right) \frac{e^{E_z/k_B T}}{(e^{E_z/k_B T}+1)^2}, \tag{3.16}$$

and presents a maximum for $k_B T \approx E_z/2$, known as a Schottky anomaly.

As stated earlier, Equations 3.11 and 3.16 assume that the magnetic moments are non-interacting. This assumption serves as a starting point to qualitatively assess the behavior of the paramagnetic alloy to a first order. For erbium concentrations of a few hundred ppm or more, the reduced distances between ions allow both direct and indirect exchange interactions to take place between the magnetic moments. Dipole-dipole interactions between magnetic moments constitute a form of direct exchange, while indirect exchange interactions are mediated by the conduction electrons of the metal host through the Ruderman-Kittel-Kasuya-Yoshida (RKKY) mechanism [128].

Determining the magnetization and heat capacity of a system with randomly distributed interacting spins requires numerical simulations, as no closed-form analytical expression exists to acount for these complex interactions. A Monte Carlo simulation tool was developed within this thesis, following algorithms presented in literature [129, 130]. A simulated face-centered cubic (fcc) lattice is randomly populated with a given number of Er^{3+} ions, within a specified volume of the host material. The erbium-to-host atom ratio is controlled by adjusting the simulated sample volume (V). The simulated volume consists of a cubic arrangement of allowed positions that follow the fcc crystalline structure, as illustrated in Figure 3.2. Erbium ions positioned near the edges of the simulated volume experience slightly weaker interactions with their neighbors. This edge effect can lead to an underestimation of the overall interaction strength, potentially resulting in an overestimation of the detector's sensitivity. To mitigate this artifact, the simulation volume was replicated 26 times, forming a $3 \times 3 \times 3$ arrangement of identical volumes. Interactions are calculated, accounting for the nearest ions in this extended configuration, ensuring a more accurate representation of the system's physical behavior.

The system is considered as a canonical ensemble. The Hamiltonian, H_{sen}, is constructed for each iteration by adding the Zeeman splitting energy, the dipole-dipole interaction, and RKKY interaction for the given Er^{3+} ion distribution. The energy states (E_i), i.e, the eigenvalues of H_{sen}, are determined and used to calculate the thermodynamic properties using the partition function (Z)

$$Z = \sum_i e^{E_i/k_B T}. \tag{3.17}$$

The values of C_{Er}, M, and $\partial M/\partial T$ are then calculated for each iteration with the resulting energy states:

$$C_{\mathrm{Er}} = \frac{n_{\mathrm{Er}}}{V k_{\mathrm{B}} T^2}\left\{\langle E^2\rangle - \langle E\rangle^2\right\}, \tag{3.18}$$

$$M = -\frac{n_{\mathrm{Er}}}{V}\left\langle \frac{\partial E}{\partial B}\right\rangle, \text{ and} \tag{3.19}$$

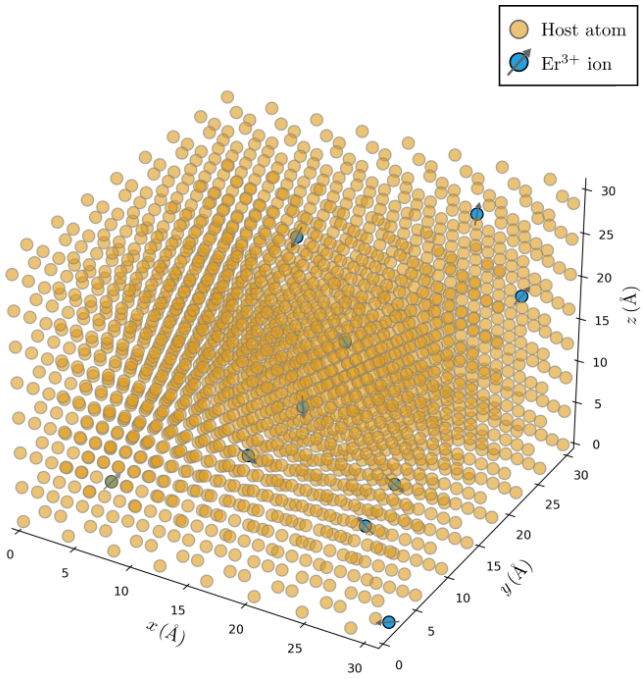

Figure 3.2: Representation of an Au:Er or Ag:Er sample volume from one Monte Carlo iteration. The number of Er^{3+} ions determines the cubic fcc lattice size needed to simulate the desired erbium concentration.

$$\frac{\partial M}{\partial T} = \frac{n_{\mathrm{Er}}}{V k_{\mathrm{B}} T^2} \left\{ \left\langle E \frac{\partial E}{\partial B} \right\rangle - \langle E \rangle \left\langle \frac{\partial E}{\partial B} \right\rangle \right\}. \tag{3.20}$$

Several thousand iterations are required to produce statistically meaningful results.

A parameter α which describes the relative strength of the RKKY interaction with respect to dipole-dipole is introduced to simplify the analysis of the interactions. As these interactions show the same distance-scaling, higher α values indicate stronger interactions and lead to degraded performance. The value of α is kept as a free parameter when fitting measured data, in particular, $\alpha \approx 5$ for Au:Er and $\alpha \approx 12.8$ for Ag:Er was determined.

Figure 3.3 presents the simulated heat capacity C_{sen} and magnetization M per mole of a Au:Er sample with an erbium concentration of 492 ppm. The simulation was performed with 2170 iterations, considering six interacting Er^{3+} ions and assuming an applied magnetic field of 10 mT. The results also account for the host material contribution to the specific heat [131]. Magnetization is often plotted against inverse temperature to emphasize Curie-law linearity and enhance resolution at very low temperatures. In this thesis, however, a logarithmic temperature scale is used, as it provides uniform representation across the sub-kelvin range ($T < 1$ K). This choice is particularly appropriate for MMBs, whose operating temperatures are higher than those of conventional MMC detectors.

M and C follow scaling laws, therefore, there is no strict requirement to simulate the exact concentration of the material used, as results obtained for different concentrations can be appropriately adjusted post-calculation. The relative change in material concentration will have a direct or inverse proportional effect on the other physical quantities. If we take two paramagnetic samples of concentrations x_1 and x_2, with heat capacities $C_1(T, \vec{B})$ and $C_2(T, B)$ and magnetization $M_1(T, B)$ and $M_2(T, B)$, the following relations hold [132]:

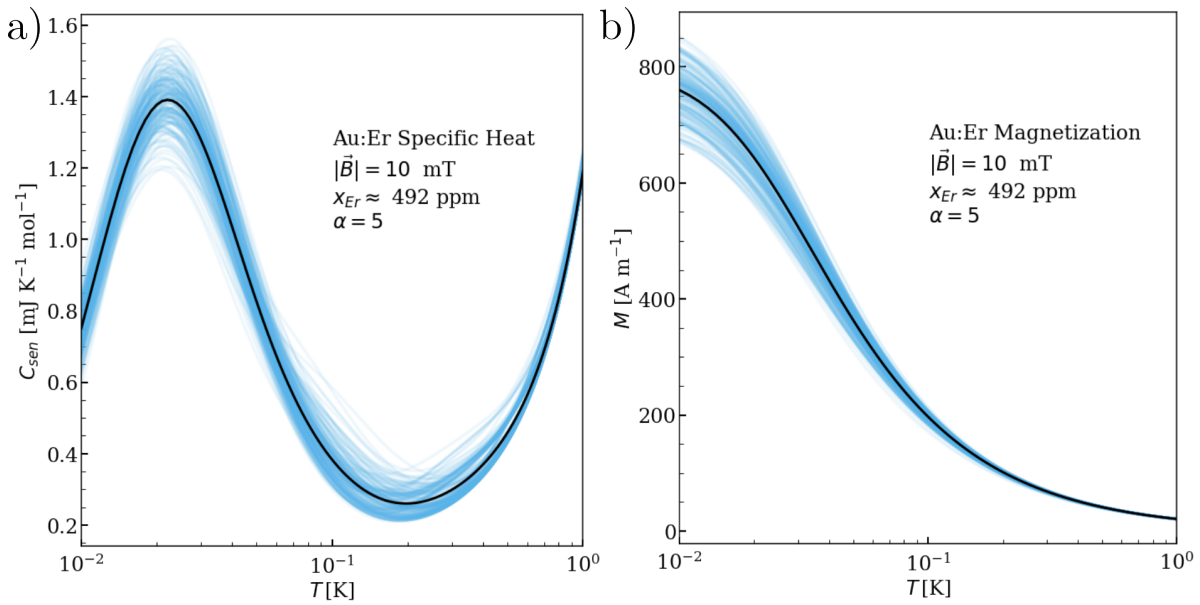

Figure 3.3: Results of the Monte Carlo-based calculation of the specific heat (**a**) and magnetization (**b**) for an Au:Er sample with an Er concentration of $x_{Er} \approx 492$ ppm, placed in a 10 mT magnetic field. The black solid line represents the mean values, while the soft light blue traces indicate the mean values over 10 iterations (thus 217 blue traces are visible in these plots). Magnetization curves plotted with a logarithmic temperature scale, providing uniform representation below 1 K; this representation is chosen since MMBs operate at higher temperatures than MMC detectors.

$$C_2(T, B) = \frac{x_2}{x_1} C_1\left(\frac{x_2}{x_1}T,\ \frac{x_1}{x_2}B\right), \text{ and} \tag{3.21}$$

$$M_2(T, B) = \frac{x_2}{x_1} M_1\left(\frac{x_2}{x_1}T,\ \frac{x_1}{x_2}B\right). \tag{3.22}$$

Figure 3.4 illustrates how the scaling laws described in equations 3.21 and 3.22 can be applied to estimate the thermodynamic properties of a paramagnetic sample with different erbium concentrations. In this example, results for erbium concentrations of 257, 492, 768, 986, 1296, 1471, and 2052 ppm are scaled down to a reference concentration of 300 ppm. An external magnetic field of 10 mT is assumed. All scaled curves overlap, showing similar results independently of the actual concentration used during calculation. Differences become more apparent at the lowest temperatures where exchange interactions appear to have more influence on the calculated properties.

In Figure 3.5, the results obtained for the specific heat and magnetization of a Au:Er sample with concentration $x_{\mathrm{Er}} \approx 300$ ppm have superimposed measurements [129] showing an excellent agreement with the simulation results. Additionally, a similar simulation tool was produced independently by another group [133] and when compared to the one developed in this thesis, they also show excellent agreement with each other.

Au:Er is a superior material when considering the α parameter. However, the nuclei of the host material also affect performance. ^{198}Au has a nuclear spin $I = 3/2$, and

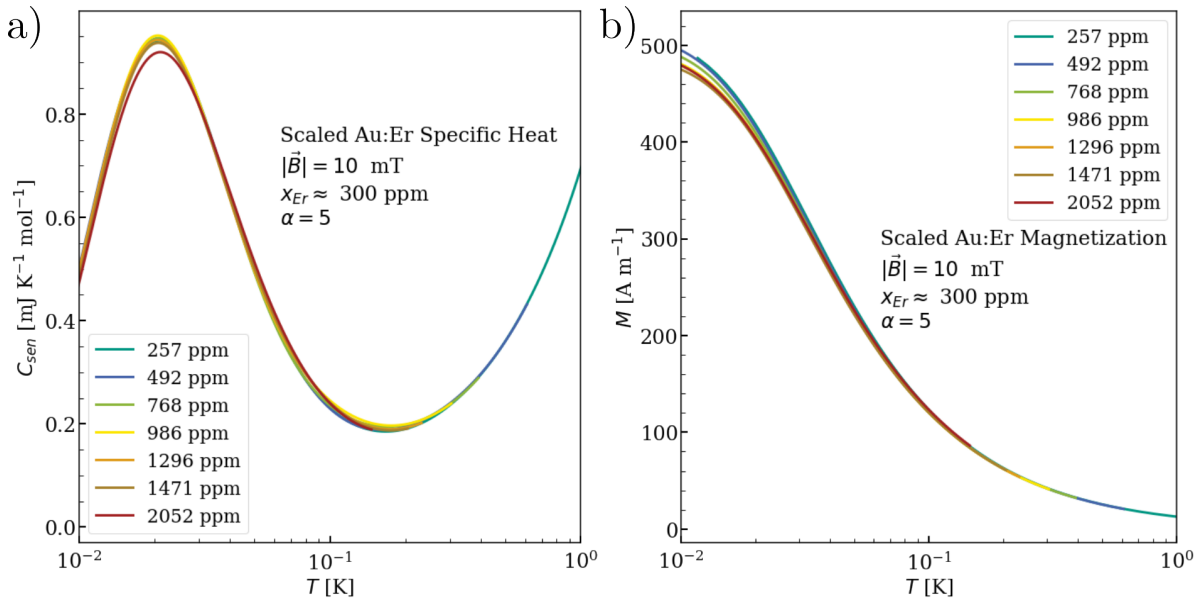

Figure 3.4: Scaling laws applied to simulations conducted with varying erbium concentrations. The results are adjusted to a final concentration of 300 ppm and correspond to an external magnetic field of 10 mT.

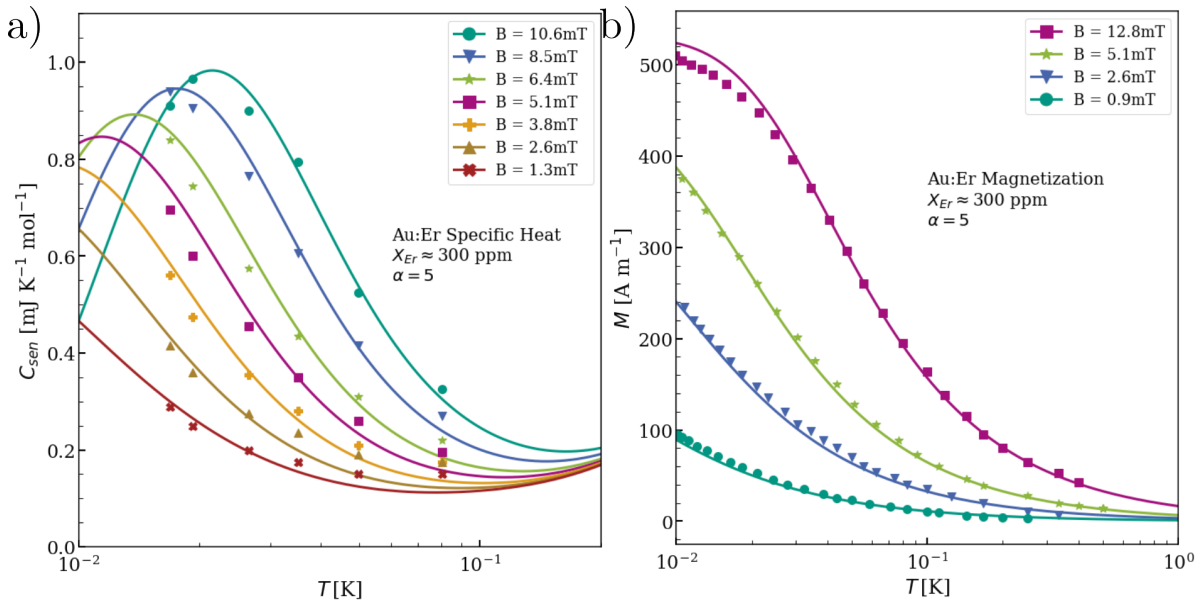

Figure 3.5: Results of our Monte-Carlo method based calculation of the specific heat (**a**) and magnetization (**b**) of a Au:Er sample with a concentration $x_{Er} \approx 300$ppm biased with various magnetic fields. Solid lines represent the simulation results, and the data points are taken from measurements presented in [129].

non-zero quadrupole moment. For nuclei in the vicinity of the Er^{3+} ions, the electric field gradient is sufficient to lift the degeneracy of Au nuclear levels and present an additional heat capacity [79]. In contrast, both ^{107}Ag and ^{109}Ag isotopes have nuclear spin $I = 1/2$ and do not present a quadrupole moment, so the unwanted contribution to the specific heat present for gold is not present when using silver as a host.

It is worth mentioning that Er comes with different isotopes, among which ^{167}Er isotope carries a nuclear spin, $I = 7/2$, the resulting hyperfine splitting creates an additional contribution to the sensor heat capacity which reduces the sensitivity. For this reason, In the production of the sensor material, isotopically enriched ^{166}Er that presents no nuclear spin is used for the production of the sputter target used within this thesis.

3.4 Magnetic bias field and signal readout

The magnetization change of the paramagnetic sensor is measured as a change of magnetic flux threading a superconducting pickup coil that simultaneously provides the required bias magnetic field by storing a persistent bias field current (I_{field}). This generates a constant magnetic field free of noise, with which the sensor is biased. A variation in magnetization of the sensor generates a current change through the pickup coil due to flux conservation in closed superconducting loops.

The temperature-to-magnetic-flux conversion coefficient $\partial\Phi/\partial T$ (cf. Equation 3.1) depends on the actual pickup coil geometry (Figure 3.6 (a)), the latter determining the magnetic field distribution inside the sensor. The magnetic field distribution ($\vec{B}(\vec{r})$) was calculated using FEMM[1]. The obtained distribution (Figure 3.6 (b)) is divided into small elements in which the field is assumed homogeneous, and their respective partial volumes (V_i) of the sensor material are considered. With the Monte-Carlo simulation tool, the partial derivative $\partial M/\partial T$ is determined for each volume element V_i. The overall temperature-to-magnetic-flux conversion coefficient is then obtained by summing the contributions from the partial volume elements over the entire sensor:

$$\frac{\partial\Phi}{\partial T} = \sum_i \frac{\mu_0 \mathrm{G}(\vec{r})}{p} \frac{\partial M}{\partial T}\Big|_{\vec{r}} V_i, \tag{3.23}$$

with

$$\mathrm{G}(\vec{r}) = \frac{B(\vec{r})}{\mu_0 I_{\text{field}}}\, p \tag{3.24}$$

Here, $\mathrm{G}(\vec{r})$ is the geometrical factor relating the field distribution at position $\vec{r}$ with the applied field current I_{field}. The pitch p and line width w of the meander-shaped pickup coil have an important influence on the magnetic field $B(\vec{r})$. The smaller the pitch (and smaller line widths maintaining the w/p ratio), the greater the generated average magnetic field in the sensor volume at a constant field current. For this reason, micrometer-structured, meander-shaped pickup coils are preferred when designing an MMB.

[1] Meeker, D. (2004). Finite Element Method Magnetics (FEMM).

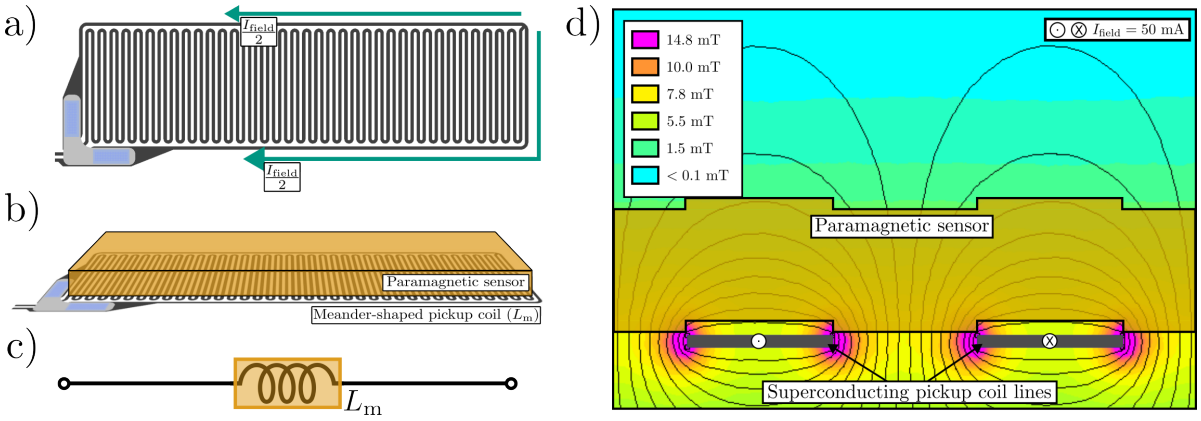

Figure 3.6: a) Meander-shaped pickup coil design used in the MMB. **b)** Side-view of the meander-shaped pickup coil with the paramagnetic sensor placed on top. **c)** Representation of the pickup coil coupled to the sensor in schematic circuits. **d)** Calculated magnetic field distribution when a field current of $I_{\text{field}} = 50\,\text{mA}$ flows through the inductor considering periodic boundary conditions. The meander-shaped pickup coil has a line width of $w = 2.5\,\mu\text{m}$ and a pitch of $p = 5\,\mu\text{m}$.

External magnetic fields become a considerable issue when the detector is placed in the focal plane of a radio telescope, requiring a large opening to be illuminated. This setup makes effective shielding impractical, and when the telescope moves, the external field variations can introduce unwanted signals. The solution proposed to this problem is to design the detector with self-symmetric inductors. A redundant return line is added to the meander-shaped inductor to obtain an equal area producing magnetic fields into and out of the plane [79]. Thus, any external magnetic field component is effectively canceled out, minimizing the impact of environmental magnetic fluctuations on the detector's performance. We used InductEx[2] to calculate the coupling between the self-symmetric meander-shaped pickup coils and a large loop that emulates external magnetic fields. The related simulation configuration is shown in Figure 3.7. Results of this simulation are summarized in Table 3.1. by comparison to a regular meander-shaped pickup coil, it was determined that the redundant return lines lowers the coupling to external fields by at least a factor of 100.

Parameter	Regular meander-shaped coil	Self-symmetric meander-shaped coil
L_{m}	2.39 nH	2.18 nH
L_{ext}	1.37 nH	1.34 nH
$M_{\text{m-ext}}$	79.15 nH	0.53 nH
$k_{\text{m-ext}}$	4.38×10^{-2}	3.12×10^{-4}

Table 3.1: Results of the external field rejection simulation comparing a self-symmetric with a regular meander. The self-symmetric design achieves a large external magnetic field rejection.

[2]SUN Magnetics Ltd, Integrated Circuit Inductance Extraction

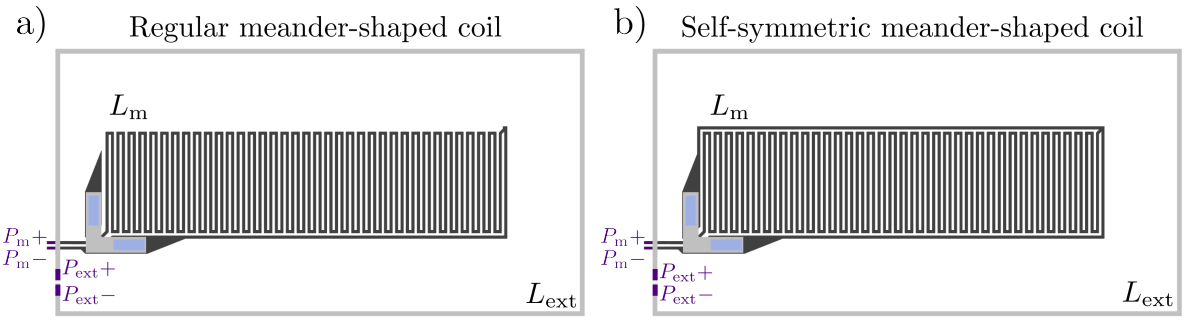

Figure 3.7: **a)** InductEx external field rejection simulation for the self-symmetric meander-shaped pickup coil. **b)** Simulation performed with a regular meander-shaped inductor, removing the redundant return line.

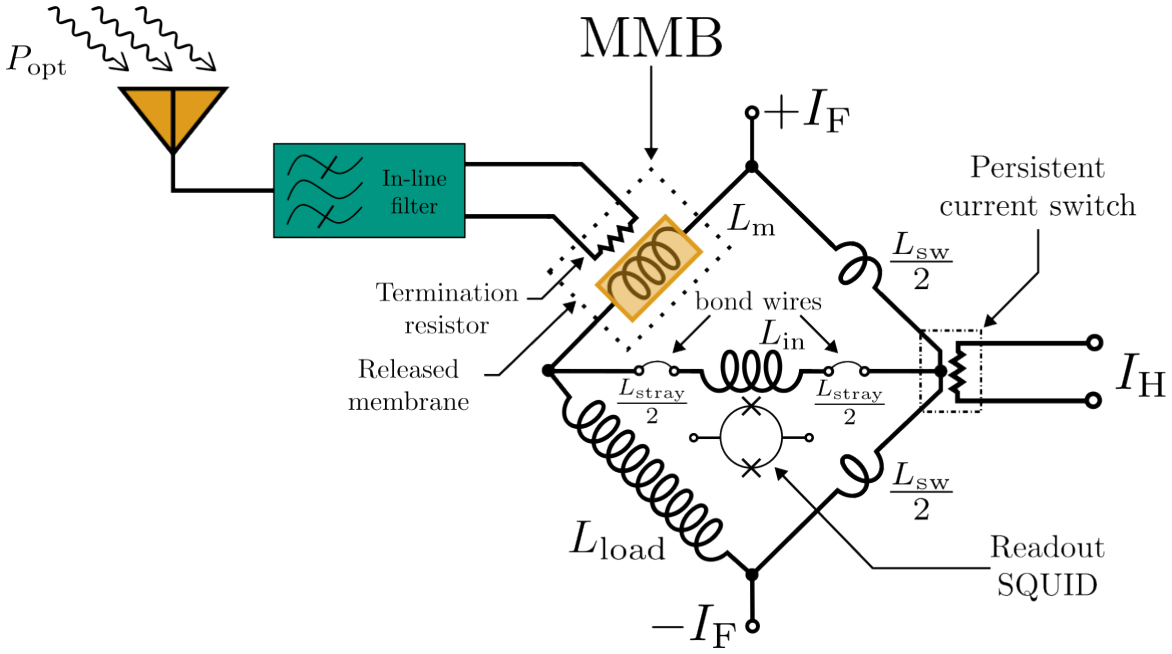

Figure 3.8: Schematic circuit of the MMB-based CMB detector pixel developed within this thesis. Incoming optical power (P_{opt}) is coupled by the radiation coupling circuit and guided towards a termination resistor. The resistor and the paramagnetic sensor, coupled to the pickup coil (L_m), constitute the MMB which is placed on a released dielectric membrane that provides a weak thermal coupling to the heat bath (low G_{bath}). The schematic also shows the bias circuit consisting of a load inductor (L_{load}) and the persistent current switch. The switch consists of a resistive heater placed on top of a Nb wire with inductance L_{sw}. The switch is operated by a current pulse delivered to the I_H leads. A current applied to leads $\pm I_F$ while the switch is operated will trap flux in the pickup coil, biasing the paramagnetic sensor. The current change produced in the pickup coil upon variation of the sensor magnetization is read out by a SQUID. There also exists a parasitic inductance (L_{stray}) in the connection to its input coil (L_{in}).

Figure 3.8 shows the schematic of the full MMB-based CMB detector as developed within this thesis. For simultaneous biasing and readout, a closed superconducting bias circuit is formed by the pickup coil (L_m) and a load inductor (L_load). The field current is injected in L_m and L_load. A highly sensitive SQUID coupled to an input inductance (L_in) is used to measure the current change generated by the change in sensor magnetization. For injecting the persistent current, a persistent current switch is used, consisting of a thin film resistor placed in on top of a portion of the circuit. The individual steps during the injection process are shown in Figure 3.9. The lines that are opened by the switch have a small but considerable parasitic inductance (L_sw). The switch design is assumed symmetric, resulting in equal inductance ($L_\mathrm{sw}/2$) on each side. There also exists a parasitic inductance (L_stray) in the connection to the readout SQUID that is associated with the path that connects L_m to L_in, it includes bond wires and the parasitic lines on the MMB and SQUID chips. The integration of detectors and SQUIDs into a single chip is of particular interest, as it reduces parasitic inductance; however, such integration increases fabrication complexity due to the need for compatibility between multiple fabrication processes.

A relationship between injected field current I_field and the forward current I_F applied to the bias leads can be determined using Kirchhoff rules and magnetic flux conservation in closed superconducting loops. The result of this calculation is

$$\frac{I_\mathrm{field}}{I_\mathrm{F}} = \left[1 + \frac{L_\mathrm{sw}/2[L_\mathrm{load} + L_\mathrm{sw}/2 + 2(L_\mathrm{in} + L_\mathrm{stray})]}{(L_\mathrm{m} + L_\mathrm{load}) + L_\mathrm{m}(L_\mathrm{load} + L_\mathrm{sw}/2)}\right]^{-1}, \tag{3.25}$$

an additional persistent current circulates through the input coil of the SQUID that is given by

$$\frac{I_\mathrm{SQ}}{I_\mathrm{F}} = \frac{L_\mathrm{sw}/2(L_\mathrm{m} - L_\mathrm{load})}{(L_\mathrm{m} + L_\mathrm{sw}/2 + L_\mathrm{in} + L_\mathrm{stray})(L_\mathrm{load} + L_\mathrm{sw}/2 + L_\mathrm{in} + L_\mathrm{stray}) - (L_\mathrm{in} + L_\mathrm{stray})^2}, \tag{3.26}$$

in the limit of $L_\mathrm{sw} \to 0$, it can be seen that, $I_\mathrm{field} \to I_\mathrm{F}$. This implies that for optimal design of the detector, the distance of the current injection points to the persistent current switch should be minimized, but, at the same time, some minimal distance must be maintained to prevent the switch from opening the bias leads carrying I_F to the detector. Reducing the switch inductance L_sw also minimizes the persistent current running through the SQUID loop (cf. Equation 3.26).

State-of-the-art MMC detectors have a gradiometric, $L_\mathrm{m} = L_\mathrm{load}$, allowing a single SQUID to read out two detectors simultaneously, this also improves performance by cancelling temperature fluctuations and external fields. In such cases, the current trapped in the SQUID loop is zero independently of the value of L_sw, and the expression for I_field simplifies to

$$\frac{I_\mathrm{field}}{I_\mathrm{F}} = \frac{2L_\mathrm{m}}{2L_\mathrm{m} + L_\mathrm{sw}}. \tag{3.27}$$

In the case of the MMB, there is no benefit in associating two detectors in a gradiometric configuration. The inductance L_load is therefore designed to be as large as possible

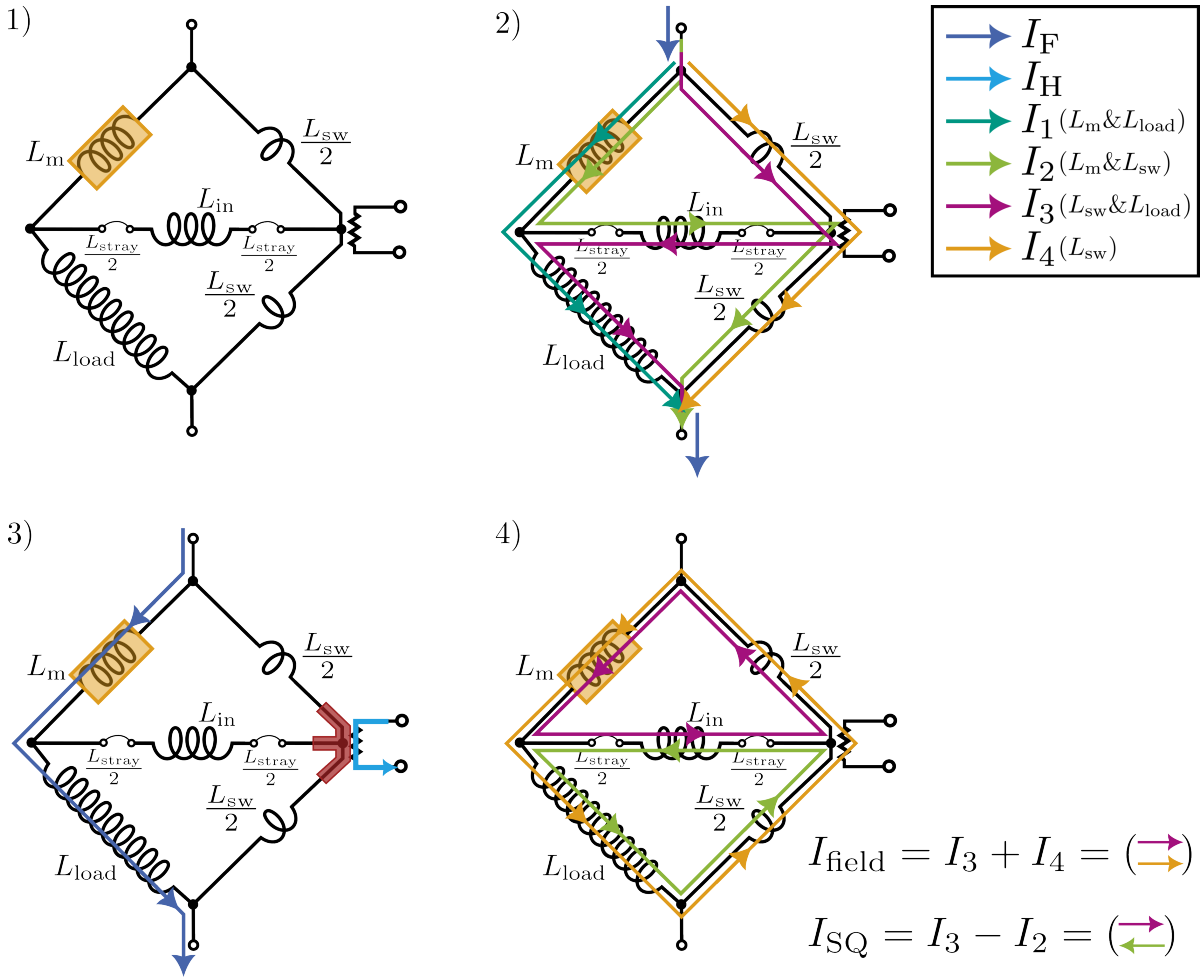

Figure 3.9: Schematic representation of the different steps during persistent current injection. **1)** Prior to the injection, the initial magnetic flux threading all closed superconducting loops is considered zero. **2)** A forward current I_F is applied to the circuit, and is distributed through each superconducting coil such that the total flux is kept constant. **3)** A current pulse is applied to the persistent current switch, opening all superconducting loops and allowing magnetic flux to enter the circuit. The red area represents a hotspot where the circuit presents non-zero resistance. **4)** The forward current I_F is turned off, and three persistent currents appear in the circuit, preserving the flux trapped during the injection.

with respect to L_m, maximizing the flux transformer gain ($\partial\Phi_{SQ}/\partial\Phi$ in equation 3.1). When $L_{load} \gg L_m$, equations 3.25 and 3.26 simplify to

$$\frac{I_{field}}{I_F} = \frac{L_m + L_{in} + L_{stray}}{L_m + L_{in} + L_{stray} + L_{sw}/2}, \tag{3.28}$$

and

$$\frac{I_{SQ}}{I_F} = \frac{L_{sw}/2}{L_m + L_{in} + L_{stray} + L_{sw}/2}. \tag{3.29}$$

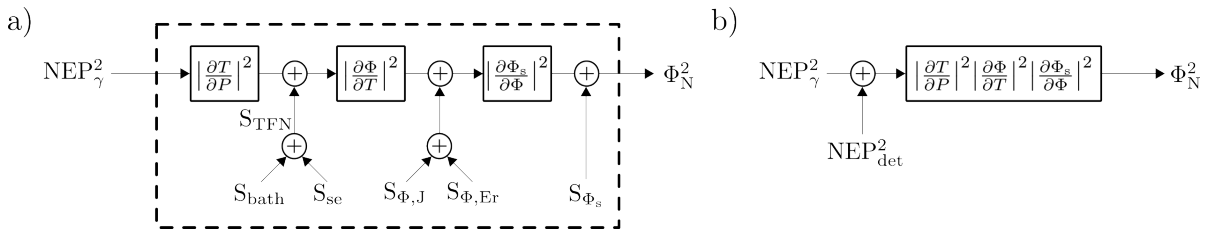

Figure 3.10: a) Noise contribution diagram showcasing each noise source in the MMB. All these sources contribute to flux noise Φ_N threading the readout SQUID. At the input of the detector the photon noise equivalent power, NEP_γ, is introduced. **b)** All noise sources are referred to the input and regarded as a single intrinsic detector noise equivalent power (NEP_{det}).

The expression for the flux coupling factor then takes the form

$$\frac{\partial \Phi_{SQ}}{\partial \Phi} = \frac{M_{in}}{L_m + L_{sw}/2 + (1 + \frac{L_m + L_{sw}/2}{L_{load} + L_{sw}/2})(L_{stray} + L_{in})}, \tag{3.30}$$

where $M_{in} = k\sqrt{L_{in} L_s}$ is the mutual inductance between the input coil and SQUID loop and k is the magnetic coupling between them. When $L_{sw} \to 0$ and $L_{load} \gg L_m$, equation 3.30 reduces to

$$\frac{\partial \Phi_{SQ}}{\partial \Phi} \approx \frac{M_{in}}{L_m + L_{stray} + L_{in}}. \tag{3.31}$$

3.5 Noise contributions

To evaluate the MMB performance and to asses its suitability for CMB polarimetry, the detector's noise contributions are calculated to determine whether it can achieve background-limited photometry of the sky. The primary noise sources that must be considered include thermal fluctuation noise (S_{TFN}), magnetic Johnson noise ($S_{\Phi,J}$), erbium $1/f$ excess noise ($S_{\Phi,Er}$), and readout SQUID noise (S_{Φ_s}). Each noise source appears at different stages within the detector's responsivity as depicted in Figure 3.10 (a). All noise sources are referred to the detector input, and referenced as the detector's intrinsic noise equivalent power (NEP_{det}), as shown in Figure 3.10 (b). NEP_{det} is determined as

$$\mathrm{NEP}_{det}^2 = \frac{S_{TFN}}{\left|\frac{\partial T}{\partial P}\right|^2} + \frac{S_{\Phi,J} + S_{\Phi,Er}}{\left|\frac{\partial T}{\partial P}\right|^2 \left|\frac{\partial \Phi}{\partial T}\right|^2} + \frac{S_{\Phi_s}}{\left|\frac{\partial T}{\partial P}\right|^2 \left|\frac{\partial \Phi}{\partial T}\right|^2 \left|\frac{\partial \Phi_s}{\partial \Phi}\right|^2}, \tag{3.32}$$

with the terms S_{TFN}, $S_{J,\Phi}$, $S_{\Phi,Er}$ and S_{Φ_s} representing the power spectral density of each noise source.

Thermal fluctuation noise S_{TFN} includes fluctuations of phonon energy in the thermal link to the heat bath (S_{bath}), and energy fluctuations between the conduction electrons and the spin subsystems within the sensor (S_{se}). The first contribution can be estimated by [134]

$$S_{\text{bath}} = 4\gamma k_B T^2 G_{\text{bath}}, \tag{3.33}$$

where

$$\gamma = \frac{\beta+1}{2\beta+3} \cdot \frac{1-(T_{\text{bath}}/T)^{2\beta+3}}{1-(T_{\text{bath}}/T)^{\beta+1}}, \tag{3.34}$$

is an empirical factor that depends on the temperature ratio T_{bath}/T. The coefficient β depends on the type of heat transfer and is $\beta = 3$ for pure phononic heat transfer. The energy fluctuations between the conduction electrons and the spin subsystems can be modeled and estimated by a similar method, arriving at the following expression for S_{se} [79]:

$$S_{\text{se}} = 4k_B T^2 G_{\text{se}}. \tag{3.35}$$

The total contribution of thermal fluctuation to the detector noise equivalent power is determined by including the expressions for S_{bath} and S_{se} to their respective current source in the analog electrical circuit shown in Figure 3.1 arriving to the following system of differential equations in matrix form:

$$\begin{bmatrix} \dot{T}_{\text{host}} \\ \dot{T}_{\text{Er}} \end{bmatrix} = \begin{bmatrix} -\frac{G_{\text{bath}}+G_{\text{se}}}{C_{\text{host}}} & \frac{G_{\text{se}}}{C_{\text{host}}} \\ \frac{G_{\text{se}}}{C_{\text{Er}}} & -\frac{G_{\text{se}}}{C_{\text{Er}}} \end{bmatrix} \begin{bmatrix} T_{\text{host}} \\ T_{\text{Er}} \end{bmatrix} + \begin{bmatrix} \frac{1}{C_{\text{host}}} & -\frac{1}{C_{\text{host}}} \\ 0 & \frac{1}{C_{\text{Er}}} \end{bmatrix} \begin{bmatrix} \sqrt{S_{\text{bath}}} \\ \sqrt{S_{\text{se}}} \end{bmatrix} \tag{3.36}$$

The system is solved to obtain the frequency-dependent thermal noise affecting the temperature of the erbium susbsytem T_{Er}, the noise equivalent power is determined summing both thermal fluctuation noise contributions and referring them to the input of the detector:

$$\frac{S_{\text{TFN}}}{\left|\frac{\partial T}{\partial P}\right|^2} = 4\gamma k_{\text{B}} T^2 G_{\text{bath}} + 4k_{\text{B}} T^2 \frac{G_{\text{bath}}^2}{G_{\text{se}}} \cdot \left(1 + \frac{\omega^2 C_{\text{host}}^2}{(G_{\text{bath}}+G_{\text{se}})^2}\right). \tag{3.37}$$

Magnetic Johnson Noise is generated by the thermally excited random motion of free electrons in the paramagnetic sensor and all metallic components (non-superconducting) close to the pickup coil are relevant, generating a fluctuating magnetic field that couples to the pickup coil seemingly as a part of the measured signal. This noise contribution can be calculated as [79]

$$S_{\text{J},\Phi} = \mathfrak{K} \cdot \sigma \cdot k_{\text{B}} T, \tag{3.38}$$

where $\mathfrak{K}$ is a constant that depends on the geometry of the detector and σ, the electrical conductance of the paramagnetic sensor.

Each erbium ion in the sensor exhibits a fluctuating magnetic moment, manifesting as flicker noise. The exact origin of these magnetic fluctuations is not fully understood, but experimental observations indicate that they are independent of temperature [80]. As a form of flicker noise, it predominantly appears at low frequencies, following a characteristic $1/f$ dependence. This phenomenon is commonly referred to as erbium $1/f$ excess noise. The spectral density of this contribution is given by:

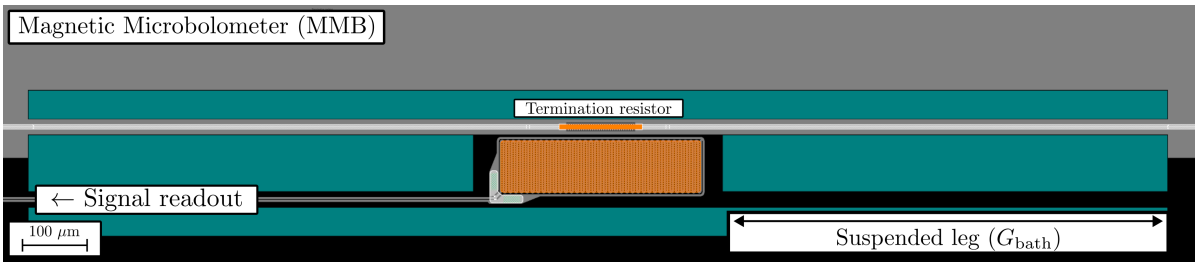

Figure 3.11: Detailed view of the MMB detector. The coupled and filtered CMB signal is guided via microstrip transmission lines and fed to the termination resistor thermally anchored to the paramagnetic sensor. The sensor is magnetically coupled to the superconducting meander-shaped pickup coil that bias and readsout the temperature-dependent magnetization. These components are placed on a rectangular dielectric island, held in place by four dielectric legs. The length of the legs determines the effective heat conductance to the thermal bath (G_{bath}). The leg-isolated dielectric island is defined by the rectangular openings represented in green.

$$S_{\Phi,Er} = N_{Er} \frac{\mu_0^2 \langle G^2 \rangle}{p^2} S_{\text{m}}(f), \tag{3.39}$$

where N_{Er} is the number of erbium ions in the sensor and $S_{\text{m}}(f)$ is the power spectral density of the magnetic moment of a single erbium ion. $S_{\text{m}}(f) = 0.115\mu_B^2 \,/\, f^{\alpha}$, with $\alpha \approx 1$ for Au:Er and $S_{\text{m}}(f) = 0.018\mu_B^2 \,/\, f^{\alpha}$, with $\alpha \approx 0.86$ for Ag:Er [135]. The lower excess noise measured in Ag:Er alloys translates to a substantial increase in sensitivity making it the material of choice for MMB optimization.

Regarding the SQUID noise, it can be described in two parts: there is a $1/f$ noise component ($S_{\Phi,1/f}$) at low frequencies and a white noise component ($S_{\Phi,\text{white}}$) at higher frequencies. In Chapter 5, a description of a two-stage SQUID-based amplifier is given and the noise performance is presented. For the optimization of the MMB, the obtained SQUID performance is used. The measured noise values for the readout SQUID are: $\sqrt{S_{\Phi,1/f}} = 3.30 f^{-\eta}\, \mu\Phi_0/\sqrt{\text{Hz}}$, with $\eta = 0.31$, and $\sqrt{S_{\Phi,\text{white}}} \approx 0.52\, \mu\Phi_0/\sqrt{\text{Hz}}$.

3.6 Optimization of an MMB for QUBIC

The performance of a magnetic microbolometer depends on a bunch of design and operation parameters. These parameters can be optimized to achieve a target sensitivity and detector bandwidth. Among them, the sensor thickness, the length of the suspending legs, the erbium concentration, and the bias field current can be, within certain ranges, freely varied.

The goal of the optimization process is to achieve a sensitivity that is high enough to ensure BLIP and an appropriate detector bandwidth that avoids elongation of the point-source response of the telescope. Taking into account the beam size, Θ_{beam}, and scan speed, $\dot{\Theta}$, the required time constant, τ, is [136]:

Design parameter		**Estimated performance**	
Bath Temperature	320 mK	Operating temperature	367 mK
Sensor Thickness	1 μm	Heat conductance	122.7 pW/K
Leg length	1400 μm	Total heat capacity	2.04 pJ/K
Erbium concentration	1000 ppm	Responsivity	0.17 $\mu\Phi_0$/aW
Bias field curent	70 mA	Time constant	16.7 ms
		Cutoff frequency	9.56 Hz

Table 3.2: Detector parameters and performance in the estimation of the noise contributions to achieve BLIP with MMB detectors installed in the focal plane of the QUBIC instrument. The estimated performance describes the average values corresponding to the range of expected incident power on the detector.

$$\tau \leq \frac{\Theta_{\text{beam}}}{2\pi\dot{\Theta}}. \tag{3.40}$$

The QUBIC instrument has a base temperature of 320 mK and an aperture radius of 0.3 m, implying $\Theta_{\text{beam}} = 0.39\,^\circ$ at the central frequency. The scan speed envisioned for the instrument is $\dot{\Theta} = 1\,^\circ/\text{s}$, hence, the maximum allowed time constant of the detector according to equation 3.40 is $\tau \leq 62$ ms, corresponding to a detector bandwidth of $f_{\text{BW}} \geq 2.57$ Hz. We will consider here the dual-band log-spiral antenna pixel variant introduced in Chapter 2. Within the 150 GHz band, $P_{\text{opt}} = 6.65$ pW and $\text{NEP}_\gamma = 56.98\,\text{aW}/\sqrt{\text{Hz}}$, and, within the 220 GHz band, $P_{\text{opt}} = 8.56$ pW and $\text{NEP}_\gamma = 70.08\,\text{aW}/\sqrt{\text{Hz}}$. These values correspond to the highest optical efficiency. Absence of anti-reflection coatings reduces these numbers by 25...30 % according to Table 2.6 of Chapter 2.

Another optimization goal of the MMB, besides achieving BLIP, is to ensure that the detector noise is dominated by thermal fluctuation noise. Under this condition, the detector is referred to as phonon-limited. Ideally, CMB detectors should be both background-limited and phonon-limited, meaning that not only does the background photon noise dominate, but thermal noise also remains subdominant in the detector response. In such a regime, the instrument's performance is no longer constrained by the detector technology. Consequently, the only viable strategies for improving the experiment's sensitivity are to increase the integration time or to deploy a larger number of detectors observing the sky.

Optimal values for each design parameter were obtained that maximize responsivity, maintain the required bandwidth of the MMB and achieve BLIP in the QUBIC instrument. Figure 3.12 shows the comparison of background and detector noise alongside its multiple noise contributions both at the input, expressed as noise equivalent power, and at the output, expressed as flux noise (Φ_{N}) threading the readout SQUID. The detector parameters used for these results are listed in Table 3.2. This performance analysis considers the MMB design depicted in Figure 3.11, which represents the bolometer shown in Figure 3.8.

A primary limitation identified is the presence of erbium $1/f$ excess noise, which dominates the low-frequency range. With this respect, two mechanisms can be employed

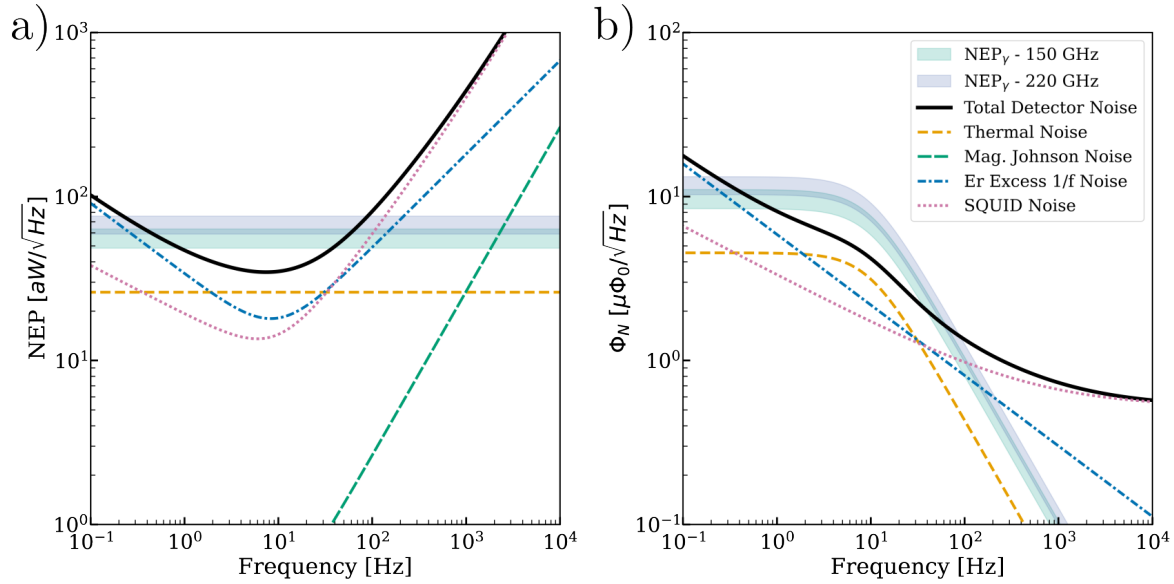

Figure 3.12: NEP and flux noise (Φ_N) of the different MMB noise contributions compared to the estimated background noise in the QUBIC technical demonstrator instrument. Dashed traces represent individual contributions to the MMB noise, highlighting their relative significance.

to mitigate this noise contribution. The first is increasing the thermal gain, allowing the thermal fluctuations and incoming photon noise to rise relative to the erbium excess noise, and the second is increasing the bias field current, which enhances the detector's gain and sensitivity to temperature variations. It should also be mentioned that the $1/f$ contribution to the photon noise arising from atmospheric water vapor pressure fluctuations and temperature variations within the instrument has not been considered in the current performance analysis. In the following paragraphs, the effect of each parameter on detector performance will be discussed, sweeping each parameter within a certain range while keeping all other parameters at the optimal values listed in Table 3.2.

The length of the supporting legs for the suspended structure can be adjusted over a wide range, with the primary limitation being the mechanical stability of the final device. This design parameter serves as a key tool for tuning the thermal conductance of the detector to the heat bath. A lower thermal conductance results in a higher thermal gain (cf. Equation 3.4), albeit at the cost of a slower response time (cf. Equation 3.5). However, increasing the length of the suspending legs (reducing G_{bath}) does not increase the responsivity indefinitely. This is because the operating temperature of the MMB increases at constant optical incoming power. At higher temperatures, the magnetization slope of the paramagnetic sensor is reduced, resulting in a weaker detector response. In Figure 3.13 (a), $\mathrm{NEP}_{\mathrm{det}}$ is shown for multiple values of the leg length at a fixed bath temperature of 320 mK. The noise of the detector is significantly reduced as the length is increased 200 μm up to a value of approximately 1400 μm. Decreasing the thermal conductance hence decreases the phonon thermal fluctuation noise contribution despite the marginal increase in the operating temperature T at constant optical incoming power

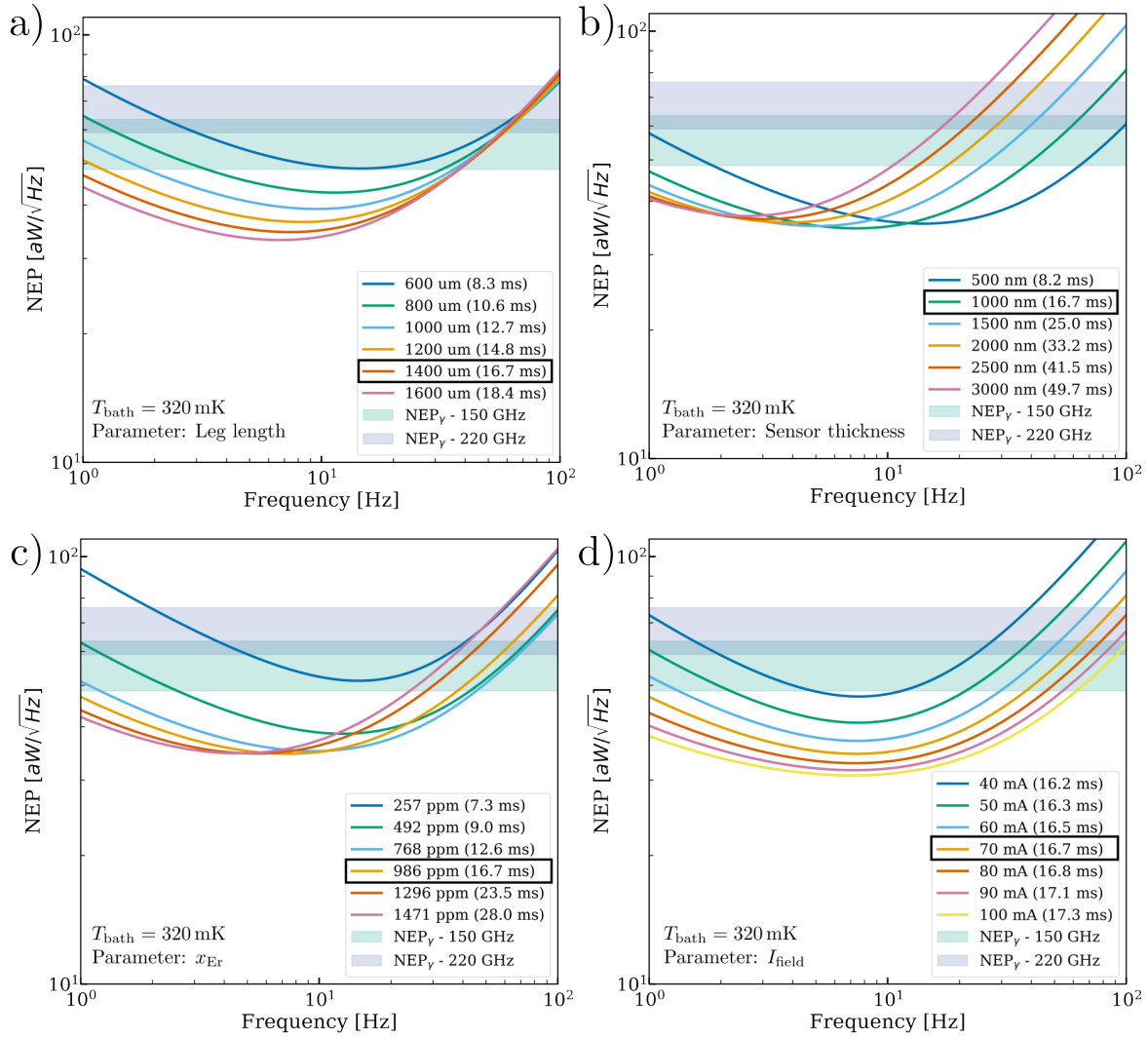

Figure 3.13: NEP_γ and NEP_{det} for each optimization parameter. In the legend for each plot the detector response time (τ) is given for each parameter value in milliseconds. **a)** Leg length. **b)** Sensor thickness. **c)** Erbium concentration (x_{Er}). **d)** Bias field currents (I_{field}). The bath temperature is fixed at $T_{bath} = 320\,mK$. Each parameter is varied while keeping the others at their obtained optimal values indicated in each legend.

P_{opt}. For larger values than 1400 μm, no significant reduction of $\mathrm{NEP}_{\mathrm{det}}$ is observed.

The area of the paramagnetic sensor is determined by L_{m}. Its optimal value is selected to match L_{in} maximizing the flux coupling factor. The readout SQUID, considering Josephson junctions with a minimum achievable critical current of a few μA with standard microfabrication facilities and a target β parameter of ≈ 0.6, allows for loop inductances in the range of $L_{\mathrm{s}} = 50...100$ pH. This imposes a constraint on SQUID size/area. Optimizing the SQUID for maximum input coupling (M_{in}) ultimately results in $L_{\mathrm{in}} \approx 2\,\mathrm{nH}$.

For a meander-shaped pickup coil with a pitch of $p = 5\,\mu$m and a line width of $w = 2.5\,\mu$m, the area corresponding to $L_{\mathrm{m}} = 2\,\mathrm{nH}$, is $360 \times 90\,\mu\mathrm{m}^2$. A rectangular shape for the pickup coil is chosen because it reduces the etching time in the detector release step during fabrication.

Increasing the sensor thickness allows more magnetic field lines to thread through it, as illustrated in Figure 3.6, but there is a point where the average magnetic field within the sensor begins to decrease. This occurs because the biasing field is concentrated in the vicinity of the pickup coil, reducing the effective coupling higher within the sensor. Additionally, a thicker sensor increases the detector's heat capacity, slowing down its response time. Therefore, an optimal sensor thickness must be identified to ensure efficient magnetic field coupling while avoiding excessive thermal load, which could make the detector too slow for the scanning speed of the telescope. In Figure 3.13 (b), The $\mathrm{NEP}_{\mathrm{det}}$ is shown for multiple sensor thicknesses. The minimum $\mathrm{NEP}_{\mathrm{det}}$ increases with increasing thickness, indicating that thinner sensors perform better. However, this reduction also translates to less signal threading the SQUID allowing erbium $1/f$ excess noise to dominate the low frequency range. An optimal thickness can be found in the range of 1 μm that ensures an acceptable level of $1/f$ erbium excess noise contribution while maintaining low response times.

Although increasing the erbium concentration naturally enhances sensitivity, it will also increase excess intrinsic noise that depends on the total number of erbium ions (cf. Equation 3.39). In addition, the detector becomes slower since it results in a higher specific heat of the erbium subsystem. This is visible in Figure 3.13 (c), multiple erbium concentrations are used to compute the resulting $\mathrm{NEP}_{\mathrm{det}}$. As erbium concentration is increased, the sensitivity improves, lowering the detector noise. This occurs until reaching a concentration of $\approx 750...1000$ ppm. Above 1000 ppm the sensitivity does not improve significantly because it becomes dominated by thermal fluctuation noise.

Increasing I_{field} enhances the signal response linearly without significantly affecting the detector bandwidth. As seen in Figure 3.13 (d), $\mathrm{NEP}_{\mathrm{det}}$ is substantially reduced when sweeping I_{field} from 40 mA to 90 mA and was not found to significantly improve thereafter. To define an optimal I_{field}, however, the critical current (I_{c}) of the superconducting pickup coil should be considered as well. In Chapter 4, the measured I_{c} of the meander-shaped pickup coil used in this performance analysis is presented, corresponding to a value of ≈ 85 mA. A conservative value of 70 mA is selected which remains below 85 % of the measured critical value. Limitations in I_{c} may be overcome by using thicker films of superconducting material to fabricate the pickup coils and/or using superconducting materials of the highest critical current density available.

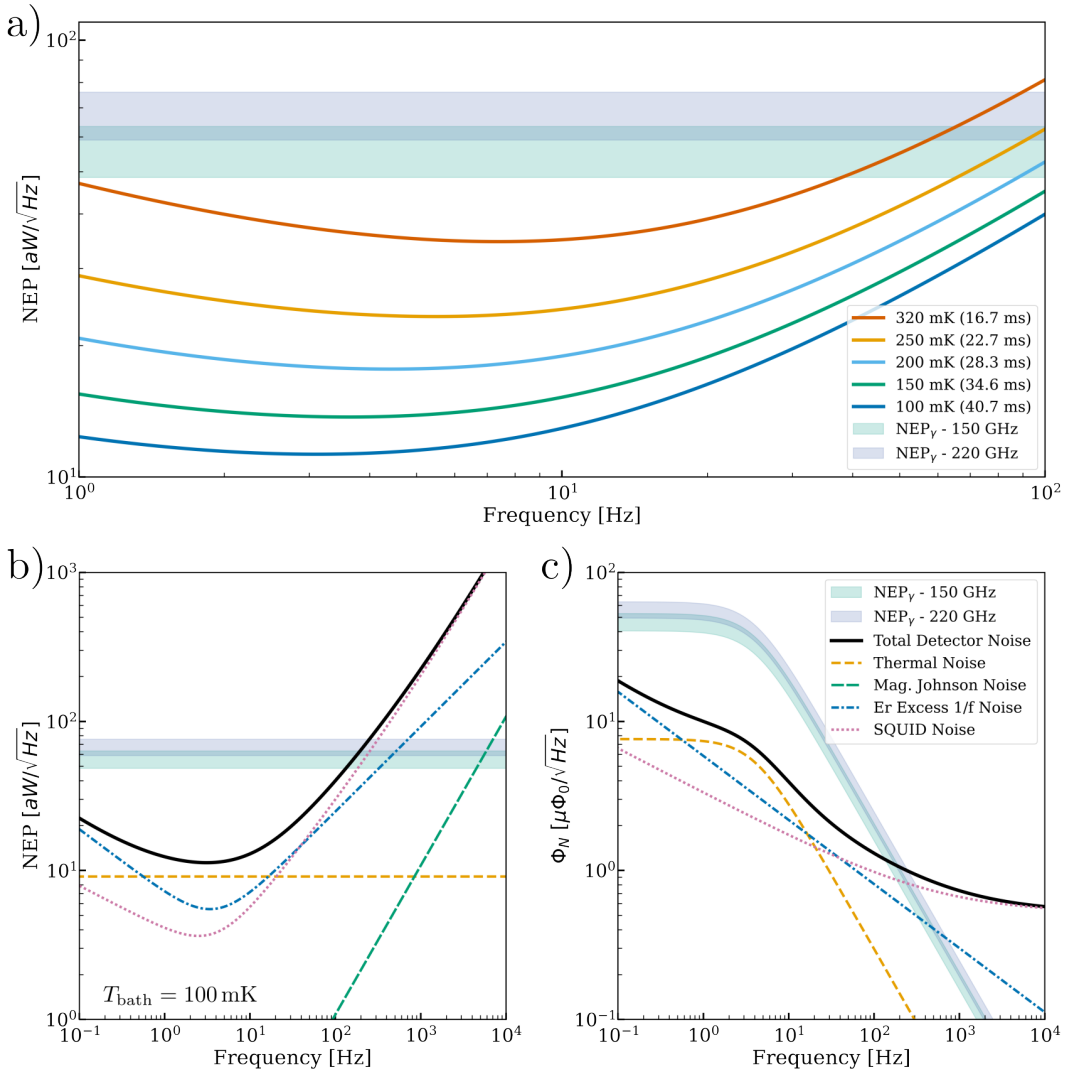

Figure 3.14: a) Detector noise equivalent power when lowering the bath temperature from 320 mK to 100 mK while keeping all other parameters constant relative to the estimated background NEP. The noise comparison in terms of (**a**) NEP and (**b**) flux noise (Φ_N) threading the readout SQUID are also presented at a fixed temperature of 100 mK representing individual contributions to the MMB noise in dashed traces.

3.7 Optimization of an MMB for other experiments

Thermal fluctuation noise can be reduced by lowering the operating temperature of the radio telescope. This would also enhance the performance of the MMB, as the magnetization of the paramagnetic sensor exhibits a steeper slope at lower temperatures. The impact of reducing the cryostat's bath temperature is illustrated in Figure 3.14 (a), where $\mathrm{NEP}_{\mathrm{det}}$ steadily decreases as the base temperature of the instrument is lowered. At lower temperatures, G_{bath} decreases according to equation 3.7, leading to an increase in thermal gain. Additionally, the paramagnetic sensor experiences a larger vari-

ation in magnetization, generating greater current change in the pickup coil. Moreover, temperature-dependent noise sources become less dominant, further contributing to the detector's enhanced sensitivity. Figure 3.14 (b) and (c) illustrate the detector noise performance at the lowest bath temperature ($T_{\mathrm{bath}} = 100\,\mathrm{mK}$) considered, showing ample sensitivity margins. In addition to the increased sensitivity, the time constant of the bolometer also remains within the admissible constraint.

3.8 The MMB Technical Demonstrator (MMB-TD)

The process of developing MMB pixels for CMB polarimetry is divided into three key stages. The first stage involves creating an MMB prototype that can be activated by current signals applied directly to the termination resistor, testing the performance of the paramagnetic sensor material in converting the power input into a measurable current signal with noise levels consistent with theoretical predictions. The second stage focuses on coupling MMBs to narrowband antennas that precisely capture radiation at specific frequencies, assisted by appropriately sized lenslets. The final stage involves using a broadband antenna, as outlined in Chapter 2, along with inline band-defining filters that require their own characterization and optimization procedures.

The primary goal of the MMB development within the scope of this thesis was to create a prototype device that is sensitive to power inputs and operates based on the principles described. This marks the initial step in the development of the MMB. This prototype device is hereinafter referred to as the Magnetic Microbolometer Technical Demonstrator (MMB-TD). The schematic diagram of the MMB-TD can be seen in Figure 3.15. Three main components can be recognized: the paramagnetic sensor coupled to a pickup coil, a load inductor that serves as ballast for persistent current injection and ensures a high signal coupled to the SQUID, and a persistent current switch that is used to momentarily suppress superconductivity in the pickup circuit to inject the persistent bias field current (I_{field}).

The termination resistor of the antenna-coupled circuit is emulated in this stage by feeding the signal directly from pads labeled I_{R}. This resistor, the paramagnetic sensor, and the pickup coil (L_{m}) are embedded in a suspended structure that ensures a weak thermal coupling to the heat bath to produce a high thermal gain.

The MMB-TD prototypes were fabricated on $20 \times 20\,\mathrm{mm}$ substrates. A total of six pairs of prototypes compose each fabricated sample. The design contemplated, first, that no dicing can take place after the detector release process because the vibrations generated would compromise the structural integrity of the detectors and, second, that the connection pads for the detector output signals must be as close to the chip border as possible so that the wire bonds connecting them to the readout SQUID have minimal length and low parasitic inductance. The MMB-TD design accounting for these considerations is shown in Figure 3.16.

A symmetrical arrangement of MMB prototypes with the detector outputs facing inwards was chosen. Dicing the substrate is only required once, splitting it through the symmetry line before performing the final detector release step. This allows the detector

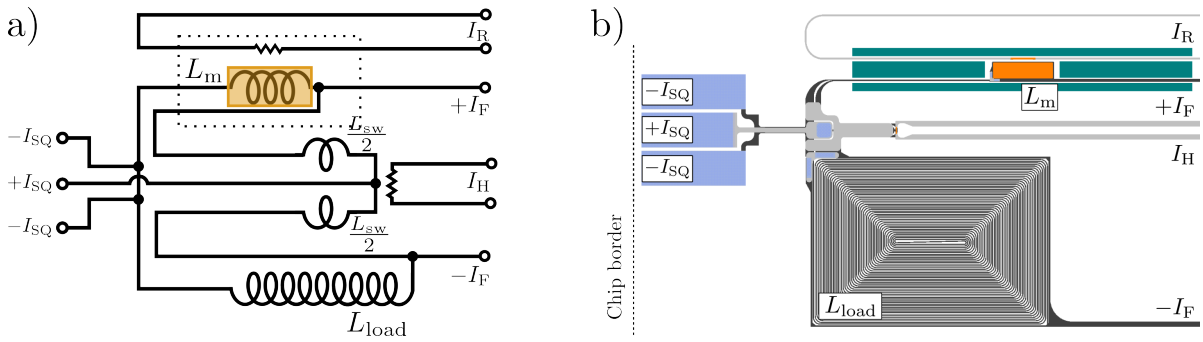

Figure 3.15: **a)** MMB-TD prototype schematic diagram. **b)** Layout design of the MMB-TD prototype. Three currents are fed to this device (I_F) is the bias field current (I_H) drives the persistent current switch and a third current is driven to the termination resistor (I_R) in contact with the paramagnetic sensor to extract the MMB-TD response characteristics. The output signals ($\pm I_{SQ}$) are measured with a SQUID connected to the output on the left via three connection pads for common-mode signal rejection.

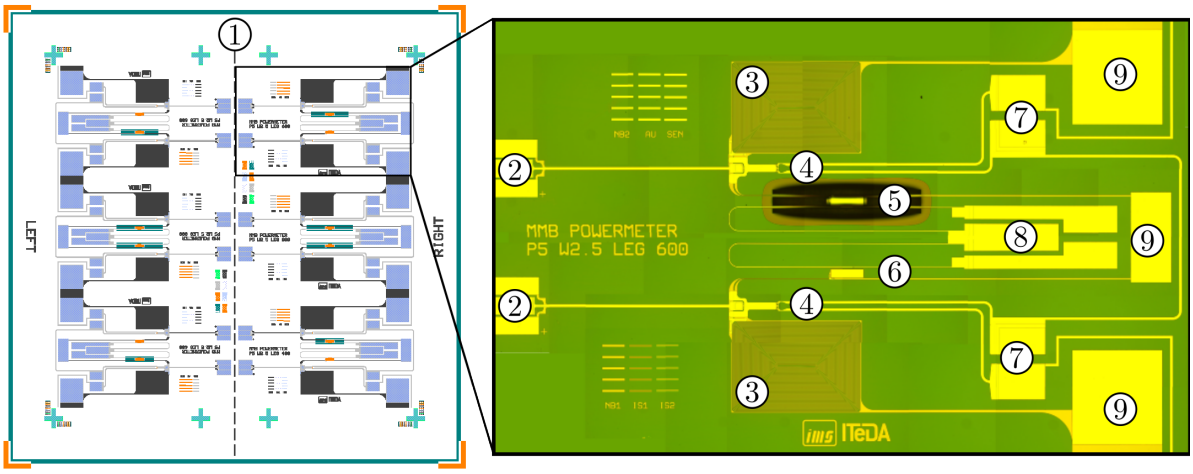

Figure 3.16: Design of the MMB-TD prototypes, the image includes a close-up view of a pair of fabricated MMB devices: One of them is released with 600 μm long legs, and the other is an non-released counterpart. 1) Pre-release dicing marks. 2) Connection pads to the readout SQUID ($\pm I_{SQ}$). 3) Load Inductor. 4) Persistent current switch. 5) Released MMB. 6) Non-released MMB. 7) Persistent current switch pads (I_H). 8) Input signal pads (I_R). 9) Persistent current injection pads (I_F).

output pads to be in proximity to the edges without requiring further dicing of the fully finished device. The structures to be released are placed in the center of the resulting 10×20 mm substrates. This last consideration was taken because when the released structures are close to the edges, the several-μm-thick photoresist required for the release produces edge beads that negatively affect the development step.

Detailed views of the MMB design can be seen in Figure 3.17. The detector design consists of a rectangular island with the active components held in place by four dielectric legs. The termination resistor is adjusted to a value of 20 Ω matching the differential lines

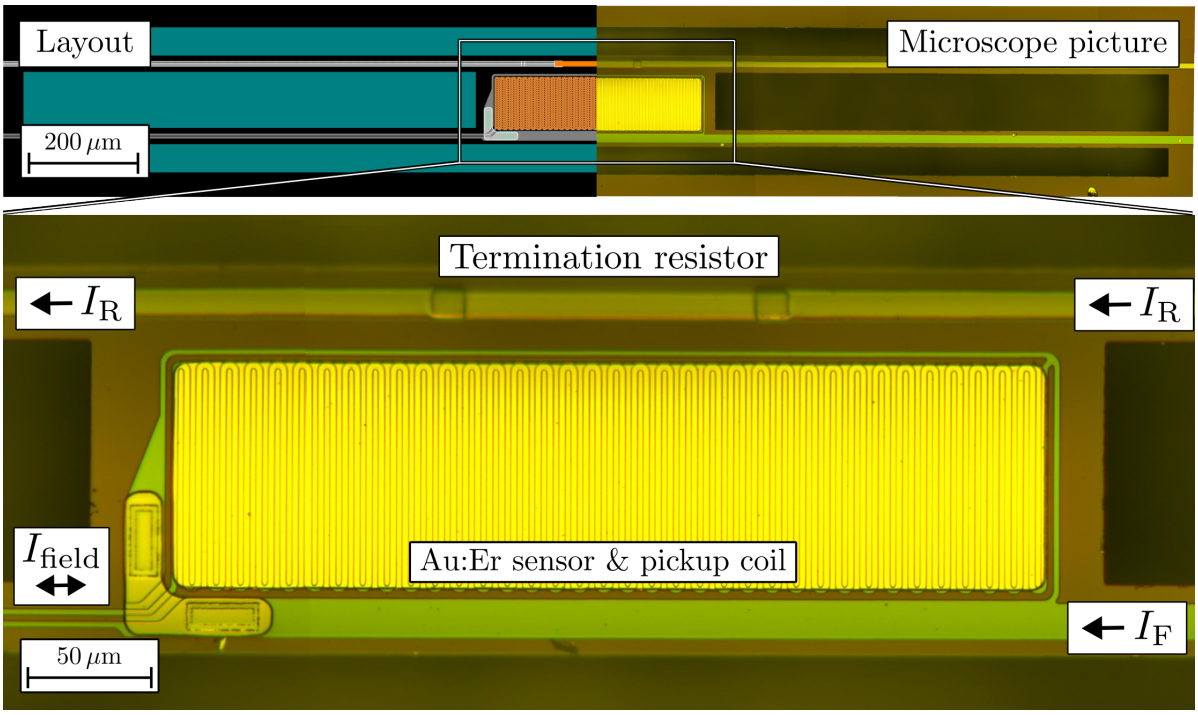

Figure 3.17: Microscope picture, layout design and zoomed-in view of a finished MMB detector. The island in the center holds the pickup coil, the paramagnetic sensor, and the termination resistor and four dielectric legs hold the island in place. Along the legs, the pickup coil lines carrying the persistent bias field current (I_{field}), one of the persistent current injection lines (I_{F}), and the termination resistor lines (I_{R}) are placed.

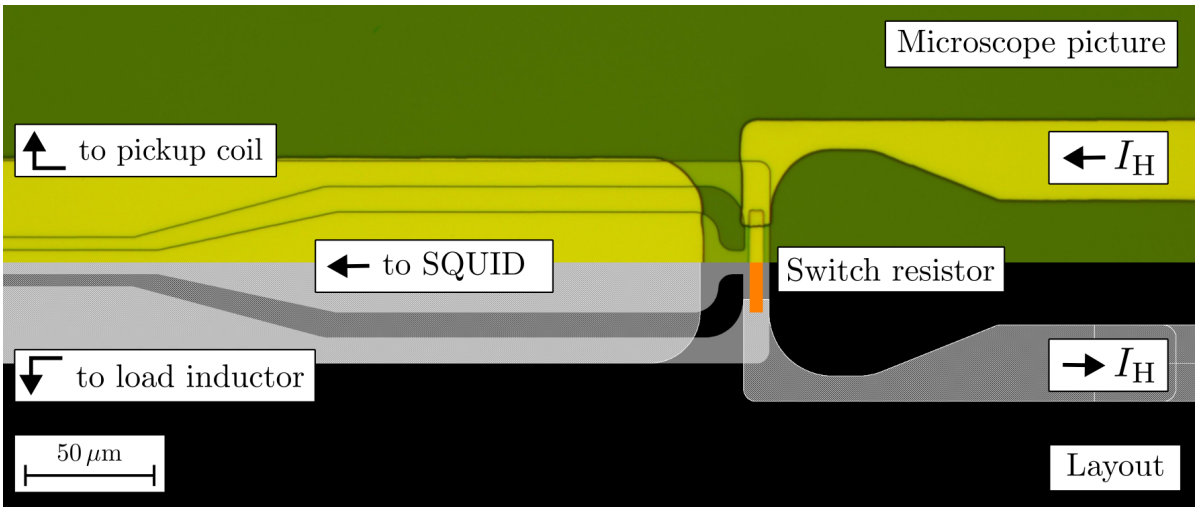

Figure 3.18: Microscope picture and layout design of the persistent current switch used to inject I_{field}. The connection of three lines connecting the pickup coil, the load inductor and the readout SQUID is placed directly underneath a resistor. A thin insulating layer separates the resistor from the superconducting line, and two additional lines are used to drive the switch pulse current (I_{H}).

that carry the filtered CMB signal from the broadband antenna. These feed lines are directed through the top legs (I_{R}). On the left bottom leg, two narrow superconducting lines carry the excess signals generated by the sensor and persistent bias field current (I_{field}), and on the right bottom leg, a wide superconducting line carries the feed current (I_{F}) used for persistent current injection. In future designs, this line will be removed from the suspended structure as it increases the inductance between the injection point and the persistent current switch (L_{sw}). The inductance between these two points decreases the effective I_{field}, as shown by Equations 3.25 and 3.28.

A detailed view of the persistent current switch is shown in Figure 3.18. The structure consists of three superconducting lines that connect the pickup coil to the load inductor and the SQUID and are effectively opened by a resistor placed on top separated by a thin insulation layer. A pair of superconducting lines connects the resistor to the switch pads. The switch is designed so that the resistor is placed on a flat surface, avoiding step-induced hot spots that would affect the heat profile. The superconducting lines are also covered with a superconducting sheet to reduce the inductance of the switch structure as much as possible and provide additional screening from external magnetic fields.

Chapter 4

Fabrication Methods

The microfabrication of the MMB prototype devices described in this thesis was produced with the combined infrastructure of the Instituto de Tecnologías en Detección y Astropartículas (ITeDA) and the Institute of Micro- and Nanoelectronic Systems (IMS). The device is built on a silicon substrate pre-coated with a low-stress, thin insulating film. The final step in the fabrication of the MMB is to release the bolometer structure from the silicon substrate. The insulating film holding the MMB is held in place by patterning narrow insulating legs. The reduced thermal coupling to the detector substrate is adjusted to achieve the required sensitivity in the operation temperature ranges found in astronomical cryogenic telescopes for bolometric detection. This type of released paramagnetic detector has never been produced in the past (to the best of my knowledge), for this reason, release processes needed to be evaluated and optimized to fabricate these prototypes.

This chapter consists of two parts: first, each process required in the production of the active detector components and the optimization considering the design goals is presented; and secondly, the detector release process is described. The latter includes the development of a specialized machine that was constructed and used for bulk isotropic etching of silicon based on xenon difluoride (XeF_2).

4.1 Active Detector Components

The prototypes presented in this thesis were fabricated on commercially available specialized p-doped silicon (Si) substrates. The bare Si substrate thickness is $(675 \pm 25)\,\mu$m. The $\langle 100 \rangle$ crystal oriented CZ-Si wafers were pre-coated with a silicon oxide (SiO_x) layer, with a measured thickness of (29.95 ± 0.42) nm, grown in a dry thermal oxidation process, and a low-stress silicon nitride (LSiN) film, with a measured thickness of (600.18 ± 11.11) nm, grown by low pressure chemical vapor deposition (LPCVD). The LSiN film holds the released MMB after the detector release process.

The initial fabrication step involves depositing a high-quality niobium (Nb) layer, which serves as the superconducting pickup circuit and, in the case of a complete CMB pixel, also functions as the antenna structure and ground plane for the microstrip trans-

mission lines. Nb is deposited using DC magnetron sputtering in a vacuum chamber with a base pressure of $\approx 10^{-8}$ mbar, in a controlled argon (Ar) atmosphere at 5 μbar. The substrate is mounted on a copper chuck, Apiezon N grease is applied under the substrate to improve thermal contact. The sputtering machine used is a Leybold UNIVEX 450 equipped with a load lock and Ar ion gun for surface cleaning. Before Nb deposition, the substrate surface is treated in-situ with the Ar ion gun. This removes any absorbed water vapor during handling. Additionally, by etching away a few atomic monolayers of the substrate, it enhances Nb adhesion. This process is repeated before each Nb deposition to ensure good electrical and mechanical contact between the Nb layers and any underlying metal structures. The Nb structures are patterned using the MLA150 maskless aligner produced by Heidelberg Instruments[1], which offers submicron resolution and high alignment precision for micrometer-scale features. A high-resolution positive-tone photoresist (AZ® MiR™ 701) is used for the patterning of the first layer. The Nb film is then etched using reactive ion etching (RIE) with an inductively coupled plasma (ICP) RIE system produced by Oxford Instruments[2].

Following the deposition of the first Nb layer, a silicon dioxide (SiO_2) film is deposited by RF sputtering in a custom-built sputtering machine. The machine is equipped with a small loadlock for quick sample conditioning. The deposition is performed in a mixed plasma at a total pressure of 6 μbar of which 60 % is Ar at a partial pressure of 3.6 μbar and 40 %, oxygen (O_2) corresponding to a partial pressure of 2.4 μbar. The SiO_2 layer demonstrated good adhesion to the underlying Nb layer and provides adequate insulation for subsequent superconducting or metallic layers. The total thickness of the SiO_2 insulating layer is divided into two separate deposition steps. Dielectric sputtering processes are prone to pinhole formation due to unbound electrons of incoming particles that charge the substrate surface. These charged regions can deflect other incoming particles during deposition, promoting the development of voids that lead to electrical shorts. Splitting the deposition into two steps reduces the chance of pinhole formation. From a design perspective, splitting the insulation layer improves via step coverage too. By creating via openings of different sizes between the two SiO_2 layers, a 300 nm total step height is broken down into two 150 nm steps, which can be more reliably bridged by a 500 nm thick second Nb layer. The design patterns are transferred to the sample by a lift-off process using AZ® nLOF™ 2020 negative-tone photoresist produced by MicroChemicals[3]. A five-minute megasonic bath in Dimethylsulfoxide (DMSO) and two ultrasonic baths in Acetone and Isopropanol are sufficient to eliminate the exposed resist and remove all unwanted SiO_2 from the sample. For the development of a complete CMB pixel a subsequent deposition of SiO_2 is required over the millimeter-wave circuits to have the adequate insulator thickness for the microstrip transmission lines which is 500 nm in the design presented in Chapter 2.

Gold palladium (AuPd) resistors are used in MMB detectors as the termination resistor for the microstrip transmission lines and the persistent current switches used to inject the persistent current in the pickup coil. AuPd is deposited by DC magnetron sputtering

[1]Heidelberg Instruments Mikrotechnik GmbH, Mittelgewannweg 27, 69123, Heidelberg, Germany
[2]Oxford Instruments Limited, Tubney Woods, Abingdon, Oxon, OX13 5QX, England
[3]MicroChemicals GmbH, Nicolaus-Otto-Str. 39, 89079 Ulm, Germany

and patterned via lift-off using AZ® nLOF™ 2020 photoresist. A short (two seconds) in-situ deposition of Nb is performed before and after the AuPd deposition. The resulting thin layers of Nb enhance adhesion and provide better contact for the Nb electrode that is sputtered in a subsequent deposition step. The AuPd film is sputtered in a 5 μbar Ar plasma with a DC sputter power of 70 W.

A second Nb layer is deposited after the AuPd layer. This second Nb layer is used to make all required bridges in the superconducting components and to connect the AuPd resistors to their respective contact pads. This layer is thick enough for adequate step coverage, around 500 nm and also patterned via lift-off process with AZ® nLOF™ 2020 photoresist.

The sensor material used for the production of the first MMB-TD prototypes was Au:Er with an erbium concentration of $\approx$ 1000 ppm. This film is deposited using a custom-built three-chamber sputtering system via DC magnetron sputtering. The sample is first mounted and placed into the loadlock chamber. The loadlock is evacuated until a base pressure of approximately 10^{-7} mbar is reached. The sample is transferred to the first sputtering chamber for Nb deposition. A thin Nb layer is sputtered onto the sample to act as an adhesion layer for the Au:Er film. A sputtering time of just four seconds, resulting in a layer thickness of only a few nanometers, is sufficient. Thicker Nb films would transition to the superconducting state, shielding the pickup coil from changes in the sensor's magnetization and thereby rendering the detector insensitive. After the Nb sticking layer is deposited, the sample is transferred into the Au:Er deposition chamber. The pre-sputtering or conditioning time in this chamber is kept short, around 30 seconds, to minimize Au:Er material loss. The sensor material is patterned with a lift-off process using AZ® nLOF™ 2020 photoresist. The sputtered sample is placed in a Dymethilformamide (DMF) bath and kept on a rocker table for at least 24 hours to ensure that the photoresist is fully dissolved. Two acetone and isopropanol baths in an ultrasonic cleaner are used to finish the removal of the excess film from the substrate. The lifted Au:Er film is then carefully removed and archived for further characterization in a magnetometer if required.

In the following sections a detailed description of the fabrication processes is given focusing on the most important components, namely the pickup coil, the persistent current switch and the production of an Ag:Er sputtering target.

4.1.1 Pickup coil

The pickup coil geometry is a meander-shaped coil with a pitch of $p = 5\,\mu$m and a line width of $w = 2.5\,\mu$m. These p and w values were selected as they maximize the magnetic field within the sensor and can be reliably fabricated with the available equipment. The quality of the fabricated Nb thin films was studied and optimized to present the best superconducting properties for MMB fabrication. It is desireable to obtain a superconducting pickup coil with high ampacity or critical current (I_c) respecting the geometry obtained from the design optimization. The ampacity of the pickup coil determines the maximum allowed I_{field} that can be used to bias the sensor and the coil must withstand the release process without observing a significant reduction in this parameter. The Nb

film thickness is 250 nm. Though ampacity increases with thickness, a thicker pickup coil requires a correspondingly thicker silicon dioxide (SiO_2) insulation layer, increasing the separation between the pickup coil and the sensor material and degrades performance. It was determined that 250 nm thickness for the pickup coil provides an optimal balance between ampacity and magnetic coupling efficiency.

Nb thin film intrinsic stress

The deposition conditions for the pickup coil geometry were first optimized to present low intrinsic stress such that the released detector would not bend excessively or break during cooling, handling, or installation in the instrument. Intrinsic stress in a thin film is defined as the internal pressure within the material, which can manifest as compressive stress (pushing the film together) or tensile stress (pulling it apart). There exist multiple studies that relate the intrinsic stress of the Nb films to their superconducting performance and deposition parameters [137–139]. In general, excessive stress and strain on superconducting films are related to reduced superconducting properties. On the other hand, excessive intrinsic stress becomes problematic when releasing the structures on thin insulating films, which is performed in the final fabrication step of the MMB.

Deposition conditions affect the intrinsic stress exhibited by Nb thin films. These are sensitive to sputtering pressure (P_{Ar}) and bias voltage which depends on the sputtering power (P) [140]. To evaluate the impact of the deposition conditions on the intrinsic stress of the Nb films produced with the UNIVEX 450 sputtering machine, both P_{Ar} and P were systematically varied. The resulting stress was assessed using the methods described by Stoney [141], by analyzing the curvature of the substrate before and after deposition. This approach is straightforward and requires minimal additional equipment beyond the deposition system itself, an accurate stylus profiler [142]. For each deposition condition, Nb was sputtered onto two 2×10 mm substrates. One was used to precisely measure the film thickness (t), while the other was used to assess substrate curvature. Curvature profiles before ($A_1(x)$) and after ($A_2(x)$) deposition were measured along a central trace, spanning 9 mm of the 10 mm substrate, with 0.5 mm margins left at each end to avoid edge effects during probing. The film's intrinsic stress ($\sigma(x)$) can be calculated as:

$$\sigma(x) = \frac{1}{6}\left(\frac{1}{R_{\mathrm{post}}(x)} - \frac{1}{R_{\mathrm{pre}}(x)}\right)\frac{E}{1-\nu}\frac{t_{\mathrm{s}}^2}{t_{\mathrm{f}}}, \tag{4.1}$$

where $R_{\mathrm{pre}}(x)$ and $R_{\mathrm{post}}(x)$ are the radius of curvature pre- and post-deposition, E is Young's modulus, ν is Poisson's ratio and t_{s} and t_{f} are the substrate and film thicknesses, respectively. For DC sputtered Nb thin films, $E = (116.02 \pm 7.35)$ GPa and $\nu = (0.41 \pm 0.03)$ [143]. The substrates used for these measurements were diced from a 380 μm thick silicon wafer coated on both sides with ≈ 100 nm layer of thermal oxide which is neglected in the analysis. $R_{\mathrm{pre}}(x)$ and $R_{\mathrm{post}}(x)$ are obtained by fitting $A_1(x)$ and $A_2(x)$ with a 5th-order polynomial ($f(x)$). The radii of curvature are calculated from their corresponding polynomial fit as:

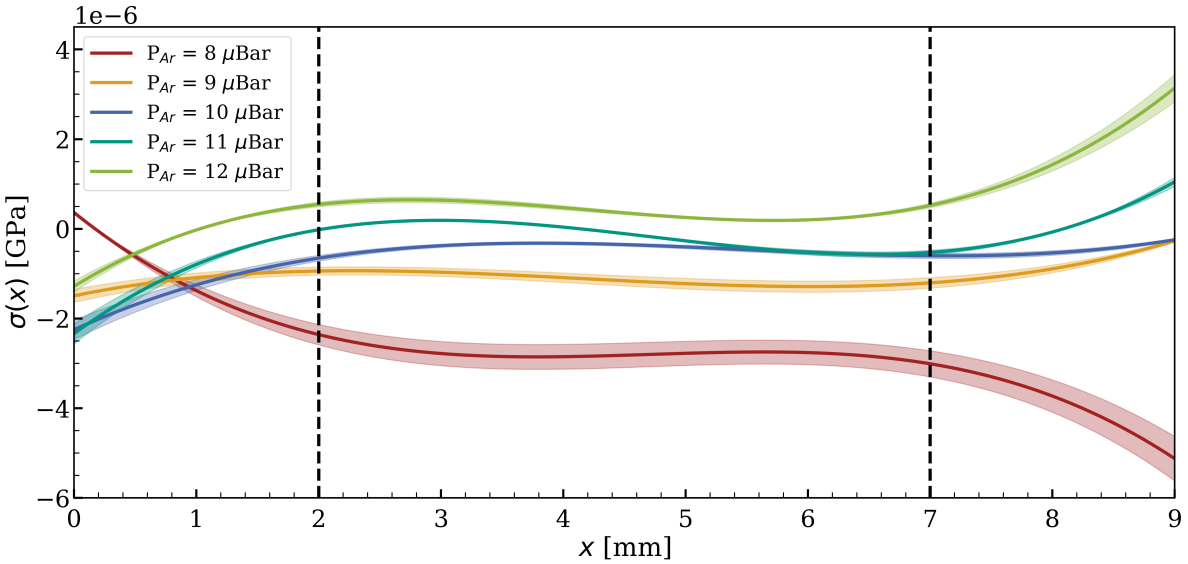

Figure 4.1: Intrinsic stress ($\sigma(x)$) curves of Nb films obtained for multiple sputtering pressures using the method described in the text. Negative values correspond to compressive stress, while positive values indicate tensile stress. Stable values of $\sigma(x)$ are observed in the central region of each sample (between dashed black traces).

$$R(x) = \frac{\left(1 + \left[f'(x)\right]^2\right)^{3/2}}{f''(x)}, \tag{4.2}$$

with $f'(x) = df(x)/dx$ and $f''(x) = d^2f(x)/dx^2$.

All samples exhibit both compressive and tensile regions along the scanned path, likely due to edge effects. These artifacts dominate a significant portion of the scan range, suggesting that for more accurate stress characterization, larger substrates and longer scan paths should be used. Despite these variations, stable values of $\sigma(x)$ are observed in the central region of each sample. By averaging $\sigma(x)$ across the sample, representative values were extracted and are summarized in Table 4.1. At lower P_{Ar}, Nb presents compressive stress, and with increasing P_{Ar} the stress becomes increasingly tensile. Among the tested conditions, a deposition pressure of 11 μbar resulted in the lowest average intrinsic stress. A similar analysis was conducted at $P_{\mathrm{Ar}} = 3\,\mu$bar while varying the sputtering power P. The results of the analysis with varying P are summarized in Table 4.2. The intrinsic stress appears to be less sensitive to sputtering power than it is to sputtering pressure within the ranges studied.

P_{Ar}	8 μbar	9 μbar	10 μbar	11 μbar	12 μbar
$\overline{\sigma(x)}$	−2671.98 Pa	−1065.55 Pa	−649.58 Pa	−286.45 Pa	547.04 Pa

Table 4.1: Nb film intrinsic stress results obtained for varying sputtering pressure (P = 60 W).

P	50 W	40 W	20 W
$\overline{\sigma(x)}$	−1539.30 Pa	−1216.18 Pa	−1145.56 Pa

Table 4.2: Nb film intrinsic stress results obtained for varying sputtering power ($P_{\mathrm{Ar}} = 3\,\mu$bar).

Ampacity of Nb straight lines and meander-shaped pickup coils

There exist several analytical expressions that describe the critical current dependence with temperature ($I_{\mathrm{c}}(T)$) in superconductors. In general, they are used to estimate the so-called depairing current, which represents the upper limit of the superconductor's ampacity. It corresponds to the point where the kinetic energy of the Cooper pairs with applied current equals their binding energy, causing the superconducting state to break down. One such analytical expression for the depairing current derived within the two-fluid model is [144],

$$I_{\mathrm{depairing}}(T) = I_0 \cdot \left[1 - \left(\frac{T}{T_c}\right)^2\right]^{3/2} \left[1 + \left(\frac{T}{T_c}\right)^2\right]^{1/2}. \tag{4.3}$$

However, in practical applications, the magnetic fields generated by the transported current will try to permeate the structure, and, in the case of type-2 superconductors such as Nb thin films, quantized magnetic vortices with a radius of $\approx 2\xi$ are formed. The transported current exerts Lorentz forces on these vortices, but they remain stationary as long as they are pinned by defects within the film. When the current reaches a sufficiently high value, the force exerted overcomes the vortex-pinning potential, causing them to move and subsequently disrupt superconductivity. This threshold current is known as the depinning current, and there exists no closed-form expression to determine its value nor its temperature dependence. To simplify the analysis, an expression replacing the exponents of Equation 4.3 with free parameters α and β was adopted to fit the observed $I_{\mathrm{c}}(T)$ dependence [145],

$$I_{\mathrm{depinning}}(T) = I_0 \cdot \left[1 - \left(\frac{T}{T_c}\right)^2\right]^{\alpha} \left[1 + \left(\frac{T}{T_c}\right)^2\right]^{\beta}. \tag{4.4}$$

Measurements of $I_{\mathrm{c}}(T)$ within the temperature range of $T_{\mathrm{c}}/2 < T < T_{\mathrm{c}}$ were performed on the Nb structures under study. Equation 4.4 was used to fit the measured data and extract the relevant parameters including I_{c} at the MMB operating temperature. At fixed temperature steps, a current is fed to the structures while monitoring the voltage across it using a four-point probe configuration. The current is increased in steps of 100 μA at fixed time intervals of 300 ms. The voltage expected in the superconducting state is zero. As the current applied reaches I_{c}, the structure transitions to the normal state and presents a certain normal-state resistance. Therefore, a large voltage swing is recorded. The change in resistance is abrupt, and its shape changes with temperature. The used voltmeter is not necessarily fast enough to measure voltages within the superconducting-to-normal transition in the full temperature range, so for the analysis, the current at which the structure presented the last superconducting voltage value was noted.

Within the frame of the three-current model [146], the I_c dependence when $T \approx T_c$ is known to shift to the depairing mechanism as the current required for vortex entry becomes close to or sometimes even higher than I_c. For this reason, I_c measurements with high resolution (smaller temperature and current steps) in the vicinity of T_c were fitted with Equation 4.3, to obtain a reliable estimation of T_c. The Nb thin films used in the production of the MMB-TD presented a value of $T_c = (9.03 \pm 0.08)\,\mathrm{K}$ with this measurement method.

Optimal Nb deposition conditions

The Nb films sputtered at $P_{Ar} = 11\,\mu$bar presented the lowest intrinsic stress, and by further optimizing P, it is possible to achieve stress-free Nb films. With such low-stress films, no challenge is foreseen when performing the detector release step. However, these deposition conditions are not optimal when considering the ampacity of the resulting meander-shaped pickup coils. Figure 4.2 shows the $I_c(T)$ dependence of Nb films deposited at $P = 60\,W$, comparing films sputtered at $P_{Ar} = 3\,\mu$bar and $P_{Ar} = 11\,\mu$bar. The measured structures are straight lines with $w = 10\,\mu$m. A significant reduction in the critical current is observed for the film deposited at $P_{Ar} = 11\,\mu$bar. In particular, a reduction from $(253.31 \pm 11.82)\,$mA to $(208.52 \pm 20.46)\,$mA, representing a 17.68 % decrease. This result suggests that Nb films sputtered at lower pressures exhibit better superconducting performance, at least in terms of their critical current. The results can be explained by considering that, in addition to reducing Nb intrinsic stress, increasing P_{Ar}, also shifts the sputtering process from a ballistic regime towards a diffusive regime in the material transfer from the target to the substrate [147]. Such a shift in the sputtering regime also plays a role in the quality of the resulting film. There is a critical value of P_{Ar} above which sputtered Nb presents a significant reduction in T_c [138]. Therefore, a compromise is met between using low sputtering pressures while keeping an acceptable level of compressive intrinsic stress.

The sputtering conditions determined for meander-shaped pickup coils in the MMB-TD are: $P_{Ar} = 5\,\mu$bar and $P = 60\,$W. Several pickup coils were produced to test their resilience after the release process. They demonstrated structural stability even when cooled to millikelvin temperatures. A picture of a released and non-released pickup coil are shown in Figure 4.3 for reference.

The comparison between the $I_c(T)$ dependence of a straight Nb lines with both released and non-released meander-shaped pickup coils is presented in Figure 4.4. All structures have similar thicknesses ($t \approx 250\,$nm) and the same width ($w = 2.5\,\mu$m). The best-fit results to the measured data are displayed in Table 4.3. In general, the empirical α and β parameters have lower values than those of the two-fluid model ($\alpha = 3/2$ and $\beta = 1/2$). Comparing the straight lines to the non-released meander-shaped pickup coil shows a reduction of $I_c(0)$ from $(98.91 \pm 3.46)\,$mA to $(89.22 \pm 3.38)\,$mA, representing a 9.80 % decrease. This was attributed to enhanced magnetic effects inherent to meander-shaped coils, where the fields created by neighboring lines are added coherently at each trace.

With respect to the released pickup coils, measuring their $I_c(T)$ introduces certain

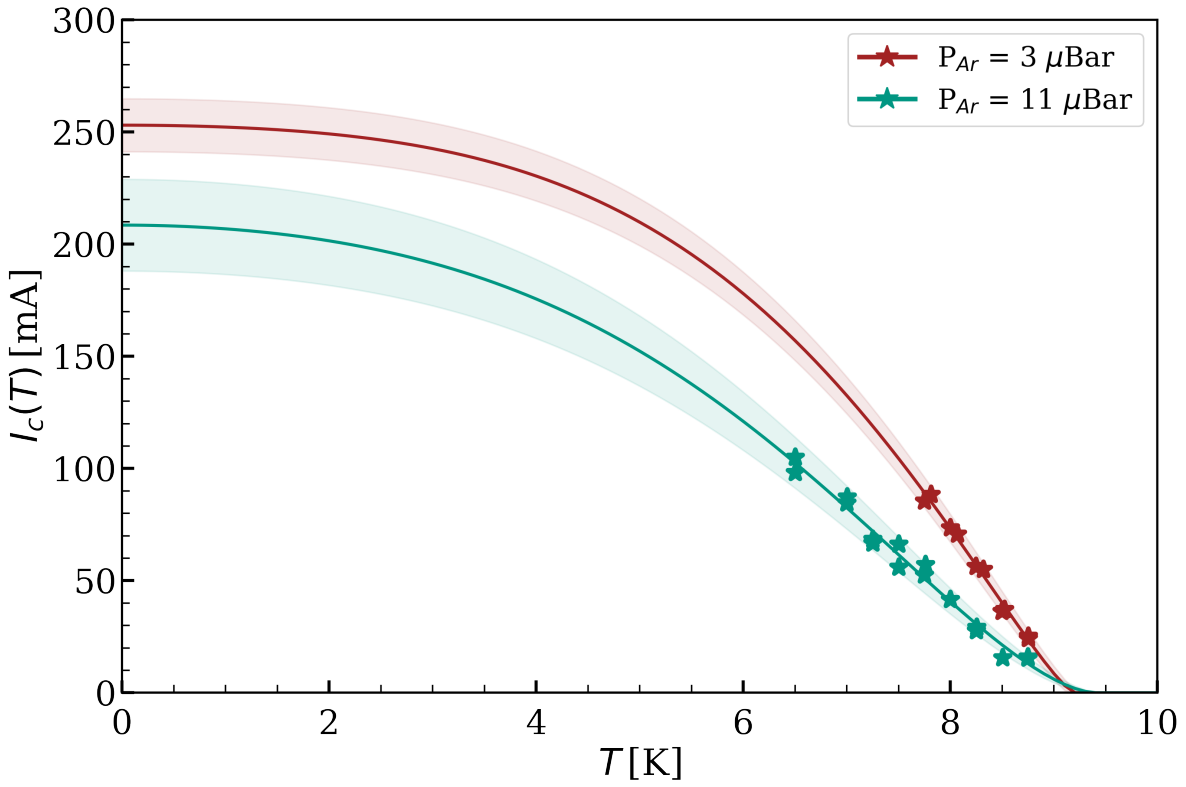

Figure 4.2: $I_c(T)$ measurements of Nb films deposited with $P_{\mathrm{Ar}} = 3\,\mu$Bar in red and $P_{\mathrm{Ar}} = 11\,\mu$Bar in green.

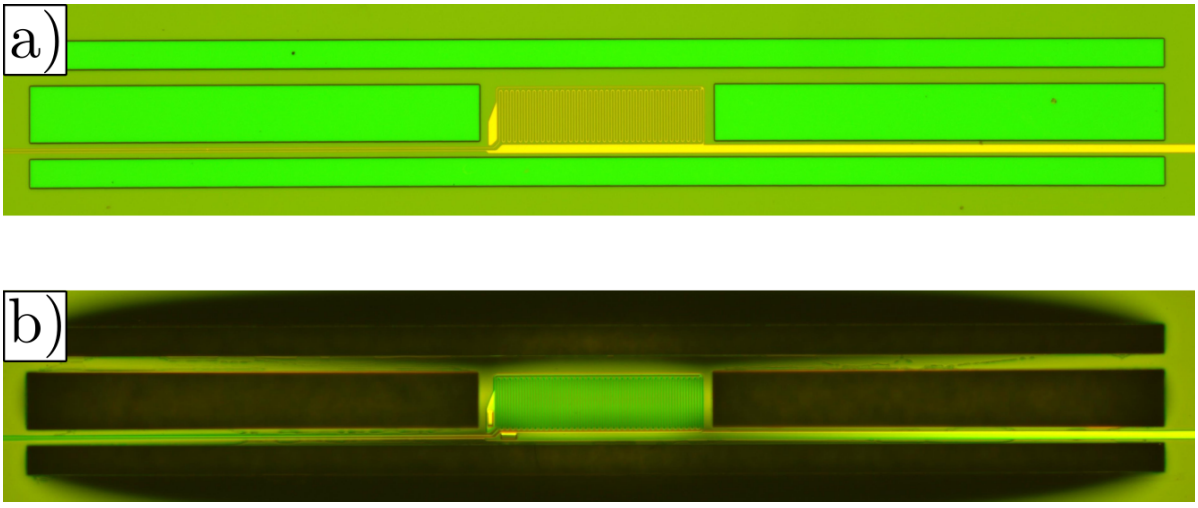

Figure 4.3: **a)** Non-released meander-shaped pickup coil. **b)** Similar Nb pickup coil standing on a released dielectric membrane.

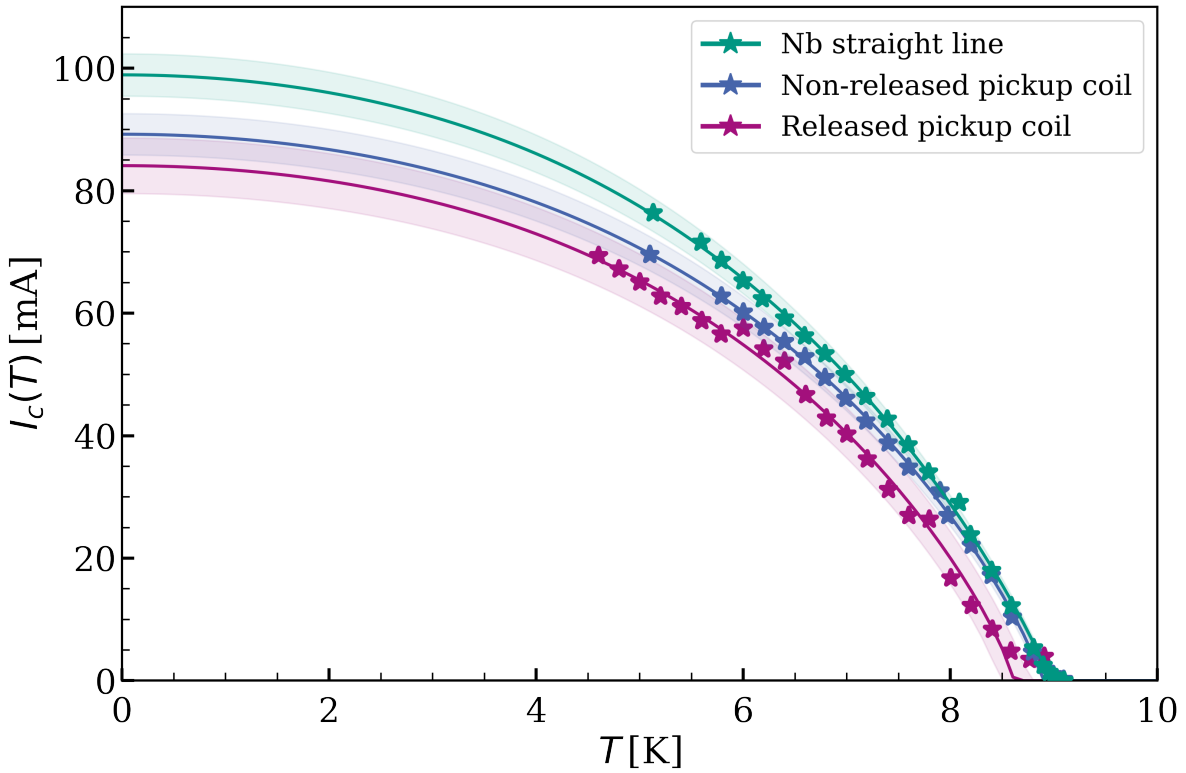

Figure 4.4: $I_c(T)$ measurements comparing Nb straight lines with released and non-released meander-shaped pickup coils.

Structure	$I_c(0)$	T_c	α	β
Nb straight line	(98.91 ± 3.46) mA	(8.96 ± 0.01) K	(0.89 ± 0.05)	(0.32 ± 0.16)
Non-released coil	(89.22 ± 3.38) mA	(8.89 ± 0.03) K	(0.83 ± 0.06)	(0.29 ± 0.18)
Released coil	(84.09 ± 4.85) mA	(8.61 ± 0.03) K	(0.81 ± 0.05)	(0.28 ± 0.16)

Table 4.3: Model fit results for the I_c measurements presented in Figure 4.4.

challenges, primarily due to the reduced thermal coupling to the substrate. These pickup coils exhibited a more erratic temperature dependence (see Figure 4.4). This is attributed to thermal effects that arise when superconductivity is suppressed and large current densities momentarily generate significant localized heating within the coil. In some cases, it was not possible to repeat the measurements. At the lowest temperature, the critical current reaches its maximum, resulting in the highest heat generated as the coil transitions to the normal state while the thermal conductivity of the structure is at its lowest. This combination caused irreversible damage to the structures. In spite of these difficulties, relevant information was extracted from ampacity measurements in these released pickup coils. They present a further reduction of the $I_c(0)$ from (89.22 ± 3.38) mA to (84.09 ± 4.85) mA, representing a 5.75 % decrease. This reduction was significantly smaller than the one seen in films deposited under higher sputtering pressures, and due to the multiple steps in the release process used (detailed in section 4.2.2), it is unclear,

with only these measurements, which step might be responsible. Excessive strain can potentially reduce the critical current in superconductors by distorting the film's structure. In one study [148], hydrostatic pressure was applied to Nb samples to improve superconducting properties by counteracting strain caused by internal stress. Although the stress in the Nb films studied here is low, releasing the MMB pickup coil alters its shape slightly, resulting in a visible bend along the coil lines, as shown in Figure 4.3 b). This deformation may introduce minor strain in the structure, contributing to the small, but measurable, decrease in I_c.

Nb/Nb vias

Connections between different superconducting layers are necessary in the realization of superconducting detectors. T_c and I_c of Nb/Nb vias of various sizes were measured. The measurements revealed no straightforward relationship between I_c and either the contact area of the via or the thickness of the second Nb layer. But certainly, the superconductivity of such multilayer structures is suppressed in comparison to that of single layer devices.

A Focused Ion Beam (FIB) system was used to study different structures and phenomena occurring during the fabrication of the via connections. Cross-section views were obtained from different fabricated samples. The FIB cuts were performed with a ThermoFisher[4] QUANTA 3D 200i. This equipment combines a FIB system for fast and precise substrate milling and a high resolution Scanning Electron Microscope (SEM) for high resolution imaging with up to 100,000x magnification. To produce the precise cuts, a platinum (Pt) strip is deposited over the structures under analysis. A highly energetic gallium ion gun is then ignited and directed towards it, the Pt strip functions as a ruler, protecting the underlying structure while exposing a straight edge for substrate milling. Higher resolution SEM pictures were taken using a Zeiss[5] Gemini Crossbeam 340 that offers magnification of up to 2,000,000x.

After analyzing the samples, the suppression of superconductivity in multilayer devices was traced to the following three main observations:

1. **Nb/Nb interface:** Even though both layers are made of Nb. During the cleaning and lithography steps required for processing of other layers in the device, the surface of the first Nb layer is exposed to various chemicals. Additionally, exposure to ambient air leads to oxidation and water vapor absorption. As a result, the surface of the Nb is modified, giving rise to an interface layer in the Nb/Nb connection. Even after an in-situ treatment of the Nb surface with an Ar ion gun for several minutes prior to deposition of the second Nb layer, surface defects thicker than a few atomic layers often prevail and contribute to the formation of the interface.
   FIB cuts performed on Nb/Nb vias show that there is a subtle and almost undistinguishable interface between both Nb layers (see figure 4.5 (a)). I_c measurements revealed that the suppression is not related to the area of via connections in a

[4]Thermofisher Scientific Inc. 168 Third Avenue, Waltham, MA, USA
[5]Zeiss GmbH, Carl-Zeiss-Straße 22, Oberkochen, Germany

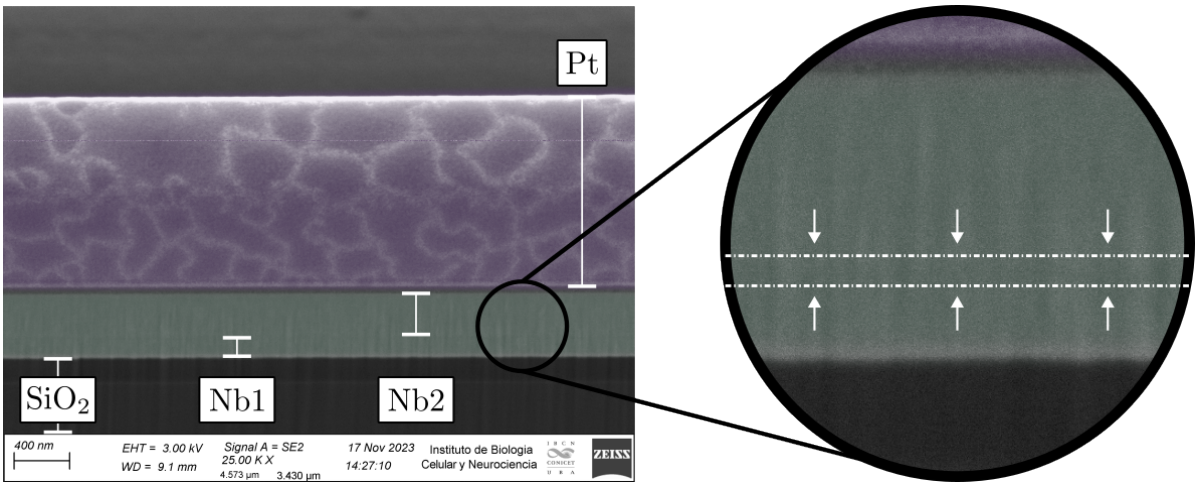

Figure 4.5: Colorized SEM picture of an FIB cut performed on one Nb/Nb via connection featuring the interface between both Nb layers. The two Nb layers showcase a subtle and almost undistinguishable black trace at the interface. A zoomed-in view of the area marks where the Nb/Nb interface should be.

large extent, indicating that the appearance of this interface may not be the most relevant issue. In any case, increasing the via connection area can mitigate it.

2. **Insulation wall defects:** Insulating layers made from silicon dioxide (SiO_2) are deposited by RF sputtering and patterned using a lift-off process. Due to the relatively isotropic nature of sputtering, the sidewalls of the photoresist windows can become coated with the sputtered material. This leads to the formation of flaps or flakes at the edges of the openings, which can interfere with via connections.
   Negative-tone photoresists are preferred for lift-off for two main reasons: they offer better thermal stability during deposition, and their development parameters can be tuned to produce vertical profiles or pronounced undercuts [149]. These undercuts help minimize sidewall coating and produce cleaner lift-off results. However, sidewall sputtering remains a persistent challenge. RF sputtering of SiO_2 typically yields low deposition rates and efficiency, and the target must be placed close to the substrate, further contributing to the isotropic nature of the deposition technique.
   The effect of insulating flaps and flakes is visible in figure 4.6 (b). The structure analyzed in this case is the connection to the top electrode of a Nb/Al/Nb window-type Jossephson junction. A thick dark side wall is evident that produces an abrupt interruption in the top Nb layer. The transported current must overcome those prominent obstacles and the superconductor cross-section is greatly reduced, producing high current densities.
   Increasing the cross-section of the second layer Nb steps can help mitigate this by reducing the current density in the via connections. On the other hand, deposition techniques such as Plasma Enhanced Chemical Vapor Deposition (PECVD) can be implemented to produce high quality and homogeneous insulating layers over the Nb structures that may then be pattered by ICP RIE to form contacting windows free of flaps or side-wall sputtering effects.

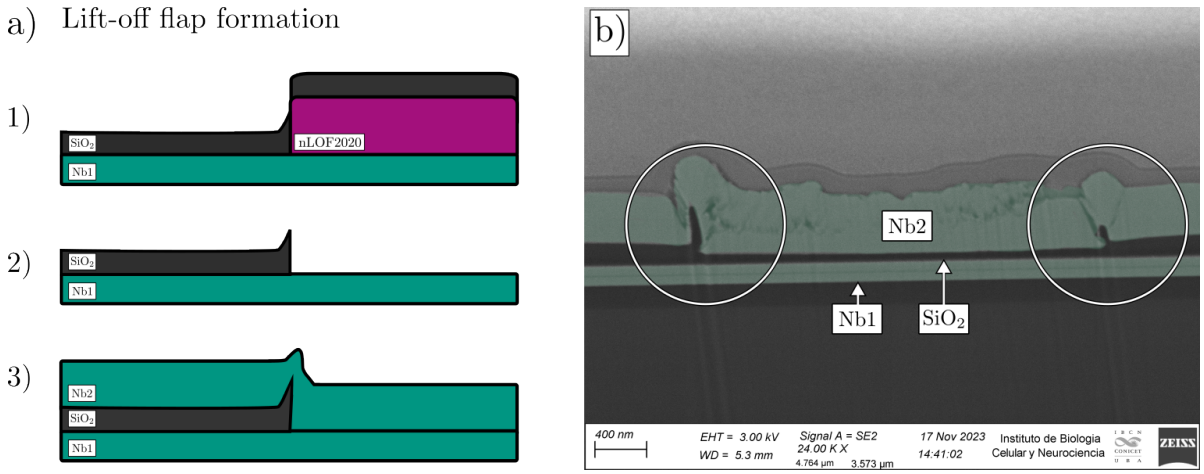

Figure 4.6: a) Effect of the lift-off flaps at the edges of the via connections. For clarity, two SiO_2 depositions took place and the picture is showing only the top-most step of the Nb2 layer in the connection. **b)** FIB cut of the Nb/Al/Nb window-type Jossephson junction.

3. **Nb sputtering step coverage:** When Nb is deposited at an angle, the crystal growth of the thin film is not ideal either. There is a critical deposition angle above which sputtered Nb can even cease to present a superconducting transition [150]. The underlying structures produce an irregular surface featuring steps and abrupt changes in height, at these positions, deposition angles of up to 90 degrees could be present. Steps in the Nb traces and also in via connections are weak spots where superconductivity can be severely suppressed. FIB cuts were performed on selected structures to examine the morphology of the second Nb layer deposited on uneven surfaces. These cuts revealed that as Nb grows on such surfaces, its crystal structure becomes disrupted at the edges of the underlying patterns resulting in the formation of voids and resemble fractures in the second Nb layer. This phenomenon is visible in figure 4.7. The cross-sectional view of a persistent current switch is shown, highlighting this effect. In the interface of the Nb trace and the gold-palladium (AuPd) resistor, no side-wall sputtering effects are seen, and the contrast between AuPd and Nb is clearly distinguishable with the SEM, making the step coverage effect more apparent. There is no straightforward solution to this issue. Planarization of the pickup coil, which will be discussed later, might help by producing a flat surface onto which the second Nb layer (Nb2) is deposited. But there will still be a step in the via connection at the insulating window. RIE etching of SiO_2 insulating layers can be optimized to present sloped steps or tapered sidewalls. In [151], the process parameters affecting the sidewall angle were explored together with tweaks in the the hard bake step of the photorresist. SiO_2 films with sidewall angles of 15° - 53° were reported.

For future optimization of the fabrication process of the MMB, insulating layers by CVD techniques patterned with a RIE etching process to present tapered sidewalls would allow the possibility to produce multilayer superconducting circuits with critical currents

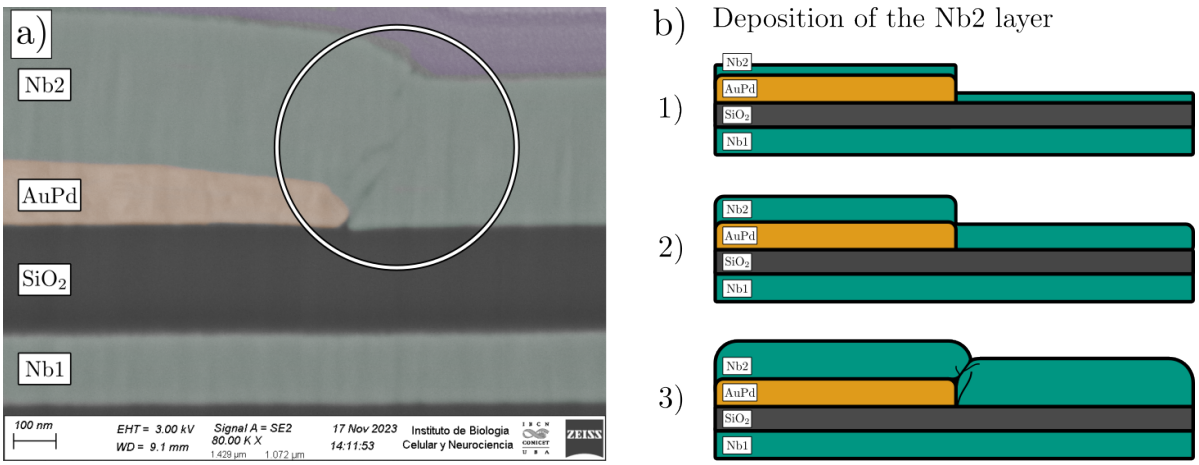

Figure 4.7: **a)** FIB cut on a persistent current switch. This image illustrates the fracture in the crystalline lattice of the second Nb layer (Nb2) when deposited on an uneven surface. **b)** Sketch offering an explanation for the formation of this fracture. During the sputtering deposition, the film is grown at different heights, and when the layer of the growing lower film encounters the already deposited first layers of the upper film, the Nb structures don't merge, producing an edge defect grain boundary.

close to the single layer device limit. Allowing more compact detector designs for detector array production. If multiple high-quality Nb layers are available, load inductors can be made smaller by using single spiral geometries in clockwise and counterclockwise orientation, for external magnetic field suppression, interconnected with bridges.

For the first design of the MMB-TD, the pickup coil and its biasing circuit are fabricated in a single Nb layer. Load inductors are designed as double spirals for external field rejection and require large areas to achieve the high inductances required for the bias and readout circuit.

Planarization techniques

Increasing the thickness of the initial Nb film can enhance I_c. However, this requires a proportionally thicker insulating layer to ensure adequate electrical isolation from the sensor material. As a result, the increased spacing between the pickup coil and the sensor reduces the average magnetic field for a given I_{field}, weakening the magnetic coupling. Planarization of the pickup coil and insulating layers can mitigate this issue by creating a flat surface onto which the sensor material can be directly deposited, minimizing the coil-to-sensor distance. Figure 4.8 compares planarized and non-planarized pickup coil configurations. An increase in the mean magnetic field from 6.63 mT to 7.11 mT is observed, corresponding to a 7.2 % improvement in detector signal strength. This comparison assumes $I_{\text{field}} = 50\,\text{mA}$ for both cases and Nb thickness of 250 nm. With planarization, thicker Nb films can be used without sacrificing sensor proximity, potentially enabling higher I_c and, consequently, larger I_{field}, improving detector sensitivity.

Planarization techniques involve surface treatments or strategically growing the films in a certain way that produces a planar or flat surface on top of the pickup coil to deposit

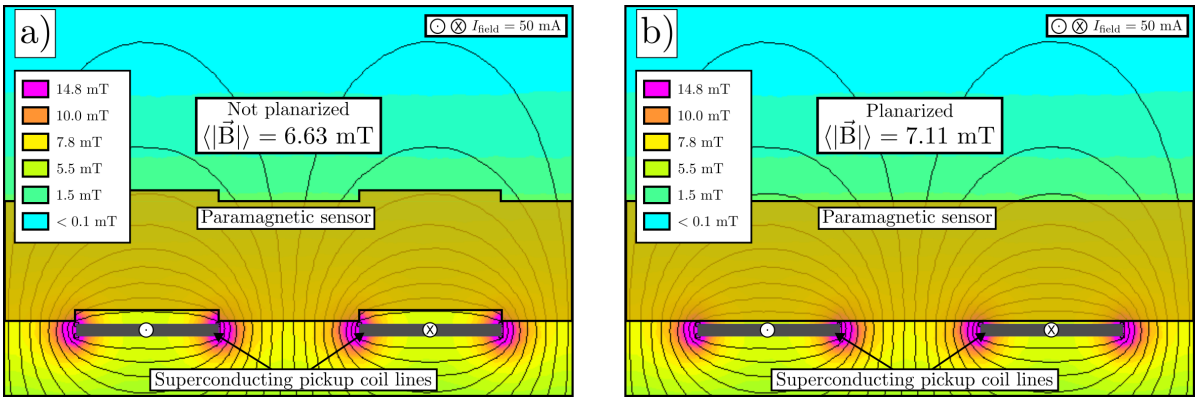

Figure 4.8: **a)** Magnetic field distribution inside the sensor material using a non-planarized pickup coil. **b)** Magnetic field distribution using a planarized pickup coil. In these simulations the same geometric parameters are used, namely a pitch of $p = 5\,\mu$m and linewidth of $w = 2.5\,\mu$m, and thickness of $t = 250\,$nm. The sensor is $1\,\mu$m thick in both cases. Assuming the same circulating current (50 mA), the mean magnetic field in each case is also specified.

the sensor material. The most adopted technique to produce a flat surface over microstructured wafers is Chemical Mechanical Polishing (CMP) [152]. To use this method, the Nb structures are patterned and a thick layer of SiO_2 is deposited on top. The surface is then chemically and mechanically etched with a rotating polishing pad and abrasive slurry. A CMP machine was not available during the development of these detectors, so another alternative was explored. A self-planarization technique was investigated, in which the photorresist after etching of the first Nb layer serves as a liftoff mask to deposit a silicon oxide layer as thick as the Nb lines. This process fills up the space between Nb structures with insulating material and when the deposition rate of Nb and silicon oxide is precisely known, equal film thicknesses can be reliably achieved with differences of just a few nanometers.

After etching the first Nb layer, the samples were introduced into a UNIVEX 300 system that was used to deposit silicon oxide by thermal evaporation. This method ensured very sharp edge features as thermal evaporation is a highly directional with virtually no scattering or dispersion between the material source and the substrate. After deposition of the silicon oxide, the photorresist is removed with a 5-minute megasonic bath in Dymethylsulfoxide (DMSO).

The self-planarization technique is detailed in Figure 4.9. Test chips were produced to assess the applicability of this self-planarization technique for the development of the MMB. The resulting profile after the first Nb etch and SiO_x deposition measured on Nb test strips is shown featuring step sizes in the order of just a few tens of nanometers, while the Nb thickness for these chips was 200 nm.

Insulation tests were performed by sputtering a 50 nm insulating layer on planarized structures followed by the deposition of a second Nb layer. The test structures included 90° stripe-over-stripe configurations and overlapping meander patterns on both Nb layers. Results revealed numerous shorts and low-resistance paths between layers, indicating a

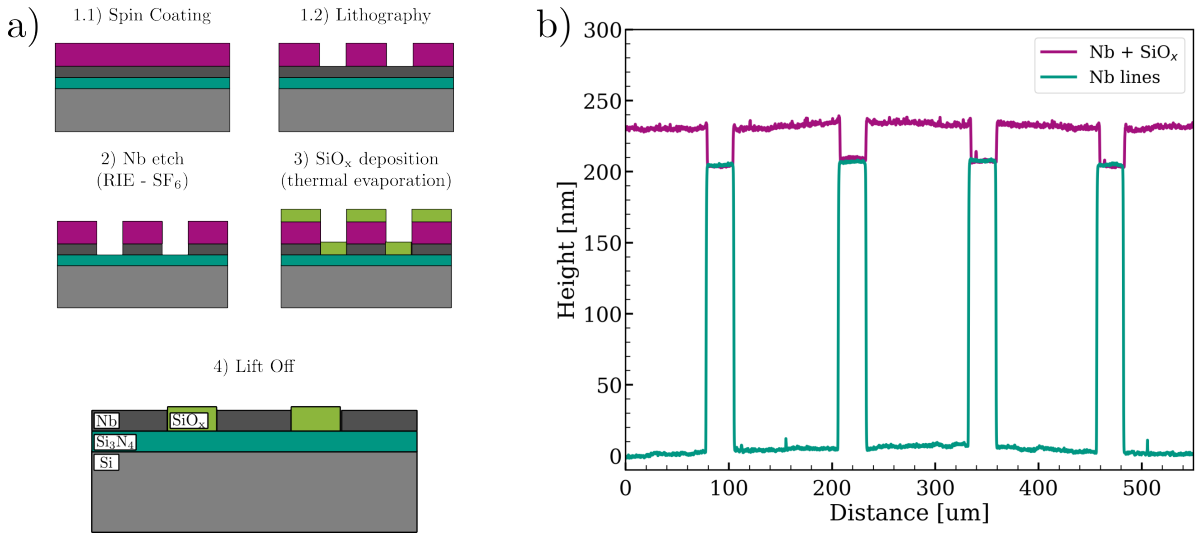

Figure 4.9: **a)** Self-planarization process involving anisotropic deposition of a silicon oxide insulating layer to fill the gaps between the meander-shaped pickup coils. **b)** Profile measurements illustrating the outcome of the process. The green trace represents the surface profile of the Nb structures without planarization, while the purple trace corresponds to a similar sample after undergoing the process. The height steps are significantly reduced, from 200 nm (Nb structures) to just 20 nm to 30 nm, indicating a much more planar surface.

flaw in the self-planarization technique described. More samples were produced, increasing the top insulating layer's thickness. Matching or exceeding the thickness of the underlying Nb significantly reduced these shorts, but defeats the purpose of planarization, which is to enable thinner, uniform insulating layers while maintaining electrical isolation.

To better understand the origin of the issue, finished samples were examined using FIB cuts to obtain a cross-sectional view of the stack. Figure 4.10 presents SEM images of the pickup coil cross-section. Although the planarization process produced an overall flat surface, a specific issue was identified. The RIE etching step used during fabrication exhibited some degree of isotropy, which resulted in undercuts in the Nb structures, clearly visible in the high-resolution SEM image on the right. When the gaps between the lines were filled via strictly anisotropic thermal evaporation, voids formed between the planarization material and the pickup coil lines, degrading the insulation. These voids are filled with sputtered insulating material, and would also be filled with sensor material in actual devices, potentially increasing the likelihood of electrical shorts in these regions.

To improve insulation between the Nb layers and reduce the likelihood of shorts, anodization of the first Nb layer was explored. This process has been successfully implemented in the development of MMC [153]. Two identical samples were prepared, each with a 300 nm thick Nb1 layer incorporating large parallel-plate capacitors and multiple meander-shaped pickup coils with bridges running above them. One of the samples underwent anodization of the Nb1 layer, while the other was left untreated. Both were subjected to the self-planarization process. The anodization process creates a dielectric

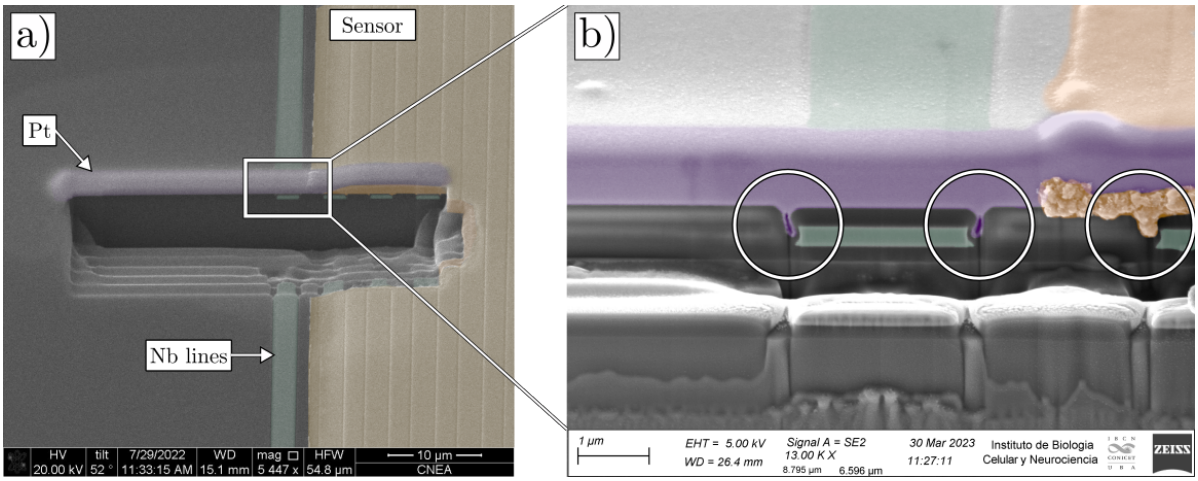

Figure 4.10: **a)** Colorized SEM image of a cross-sectional cut performed with FIB, showing a pickup coil and sensor dummy. Nb lines are highlighted in green, the sensor dummy is colorized yellow, and the platinum ruler used for the FIB cut is highlighted in purple. **b)** High-resolution SEM image of the same structure, revealing artifacts at the edges of a pickup coil lines.

coating composed of a mixture of Nb oxides (NbO and Nb_2O_5) on the surface of the Nb structures through an electrochemical reaction. The sample is immersed in a citric acid solution, and a voltage is applied between the exposed Nb and an aluminum counter-electrode. The thickness of the resulting oxide layer is directly determined by the applied voltage. The process begins with the power supply operating in current-limited mode, which helps prevent rapid electrolyte depletion and other undesirable effects. As the oxide layer grows and progressively insulates the Nb, the current gradually decreases while the voltage rises, reaching the target value of 30 V within 2 to 3 minutes. After this point, the system switches to constant-voltage mode and maintains the 30 V bias for an additional 30 minutes. Current and voltage traces for the first 15 minutes of the anodization process is shown in Figure 4.11 (a). Prolonging the anodization time helps promote a more uniform and homogeneous coating. A successful anodization is visibly indicated by the Nb changing color from metallic silver to a bluish-silver hue. Profilometer measurements (Figure 4.11 (b)) show the Nb structure profile before and after the anodization process, resulting in a coating layer with a thickness of 48.51 nm for the applied voltage of 30 V.

After the anodization process, two depositions of SiO_2 totaling a total insulating layer of 150 nm were performed, and a final Nb layer of 250 nm was deposited and patterned via a lift-off process. Different stripes going over the meander coils were placed in addition to parallel plate capacitors of different sizes. The finished samples were measured in a probe station at room temperature to determine the insulation provided by the structures. As a first observation, the Nb presents increased resistivity due to the lower effective thickness after the anodization process. The increase was of 17.76 % indicating that from an initial thickness of 300 nm, the resulting effective thickness is of $\approx$ 245 nm. Insulation tests consisted in measuring across multiple structures between the first and second Nb layers; any measurable resistance between the structures would indicate the presence of shorts or

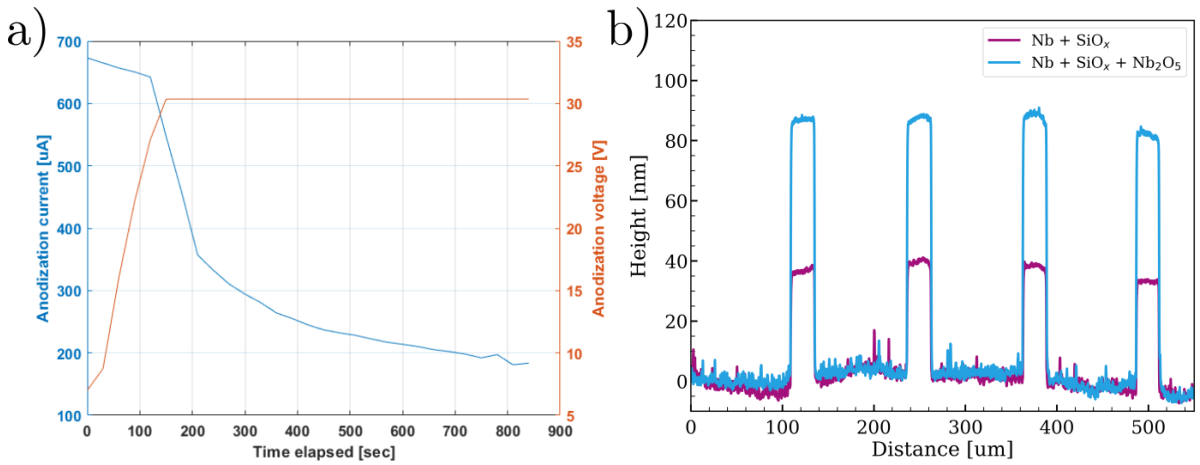

Figure 4.11: a) Anodization current and voltage as a function of time during the first 15 minutes of the process. **b)** Surface profile comparison between a planarized Nb structure before and after anodization. A thickness of 48.51 nm is attributed to the oxide coating.

compromised insulation. Two square capacitors were fabricated on each chip, one having a side length of 1400 μm (Big cap) and the other a side length of 700 μm (Small cap). In addition, meander structures on both the first and second Nb layers were fabricated featuring two Nb stripes, one having a width of 20 μm and the other a width of 200 μm which is close to the dimensions of the sensor. Table 4.4 summarizes the results of the resistance measurements for each structure.

Structure:	Nb1 meander		Nb2 meander		Big cap	Small cap
Sample:	20 μm	200 μm	20 μm	200 μm		
V1	9.240 kΩ	9.294 kΩ	31.678 kΩ	45.517 kΩ	113.19 kΩ	OVLD
V2	23.553kΩ	23.580kΩ	OVLD	OVLD	OVLD	OVLD

Table 4.4: Isolation tests results comparing two planarized samples with (V1) and without (V2) the anodization. Values indicated as OVLD were not measurable and mean the resistance is larger than 1 GΩ, in those structures, insulation is considered succesful.

Anodization appeared to have worse results, evidenced by the reduced resistance measured across the structures. It also introduces an additional fabrication step following the deposition of the Nb layer. Since no clear benefit was observed from this method, it was not included in the MMB fabrication process. The conventional approach, using 250 nm thick Nb layers and $\approx$ 300 nm thick insulating layers, has proven sufficient to achieve the necessary electrical isolation between metal layers.

For future iterations of the MMB, more advanced planarization techniques should be considered, particularly those involving CMP systems. This would help ensure truly flat surfaces, making the structural and electrical integrity of thin films almost independent of the morphology of previously deposited layers.

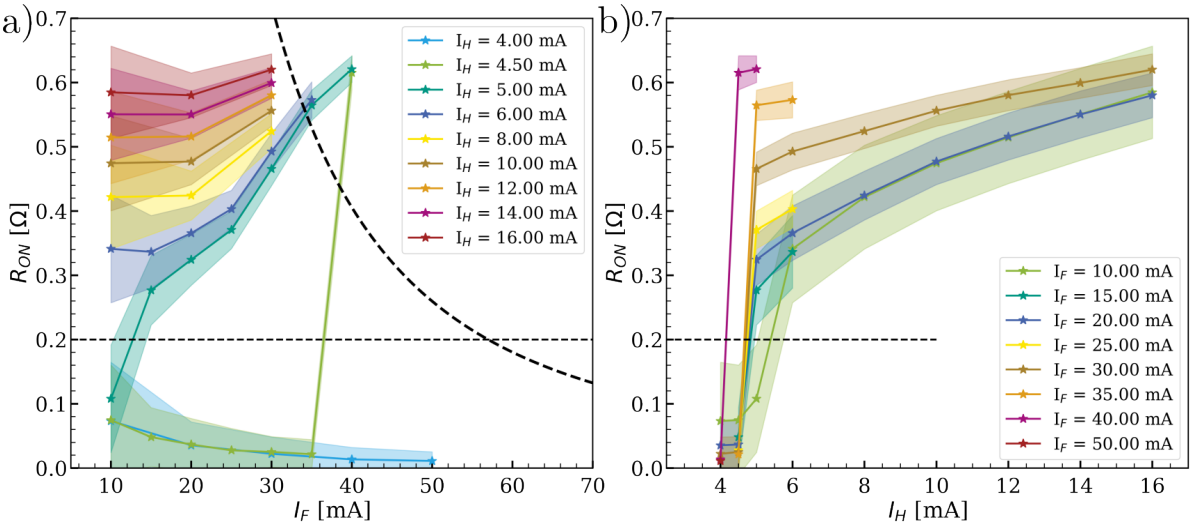

Figure 4.12: On-state resistance of the Nb trace underneath the AuPd switch resistor as a function of I_{F} (**a**) and as a function of I_{H} (**b**). A horizontal dashed trace represents a resistance value of 0.2 Ω at which the switch is considered activated (on-state). The latching condition is portrayed on the left plot in which the product of I_{F} and the on-state resistance exceeds the latching power threshold.

4.1.2 Persistent current switch

The sheet resistance of the sputtered AuPd films was measured to determine the shape of the required resistors using the Vander der Pauw method [154]. A film thickness of 200 nm was selected, resulting in a measured sheet resistance of 1.4 Ω/sq. For thicknesses in the range of 200 nm, the sheet resistance is stable, in the sense that variations of a few tens of nanometers would not vary the final resistance value substantially. The persistent current switch structure consists of a 10 μm Nb strip, and the AuPd resistor that is 5 μm wide and 30 μm long (6 squares) separated by the insulation layer. A pair of top Nb lines connects the AuPd resistor to the bias pads. The switch design is such that the AuPd resistor is placed on a flat surface. This avoids step-induced hot spots that would increase the resistance and affect the heat profile. Four-wire resistance measurements of the AuPd switch resistor were performed; the measured value is 7.8 Ω below 10 K, which coincides with the target value. These switches commonly use a resistor value between 5 Ω and 10 Ω to dissipate enough heat to open the underlying Nb trace with just a few millisecond-long current pulses with an amplitude in the milliampere range. Such short pulses prevent the localized heat from thermally loading the detector.

The design of the switch (seen in Figure 3.18) was tested at liquid-helium temperatures to verify its correct operation and extract the minimum switching characteristics. An isolated persistent current switch was fabricated. The device was cooled down and multiple forward currents (I_{F}) were driven through the underlying Nb trace while delivering current pulses to the resistor (I_{H}) of different amplitudes and a duration of 3 ms. The voltage across the underlying Nb trace was measured. A zero voltage reading indicated that the switch remained in the superconducting state (off-state). Ideally, when applying

a current pulse to the heater, the switch should turn to the on-state, and an analogous voltage pulse is measured across it. Figure 4.12 shows the result of the persistent switch characterization at $T = 4.44\,\mathrm{K}$. The on-state resistance (R_{ON}) is plotted as a function of both I_{F} (a) and I_{H} (b). The minimum I_{H} value that produces a normal conducting belt for all I_{F} currents was determined to be $I_{\mathrm{H}} = 6\,\mathrm{mA}$ with a duration of 3 ms at 4 K.

4.1.3 Sensor material

Sputtering targets of Au:Er and Ag:Er are not produced by sputter target manufacturers, as they are not subject to massive use in the microfabrication industry. The paramagnetic alloys employed in the development of MMC and MMB therefore need to be produced in-house with custom-made equipment. The fabrication of the first MMB-TD was done with Au:Er sputter target with an erbium concentration of $\approx$ 1100 ppm. The target was kindly lent to IMS by the Physikalische Technische Bundesanstalt (PTB) while the production of our own sputter target was underway. Film characterization was performed for optimized deposition parameters in MMC detector fabrication. These are built on different silicon substrates than the ones required for the MMB. Characterization with the MMB substrates was not performed to minimize the amount of material used for the first prototypes, the required characterization would have required an extensive use of the borrowed target and couldn't be afforded. As a result, certain film properties, such as internal stress, were not optimized during the initial production of MMB prototypes. Internal stress optimization in this film will be necessary, as the lifted foils of Au:Er folded inwards after being released from the chips. This indicates internal stress gradients in the deposited film that may compromise the structural integrity of the finished device. A comprehensive deposition characterization tailored to the LSiN-coated silicon substrates used in the MMB design will be necessary in future development stages.

Production of a dedicated Ag:Er sputtering target

An Ag:Er target with an approximate concentration of 1000 ppm was prepared for the continuation and further development of the MMB. This concentration results from the optimization procedure outlined in Chapter 3. The production of the target was carried out in the Kirchhoff Institut für Physik (KIP) of the University of Heidelberg. For Ag:Er deposition, an additional step involves the in-situ deposition of a Au layer over the sensor material. This coating, one hundred nanometers thick, serves to prevent oxidation and corrosion for long-term stability and durability of the sensor. To be effective, the gold must be deposited without breaking the vacuum, ensuring that the Ag:Er surface remains uncontaminated.

The fundamental ingredient in the production of these specialized targets is a certain amount of isotopically enriched ^{166}Er. The second ingredient is high-grade (5N) silver stock material in the form of pellets or pills. Small pieces of silver should be doped with an appropriate amount of erbium at a time, facilitating rapid heating and cooling, avoiding impurities being absorbed, and producing a homogeneous mixture. The pills are melted in a graphite crucible inside a vacuum to remove oxygen and other impurities present in

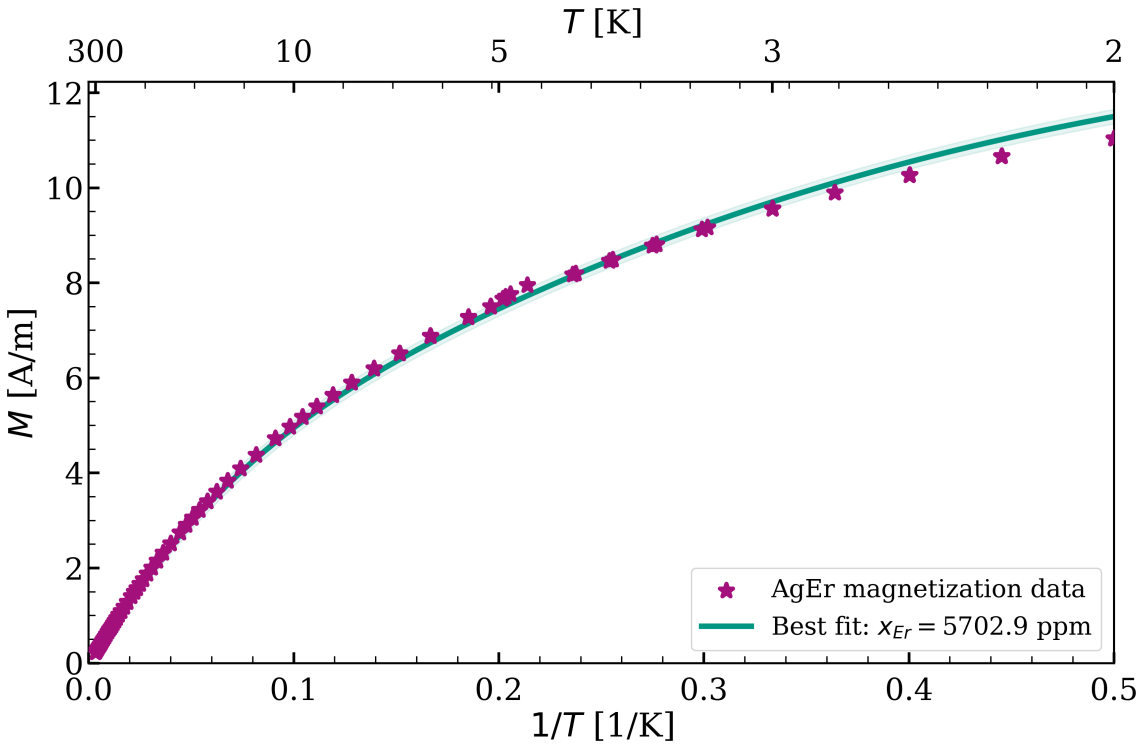

Figure 4.13: Magnetization measurement of an Ag:Er pill fragment used for estimation of the Er concentration. A best-fit to the measurement yields a concentration of 5702.9 ppm. The best-fit curve is shown in green trace.

the stock material. Each baked pill is later mechanically scrubbed and wet etched with a nitric acid solution to remove any residuals remaining on the surface. The erbium concentration should never exceed $\approx 1.6\,\%$ or 16000 ppm at room temperature. Above this concentration, stoichiometric mixtures of the AgEr system appear [123]. The formation of such molecules would trap the erbium in the incorrect state, and the paramagnetic nature of the alloy is lost.

Magnetization measurements of the finished Ag:Er pills were performed using a Quantum Design[6] MPMS SQUID magnetometer; results for one of the produced pills are shown in Figure 4.13. The Ag:Er pills exhibit the expected paramagnetic behavior; from the measured magnetic moment at each temperature, the effective concentration was extracted. The pill used in this measurement had a total mass of 1.546 g and was initially alloyed with 17.1 mg of erbium, corresponding to a nominal concentration of 7135.6 ppm. However, the fitted magnetization curve in Figure 4.13 indicates a perceived concentration of 5702.9 ppm, representing a 20.08 % reduction. This difference is due to partial oxidation of erbium during the melting process and minor material losses during handling. Similar losses of approximately 20 % were observed in other tested pills. To compensate for these losses in erbium content, the amount of silver used in the final mixing stage can

[6]Quantum Design Inc. 10307 Pacific Center Ct. San Diego, California, USA

be decreased accordingly, producing a thinner target while preserving the desired erbium concentration.

The final melting process is carried out in the vacuum oven using a graphite mold with the dimensions of the 3-inch sputtering target. The silver pills and the rest of the required silver mass are melted together multiple times, with the target being flipped between melting cycles. This repeated melting and flipping process results in a homogeneous alloy. It is essential for the erbium impurities to be evenly distributed throughout the finished target to ensure a stable and consistent concentration in the sputtered films used for each fabricated detector wafer.

4.2 Release of Detector Structures

The fabrication of an MMB is finished by releasing the detector structure. The termination resistor, the sensor and pickup coil must stand on a dielectric island to achieve a low G_{bath} as explained in Chapter 3. An appropriate release technique is required to perform this step. All structures built up to this point over the LSiN coated substrate must be protected against a carving process that defines the island structure and against the subsequent removal of the substrate material from underneath the island. There exists multiple methods available for micromachining of dielectric membranes, usually optimized for Micoelectromechanical systems (MEMS) in which micrometer-sized three-dimensional structures are reliably produced. Within this work, two membrane release processes were evaluated. The first was based on wet etching of silicon with potassium hydroxide (KOH) and the second, on dry etching of silicon using xenon difluoride (XeF_2). In the end, only the XeF_2 process was fully implemented to fabricate the MMB-TD as it showed superior results with the equipment and materials available.

4.2.1 KOH-based wet-etching technique

Solutions of KOH and trimethyl ammonium hydroxide (TMAH) are examples of liquid etchants widely used in the MEMS industry that offer a very large or even infinite selectivity of silicon to dielectric materials such as silicon oxides and nitrides [155]. These solutions, however, are aggressive towards most metal materials, and most photoresists are etched by KOH and TMAH (developers usually contain these chemicals), so special types of photoresists must be used that can protect the device during etching but can also be completely removed from the finished device without destroying the released structures. Wet-etching membrane release methods rely on the anisotropy in the etch rates resulting from crystallographic orientation of the silicon substrate. $\langle 100 \rangle$ and $\langle 110 \rangle$ planes are etched much faster than $\langle 111 \rangle$ planes. The design of the structures to be released must have an appropriate orientation with respect to the crystallographic planes in order to make use of this technique to release the bolometer islands [156, 157].

Equipment

A polytetrafluorethylene (PTFE) setup was built for processing and releasing LSiN membranes. A holder for the substrate was designed that exposes only the front face of the device to a solution with 35 % KOH concentration while shielding the back side and edges. The solution is maintained at a temperature of 80 °C using a water bath inside a closed chemical chamber; an elevated process temperature increases the etch rate, which is reported in literature to be 1.4 μm/min for $\langle 100 \rangle$ oriented silicon crystals [158]. PTFE was selected due to its chemical resistance to the etching solutions and durability to the process temperatures.

A block of PTFE was machined to form a container for the etching solution. The holder, consists of two circular PTFE caps secured together with O-rings, forming a sealed cavity that houses the sample. The sample is held in place by two additional O-rings, which seal both the front and back sides of the substrate. The front cap includes an opening to expose the front side of the sample to the solution. The back cap features a small hole connected to a stainless steel tube, which serves as a pressure relief path. This tube allows air-pressure to escape from the backside of the substrate as it rises during processing.

Figure 4.14 (a) and (b) shows a picture of the PTFE sample holder and the design cross-sectional view of the holder. The pressure relief inevitably introduces an opening through which the etching solution can evaporate, leading to an increase in KOH concentration over time and, consequently, a reduction in the etch rate. To counteract this, a glass condenser with flowing cooling water is placed around the pressure relief tube. This setup condenses the evaporated water, which then drips back into the container, maintaining a stable KOH concentration and ensuring a consistent etch rate throughout the process. The full setup, including the glass condenser, can be seen in Figure 4.14 (c).

Release process based on KOH

The wafers used for this technique had a 1 μm super low stress silicon nitride (SLSiN) coating. Figure 4.14 (d) and (e) show pictures of one of the processed samples before and after the etching process, respectively. The release process (detailed in Figure 4.15 (a)) consisted of the following steps:

1. **Lithography:** A 2.5 μm AZ® 1518 resist layer is spun on the substrate at 2000 rpm for 90 seconds. The resist is soft baked for 50 seconds at 100 °C. After exposure of the membrane patterns, AZ® 400K developer diluted in 1:4 parts of water is used to develop the sample. A development time of 10 seconds was found to completely etch the required windows exposing the substrate.
2. **SLSiN RIE etch:** The 1 μm thick SLSiN layer is etched to pattern the structures in an ICP RIE system at a pressure of 15 mTorr with 45 sccm flow of SF_6. As the SF_6 plasma also etches silicon with an even larger etch rate than silicon nitride, it is important to precisely determine the etch time required until the silicon is exposed but not go further. Any overetched silicon will result in overhanging material on the edges of the membranes.

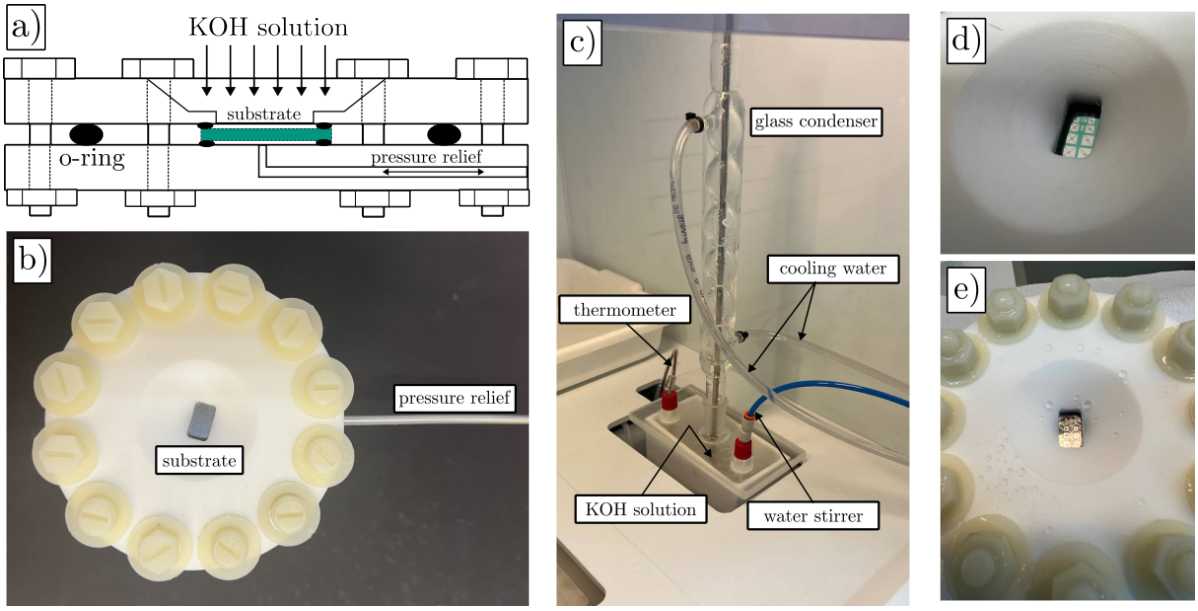

Figure 4.14: PTFE sample holder and etching system developed for testing crystal-oriented membrane release using KOH. **a)** Cross-sectional view of the sample holder, illustrating how the front side of the substrate is exposed to the etchant while the edges and backside are sealed with O-rings. Twelve nylon screws and nuts are used to press the caps together, ensuring uniform sealing pressure. **b)** Front view of the holder with a blank silicon substrate placed inside. **c)** Complete etching setup, including the PTFE container, thermometer, a pressure line for stirring the KOH solution, and a water-cooled glass condenser. **d)** and **e)** show the chip before and after the etching process, respectively.

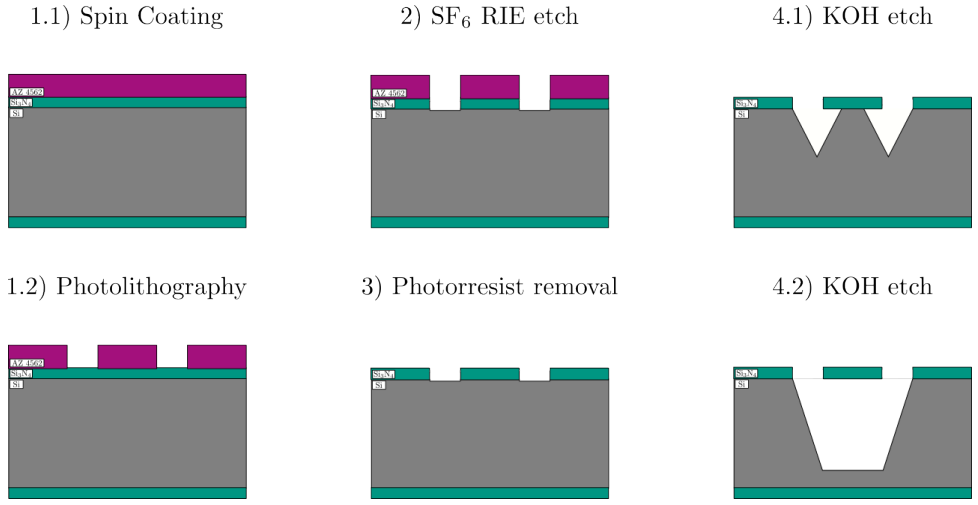

Figure 4.15: KOH-based process. (1) Photolithography to define the shape of the membrane, (2) RIE etching exposes the silicon to be etched. (3) Removal of the photorresist. (4) The substrate placed in the PTFE sample holder is etched with the KOH solution. The process can be interrupted and resumed multiple times to periodically check if the structures are fully released.

3. **Photoresist removal:** The photorresist is removed because it is sensitive to the KOH solution used for the membrane release process. Two ultrasonic baths of acetone followed by two isopropnanol baths are enough to completely remove the AZ® 1518. The patterned nitride film acts as hard mask protecting the unexposed silicon. This procedure is only useful for bare substrates without any metal structures to be released. For the use of this technique for detector development, a special photorresist that can withstand alkaline solutions is required.
4. **KOH etching of Si:** The preprocessed sample is placed in the sample holder as seen in figure 4.14 (d). The PTFE container with the KOH solution is placed in a water bath. The water bath is heated until a thermometer measuring the temperature of the KOH solution reaches 80 °C. Once the temperature is stable, the sample holder is introduced and the release etch step begins. At regular intervals, the sample holder can be removed from the etch setup and inspected to oversee the progress. Removing the substrate for short periods of time only pauses the etching process. It can be resumed by introducing the sample holder back into the KOH solution.

In Figure 4.16 (a) the layout design used to test the KOH-based technique is shown. To use this process in the release of leg-isolated detectors, it is required to have the legs of the H-type and spider-type structures oriented at a 45 degree angle with respect to the ⟨110⟩ planes. This ensures the crystal oriented etching will etch underneath the suspending legs and the island will be fully released. Cantilevers are an excellent way to evaluate the quality of the released membranes. It is a simple geometry that provides qualitative information about the intrinsic stress in the dielectric coating material. A flat released cantilever means that the film is not subject to any significant internal stress gradient. In other case, the cantilever will bend upwards or downwards accordingly. Partial results of each step are also shown in Figure 4.16 (b) for a test cantilever structure and a 45-degree oriented H-shaped membrane. The obtained results with this method were not ideal. The samples cannot be cleaned in an ultrasonic cleaner, as the vibrations would damage the delicate membranes. Instead, a rinse step in isopropanol was performed, followed by heat-drying on a hot plate to evaporate any remaining liquids. The result of such a superficial cleaning method resulted in stains from etch byproducts and other impurities that remained stuck onto the substrate surface. These are multicolored patterns visible in the remaining SLSiN layer and exposed silicon. The exact origin or chemistry of these stains was not deeply studied but hints towards the need to explore a better cleaning and drying process that would not damage the released structures.

An issue encountered during testing that ultimately forced to interrupt the release process prematurely, though not strictly related to the etching setup, was the presence of stress-induced cracks in the wafers. These cracks are believed to have originated from significant residual stress introduced during the deposition of the SLSiN layer. When a highly stressed wafer undergoes dicing, crystal-oriented cracks can form. These defects are often subtle and may go unnoticed during visual inspection, particularly when hidden beneath the nitride layer. During wet etching with KOH, these cracks become highly problematic. Because they follow crystal orientations, they are not bounded by the slow-

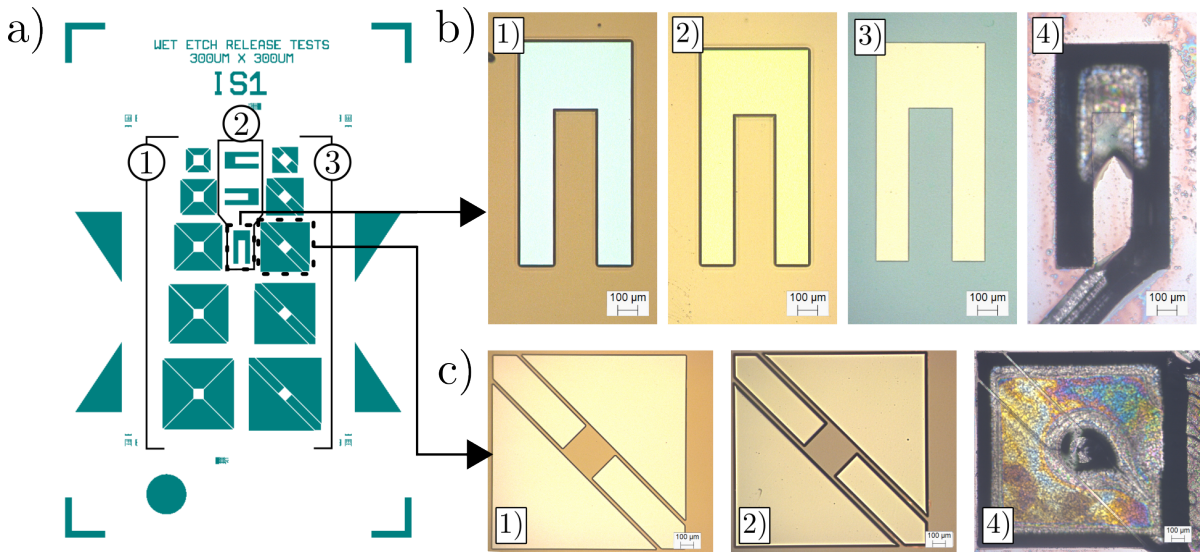

Figure 4.16: a) Design layout to test the KOH-based release technique. 1) Spyder-type structures with legs at 45 degree angle of various lengths. 2) H-type structures 45 dgree legs of various lengths. 2) Cantilever structures for a qualitative stress determination of the released dielectric membrane. **b)** Pictures of the process steps results in a cantilever structure. **c)** Process step results in 45-degree angle h-shaped membrane. The numbers in the pictures correspond to the result of the process step in each case.

etching ⟨111⟩ planes, allowing KOH to etch aggressively along their paths. Over time, the cracks can propagate to the edges of the substrate, breaching the O-ring seal. This breach allows KOH solution to enter the interior of the PTFE holder and etch from the edges inward. The resulting etch paths can run both parallel and perpendicular to each other, intersecting at various points and forming irregular cavities that further degrade the structural integrity of the device. The consequences of these cracks are clearly visible in Figure 4.16 (b). The partially released structures exhibit unexpected 45-degree angle trenches that are not part of the original design but a direct result of the crystal-oriented etching along stress-induced defects. Figure 4.17 shows the measured profile on the edge of a partially released structure. The sample total etch time was two hours, the measured etched depth is 84 μm corresponding to the ⟨100⟩ plane, resulting in a 0.7 μm/min etch rate (half of that expected from literature [124]). With subsequent tests, the etch-rate was found to be very sensitive to temperature variations during the process, making it challenging to determine with accuracy.

With an optimized KOH-based release process, the finished detector would still require protection against KOH exposure during processing. Photoresists are generally not well suited for this purpose, as they are highly sensitive to alkaline environments. Even hard-baked or cross-linked photoresists remain susceptible to KOH. Specialized protective coatings, such as AR-PC 503, AR-PC 504, and SX AR-PC 5000/41 produced by Allresist[7], can be used to shield the backside and edges of the wafer during processing. However, these materials are not photosensitive and therefore cannot be used for

[7]Allresist GmbH, Am Biotop 14, 15344 Strausberg, Germany

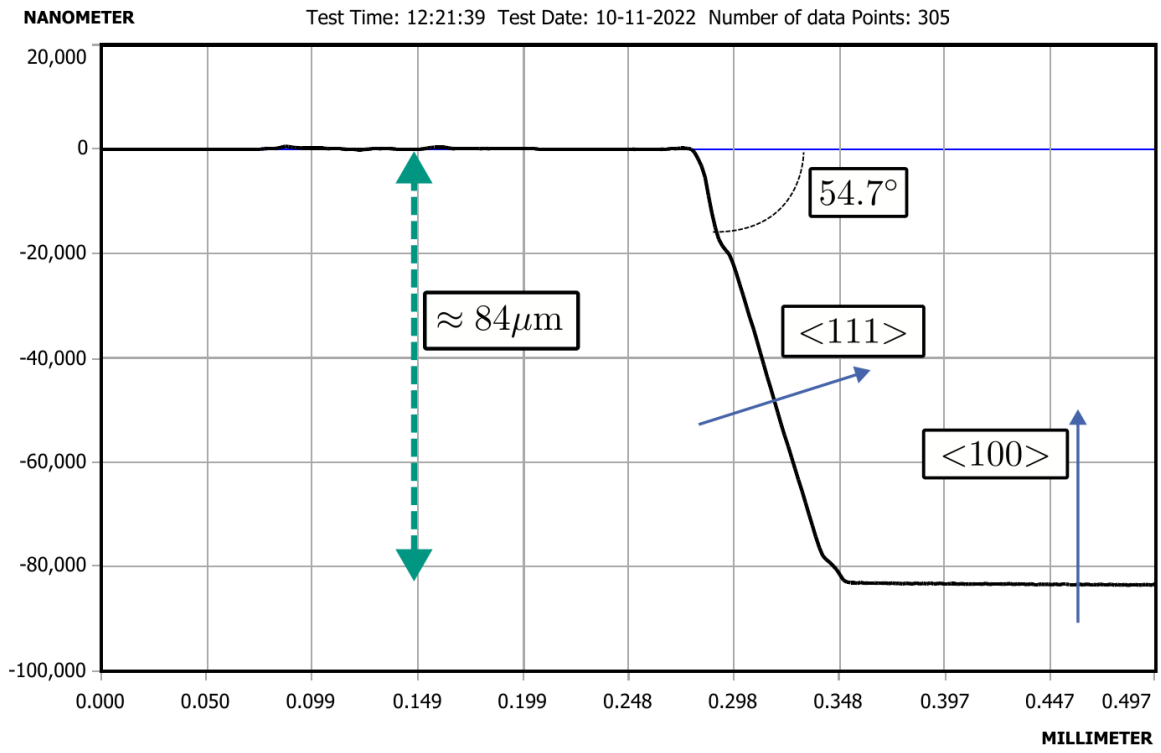

Figure 4.17: Stylus profiler measurement of an etched sample with the KOH solution. An 84 μm etched depth was measured and an $\approx$ 54.7 $^\circ$ angle was determined for the sidewall corresponding to the $\langle 111 \rangle$ crystal orientation expected in $\langle 100 \rangle$ crystal-oriented substrates used (in this depitcion x and y axes are not equally scaled, so the apparent angle looks different than in reality).

patterning the suspended detector structures.

Polymethylmethacrylate (PMMA), commonly used for high-resolution patterning, offers some resistance to KOH solutions and could be potentially used for this purpose [159]. However, PMMA requires advanced techniques such as electron beam lithography, deep UV, or X-ray lithography for patterning, which limits its use to facilities equipped with such specialized tools. Additionally, PMMA lacks durability against dry etching methods like RIE, which is problematic when etching the nitride layer to expose the silicon.

The most robust protection for such processes is achieved using hard masks made from materials like silicon nitride [160]. However, due to the considerable thickness of the sensor layer, hard masks would need to be equally thick, in the order of 1 μm or more, which introduces further complexity. A thick nitride film would also affect structural stability, presenting further stress in the suspending legs and increased heat conductance lowering the detector gain.

Certain negative-tone photoresists, such as those in the AZ® nLOF™ 2000 series, can be conditioned to enhance their resistance to KOH. However, their durability often remains inadequate for highly aggressive KOH applications, such as membrane release, where prolonged exposure at elevated temperatures is required. A robust alternative exists [161], a polymeric material was developed specifically for alkaline resistance and

can be patterned using a broadband UV light source. This material is commercialized by Brewer[8] under the name ProTEK PSB [162]. It is a negative-tone photoresist that can be used in the final stages of device fabrication for bulk silicon etching, and is particularly effective in protecting completed metal components during processing. Further tests should be performed with this photorresist, slightly changing the release process, in particular performing the photorresist removal after the KOH etching with O_2 plasma. In this way, the finished detector chip is well protected, and the final plasma ashing will also provide a cleaner surface on the finished device.

4.2.2 XeF_2-based dry-etching technique

An effective and widely adopted solution, particularly in the fabrication of cryogenic bolometer arrays for CMB applications, is the use of dry silicon etching with XeF_2 [163]. XeF_2 is a fluorinating agent commonly used for bulk isotropic etching of silicon [164, 165]. Its strong oxidative fluorination capability arises from its relatively low average bond energy (133.9 kJ/mol) and the chemical inertness of its reduction product, xenon gas [166]. The etch rate of silicon with XeF_2 is approximately, 10 μm/min according to literature [158], about ten times faster than the rate achieved with KOH solutions. Since the etching process occurs at room temperature without requiring external energy input, XeF_2 also demonstrates high selectivity against many other materials. However, unlike KOH, its selectivity toward silicon nitrides is not infinite. Etch rates between 10 nm/min and 20 nm/min have been reported for stoichiometric silicon nitride. To protect the structural LSiN layer during the release process, a thin thermal oxide layer is introduced underneath. This oxide layer, typically only a few tens of nm thick, provides effective protection due to the effectively infinite selectivity of XeF_2 toward thermal oxide.

At room temperature and atmospheric pressure, XeF_2 remains in solid form as white pale crystals, as pressure is decreased, a solid-to-gaseous phase transition is observed. The pressure at which this transition occurs increases with increasing temperature. Figure 4.18 (a) shows the vapor pressure of XeF_2 in the temperature range from 273 K to 388 K together with the triple point estimated to be (405.18 ± 0.05) K [167].

Gaseous XeF_2 in contact with silicon undergoes a spontaneous exothermic reaction; mainly silicon tetrafluoride and xenon gas are released as well as some thermal energy. There are other reactions in which silicon hexafluoride and other stoichiometric silicon and fluorine compounds are released in smaller proportions, the SiF_4 product being at least 85% abundant [168]. The main reaction can be described by the following formula:

$$2XeF_2 + Si \rightarrow SiF_4 + 2Xe + E_t. \tag{4.5}$$

Due to the excess energy E_t released in the reaction, the temperature of the substrate can increase significantly. In thermally isolated samples, a temperature rise of tens or even hundreds of degrees have been reported [169]. Since the release of the detectors is the final fabrication step, a cooling mechanism must be included for the heat produced in the reaction to not affect the finished device.

[8]Brewer Science Inc. 2401 Brewer Drive, Rolla, MO 65401, Missouri, USA

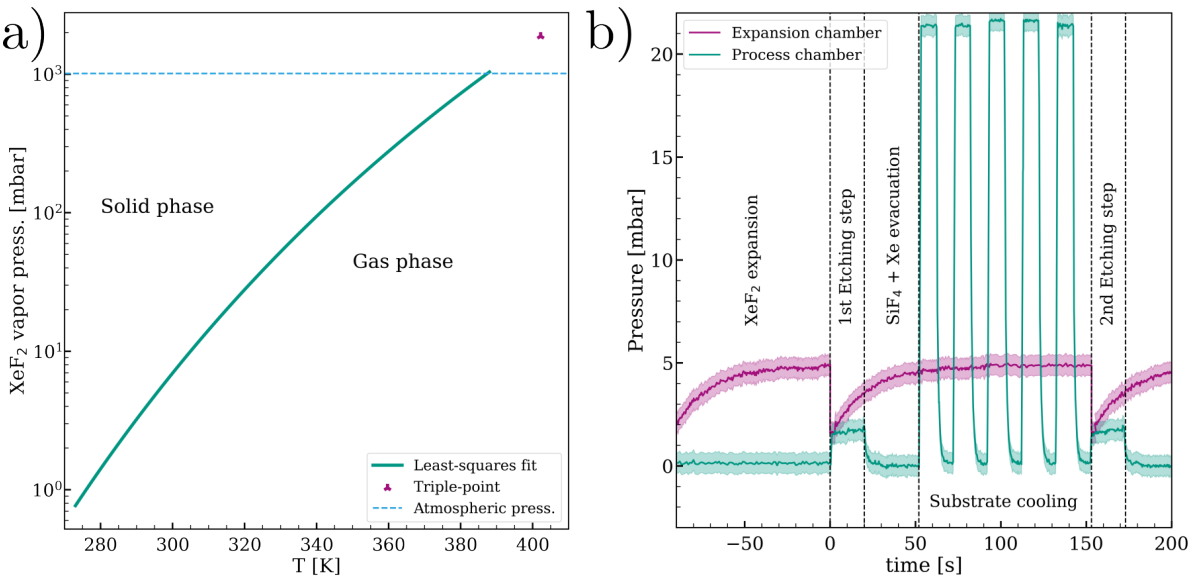

Figure 4.18: a) Phase diagram constructed from vapor pressure and triple point measurements of XeF_2 [167]. **b)** Measured pressure curves in the expansion chamber (violet trace) and process chamber (green) during the pulsed-controlled etching of silicon in the custom-built XeF_2 etching system developed.

Equipment

As part of this thesis, due to the unavailability of a specialized XeF_2-based etching system, one was fully developed. The design was inspired by typical controlled pulse-etching machines [170]. In such systems, an expansion chamber is positioned between the XeF_2 reservoir and the main process chamber. This expansion chamber is first evacuated and then connected to the XeF_2 container. During the expansion stage, XeF_2 gas slowly fills the expansion chamber, with the expansion rate mostly determined by the resistance of the connecting tubing and the chamber volume. Etching begins when the expansion chamber is opened to the evacuated process chamber, allowing the expanded gas to contact the substrate. Once the pressures of both chambers are equal, the expansion chamber is isolated again and refilled with XeF_2 gas for the next cycle. After each etching pulse, the process chamber is evacuated and purged with nitrogen (N_2) gas to cool the substrate, preparing it for the next pulse. This method allows for accurate gas-flow control throughout the etching process and, in addition, optimizes XeF_2 usage, minimizing waste.

The pressure signals recorded during an etch step are shown in Figure 4.18 (b). The expansion chamber is connected to the process chamber only briefly, just long enough for the pressures to equalize, before being disconnected to avoid contamination of the remaining gas with etch products. To optimize time, the expansion chamber is refilled with XeF_2 gas during the ongoing etch step, utilizing the residual expanded gas from the previous cycle. Both the process and expansion chambers, along with the XeF_2 reservoir, are maintained at a temperature of 40 °C because the vapor pressure of XeF_2 increases with temperature, as shown in Figure 4.18. A higher vapor pressure results in a greater

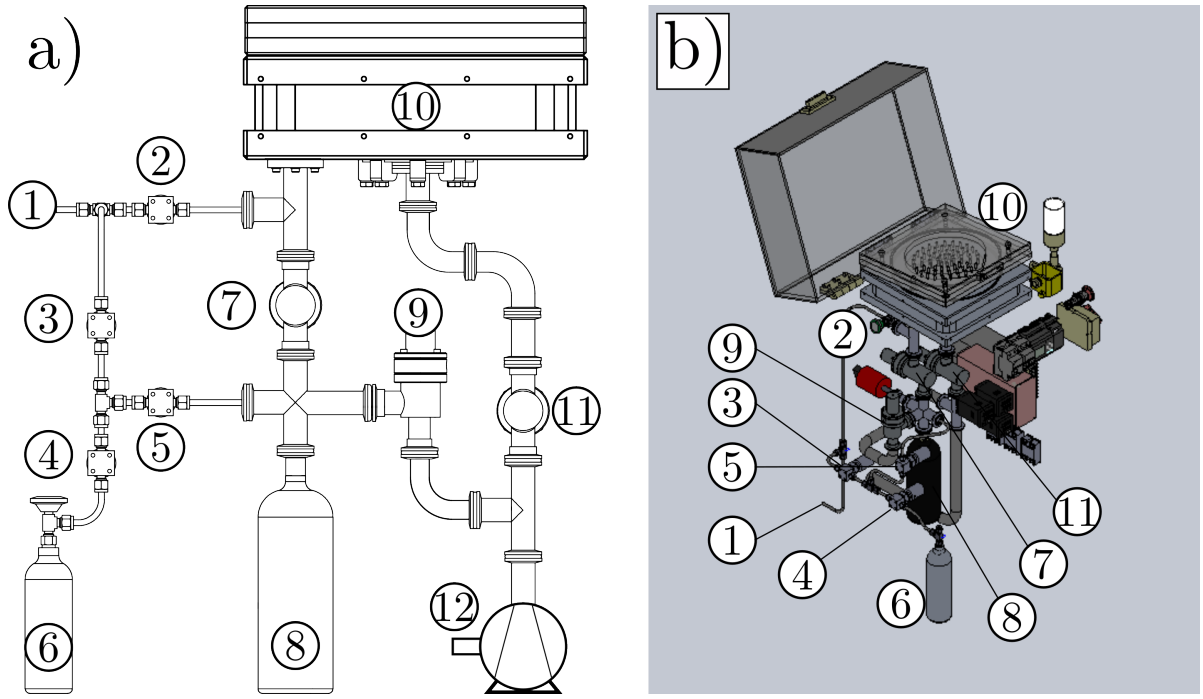

Figure 4.19: a) Schematic design of the XeF_2 etching system. **b)** CAD model with the physical layout and placement of the system's components. 1) N_2 gas inlet. 2) Process chamber venting valve. 3) Expansion chamber venting valve. 4) XeF_2 gas valve. 5) Expansion chamber gas inlet valve. 6) XeF_2 reservoir. 7) Interconnect valve between the expansion and process chambers. 8) Expansion chamber. 9) Expansion chamber vacuum valve. 10) Process chamber. 11) Process chamber vacuum valve. 12) Mechanical vacuum pump.

number of XeF_2 molecules reaching the substrate, which enhances the etch rate and allows for shorter pulse durations.

A schematic and a Computer-Assisted-Design (CAD) model of the developed system are presented in Figure 4.19. The N_2 inlet and the XeF_2 reservoir are connected to a gas handling manifold where high-quality pneumatic actuated Swagelok®[9] valves are used to introduce these gases into the expansion chamber in a controlled sequence. An additional valve connects the N_2 inlet directly to the process chamber for venting and substrate cooling steps. The gas manifold piping was constructed with 1/2-inch stainless-steel tubing. The vacuum valves for both chambers are a larger format (KF-25 flanged) produced by Lesker[10], more appropiate for efficient pumping down to base pressure. A similar valve was chosen as the expansion and process chambers interconnect valve, to ensure a rapid pressure stabilization between them after expansion. All gas handling valves are operated in a double-stage configuration. Pressurized air is first supplied to a series of solenoid valves, which indirectly control the high-quality, vacuum-tight pneumatic valves. Such double-stage configurations prevent electrical failures from damaging the high-vacuum-

[9]SwageLok Company, Solon, Ohio, USA
[10]Kurt J. Lesker Company, 1925 Route 51, Jefferson Hills, PA 15025 USA

grade valves; in contrast, the solenoid valves are less critical (do not handle process gases) and can be easily replaced when such failures occur. A Programmable Logic Controller (PLC) serves as the central control unit, managing the timing and sequencing of valve operations. The PLC executes basic control logic to prevent simultaneous opening of incompatible valves and implements safety flags to ensure correct operation of the system. The sequencing of the etching process, based on the specified recipe parameters, is managed by software running on an external PC. This software sends command signals to the PLC, which interprets them and autonomously executes the pulse etching steps in a safe and controlled manner. In the event of an interruption, the PLC handles the situation internally, responding appropriately based on the specific step that was in progress at the time.

The process chamber is large enough to accommodate 6-inch wafers with spare room for enhanced gas flow. For small substrates, aluminum holder plates with appropriate carvings were produced to accommodate several square and rectangular chips of various sizes. Every component in the machine is sealed with fluorocarbon (Viton) O-rings, this type of O-rings is selected because of its durability and resistance toward fluorinating agents. With time, they are known to deteriorate but can be inspected and exchanged with relative ease. The built system is shown in Figure 4.20. The process chamber is machined from a single block of aluminum. Evacuation of the chamber occurs from the center, directly beneath the substrate plate using a standard mechanical vacuum pump. The XeF_2 gas, once expanded, is introduced from above through an acrylic lid designed with a showerhead configuration. The process gas is routed through the lid, which contains a large number of small holes that distribute the gas evenly, ensuring uniform exposure across the substrate surface and preventing localized gas accumulation.

While XeF_2 is relatively harmless on its own, its contact with atmospheric moisture generates hydrofluoric acid (HF) vapor, which is highly toxic and poses significant safety risks. To mitigate this, the system is fully enclosed and features a forced ventilation setup to extract ambient air from around active components. Additionally, an HF gas detector is installed near the system within the cleanroom. If any HF is detected, the system automatically triggers an alarm, shuts down all gas-handling operations, closes all valves, and opens the vacuum line to evacuate any remaining gas from the chamber. The control unit is housed in an external sealed metal container (Figure 4.20 (b)), to prevent corrosion of its associated components in the event of a leak within the system.

Release process based on XeF_2

With the fully operational XeF_2 etching machine, a front-side release process was developed. In this process, the sample is etched from the device side and a cavity is formed underneath the released sections of the design. The 45 degree orientation that is required for KOH-based techniques is not required with XeF_2, therefore, the released detector can be designed with a much smaller footprint. The release process implemented consists of five main steps (see Figure 4.21):

1. **Lithography:** A thick AZ® 4562 resist layer is spun on the substrate at 2000 rpm for 1 minute. The resist is soft baked for 5 minutes at 100 °C. After exposure of the

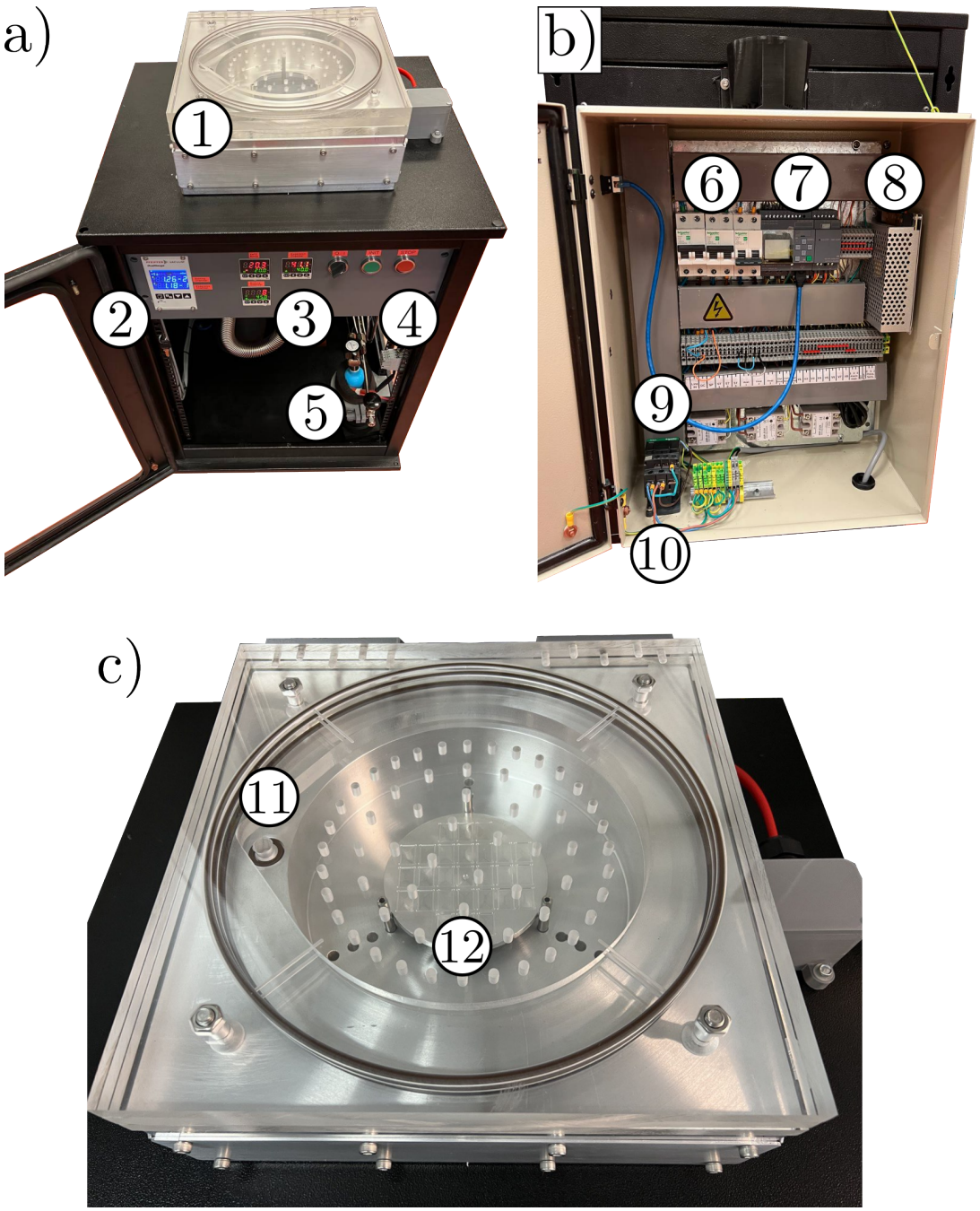

Figure 4.20: Pictures of the finsihed XeF_2 etching system. **a)** Front-view (user side) of the machine. **b)** Back-view (service side) of the machine showing the electronic control system enclosed in a sealed backpack. **c)** Close-view of the main process chamber. 1) Main process chamber. 2) Pressure gauges. 3) Temperature control units. 4) Power, intialization and process-stop switches. 5) XeF_2 reservoir. 6) Main, control and heater circuit breakers. 7) PLC control unit. 8) Power supply. 9) Ethernet connection to user PC. 10) Safety magnetic latching contactor. 11) Process gas inlet to the process chamber. 12) Substrate plate standing below the lid showerhead and on top of the main vacuum outlet.

membrane patterns, AZ® MiF 2026 developer is used to develop the sample. A development time of 5 minutes was found to completely etch the required windows in the substrate.

2. **LSiN + SiO_x RIE etch:** The membrane material must be etched to define the shapes of the suspended structures. The 600 nm thick LSiN thermal oxide layers are etched in an ICP RIE system at a pressure of 20 mTorr with 45 sccm flow of SF_6. The remaining thermal oxide underneath the LSiN is etched in situ with a mixture of C_4F_8 (27 sccm) and O_2 (3 sccm) at a pressure of 8 mTorr. This process exposes the silicon that will be etched in the following steps.
3. **Si Deep-RIE etch:** A BOSCH process is used to produce an anisotropic etch into the silicon. This process optimizes the release step with XeF_2 as it exposes a greater amount of silicon surface while at the same time lowering the amount of underetch occurring surrounding the released membrane. The BOSCH process consists of two alternating steps, an etching step using an SF_6 and O_2 mixture plasma and a passivation step with a mixture of C_4F_8 and SF_6. The process results in deep, straight trenches into the silicon surface. The etched depth is ≈ 25 μm.
4. **XeF_2 bulk etching of Si:** Etching of silicon with XeF_2 in this step is isotropic and ensures minimal overhanging membranes in the edges surrounding the structure when the deep RIE trenches have an aspect ratio close to 2:1, as seen in figure 4.21 left after the third step. The sample is placed in the process chamber of the XeF_2 etching system. The controlled XeF_2 pulses are delivered to the sample until no silicon remains underneath the released structures. A camera was installed which helped control the etching process.
5. **Photoresist removal:** Once the silicon underneath the membranes is etched, the photoresist must be removed from the chip with the released structure. Rinsing with acetone and dry blowing the samples is not possible, as it could permanently damage the delicate detector devices. The photoresist is removed instead by plasma ashing. O_2 plasma reacts with the photoresist molecules, burning the resist layer off the sample in fully dry form. An RF source outputting 300 W of RF power ignites a low-pressure O_2 atmosphere created inside a vacuum chamber in which the sample is introduced. The plasma ashing process is performed for 2 to 3 hours to remove any photoresist residuals from the finished detector.

Silicon substrates with a 400 nm layer of SiO_2 were used first to test the system and extract the etch rate as well as test its operation before patterning the LSiN substrates and fully developed MMB prototypes. The results obtained are shown in Figure 4.22. The goal of these first tests didn't include fully releasing the structures, as the SiO_2 layer intrinsic stress was not optimized for such results. Wrinkles in the partially released structures can be seen due to the non-optimized SiO_2 film, however, the tests were useful to verify the correct operation of the machine. Mesh structures were also included to test the XeF_2 equipment for alternative types of detector geometry based on resistive absorbers for radiation coupling. The XeF_2 etch pulses used had a duration of 20 seconds at a process pressure of 2.4 mbar, the temperature of the expansion and process chambers and the XeF_2 reservoir was kept at 40 °C. With these parameters the etch rate observed

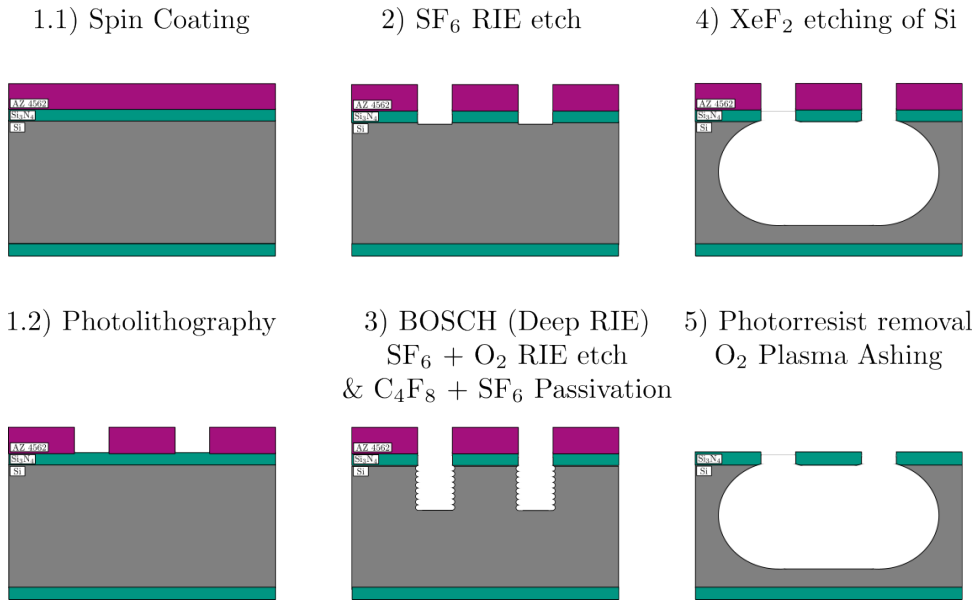

Figure 4.21: Front-side XeF_2 release process used in the development of the MMB-TD. **1)** Photolithography to define the shape of the membrane, **2)** RIE etching is used to etch the LSiN and thermal oxide layer exposing the silicon substrate. **3)** The BOSCH process is used to etch into the silicon substrate. **4)** The sample is placed in the XeF_2 etching system and etched with several etching cycles. The sample can be observed during the process to determine if the structures are fully released. **6)** Photorresist removal carried out in an O_2 plasma ashing system.

was $\approx 3.39\,\mu$m/cycle. This value is valid for samples with a similar area of exposed Si. It was verified that by increasing the area of exposed Si, the number of XeF_2 pulses must be increased to achieve similar results.

Subsequent tests were performed with the same design layouts on bare LSiN substrates. Figure 4.23 presents pictures taken with an SEM of the obtained results for the release H-structures and two cantilevers. The process developed demonstrated high repeatability. Appropiate mechanical stability of the completely released structures was observed when using the LSiN dielectric layer. This indicated that fully fabricated MMB-TD chips could be processed with this release technique. The cantilevers showed a subtle bend upwards, indicating some amount of internal stress gradients, but no evident deformation was observed in the released H-shaped structures.

The release process was ultimately performed on the finished MMB-TD samples, and successful results were obtained. Figure 4.24 illustrates the result of each step and shows a picture of released and non-released MMB detectors side by side. Once the photoresist is removed, the free-standing detector exhibits a noticeable bend, primarily in the direction of the pickup coil lines. This behavior had been anticipated to some extent based on earlier experiments with released meander-like pickup coils, though the effect was less pronounced at that stage. The more substantial bending seen in the fully fabricated detector is likely due to internal stress gradients in the $\approx 1\,\mu$m thick sensor material, which appears to introduce additional strain into the structure. The Au:Er

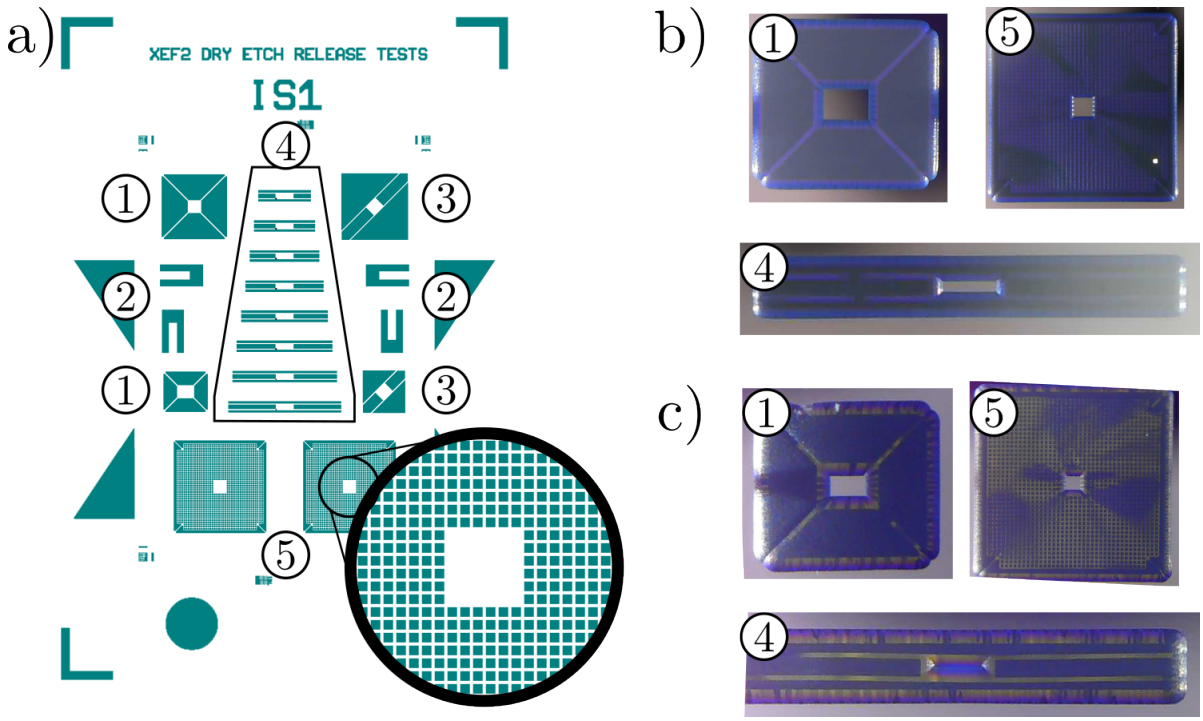

Figure 4.22: a) Layout design used for testing the XeF_2 etching system. 1) Spyder-type structures with legs at 45 degree angle of various lengths. 2) H-type structures 45 dgree legs of various lengths. 2) Cantilever structures for a qualitative stress determination of the released dielectric membrane. 4) Small footprint H-type structures with legs of various lengths. 5) Mesh structures often used for absorber-coupled detectors. **b)** Pictures of the results obtained on some of the tested structures after 15 XeF_2 etching pulses. **c)** Pictures of the results obtained after 25 XeF_2 etching pulses.

foils themselves had previously shown a tendency to bend upon lift-off, suggesting they could indeed contribute to the observed deformation in the final device. An optimal set of deposition parameters for the sensor material must be found to present reduced stress in the fully developed detector. This will be done in upcoming development with the dedicated Ag:Er sputtering target produced for this project.

An optical profilometer was used to quantify the bending of the structure, as its visual appearance is sensitive to the depth of focus in microscope and camera optics. A narrow depth of focus exaggerates the perceived curvature, while a broader depth of focus can render the deformation nearly imperceptible. Profilometric scans were conducted along directions parallel and perpendicular to the pickup coil lines, revealing a saddle-like shape with opposing curvatures along orthogonal cross-sections. A convex bend of approximately 3.5 μm, corresponding to approximately 4 % curvature of the sensor material, was observed along the direction of the pickup coil lines. In the perpendicular direction, a concave bend of about 2 μm was measured, amounting to a curvature of approximately 0.56 %. Although this deformation does not necessarily compromise the functionality of the MMB, a reduction in the pickup coil's critical current is anticipated, consistent with earlier observations in released pickup coils. Additional deformation during cooldown

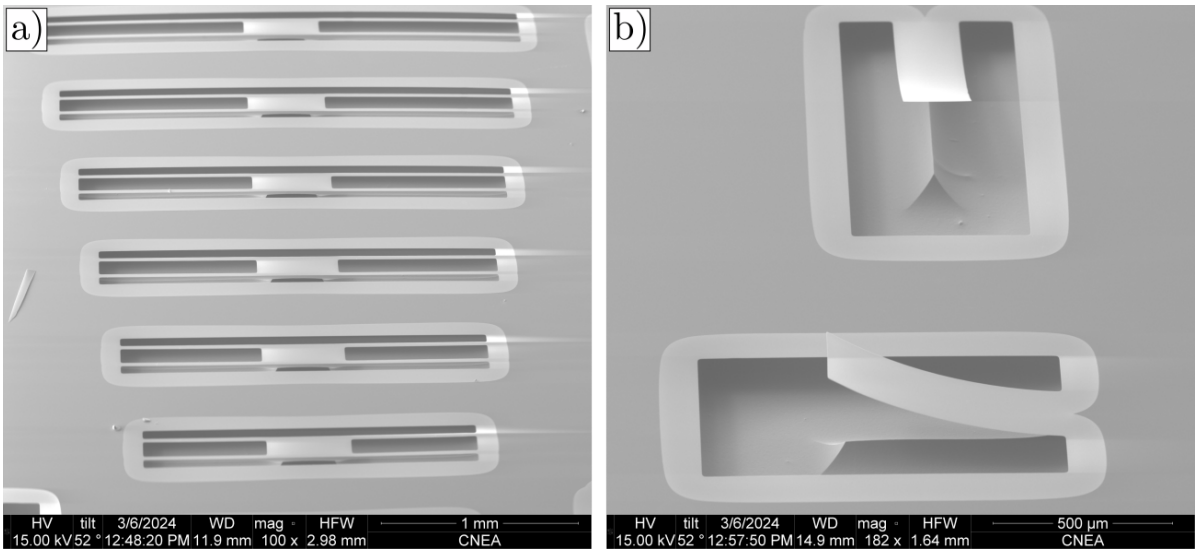

Figure 4.23: SEM pictures of fully released silicon nitride structures of various shapes and sizes. **a)** H-shaped membranes of various leg lengths spanning from 600 μm to 1100 μm. **b)** Cantilever structures at 90-degree angles featuring an upward bending after the XeF_2-based release process.

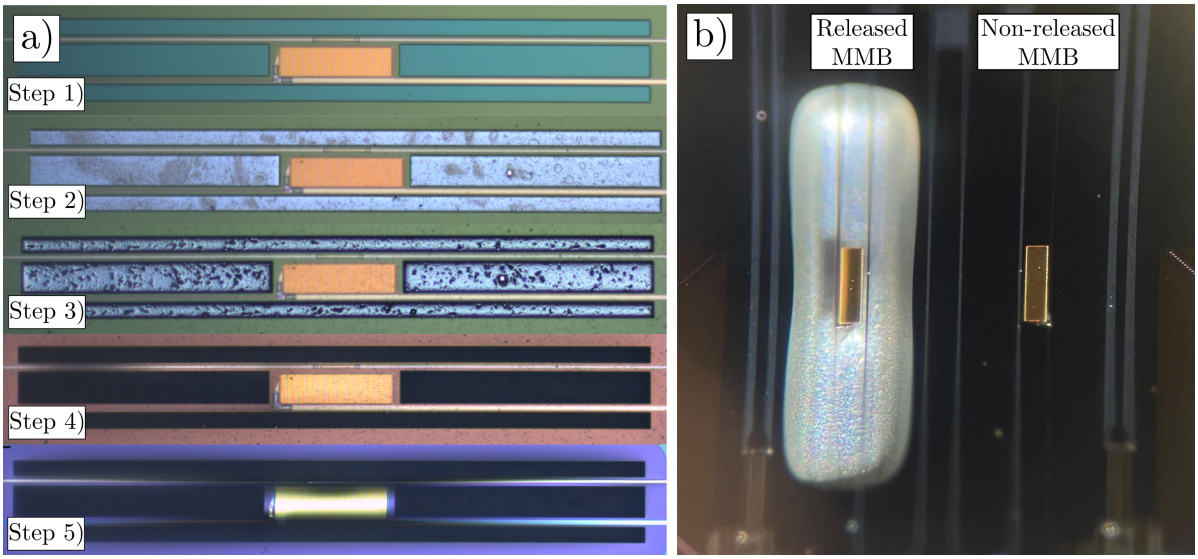

Figure 4.24: **a)** Microscope pictures of the results obtained after each step in the release process during the MMB-TD fabrication. Each step is identified in the corresponding picture. **b)** Picture of a released and non-released MMB taken prior to their low-temperature characterization.

may occur; however, multiple MMB detectors have undergone repeated thermal cycling down to millikelvin temperatures and have demonstrated sufficient structural resilience.

Chapter 5

Characterization Methods

This chapter presents the experimental methods implemented within the framework of this thesis for the characterization of the MMB prototypes. Firstly, the cryogenic systems utilized to perform measurements at liquid-helium and millikelvin temperatures are described followed by a detailed description of the low-noise cryogenic readout system assembled for the characterization of the MMB protoypes inlcuding its noise performance and bandwidth.

5.1 Cryogenics

For the cryogenic characterization of superconducting films and components down to liquid helium temperatures, a commercially available two-stage pulse tube cryocooler (PTC) cryostat developed by TransMIT[1] was employed. The system (illustrated in Figure 5.1 (a)) operates continuously, allowing fast and efficient exchange of samples. The latter are inserted using dipsticks based on pipes made from materials that present low thermal conductivity such as nickel-silver, and at the cold end, a copper (Cu) holder is attached, which contains a printed circuit board (PCB) with space to accommodate samples of various shapes and sizes. Each sample is wire bonded to the PCB with aluminum bond wires and the PCB is connected to room-temperature measurement equipment via copper-nickel wires, which present sufficiently low parasitic heating to the cold-stage.

Characterization of devices and detectors down to millikelvin temperatures was carried out with a commercial ^{3}He/^{4}He dilution refrigerator (LD250 unit produced by Bluefors[2] shown in Figure 5.1 (b)). This model can reliably reach temperatures of 7 mK without thermal load. Custom wiring harnesses were prepared used to connect the devices under test. The harnesses are composed of several channels, each channel is wired via twisted pairs of copper-nickel wires thermally anchored at each stage within the cryostat.

[1] TransMIT GmbH, Heinrich-Buff-Ring 16, D-35392 Giessen, Germany
[2] Bluefors Cryogenics Oy, Arinateie 10, 00370 Helsinki, Finland

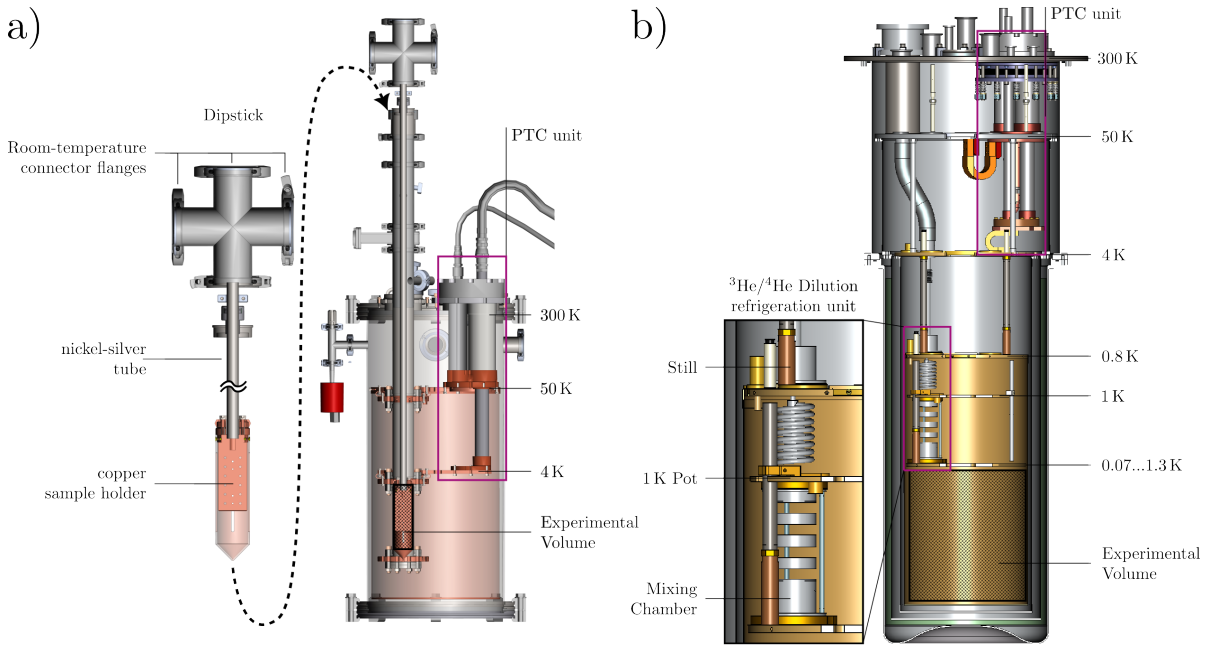

Figure 5.1: **a)** Illustration of the TransMIT Pulse-Tube Cryocooler (PTC) cryostat used for 4 K characterization of superconducting films and components. **b)** Illustration of the Bluefors ^{3}He/^{4}He dilution refrigerator utilized for characterization at milikelvin temperatures.

5.1.1 Pulse-tube cryocooler (PTC)

The PTC relies on periodic compression and expansion of the working fluid (helium gas) to remove heat [171]. The main difference between a PTC and other cooling systems is its lack of moving parts at the cold end, which minimizes vibrations and mechanical wear. Instead of a physical piston, the compression is driven by oscillating pressure waves in the helium itself. A thermal regenerator placed between the compressor and the cold end of the pulse tube stores heat from the high-pressure gas during compression. At the opposite (hot) end of the pulse tube, an inertance tube and buffer volume (or reservoir) are connected. These components introduce a phase shift between pressure and gas flow by delaying the moving mass, enabling the cold end temperature to drop below the initial temperature at the beginning of each cycle. With each compression–expansion cycle, the starting temperature of the gas in the pulse tube is progressively reduced until thermal equilibrium is reached. At this point, the cooling power balances the heat load introduced by the experimental setup or any other element in contact with the cold end [172, 173]. The TransMIT cryostat uses a two-stage configuration because a single stage to cool the experimental volume down to 4 K is impractical, a two-stage confiuration uses two PTCs in series. The first stage reaches a temperature in the range of 50...70 K, and from this cold starting point, a second PTC stage is used to reach the target base temperature in the range of 4 K.

5.1.2 ^{3}He/^{4}He dilution refrigerator

The cooling principle behind dilution refrigerators [174, 175] relies on the phase separation that occurs in liquid mixtures of helium-3 (^{3}He) and superfluid helium-4 (^{4}He). At very low temperatures (approaching 0 K), and at a concentration of about 6.5 % ^{3}He, the binding energy of the ^{3}He to the ^{4}He becomes lower than their kinetic energy, preventing further dissolution of ^{3}He into the mixture. The mixture thus separates into two distinct phases: A ^{3}He-rich phase (concentrated phase), and a ^{4}He-rich phase (dilute or heavy phase). The heavy phase will sit at the bottom of the mixture due to its higher density. The exact concentration of ^{3}He at which phase separation occurs depends on the temperature and the vapor pressure above it.

The cold end of a dilution refrigerator consists of three key components: a mixing chamber, a still, and a heat exchanger. The ^{3}He/^{4}He mixture is liquefied using a PTC and stored in the still. Here, the helium is pumped down, lowering its temperature and heated to approximately 0.8 K. The vapor above the liquid is enriched in ^{3}He, often over 90 %. The extracted helium vapor is reintroduced into the system and condensates as it passes through a cold pot (maintained at $\approx$ 1 K) via high-impedance capillaries. The liquid ^{3}He is delivered through the heat exchanger to the mixing chamber, where the ^{3}He/^{4}He mixture is maintained in the phase-separated state. The added liquid ^{3}He enriches the concentrated phase. A capillary at the bottom, extracts helium from the dilute phase (the ^{4}He-rich phase containing about 6.5% ^{3}He), which flows back to the still through the heat exchanger in the opposite direction. In this process, the returning mixture precools the incoming ^{3}He stream. As ^{3}He atoms from the dilute phase are continuously removed from the mixing chamber and sent to the still, ^{3}He atoms from the concentrated phase are forced across the phase boundary to maintain equilibrium. This transfer of ^{3}He atoms into the dilute phase reduces their kinetic energy, producing the cooling effect used in this refrigerator system. Temperatures as low as 1.8 mK have been reported using this concept [176].

5.2 Superconducting QUantum Interference Device (SQUID)

Superconducting QUantum Interference Devices (SQUIDs) are required to observe flux coupled by the flux transformer described in Chapter 3 to measure the change in magnetization of the sensor upon dissipation of incoming optical power (or excitation signals) by the termination resistor. The concept behind SQUIDs depends on phenomena related to certain configurations of Josephson junctions that can produce signal amplification nearly reaching the quantum limit [177, 178]. A dc-SQUID is built by interrupting a closed superconducting loop with two Josephson junctions. The transition from the zero-voltage state to the finite-voltage state is modulated with applied flux and is Φ_0-periodic. When the dc-SQUID is biased at a stable working point in the vicinity of its transition, the coupled flux to the SQUID loop will produce a current and/or voltage change across its leads depending on whether it is operated at constant voltage (voltage bias), constant

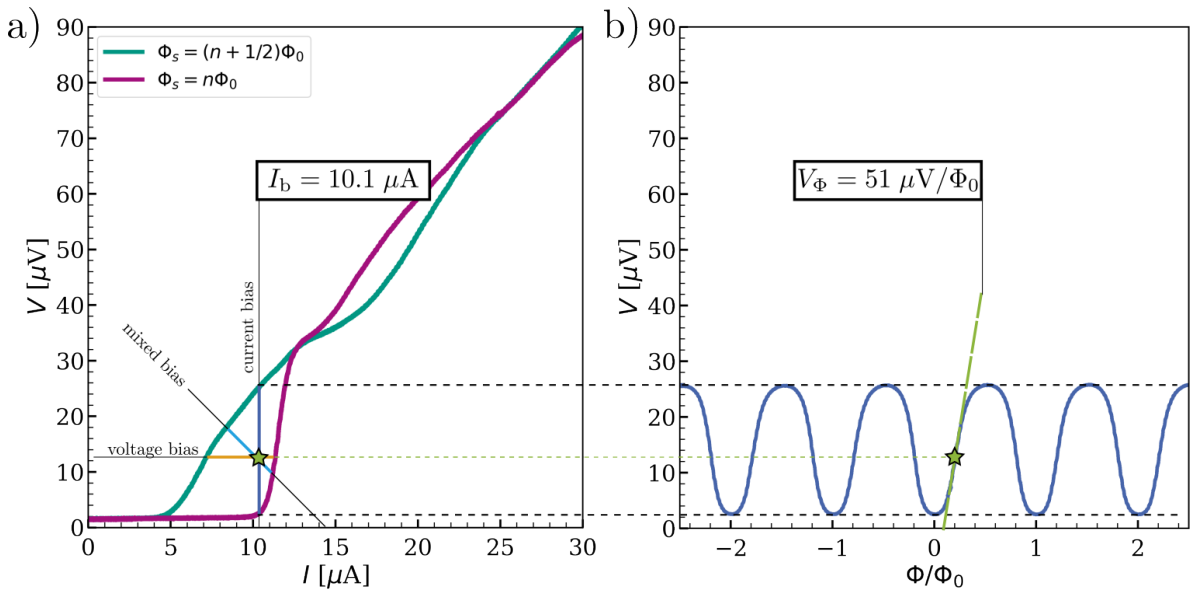

Figure 5.2: a) dc-SQUID I-V curve demonstrating its dependence on externally applied magnetic flux, highlighting the behavior at extrema values, $\Phi_{max} = (n + 1/2)\Phi_0$ in green and $\Phi_{min} = n\Phi_0$ in purple traces. **b)** Voltage response at a constant current bias as a function of the applied magnetic flux, normalized to the magnetic flux quantum Φ_0. The flux-to-voltage gain (V_Φ) of the dc-SQUID corresponds to the slope presented at the working point (marked as a green star).

current (current bias), or a combination of both (mixed bias) as illustrated in Figure 5.2.

The SQUID loop is inductively coupled to two coils: the input coil (L_{in}), connected to the sensor or signal source, and the feedback coil (L_{fb}), used operation in Flux-Locked Loop (FLL) mode. In this mode, the SQUID output signal is integrated and fed back into the device via the feedback coil to cancel flux changes within the SQUID loop. This feedback mechanism linearizes the SQUID's response at the expense of a reduced bandwidth. The latter is ultimately defined by the readout electronics maximum operating frequency. Commercial XXF-1 SQUID electronics produced by Magnicon[3] were used characterize and operate the dc-SQUID amplifier. This model includes precision current sources capable of delivering signals in the microampere range, as well as amplifiers configurable for both open-loop (AMP) and FLL operation, with bandwidths of up to 50 MHz and 20 MHz, respectively.

To suppress hysteretic behavior observed in the voltage state and ensure stable operation, practical dc-SQUIDs incorporate shunt resistors R_J in parallel to each Josephson junction. These resistors introduce a damping factor given by $\beta_C = 2\pi I_{c,J} R_J^2 C/\Phi_0$, where $I_{c,J}$ is the junction critical current and C is the junction capacitance. While the inclusion of these shunt resistors stabilizes the SQUID, it also introduces Johnson noise into the system. At frequencies $f < k_B T/h$, where h is Planck's constant, this noise source is considered white and the voltage noise level is $S_V = 4k_B T(R_J/2)$, considering both shunt

[3]Magnicon GmbH, Barkhausenweg 11, 22339 Hamburg, Germany

resistors R_{J} for each junction in parallel. Inlcuding the SQUID flux-to-voltage gain (V_Φ), the resulting white flux noise referred to SQUID loop is [177]:

$$S_{\Phi,\mathrm{white}} = \frac{8\pi k_{\mathrm{B}} T R_J}{V_\Phi^2}. \tag{5.1}$$

Optimal performance is achieved when the hysteresis parameter $\beta_L = LI_{\mathrm{c,J}}/\Phi_0 = 1$, where L is the SQUID loop inductance, and the damping factor β_C is set just below the hysteretic threshold, which also occurs near unity [179]. In addition to white flux noise, a source of flicker noise is also present in the dc-SQUID, it has a $1/f$ dependence and its origin can partially be explained by thermal fluctuations that modulate the junction critical current [180, 181] although other explanations for its origin have also been proposed and experimentally demonstrated [182]. With these considerations, the total dc-SQUID flux noise can be regarded as:

$$S_\Phi = \frac{S_{\Phi,1/f}}{f^\eta} + S_{\Phi,\mathrm{white}} \tag{5.2}$$

the parameter η can take different values and modify the slope of the $1/f$ contribution.

5.3 The two-stage SQUID-based amplifier

An amplifier based in a single SQUID will be limited in sensitivity due to the low flux-to-voltage gain offered. Even with great energy resolution and low SQUID noise, the readout electronics noise typically dominates in this configuration and results in non-optimal noise performance. A two-stage SQUID-based amplifier [183] makes use of two SQUID stages to increase the flux-to-voltage transfer coefficient using a second SQUID as a low-noise amplifier. In this thesis, dc-SQUID arrays were used as the second amplification stage. They consist of several dc-SQUIDs connected in series and coherently coupled to the same input and feedback coils. The device operates effectively as a single SQUID with a larger flux-to-voltage transfer coefficient proportional to the number of SQUID loops used [184].

The detector-under-test is connected to the input coil of the front-end dc-SQUID, and its output is connected to the input coil of the dc-SQUID array. The XXF-1 SQUID electronics module provides all required bias sources and low noise amplifiers to operate such a two-stage amplification setup. The schematic circuit shown in Figure 5.3 represents the complete two-stage SQUID-based amplifier, including a simplified version of the XXF-1 read-out electronics board [185].

The front-end SQUID is biased with a bias resistor (R_{b}), connected between the front-end SQUID leads and the input coil of the SQUID array. The front-end bias current (I) flows through this resistor in parallel with the SQUID coil, allowing the device to operate in a mixed-bias regime. A small input signal causes the SQUID to move dynamically along a resistive trace in its I-V characteristic curve with slope $-1/R_{\mathrm{dyn}}$, where R_{dyn} is the dynamic resistance. The low-frequency small-signal flux gain (G_Φ) at a stable working point is given by [183]:

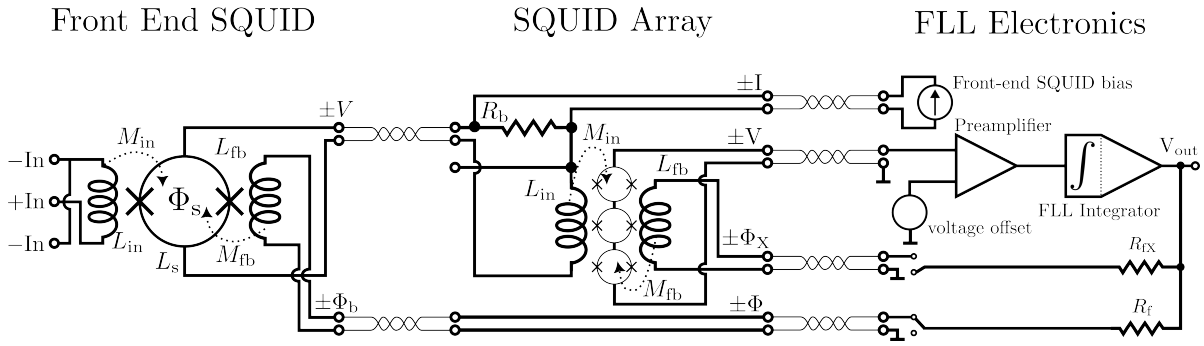

Figure 5.3: Two-stage SQUID-based amplifier schematic circuit consisting of the front-end dc-SQUID, the second stage dc-SQUID Array and a simplified schematic of the read-out electronics [185]. The amplifier can operate in AMP (open-loop) mode by bypassing the FLL integrator, or FLL (closed-loop) mode by using the feedback resistors. The feedback signal can be connected either to the front-end SQUID, the SQUID array or both with their respective feedback resistors R_f and R_{fX}.

$$G_\Phi = \frac{\partial \Phi_2}{\partial \Phi_1} = \frac{M_{in,2}}{R_b + R_{dyn}} V_{\Phi,1}, \tag{5.3}$$

where $M_{in,2}$ is the input coupling of the SQUID array, and $V_{\Phi,1}$ is the flux-to-voltage gain of the front-end SQUID.

The FLL feedback can be connected either to the front-end SQUID and/or to the SQUID array through individually selectable feedback resistors R_f and R_{fX}, double feedback techniques are also possible and useful in cases where the reduced system slew rate resulting from the enhanced SQUID sensitivity must be mitigated. In FLL mode, the low frequency flux-to-voltage gain is linearized and independent of the intrinsic SQUID non-linear response. Under appropriate conditions, this flux-to-voltage gain can be calculated as:

$$\frac{V_{out}}{\Phi_s} = \frac{R_f}{M_{fb}}, \tag{5.4}$$

where Φ_s is the magnetic flux threading the SQUID and M_{fb} is the mutual inductance to the feedback coil. Equation 5.4 holds as long as the slew rate of the input signal remains within the tracking capability of the integrator and the SQUIDs are biased at a stable working point, allowing a small-signal linear flux-to-voltage conversion. When FLL mode is performed with just the array (through R_{fX}), the amplified V-Φ_s characteristics of the front-end SQUID can be observed directly.

5.3.1 Frequency response

The block diagram presented in Figure 5.4 considers the amplifier in single feedback mode to the front-end SQUID. The gain-bandwidth product (GBP) in such case corresponds to the combination of the flux gain (G_Φ), the SQUID array flux-to-voltage gain ($V_{\Phi,2}$), and the preamplifier gain (A) multiplied with the integrator pole:

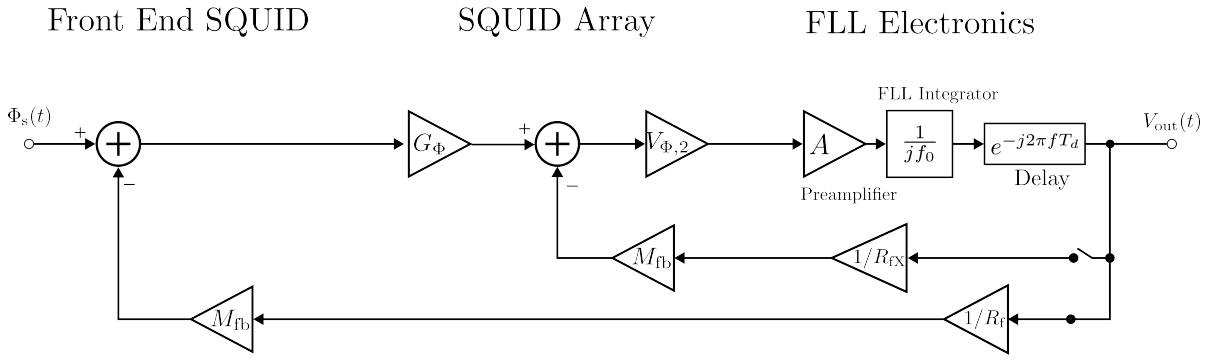

Figure 5.4: Small-signal block diagram of the two-stage SQUID amplifier used to extract the frequency response. In this diagram the amplifier is configured to operate in FLL mode with the feedback signal connected to the front-end SQUID. A finite loop delay is introduced in the direct forward path and represents the signal lag introduced by the FLL electronics.

$$\mathrm{GBP} = G_\Phi V_{\Phi,2} A f_0. \tag{5.5}$$

The block diagram includes an additional element in the signal's direct path to account for a finite delay inherent in the operation of the electronics, typical values for this delay are considered in the 10...100 ns range. The effect of such delay on the overall system behavior is non-negligible. It can be modeled using a complex exponential transfer function of the form, $e^{-j2\pi fT_\mathrm{d}}$, where T_d is the effective time delay. To simplify the analysis and retain a rational transfer function form, this exponential was approximated using a first-order Padé approximation [186, 187]:

$$e^{-j2\pi fT_\mathrm{d}} \approx \frac{j\pi fT_\mathrm{d} - 1}{j\pi fT_\mathrm{d} + 1}, \tag{5.6}$$

The inclusion of this factor introduces an additional pole-zero pair. Solving the block diagram of Figure 5.4 (b) in the Fourier space yields the frequency response of the two-stage SQUID-based amplifier in FLL mode resulting in a linear two-pole transfer function:

$$\frac{V_\mathrm{out}(f)}{\Phi_\mathrm{s}(f)} = H(f) = \frac{R_\mathrm{f}}{M_\mathrm{fb}} \cdot \frac{1 - jf\pi T_\mathrm{d}}{1 - (f/f_\mathrm{c})^2 + j2\xi \cdot f/f_\mathrm{c}}, \tag{5.7}$$

where the intrinsic cutoff frequency (f_c), the damping factor (ξ), and T_d can fully describe the frequency response of the amplifier. The values of f_c and ξ are:

$$f_\mathrm{c} = \sqrt{\frac{M_\mathrm{fb}}{R_\mathrm{f}} \frac{\mathrm{GBP}}{\pi T_\mathrm{d}}}, \tag{5.8}$$

and

$$\xi = \frac{R_\mathrm{f}/M_\mathrm{fb} - \pi T_\mathrm{d}\mathrm{GBP}}{\sqrt{R_\mathrm{f}/M_\mathrm{fb}\pi T_\mathrm{d}\mathrm{GBP}}}. \tag{5.9}$$

In the XXF-1 electronics board, both R_f and the preamplifier gain (A) are user-selectable over a wide range of values. To achieve higher voltage gain in the FLL configuration and therefore an improved noise performance, a larger R_f is chosen, as per Equation 5.4. The preamplifier gain is then adjusted to ensure that the system presents a large enough bandwidth, modifying the gain-bandwidth product of the amplifier. Increasing GBP decreases the value of the damping factor ξ (cf. Equation 5.9). Therefore, the selection of R_f and A must be balanced to find a regime that preserves linearity and fast response while avoiding parasitic oscillations resulting from the under-damped or unstable response associated with low ξ values.

5.3.2 dc-SQUID characterization

The dc-SQUIDs used for MMB characterization (shown in Figure 5.5) were produced by IMS and are based on in-situ deposition of $Nb/Al_2O_3/Nb$ trilayers to produce the Josephson junctions. The design values were chosen such that the hysteresis-related factors, β_L and β_C, remain below unity, mitigating the risk of hysteretic behavior due to systematic fabrication variations [188]. The dc-SQUID arrays (also shown in Figure 5.6) incorporate 16 SQUID elements with two additional pairs of dummy element structures at either end to mitigate fringing artifacts from the first and last SQUID in the array.

Measurements conducted at approximately 4 K were used to extract the optimal working point, the inductive couplings of the input and feedback coils, and the flux-to-voltage gain. The characteristics of the SQUIDs are summarized in Table 5.1. The optimal bias current (I_b) is determined as the value that maximizes the peak-to-peak voltage swing in the SQUID response and corresponds to the highest flux-to-voltage gain that can be achieved. The critical current of the SQUID ($I_{c,SQ}$) is determined from the optimum bias current using the following expression [188]:

$$I_{c,SQ} = I_b + \frac{2k_B T}{\Phi_0}\left(1 + \sqrt{1 + \frac{I_b \Phi_0}{k_B T}}\right), \tag{5.10}$$

where T is the temperature at which the characterization is performed. The feedback and input inductive couplings of the SQUID are extracted by passing an increasing current signal through the feedback and input coils (I_{FB} and I_{in}, respectively) while maintaining the previously determined optimal I_b. The resulting voltage signal exhibits a periodic response, where the period is directly related to the magnetic coupling between each coil and the SQUID loop. Multiple SQUIDs were characterized, however, for reference, the results presented correspond to a single representative device whose performance is consistent with the values observed across all measured samples.

5.3.3 Noise performance and bandwidth

The flux noise of the two-stage SQUID-based amplifier at the front-end SQUID is determined by [183]:

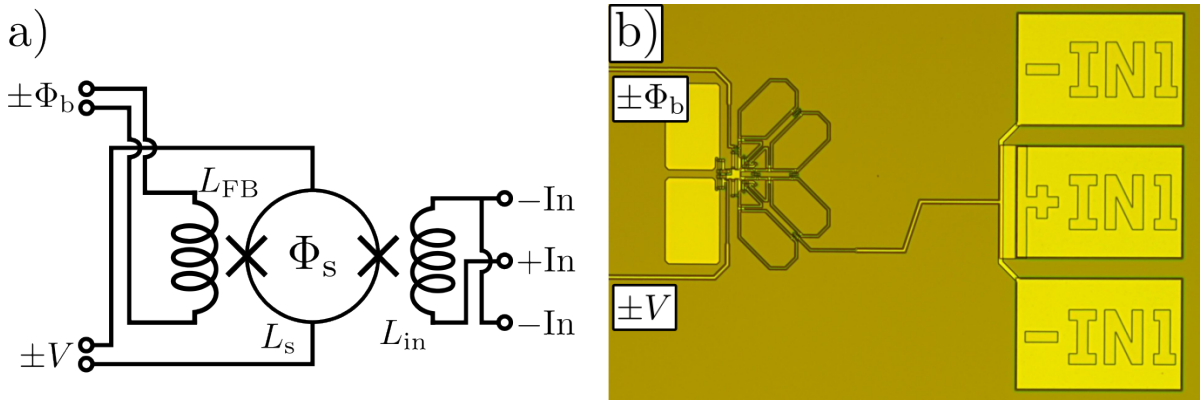

Figure 5.5: **a)** Schematic diagram of the dc-SQUID **b)** Microscope picture of a dc-SQUID designed and developed by IMS used as the front-end SQUID in this thesis for MMB-TD characterization.

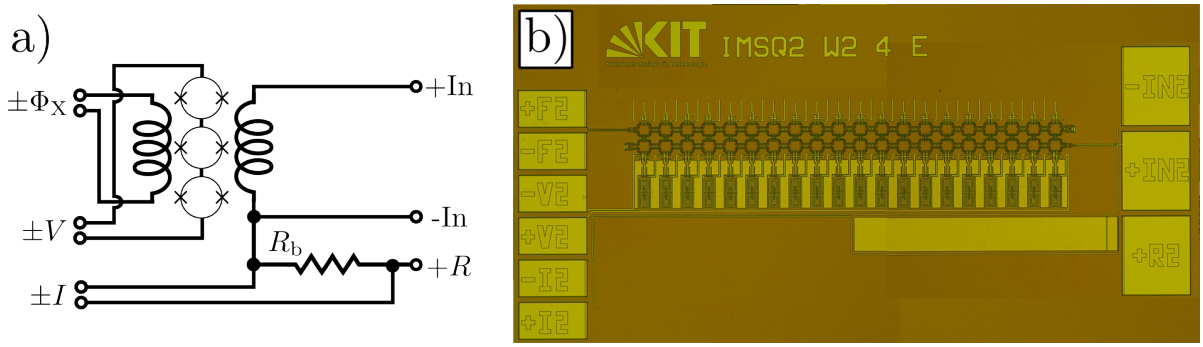

Figure 5.6: **a)** Schematic diagram of a SQUID array. **b)** Microscope picture of the dc-SQUID arrays, designed and developed by IMS, used in this thesis.

Parameter	**Front-end dc-SQUID**	**dc-SQUID array**
L_s (SQUID loop)	89.17 pH	120 pH
L_{in} (input coil)	1.12 nH	215 pH
L_{FB} (feedback coil)	318.23 pH	215 pH
M_{in}^{-1} (input coupling)	8.84 μA/Φ_0	28.80 μA/Φ_0
M_{FB}^{-1} (feedback coupling)	41.88 μA/Φ_0	28.25 μA/Φ_0
$M_{in\text{-}FB}^{-1}$(parasitic coupling)	0.14 mA/Φ_0	213.73 μA/Φ_0
$I_{c,SQ}$ (critical current)	11.22 μA	12.76 μA
I_b (optimal bias current)	10.10 μA	11.57 μA
V_Φ (flux-to-voltage gain)	51 μV/Φ_0	787 μV/Φ_0

Table 5.1: Parameters of the front-end dc-SQUIDs and SQUID arrays used to characterize the MMB-TD prototypes.

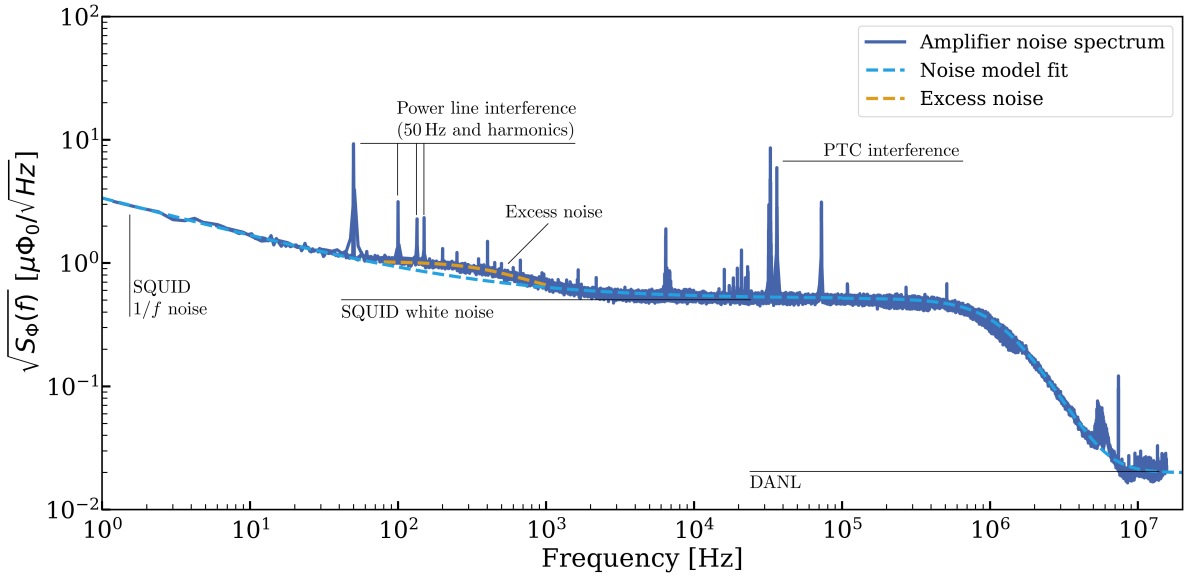

Figure 5.7: Noise spectrum of the two-stage SQUID-based amplifier referred to the flux noise in the front-end SQUID. The spectrum was fitted to extract relevant amplifier parameters such as the amplifier bandwidth and overall noise peroformance (shown in light blue dashed trace). An additional low-frequency noise not originally considered in the noise model was observed and fitted with a low-pass first order function (yellow dashed trace) to extract its level and cut off frequency.

$$S_\Phi(f) = S_{\Phi,1}(f) + \frac{S_{\mathrm{R_b},J}}{V_{\Phi,1}^2} + \frac{1}{G_\Phi^2}\left(S_{\Phi,2}(f) + \frac{S_{V,\mathrm{amp}}(f)}{V_{\Phi,2}^2} + \frac{S_{I,\mathrm{amp}}(f)}{M_{\mathrm{in},2}^2}\right), \tag{5.11}$$

where $S_{\mathrm{R_b},J} = 4k_\mathrm{B}TR_\mathrm{b}$, is the bias resistor Johnson noise, and $S_{V,\mathrm{amp}}(f)$ and $S_{I,\mathrm{amp}}(f)$ denote the equivalent voltage and current noise of the room-temperature preamplifier, respectively. With the large flux gain (G_Φ) obtained in the two-stage configuration, the terms in brackets become increasingly less dominant, and the flux noise can be considered dominated by the front-end SQUID noise ($S_{\Phi,1}(f)$) and by the Johnson noise of the bias resistor. The latter, however, is negligible at the operating temperature of the MMB as R_b has a relatively small value of a few hundred mΩ:

$$\sqrt{S_{\mathrm{R_b},J}/V_{\Phi,1}^2}\Big|_{T=320\,\mathrm{mK}} \approx 50\,\mathrm{n}\Phi_0/\sqrt{Hz}, \tag{5.12}$$

while the SQUID white noise with the measured dc-SQUID shunt resistance of $R_J/2 \approx 3\,\Omega$ yields

$$\sqrt{S_{\Phi,\mathrm{white}}}\Big|_{T=320\,\mathrm{mK}} \approx 500\,\mathrm{n}\Phi_0/\sqrt{Hz},. \tag{5.13}$$

The total flux noise was analyzed by measuring the output voltage spectrum of the amplifier with no device connected at the input. The voltage spectrum was referred to

Gain	f_c	ξ	$\sqrt{S_{\Phi,\mathrm{white}}}$	$\sqrt{S_{\Phi,1/f}}$	η	$\sqrt{S_{\mathrm{DANL}}}$	$\sqrt{S_{\mathrm{exc}}}$	f_{exc}
$4.23\,\mathrm{V}/\Phi_0$	1.23 MHz	0.89	$0.52\,\frac{\mu\Phi_0}{\sqrt{\mathrm{Hz}}}$	$3.30\,\frac{\mu\Phi_0}{\sqrt{\mathrm{Hz}}}$	0.31	$19.93\,\frac{\mathrm{n}\Phi_0}{\sqrt{\mathrm{Hz}}}$	$0.88\,\frac{\mu\Phi_0}{\sqrt{\mathrm{Hz}}}$	535 Hz

Table 5.2: Amplifier bandwidth and noise performance parameters extracted from the noise spectrum measurement presented in Figure 5.7.

the front-end SQUID by dividing it with the closed-loop DC flux-to-voltage gain (cf. Equation 5.4). The measured spectrum (shown in Figure 5.7) was fitted with a noise model of the form:

$$S_\Phi(f) = \left(\frac{S_{\Phi,1/f}}{f^\eta} + S_{\Phi,\mathrm{white}}\right)|H(f)|^2 + S_{\mathrm{DANL}}. \tag{5.14}$$

Here, S_{DANL} was added to account for the displayed average noise level. This white noise source can either be voltage noise at the output of the FLL electronics or acquisition noise from the spectrum analyzer and it naturally extends above the cut off frequency of the SQUID amplifier. An additional low-frequency excess noise was observed and fitted with a low-pass first-order function to extract its noise level (S_{exc}) and cut off frequency (f_{exc}). In low-noise high-speed SQUID electronics, composite preamplifiers consisting of a combination of two separate dc and ac amplifiers have been proposed and do typically present an increased noise level with a cut off frequency of ≈ 100 Hz [189]. In this case, the fitted excess noise cutoff frequency is higher, $f_{\mathrm{exc}} = 535$ Hz and could otherwise be explained as magnetic Johnson noise generated by the copper sample holder to which the SQUID is attached. The resulting performance of the two-stage SQUID-based amplifier is summarized in Table 5.2.

Besides noise, multiple spurious signals can be identified in the spectrum of Figure 5.7. A strong 50 Hz signal and multiple harmonics picked up from mains power. Additionally, multiple peaks in the range of a few kHz and up to 100 kHz that arise mostly from the pulse-tube-cryocooler. Such PTC spurious signals are common in this configuration and were observed to dissapear when briefly turning off the PTC. Such spurious signals are presumably coupled by the wiring. Copper wires are used to connect the front-end SQUID to the SQUID array and long copper-nickel twisted pairs to connect the cryogenic setup at the mixing chamber stage to the room-temperature XXF-1 electronics for bias and readout. Although the wiring may increase susceptibility to interference, the setup has presented sufficiently low readout noise for detector characterization. Further refinement of the setup may include using shorter wires between SQUID stages, using integrated front-end SQUIDs and SQUID arrays in a single chip and/or including additional low-pass filters to the bias and readout wiring.

Chapter 6

Experimental Results

This chapter presents the experimental results obtained during the characterization of the first MMB detector prototypes. Due to the unavailability of a dedicated Au:Er or Ag:Er sputtering target specifically designed for the development of the MMB, only a limited number of samples could be fabricated, therefore a preliminary evaluation conducted pertaining the detector characterization is presented here. The injection of a persistent current could be clearly proven, confirming the correct operation of the biasing concept. Important information was also extracted related to the thermal and mechanical stability of the fabricated MMBs. In spite of succesfully performing the preliminary tests to the fabricated samples, the final goal of extracting the response to excitation signals could not be performed due to an apparent lack of magnetization observed in Au:Er sensors that underwent the detector release process. Even though a response couldn't be demonstrated, the results provide valuable insight regarding the integration and operational behavior of the MMB that will aid further development pursued beyond the scope of this thesis.

6.1 Measurement setup

The characterization strategy consisted in delivering rectangular current pulses to the excitation pads connected to the termination resistors of the released bolometer prototypes after injection of a persistent bias field current. By observing the amplitude and overall shape of the output signals, both sensitivity and timing characteristics can be extracted. Preliminary steps included determining the inductance of each coil in the fabricated MMB-TD samples, testing the persistent current switches at the operating temperature of the detector and analyzing the magnetization of the sputtered Au:Er paramagnetic sensor material to extract the required calibration curves. The cryogenic setup used is shown in Figure 6.1. A custom sample holder was developed to accommodate the MMB and the front-end SQUIDs of the two-stage SQUID-based amplifier. The design of this sample holder prioritized external magnetic field rejection. In this first stage of characterization, the intrinsic behavior of the device should be extracted before tackling its performance under more real and noisy environments. The sample holder for

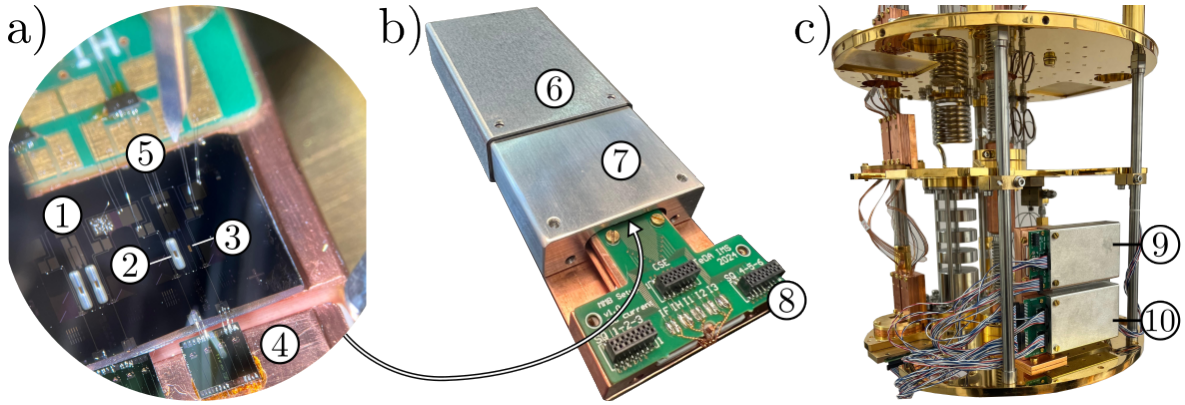

Figure 6.1: Cryogenic setup used for MMB characterization. **a)** The bonded chips are shown. **b)** Sample holder designed and built for this measurement. **c)** Setup installed in the mixing chamber flange of the LD250 refrigerator. 1) MMB-TD chip. 2) Released MMB. 3) Non-released MMB. 4) Front-end dc-SQUID chip. 5) Bias and excitation lines 6) CryoPhy® magnetic shield. 7) Aluminum housing. 8) Sample-holder body with connector PCB. 9) MMB-TD module installed. 10) Similar module containing dc-SQUID arrays required for two-stage SQUID amplification.

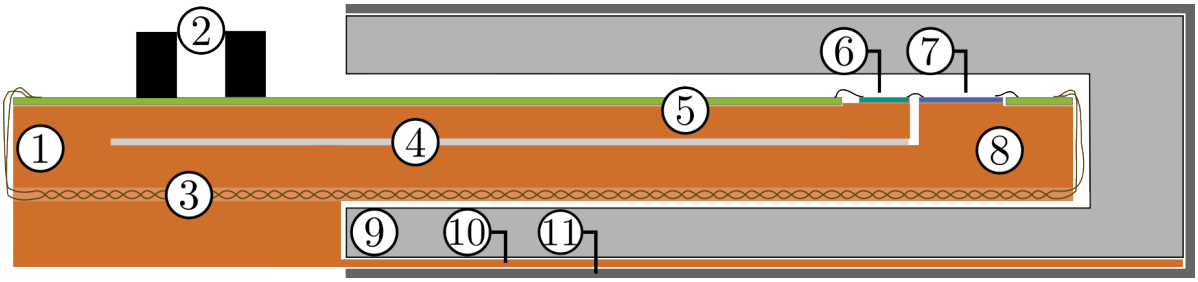

Figure 6.2: Schematic cross-section view of the MMB-TD sample holder. 1) Thermal anchor. 2) Connectors to SQUID arrays and current sources for biasing and excitation. 3) Forward current I_{F}, persistent current switch pulse I_{H} and excitation signal I_{R} wiring. 4) Plastic (ABS) thermal insulation between copper fingers. 5) Front-end SQUID finger. 6) Front-end SQUID chip. 7) MMB-TD chip. 8) MMB device finger. 9) Aluminum housing for magnetic screening. 10) Copper plate to thermalize the aluminum housing. 11) CryoPhy® magnetic shield.

the MMB-TD chip was designed to fulfill the following requirements:

- Provide magnetic shielding.
- Present adequate space to place the chip in close proximity to the readout SQUIDs to reduce parasitic inductance in the flux transformer (L_{stray}).
- Thermally decoupling of the detector from the front-end SQUIDs to mitigate parasitic heating effects.
- Provide connection pads for the SQUID signals and the required current sources to the detector for forward bias current (I_{F}), the persistent current switch pulse (I_{H}), and the excitation signal (I_{R}) to the resistors of the released MMB.

The setup consists of a copper platform that is inserted into a machined aluminum body. The sample is placed at the end of the platform, deeply located within the aluminum housing. The setup is enclosed by a CryoPhy® shield developed by Magnetic Shields[1]. CryoPhy® is a high-permeability material designed to operate at cryogenic temperatures ($< 40\,\mathrm{K}$) that diverts and traps ambient magnetic flux. This two-stage shielding, combining a superconducting inner shield with a high-permeability outer layer, ensures strong attenuation of external magnetic flux across a large bandwidth.

The same concept has been applied for SQUID arrays used for additional signal amplification in the two-stage SQUID-based amplifier. These arrays are placed on a different sample holder thermally anchored to the mixing chamber. This configuration maintains heat dissipation from the SQUID arrays away from the MMB at the expense of additional wiring.

For persistent current injection a CSE-1 module is used. This module is a current source extension board developed by Magnicon which offers several low-current sources similar to the ones used for SQUID biasing and, additionally, high-current sources reaching 150 mA. It is ideal for persistent current injection as it allows to sequence the operation of the current sources by software. Two low current sources are used for delivering the persistent current switch pulse (I_H) and the excitation signals to the termination resistors (I_R) while a high-current source is used to supply the forward bias current (I_F). Twisted pairs carrying these currents are plugged into the MMB sample-holder and are fed directly to the MMB-TD pads.

When the MMB is connected to the front-end SQUID of the two-stage SQUID-based amplifier, flux noise increases due to noise coupled from the I_F current source. This is because there is a non-zero transfer coefficient from the I_F leads of the MMB to the output pads connected to the readout SQUID due to its asymmetric bridge-type circuit shown in Figure 3.8 of Chapter 3, and non-zero switch inductance (L_sw). This noise contribution can be mitigated by including low-pass filters to the I_F lines and reducing the switch inductance to the minimum possible value in subsequent designs.

6.2 Inductance measurements

An inductance measurement method was used to extract the inductance of superconducting coils by analyzing noise spectra. Above T_c of the aluminum bond wires that connect the detector to the front-end SQUID produce thermal Johnson noise. This noise source produces a constant current noise spectral density level that can be calculated as $\mathrm{S}_\mathrm{bond} = \frac{4k_\mathrm{B}T}{R_\mathrm{bond}}$, where R_bond is the resistance of the normal conducting aluminum wires. The resulting equivalent circuit is presented in Figure 6.3.

The three inductances appearing in Figure 6.3 form an L/R low-pass filter with the resistance of the bond wires. We can therefore model the flux noise signal $S_{\Phi,\mathrm{bond}}(f)$ threading the front-end SQUID as,

[1]Magnetic Shields Limited, Headcorn Road, Staplehurst, TN12 0DS, United Kingdom

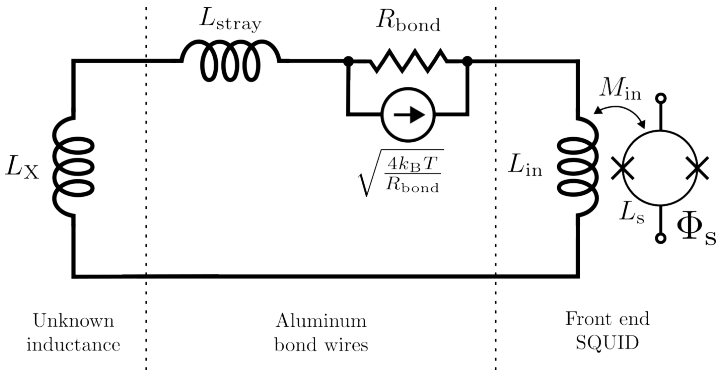

Figure 6.3: Schematic circuit of an unknown inductance (L_{X}) connected to the front-end SQUID. The noise source arising from the normal conducting wire bonds is represented as a current source in parallel to its resistance R_{bond}.

$$S_{\Phi,\mathrm{bond}}(f) = M_{\mathrm{in}}^2 \frac{S_{\mathrm{bond}}}{(1+f/f_0)^2}, \text{ with } f_0 = \frac{R_{\mathrm{bond}}}{2\pi L} \tag{6.1}$$

where L is the total inductance

$$L = L_{\mathrm{X}} + L_{\mathrm{in}} + L_{\mathrm{stray}}. \tag{6.2}$$

Equation 6.1 shows a direct relationship between the absolute value of the noise magnitude and the bond wire resistance, together with a cutoff frequency depending on both the same resistance and total inductance. The measured spectra are fitted with a noise model based on Equation 6.1 using R_{bond} and L as free parameters, thereby extracting the total inductance of the circuit. Additionally, the previously determined amplifier noise performance is added to the model to account for the amplifier response. The noise model used is therefore:

$$S_{\Phi}(f) = \Big(S_{\Phi,\mathrm{bond}}(f) + S_{\Phi,1} + S_{\mathrm{exc}}(f) \Big) |H(f)|^2 + S_{\mathrm{DANL}}. \tag{6.3}$$

The measurement method is inherently limited in bandwidth by the response of the SQUID amplifier. In principle, the expected values for R_{bond} and L must satisfy the following condition:

$$\frac{L}{2\pi R_{\mathrm{bond}}} < f_c. \tag{6.4}$$

In case this condition is not fulfilled, the relative uncertainty in the extracted inductance L increases as the inductance value decreases. This limitation must be considered when interpreting low-inductance measurements near or beyond the amplifier's bandwidth capability. Despite this constraint, the analysis model has consistently enabled the extraction of reliable values for L even when the corresponding characteristic frequencies were close to f_{c}. Total inductances as low as 3 nH were measured and showed repeatable results. This is particularly advantageous for the actual MMB design, which employs pickup coil inductances on the order of 2 nH. The 20 MHz (high-bandwidth) version of the XXF-1 electronics was required for such measurements.

A total of three measurements were required to extract the inductance values. One measurement was performed shorting the input inductance of the front-end SQUID with

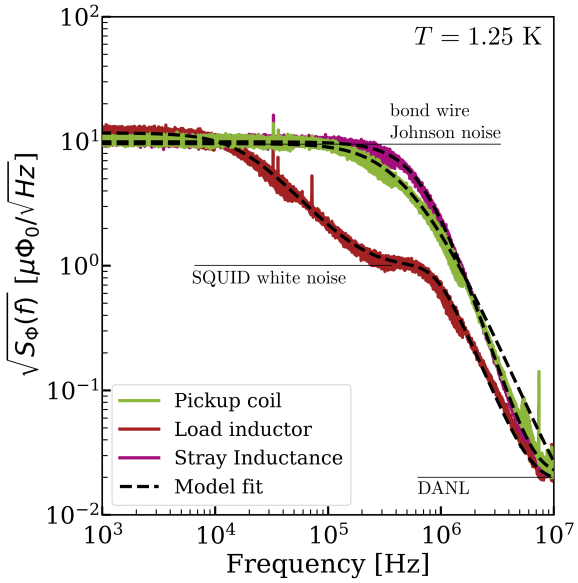

Figure 6.4: Noise measurements taken at $T = 1.25\,\mathrm{K}$ to perform each inductance extraction step. The resulting output parameters R_{bond} and L_{X} were obtained by fitting the model described in Equation 6.3. The model fit for each case is plotted over the spectra in black dashed traces.

Inductor	**Simulated**	**Measured**
$L_{\mathrm{in}} + L_{\mathrm{stray}}$	–	$(3.36 \pm 0.01)\,\mathrm{nH}$
L_{in}	$1.12\,\mathrm{nH}$	–
L_{stray}	–	$(2.24 \pm 0.01)\,\mathrm{nH}$
L_{m}	$2.18\,\mathrm{nH}$	$(2.01 \pm 0.01)\,\mathrm{nH}$
L_{load}	$51.01\,\mathrm{nH}$	$(58.18 \pm 0.07)\,\mathrm{nH}$

Table 6.1: Simulated and/or measured inductance values of L_{stray}, L_{in}, L_{m} and L_{load} of the MMB-TD.

bond wires of similar length to those used in the connection to the device-under-test to extract the value of $L_{\mathrm{stray}} + L_{\mathrm{in}}$. In another measurement, the MMB pickup coil was connected to the SQUID, in this case, $L_{\mathrm{m}} = L_{\mathrm{X}} = L - (L_{\mathrm{stray}} + L_{\mathrm{in}})$. In a third measurement, a load inductor was connected to the same setup to extract its value similarly.

Figure 6.4 shows the measured flux noise spectra fitted with the noise model described by Equation 6.3. The spectra were taken at a temperature above T_{c} of aluminum ($T \approx 1.25$ K) where the the Johnson noise produced by the normal conducting bond wires is produced. The inductance values were extracted for each case and are summarized in Table 6.1 together with their previously simulated values. The large values of stray inductance obtained produce a significant reduction in detector sensitivity according to the flux transformer transfer function (cf. Equation 3.31). This reduction can be mitigated by reducing the length of the bond wires or using multiple wires in parallel for each connection. During these tests, two parallel bond wires for each contacting pad with lengths of approximately 2 mm each were used.

6.3 Bias field injection

Due to the asymmetric layout of the MMB ($L_\mathrm{m} \neq L_\mathrm{load}$), a persistent current driven through the input inductance of the SQUID appears (I_SQ) in addition to I_field after persistent current injection. In Chapter 3, equations to calculate these currents are presented. By measuring I_SQ, a correct operation of the persistent current switch can be verified. This verification method is a superior design aid when developing layout designs for persistent current switches.

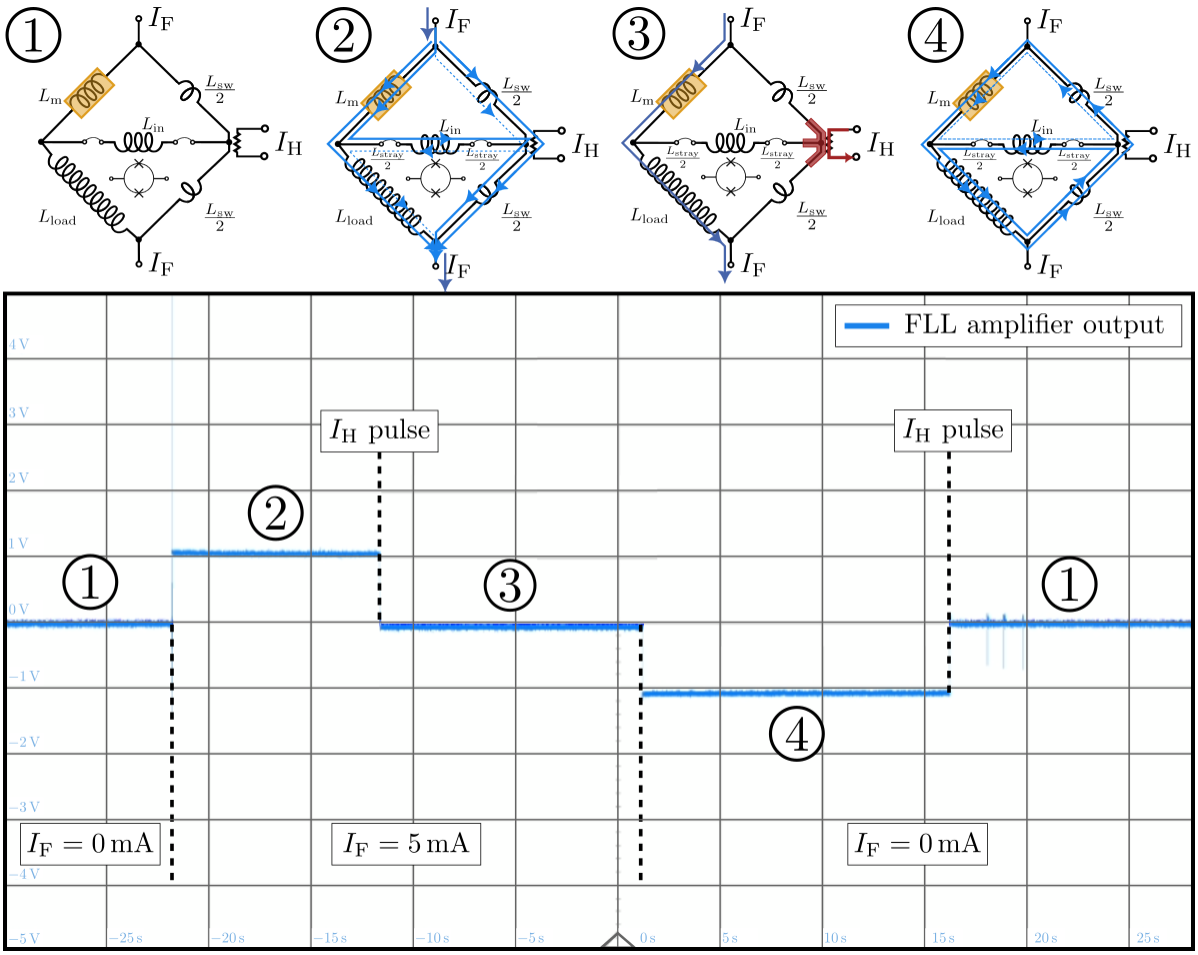

Figure 6.5: Persistent current injection stages observed with an oscilloscope. 1) Initial stage of the persistent current injection process. 2) A forward current $I_\mathrm{F} = 5\,\mathrm{mA}$ is applied to the circuit. 3) A current pulse (I_H pulse) is delivered to the switch, and the trapped flux cancels the flux introduced by I_F. 4) After removing I_F, the trapped flux remains in the circuit until a subsequent switch pulse is used to reset the detector.

The flux threading the SQUID loop during the persistent current injection was monitored, and the four distinct stages of the current injection (see Figure 3.9) are identified in the oscilloscope trace shown in Figure 6.5 in light blue color. In this example, a forward current $I_\mathrm{F} = 5\,\mathrm{mA}$ was introduced, a switch pulse $I_\mathrm{H} = 4.5\,\mathrm{mA}$ for a duration of 10 ms and the voltage at the output of the two-stage SQUID amplifier was recorded.

This procedure was used to determine the lower bound of the switch pulse parameters at millikelvin temperatures that can be used to inject the currents. These bounds are lower compared to those obtained at temperatures above 4 K in the isolated switch characterization described in Chapter 4. At lower temperatures, the cooling power is lower and the persistent current switch is less thermally coupled to the sample holder allowing a higher temperature rise with similar heat inputs. Using lower pulse heights and durations implies less thermal energy reaching the detector chip during I_{field} injection. For the switch design used in the MMB-TD, $I_{\text{H}} = 3\,\text{mA}$ and $t_{\text{ON}} = 1.5\,\text{ms}$ were identified as the lowest values that allow a persistent current to be reliably injected in the MMB.

6.4 Thermally-induced detachment of the Au:Er sensor

The I_{R} pulses were originally delivered directly to the termination resistors. The value of these resistors is $20\,\Omega$ to ensure appropriate matching to the differential transmission lines that carry the CMB signal. During the MMB-TD characterization, this resistor value combined with the lowest configurable value in the current source, imposes a minimum power input (P_{R}) that can be emulated. The current source used (low current sources of the CSE-1 board) presents a minimum output of $2.44\,\mu\text{A}$, resulting in $P_{\text{R}} = 119.1\,\text{pW}$ dissipation at the MMB. At an operating temperature of $T \approx 300\,\text{mK}$, this large P_{R} value is not an alarming issue, but when $T < 100\,\text{mK}$, the MMB thermal coupling to the heat bath becomes orders of magnitude lower. Such low thermal coupling produces instantaneous temperature variations (ΔT) in the range of several kelvin with the minimum P_{R} achieved, causing irreversible damage to the MMB device under test.

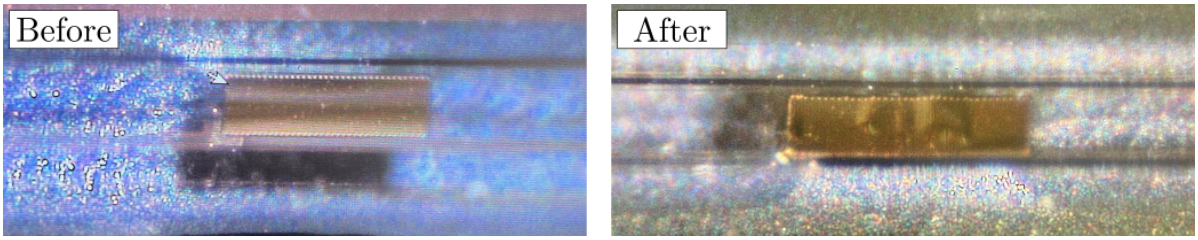

Figure 6.6: MMB device appearance before and after a cooldown. Bulging of the Au:Er sensor is evident and hints to partial detachment of the sensor material from the released membrane.

In the first cooldown of the MMB prototypes, this detail was overlooked. $I_{\text{R}} = 2.44\,\mu\text{A}$ pulses were fed to an MMB detector and did not produce any measurable output signal. Noticeable effects, however, were recognized upon visual inspection. Figure 6.6 shows images of the MMB device before and after this first cooldown. In this particular case, the Au:Er sensor became partially detached from the released structure, evidenced by the appearance of bulges in different locations in the sensor area. MMBs that underwent thermal cycling but were not fed with I_{R} pulses nor biased with a persistent current did not exhibit this bulging of the Au:Er sensor. Even though the thermal load in the devices was excessive, it also indicated that the mechanical stability of the released membrane

and the adhesion of the Au:Er sensor layer are not ideal. It highlights the need for further optimization of the intrinsic stress of the Au:Er films, which was not possible during the first iterations.

For subsequent cool downs, shunt-resistors with values of $\approx 1\,\Omega$ were connected in parallel to the termination resistors of each MMB. Lower power inputs could be achieved in this configuration, and as a safety measure, no I_{R} pulses were injected to the MMB detectors for $T \leq 100\,\mathrm{mK}$ thereafter. The resistors used were custom made using sputtered AuPd as resistive material and Nb as superconducting contacts. This provided better control in the resistance values and reliability throughout all used resistors. If commercial resistors were used, values at or below $1\,\Omega$ are not common and, in addition, each resistor would have to be individually characterized to know its actual value at millikelvin temperatures.

6.5 Thermal runaway breakdown

The MMB is also susceptible to mechanical failure when a hotspot forms somewhere in the pickup coil with a persistent current circulating through it. If the biased detector experiences a temperature rise beyond a threshold, a normal-conducting belt can form at the weakest point of superconductivity. The power dissipated, calculated as the product of the normal belt resistance and the square of the persistent current, can cause the superconducting line to evaporate due to the poor thermal conduction out of the released region. This process is referred here as thermal runaway breakdown of the MMB.

A documented thermal runaway breakdown event occurred while attempting to observe a signal. A periodic pulsed I_{R} signal was applied to the shunted termination resistor of an MMB, and the amplifier output was monitored with an oscilloscope. A persistent current $I_{\mathrm{field}} = 30\,\mathrm{mA}$ had been previously injected into the circuit, and the temperature was stabilized at $T = 150\,\mathrm{mK}$. As no clear output signal was observed, the I_{R} source was switched off. At that moment, a large voltage spike appeared on the oscilloscope screen. Subsequent resistance measurements of the I_{F} channel revealed an open-circuit, indicating that the pickup coil had become electrically disconnected from the detector. Noise measurements performed at $T > 1.2\,\mathrm{K}$ confirmed this failure. A significantly reduced cutoff frequency was observed when measuring the Johnson noise from the bond wires, which is consistent with an increased inductance at the front-end SQUID input, suggesting that only the load inductor remained connected, confirming the disconnection of the pickup coil. The problem was traced to current spikes that are delivered by the CSE-1 boards sporadically when turning on or off its current sources. A test was performed on the used CSE-1 board, measuring the outputs with an oscilloscope by feeding them to a dummy resistive load. It was determined that the particular current source used to feed the termination resistor of the destroyed MMB would output a spike when turning it off and continuous pulse mode was selected (replicating the measurement conditions). The current spikes delivered have an amplitude equal to the maximum value, which is $20\,\mathrm{mA}$, resulting in $P_{\mathrm{R}} = 19.05\,\mu\mathrm{W}$ dissipated in the MMB (accounting for the added shunt resistor).

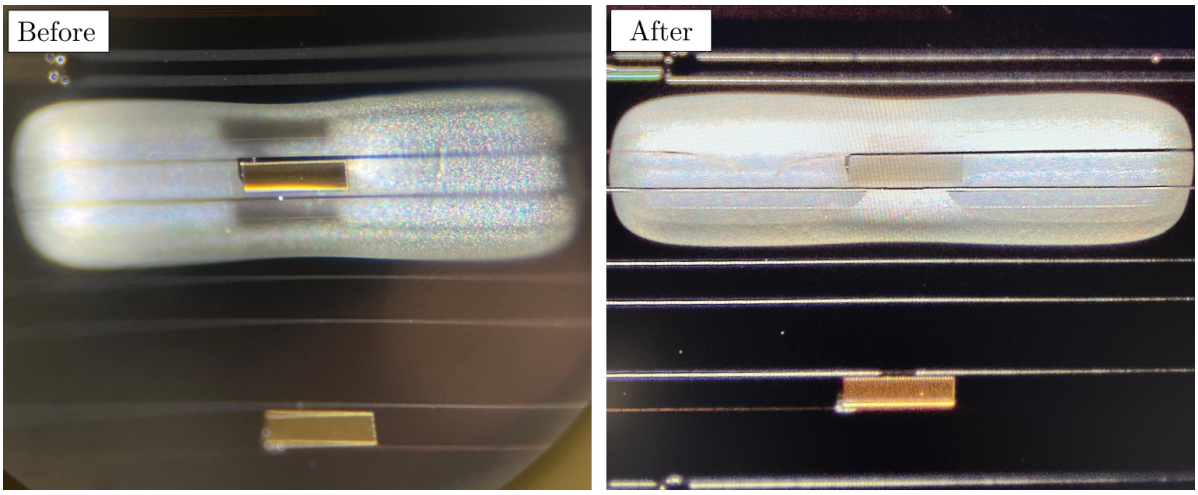

Figure 6.7: Pictures of an MMB before and after thermal runaway breakdown. The Nb lines that carry the persistent current were found broken at a specific point. Additionally, the Au:Er sensor disappeared from above the pickup coil.

Photographs of the MMB are displayed in Figure 6.7, taken before and after the cooldown. The leg carrying the pickup coil lines, responsible for conducting the persistent current, was found broken after the event, the leg carrying these lines snapped at a very precise point. Interestingly, the Au:Er sensor appears to have completely vanished from the released structure, either evaporated or mechanically detached, leaving behind an intact, released pickup coil. The curvature of the released membrane noticeably relaxed following the breakdown, resulting in a substantially flatter geometry compared to the pre-breakdown state. Confirming, that there exists internal stress gradients in the Au:Er films and are the primary suspect concerning the curvature observed in the released MMB detector prototypes.

6.6 Sensor magnetization measurement

Temperature-flux ($\Phi(T)$) curves were used to probe the magnetization of the paramagnetic sensors. A modified detector circuit based on the architecture of a conventional MMC was used for this purpose. In this design, two identical meander-shaped coils function as the pickup coil and the load inductor, respectively. Only the pickup coil is coated with the paramagnetic sensor material. The design and fabricated structures can be seen in Figure 6.8 together with a schematic of the design. Two magnetization test device chips (MT01 and MT02) were produced featuring 4 of these structures each. The thickness of each individual layer was measured to determine the expected signal. The design parameters and measured layer thicknesses are specified in Table 6.2 for both samples.

Persistent currents were injected in the superconducting circuit at a temperature $T \approx 600\,\mathrm{mK}$ and the detector signal was monitored using a two-stage SQUID amplifier while the temperature was lowered down to base temperature. As the temperature changes, the magnetization of the paramagnetic sensor varies. This variation in magnetization

Parameters		Layer	MT01	MT02
Pitch	10 μm	Nb1	251.0 nm	256.8 nm
Line width	5 μm	SiO_2 1	152.7 nm	161.7 nm
Sensor length	360 μm	SiO_2 2	158.8 nm	157.4 nm
Sensor width	360 μm	AuPd	205.5 nm	206.5 nm
L_m (simulated)	4.362 nH	Nb2	494.4 nm	503.1 nm
L_m (measured)	(4.07 ± 0.01) nH	Au:Er	822.5 nm	656.9 nm

Table 6.2: Design parameters and measured layer thicknesses of MT01 and MT02 chips used for characterization of the Au:Er sensor film.

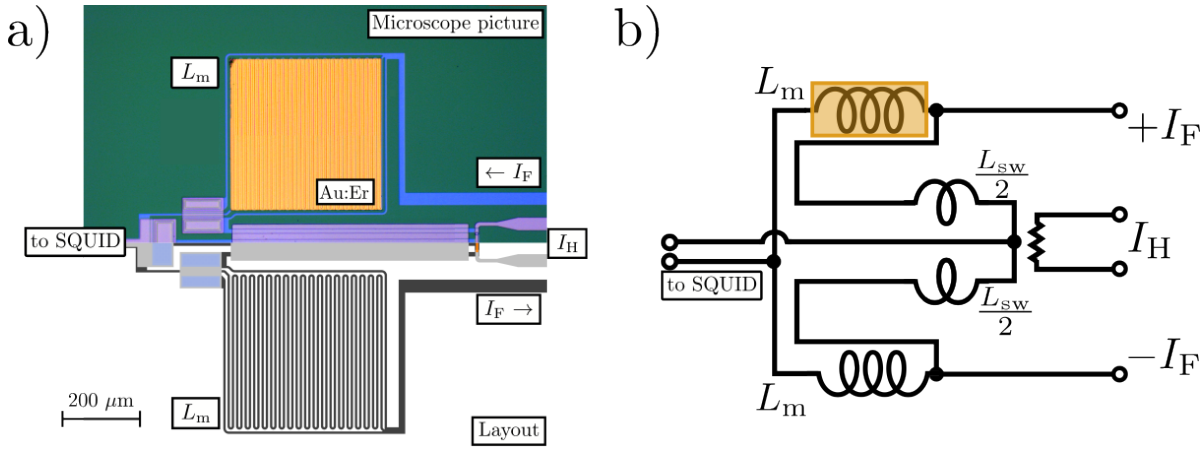

Figure 6.8: Device chip designed and produced to characterize the sensor material. a) Microscope picture and layout design. b) Schematic of the circuit, identifying all components involved.

induces a change in the magnetic flux threading the pickup coil, which, in turn, causes a variation of current running through the SQUID input coil, thus providing a sensitive probe of the temperature-dependent magnetization of the paramagnetic alloy.

The flux signal readout was performed using the two-stage amplifier in FLL mode, with the feedback signal routed to the SQUID array rather than the front-end SQUID. The front-end SQUID was biased significantly below its optimal value. As a result, the amplifier output exhibited voltage spikes that were Φ_0-periodic with respect to the magnetic flux threading the front-end SQUID loop. As the flux through the SQUID varies, the voltage-flux characteristics shift accordingly, moving from left to right or vice versa. The output voltage is then recorded and the temperature at which each spike appears at the signal is noted as it corresponds to a full Φ_0 variation threading the front-end SQUID. Therefore, by counting the number of flux quanta as the temperature is swept, the total flux variation through the SQUID can be determined. This readout method was selected because operating in the standard FLL mode, used, for example, during inductance extraction, leads to notable heat dissipation by the front-end SQUID. While this is not a major concern at temperatures above 100 mK, where the conduction

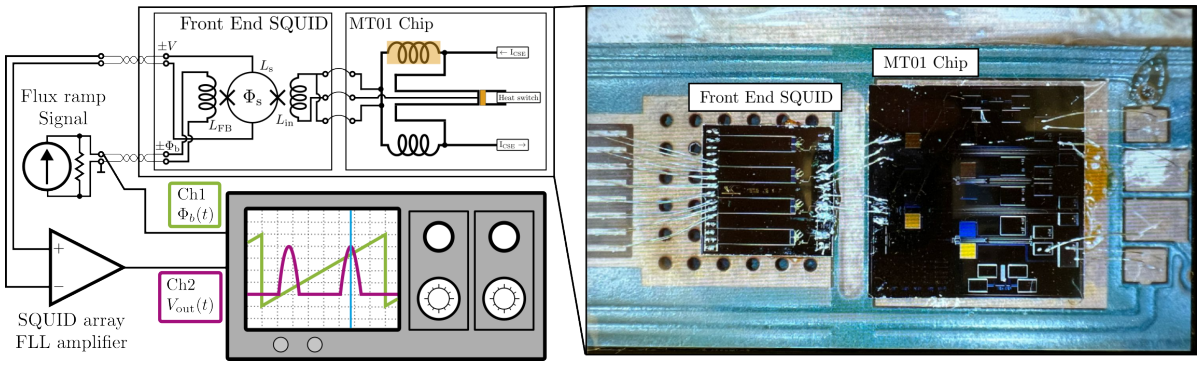

Figure 6.9: Magnetization measurement setup. A periodic flux ramp signal is fed to the feedback coil of the front-end SQUID and monitored with an oscilloscope (green trace). The output signal from the SQUID is amplified using a single stage FLL amplifier formed by a SQUID array and the XXF-1 module (purple trace). A vertical cursor (shown in cyan) is positioned on one of the voltage peaks and used as a reference to follow the flux variations in the front-end SQUID as the temperature is swept. A picture of the experimental setup is also shown.

electrons in the copper components of the cryostat ensure good thermal coupling and keep the sample temperature close to that of the mixing chamber, it becomes problematic at lower temperatures. At these lower temperatures, the detector, built on a silicon substrate, tends to become thermally decoupled from the mixing chamber stage. This results in significant discrepancies between the thermometer reading and the actual sensor temperature. By strongly under-biasing the front-end SQUID, the heat it dissipates is minimized, thereby reducing parasitic heating of the sample. This approach significantly mitigates the effects of thermal decoupling, allowing for a more accurate reconstruction of the magnetization curve at sub-100 mK temperatures. Even though the MMB will operate at higher temperatures, characterization of the sensor material in the full temperature range allows a better comparison to theory.

The measurement method also incorporates a periodic ramp signal applied to the feedback coil of the front-end SQUID. The ramp amplitude is set such that each cycle spans a full period of the front-end SQUID's $V - \Phi$ characteristics. Initially, the cryostat is heated to 600 mK, and a horizontal reference cursor is positioned on a voltage peak in the SQUID response using an oscilloscope. Once the heater is turned off, the system cools down, and as the temperature decreases, the voltage peaks shift horizontally due to the changing magnetic flux. Each time a voltage peak crosses the reference cursor, the corresponding temperature is recorded. A schematic representation of the measurement setup is depicted in Figure 6.9.

The sample (as shown in the right panel of Figure 6.9) is glued and wire-bonded to a PCB that is thermally anchored to a copper finger. This assembly is inserted into a cylindrical enclosure machined from a single block of aluminum to provide magnetic screening and further enclosed within a CryoPhy® shield similarly to the MMB-TD setup described.

Using the simulation framework developed, the flux curves expected from these mea-

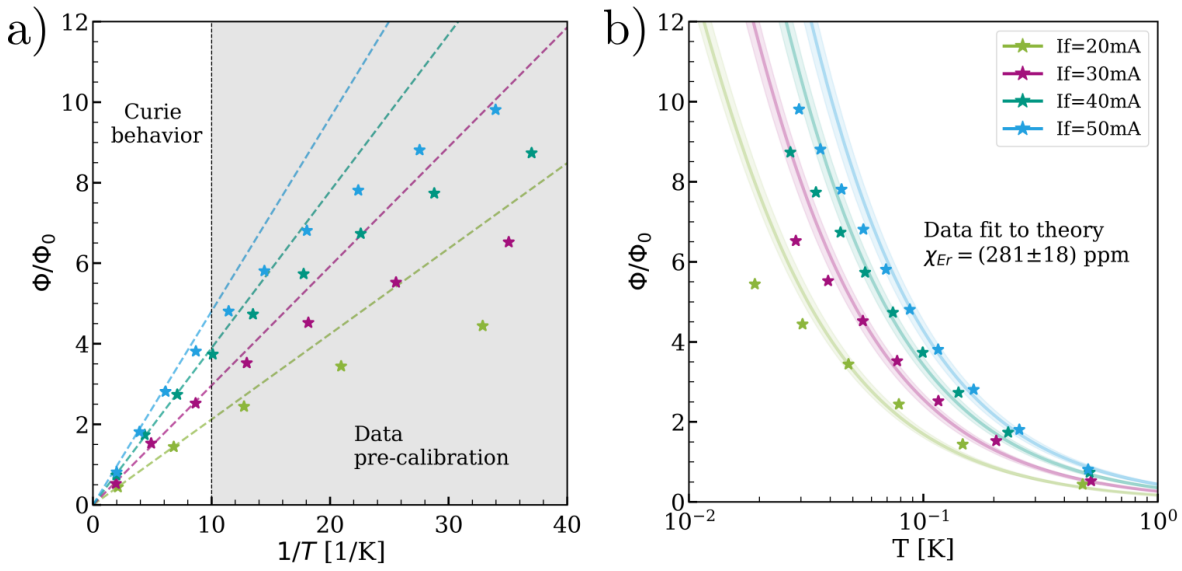

Figure 6.10: Results of the flux signal measurement for chip MT01. **a)** The flux offset is determined by fitting a straight line in the inverse temperature space corresponding to the almost Curie behavior of Au:Er above 100 mK. Data points in gray-shaded region do not follow this behavior and are thus ignored in the pre-calibration step. **b)** The pre-calibrated data is then fitted with the simulated flux signal with the erbium concentration as a free parameter.

surements are calculated. The erbium concentration is used as a free parameter to find the value that best fits the measured flux variation in the front-end SQUID. Data pre-calibration is first performed by adjusting the vertical offset of the measured flux to follow Curie-law behavior in the high-temperature limit. The data pre-calibration step and the theoretical fit for the MT01 chip are presented in Figure 6.10.

The erbium concentration obtained was (281 ± 18) ppm. This value is significantly lower than expected. A strong reduction in the signal amplitude prevented the fitting algorithm from determining the correct erbium concentration of the sample, which we knew beforehand should be around 1000 ppm. Additional measurements were used to extract the erbium concentration of the target and used to estimate the signal degradation observed.

Production of chips with an improved design was not possible at the time, so two additional measurements performed on half-gradiometers of similar detector topology were used to contrast the measured values of MT01. These measurements did present a predictable signal amplitude with the developed framework and helped determine the erbium concentration of the Au:Er alloy used. The used chips are modified MMC detectors developed by IMS for a different project. The results from these measurements are presented in Figure 6.11 (a). To further validate the theoretical model, an additional measurement was performed using a detector based on an Ag:Er sensor. This test served to evaluate the consistency and reliability of the simulation framework developed within this thesis. The results of the Ag:Er measurement are shown in Figure 6.11 (b). The Ag:Er target

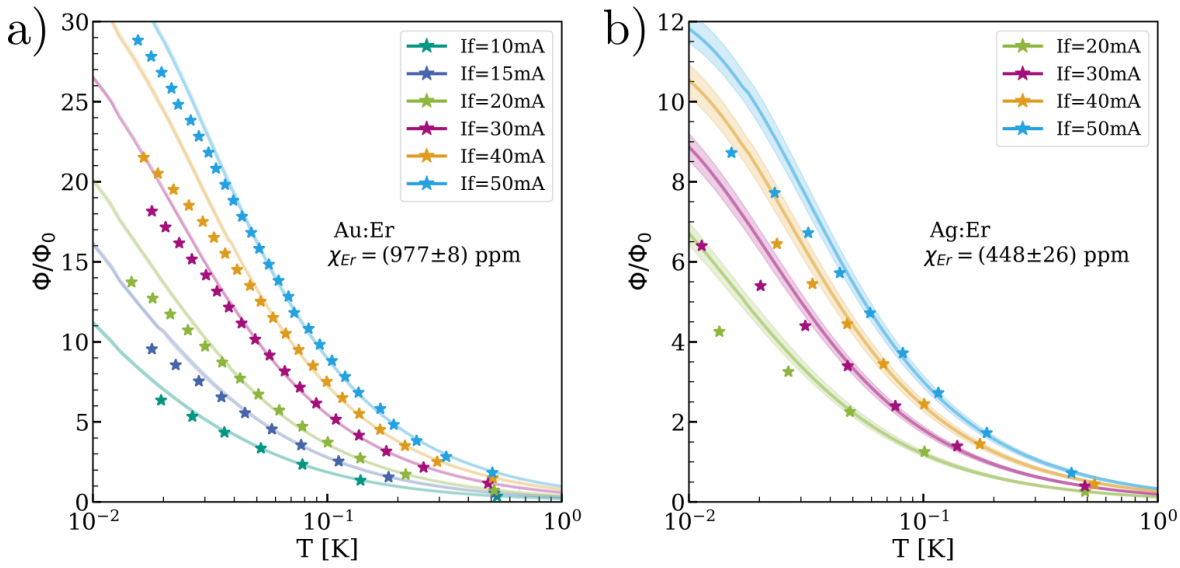

Figure 6.11: Flux measurement performed in the modified MMC detector chips. **a)** With the Au:Er sensor material, yielding an erbium concentration of (977 ± 8) ppm. **b)** With an Ag:Er sensor material with an estimated erbium conceration of (448 ± 26) ppm. The increased uncertainty in the latter measurement is related to the lower signal amplitude and fewer effective data points available due to the lower amount of Φ_0 of flux variation in the SQUID. Both detectors with different sensor materials were correctly measured and fitted with the simulation scripts developed within this thesis.

used for this variant was extensively used in the production of MMC detectors for years, and it is known to have an erbium concentration of roughly 450 ppm.

In the final set of measurements, the model fits exhibit a noticeable drift between the predicted and the actual detector response at the lowest temperatures. A plausible explanation for this discrepancy is thermal decoupling of the detector from the mixing chamber as the system approaches base temperature. This thermal decoupling arises primarily due to the dynamic nature of the measurement method: flux readings are acquired continuously during the cooldown, without allowing the system to reach thermal equilibrium at each step. Above approximately 60 mK, this non-equilibrium condition is less critical, as the thermal conductance between the sensor and the mixing chamber, provided by the copper finger on which the sample is mounted, is sufficient to maintain temperature tracking. However, below this threshold, the thermal conductivity of the copper decreases significantly due to the reduced activity of conduction electrons, which dominate heat transport in metals at cryogenic temperatures. As a result, the actual sensor temperature (T_S) deviates from the measured mixing chamber temperature (T_{MXC}) which is recorded by a thermometer located some distance away from the sensor within the mixing chamber. This thermal lag introduces systematic errors in the magnetization reconstruction at low temperatures. The relationship between T_S and T_{MXC} is analyzed with a heat transport model describing the thermal decoupling behavior and is given by:

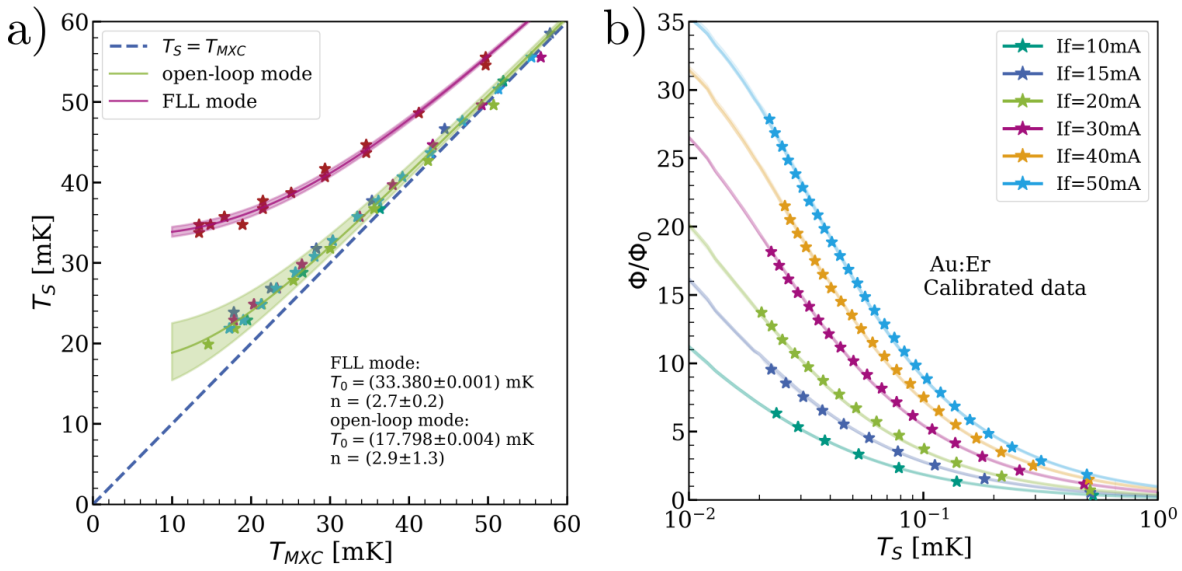

Figure 6.12: Thermal calibration of the magnetization data. **a)** Actual sensor temperature T_S as a function of cryostat temperature, T_{MXC}. The previous magnetization fit is used to extract the T_S values. The plot also includes the thermal decoupling model applied to an FLL measurement performed on the same sample. **b)** Magnetization plot with calibrated temperatures below 60 mK.

$$T_S = \left((T_{MXC})^n + (P/K)^n\right)^{1/n}, \tag{6.5}$$

where P is the heat load on the sensor, primarily due to the SQUID bias current and radiative coupling, K is the thermal conductance prefactor of the link (e.g., the copper finger), n is a temperature exponent characterizing the thermal transport (typically between 2 and 4 for electronic or phononic heat transport, respectively).

Equation 6.5 illustrates why operating the SQUID amplifier in FLL mode with the feedback signal connected to the front-end SQUID degrades measurement performance. In such configurations, the SQUID dissipates a higher bias power P which, according to the thermal decoupling model, leads to a significant increase in the sensor temperature drift. By contrast, the method used during this characterization, in which the front-end SQUID is operated in open-loop mode with a bias current substantially lower than that of the optimum operating point, minimizes power dissipation, reducing parasitic heating on the sensor and preserving the accuracy of the magnetization measurements. $T_0 = P/K$ represents the minimum achievable temperature at the sensor. The outcome of the low-temperature calibration procedure is illustrated in Figure 6.12. The thermal decoupling evidenced when performing the measurement in FLL mode with the feedback signal fed to the front-end SQUID is also presented for comparison. A reduction in T_0 from 33.38 mK down to 17.8 mK is achieved with the method used.

While this calibration is not strictly necessary for determining the erbium concentration in the sensor material, it provides valuable correction data that can enhance the fidelity of temperature readings under dynamic conditions. Moreover, by performing this

calibration, half-gradiometer setups, such as those used in these measurements, can serve as in-situ thermometers. When placed near active detector chips, they can be used to correct the cryostat's temperature readouts and yield more accurate estimates of the true sensor temperature inside the sample holders. This capability is particularly important in experiments where thermal gradients or decoupling effects may introduce significant systematic uncertainties.

6.7 Released Au:Er sensor in the MMB-TD

Temperature-flux ($\Phi(T)$) curves were extracted from both released and non-released MMBs within the same substrate to determine the erbium concentration in the sensor material and to obtain a flux gain calibration curve, to characterize detector performance in a subsequent step. Under these conditions, the flux through the SQUID was expected to vary with temperature, as predicted by theory and verified by previous measurements using a similar procedure, shown in Figures 6.10, 6.11, and 6.12. The results indicated that there is an apparent lack of magnetization of the sensor which was unexpected, as there was no prior indication that the Au:Er sensor would fail to exhibit a measurable magnetic response.

The fabricated and measured samples featured both released and non-released MMB detectors, and in both cases failed to exhibit a measurable flux signal. Therefore, excessive parasitic heating leading to partial detachment of the Au:Er sensors in released MMB don't account for the absence of magnetization on their own. While the specific mechanism remains unidentified, possible effects are currently being considered to explain it. One hypothesis is that chemical modification of the Au:Er sensor may occur during the membrane release process, particularly due to exposure to reactive fluorine ions generated during RIE or XeF_2 etching. While the sensor is nominally protected by a thick photoresist layer (AZ® 4562) during the process, it is conceivable that the small fluorine radicals could penetrate or diffuse through the resist, resulting in chemical alterations of the underlying alloy. Another possible source of degradation is contamination or thermal alteration during the O_2 plasma ashing step. In addition to significantly heating the sample, this process may also chemically modify the sensor material. In particular, the formation of erbium oxides is a plausible mechanism for the suppression of paramagnetism, as oxidation can disrupt the magnetic moment of erbium atoms within the alloy. These effects, if present, could contribute to the observed loss of magnetization in both released and non-released devices.

Sensor compatibility with XeF_2-based release techniques

To test these hypotheses, a preliminary evaluation of the possible causes for signal degradation was carried out with the MT02 device chip. This sample was measured and subjected to each step of the MMB release process in order to emulate the conditions experienced by the bolometer chips during fabrication. The $\Phi(T)$ curves were measured to establish a baseline for comparison, allowing us to quantify any subsequent signal degradation. The release steps were then applied in reverse order to isolate the impact of each

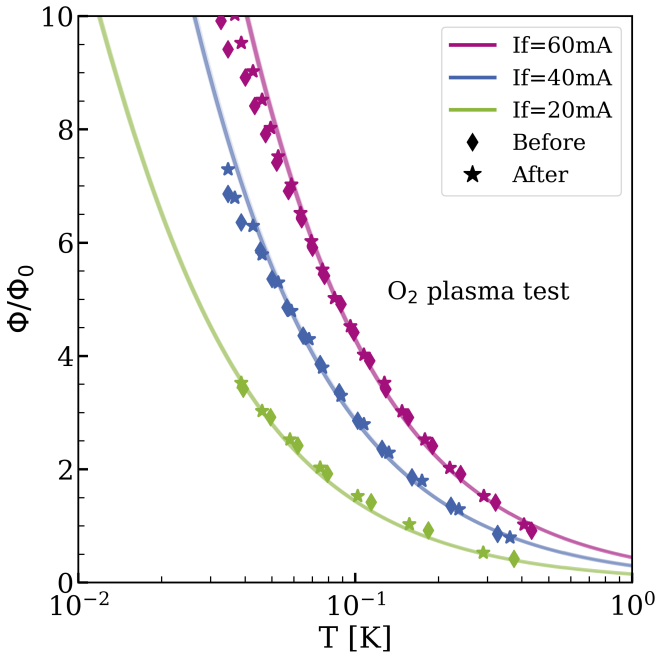

Figure 6.13: Flux measurement of the MT02 device chip before and after being exposed to the O_2 plasma. Theoretical curves are built from the obtained best-fit erbium concentrations in each case. Three representative curves are shown for each measurement, the legend shows the forward current utilized for the injection in each case.

process individually and to determine whether the observed suppression of magnetization in the fabricated sensors arises from a single step or from a combination of process effects.

For each test, various persistent currents were injected,e and the flux change within the temperature range of 500 mK down to 30 mK was recorded. The measurements were fitted to theory to extract a reference erbium concentration to which to compare between measurements. Variations in the fitted concentration after each etching step can hint towards the likely source of signal degradation in the MMB. The baseline reference erbium concentration obtained was: (280.39 ± 3.97) ppm.

O_2 plasma

After the initial measurement, the chip was removed from the sample holder and placed in the O_2 plasma ashing machine without photoresist. The chip was exposed to the plasma for a total duration of 15 minutes. The measurement results after this step are shown in Figure 6.13. The comparison with the previously obtained flux curves reveals no clear signal degradation. The erbium concentration extracted after the O_2 plasma exposure and analysis was: (278.16 ± 4.13) ppm. From this result, a contribution of the O_2 plasma ashing step, used for photoresist removal, to the signal degradation observed in the MMB can be mostly ruled out. Consequently, this process was adopted for photoresist removal in subsequent tests.

XeF_2 gas exposure

The XeF_2 evaluation test was carried out by fully covering the chip with AZ® 4562 positive-tone photoresist. Without patterning, the photoresist was developed using AZ® MiF 2026 developer. The exact same spin-coating parameters and development processes

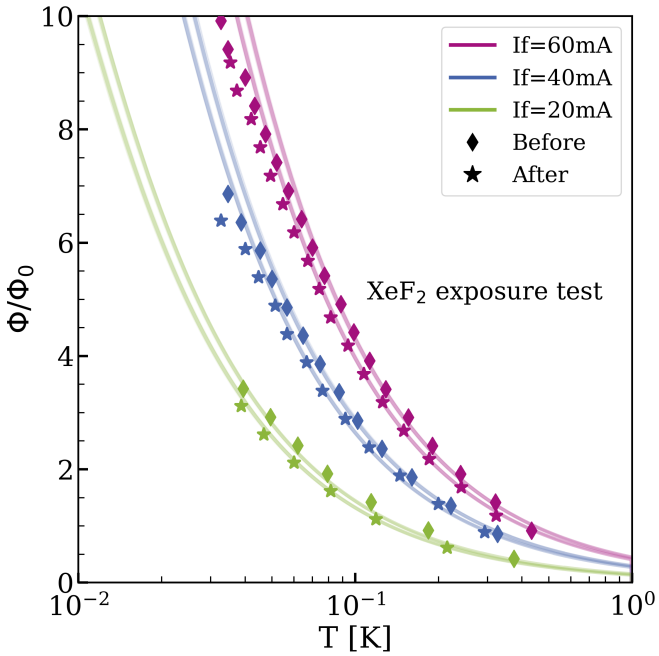

Figure 6.14: Flux measurement of the MT02 device chip before and after being exposed to the XeF_2 etching step for detector release, showing a subtle signal degradation compared to the baseline reference.

used in MMB fabrication were replicated. 15 XeF_2 etching steps were performed on the fully coated sample. To ensure comparable exposure conditions, the device was placed in proximity to a small broken silicon substrate, so that the XeF_2 gas would react with a similar amount of exposed silicon as in the actual fabrication process, and as close as possible to the Au:Er sensor. After etching, the photoresist was removed in the O_2 plasma ashing machine, with the chip exposed to plasma for a total duration of one hour.

Flux curves obtained after this process are shown in Figure 6.14. The fitted erbium concentration was (256.24 ± 4.31) ppm. This result reveals a non-negligible signal decrease of 8.61 %. During MMB fabrication, the Au:Er sensor is protected from direct XeF_2 exposure, being covered from above by photoresist and from below by silicon nitride and a thermal oxide layer. Although the XeF_2 reaction with silicon can generate a substantial localized temperature increase, in principle no chemical modification of the sensor material should occur. Nevertheless, the observed decrease in signal indicates that this step may introduce secondary effects and therefore demands further investigation.

Chapter 7

Summary and Outlook

The MMB, a novel bolometer for CMB polarization survey based on paramagnetic temperature sensors, was proposed throughout this thesis and the fabrication pathway and preliminary characterization of the prototypes was described in detail. In this last chapter of my dissertation I introduce final remarks and considerations that will be the basis of future research in MMB development.

The theoretical study of the MMB revealed a promising forecast. A set of optimized parameters was identified that enables BLIP of the sky using the current QUBIC Technical Demonstrator design as reference. The analysis indicated that erbium excess noise is the primary contributor to signal degradation at lower frequencies in MMB detectors. The use of Ag:Er as the sensor material reduces this noise contribution considerably, and in addition, two methods can be employed to further reduce it further, these are:

- Extending the suspending legs to decrease the thermal conductance (G_{bath}),
- Increasing the bias field current to enhance the MMB's responsivity.

Both approaches are subject to technological limitations. Longer suspending legs may compromise the mechanical integrity of the detector, while higher bias currents are constrained by the critical current of the superconductors used in the biasing circuit. In addition, lowering the cryostat bath temperature was identified as a particularly effective strategy for enhancing MMB performance. A reduced bath temperature simultaneously lowers phonon-induced thermal fluctuation noise and increases responsivity, as the temperature dependence of the magnetization becomes steeper. Key considerations for implementing MMB technology in CMB polarimetry include:

- Increasing the critical current of the biasing circuit.
- Minimizing the bath temperature of the instrument.

The path from a theoretical proposal to the implementation of a physical device was explored. The fabrication process of the MMB-TD is presented, including the deposition conditions for each layer, along with relevant design considerations and process optimizations. These early fabrication efforts have laid the groundwork for the development of a more refined and capable generation of MMB devices. As with any new detector concept, the first iterations did not fully realize the potential of the technology due to the

limited knowledge available at the time. However, knowledge gained during this initial development revealed a path towards future improvements.

In the first prototypes, the deposition conditions for the initial Nb layer were chosen to provide a reliable and predictable baseline, ensuring adequate insulation and manageable stress levels compatible with the MMB release process. Moving forward, optimizing deposition conditions to improve superconducting properties, such as increasing the critical current and residual resistivity ratio (RRR), will be crucial. This can be achieved by incorporating substrate heating during sputtering, which was not available during the MMB-TD development but would significantly enhance film quality and superconducting performance.

Planarization capabilities such as chemical-mechanical polishing (CMP) would enable the use of thicker Nb films for the pickup coils without compromising the magnetic coupling to the sensor and allowing larger bias field currents. The combined stress of thicker superconducting and dielectric layers should characterized to ensure that the mechanical integrity of the released device is preserved. In addition to planarization, future processes should integrate tailored RIE etching of the insulation layer to control via sidewall profiles, to enable high-quality multilayer circuit fabrication. These advancements will be vital for scaling to large detector arrays, where multilayer interconnects are necessary.

The development of a dedicated Ag:Er sputtering target with optimized deposition parameters for the MMB substrate is a priority. This target has not yet been tested, as it is awaiting final processing step, which is the melting and conditioning in the 3-inch graphite mold. The characterization of a reproducible process for Ag:Er deposition will be an essential step toward realizing fully functional, application-ready MMB detectors.

A reliable release technique was developed which is the final fabrication step of the MMB. This process is based on bulk dry silicon etching using xenon difluride (XeF_2). As part of this thesis, a controlled-pulse etching system was designed, built, tested and optimized in-house for its use in MMB detector production.

Fabrication of the MMB-TD with the described methods is straightforward and reliable. Nuances related to the design and implementation were noted and key items which are worth investigating were identified. In future iterations, these methods will allow to produce full CMB pixels based on paramagnetic temperature sensors.

Despite successful fabrication and assembly of the MMB-TD, no measurable flux signal was observed in the first porototypes. A range of potential mechanisms for this suppression were identified, including chemical modification of the sensor material during fabrication. Preliminary tests were conducted on conventional MMC-type devices to evaluate the effect of the membrane release required for MMB fabrication on the sensor material. The results are not fully conclusive yet but a measurable signal degradation was observed after an emulated XeF_2 etching step and will require further investigation. Localized mechanical deformation observed in released devices also suggests the need for an optimized deposition process that reduces intrinsic film stress during fabrication. A case of thermal runaway breakdown was observed, offering important insight into operational stability limits of the device under test conditions. Taken together, these findings highlight critical areas for further investigation and refinement in the MMB fabrication process and provide a foundation for future iterations of this promising detector.

List of Figures

1.1 **a)** ILC map of the CMB produced by the WMAP survey with a nine-year observation dataset. **b)** CMB temperature auto-correlation power spectrum expressed as $\ell(\ell+1)C_\ell^{\mathrm{TT}}/2\pi$ obtained from the ILC CMB map. The plot also includes error bars in black and a best-model fit in red [7]. 2

1.2 **a)** Temperature anisotropy map of the CMB. **b)** Polarization field superimposed on the temperature map smoothed for visibility purposes. Both maps were extracted and published by the Planck Collaboration [14]. . . 3

1.3 Rms Brightness temperature as a function of frequency of the CMB and foreground contribution signals for temperature (**a**) and polarization (**b**). The gray-shaded regions correspond to the multiple spectral bands observed by the Planck Satellite Mission (PLANCK) to perform foreground extraction [27]. 4

1.4 **a)** Observed B-mode power spectrum reported by finished CMB experiments. **b)** Current bounds of the B-mode signal. The plots contain dashed traces showing the theoretical curves for a ΛCDM model with $r = 0.1$ (black) and $r = 0.01$ (blue) as well as the lensing B-mode spectrum, the sum of both spectra is shown in solid trace [28]. 5

1.5 Antenna-coupled bolometer architecture investigated in this thesis for the development of the MMB detector concept. Incoming radiation is coupled to a broadband antenna, in-line band-pass filters define the observation bands of the instrument and the filtered signals are measured with MMB detectors. The detectors are readout by a SQUID-based readout system. 9

2.1 Surface inductance of superconducting niobium at $T = 300\,\mathrm{mK}$. The superconducting properties used to create the plot are $\Delta(0) = 1.76\,k_B\,T_c$, $\xi_0 = 39\,\mathrm{nm}$, and $l = 33\,\mathrm{nm}$ [88]. The critical temperature (T_c) was set to $8.9\,\mathrm{K}$ (orange) and $9.25\,\mathrm{K}$ (purple), to account for sample variability during fabrication. The shaded regions in the plot correspond to the observation bands considered in the pixel design for the QUBIC instrument. 12

2.2 Estimated attenuation term associated with dielectric losses for our $Nb/SiO_2/Nb$ microstrip transmission lines as a function of frequency assuming $\tan\delta = 1\times10^{-3}$. Green and blue shaded regions represent QUBIC observation bands. 13

2.3 Antenna geometries designed for the multichroic detector pixel with their respective design parameters. **a)**: Sinuous antenna with a self-complimentary design ($\alpha = \pi/4$ and $\delta = \pi/8$). **b)**: Logarithmic spiral antenna also with a self-complimentary design ($\delta = \pi/8$). 15

2.4 **a)** Simulated radiation lobe of the log-spiral antenna, including the extended hemispherical lens. **b)** Side-view sketch of the resulting structure with the radiation lobes for various lens radii (R_{lens}). 16

2.5 Relectance at the vacuum-silicon interface of the coupling lenses with increasing number of anti reflection coatings. The reflection considering the AR coatings with the materials used in SPT-3G [101] focal plane are also shown. The observation bands at 150 GHz and 220 GHz with 25 % fractional bandwidth are also shown in green and blue shaded regions, respectively. 18

2.6 Smith charts displaying simulated Γ curves of **a)** the sinuous antenna and **b)** the log-spiral antenna. Both Smith charts are normalized to an impedance $Z_0 = 50\,\Omega$. Γ is shown as a solid blue trace within the bandwidth of interest. The frequency-independent values of Γ for each antenna calculated with the Booker-Babinet equations are also displayed with a purple star. 19

2.7 Simulated Z_{in} of **a)** the sinuous antenna and **b)** the log-spiral antenna. The real (blue) and imaginary (green) parts of Z_{in} are displayed. The frequency-independent value calculated with Booker-Babinet equations is also shown for each antenna with dashed purple traces. 20

2.8 **a)** Different impedance profiles following linear, exponential, Klopfenstein and Dolph-Chebyshev profiles used to compute the impedance of the short line sections in the theoretical taper model. **b)** The modulus of the resulting transmission coefficient $|S_{21}|$ and reflection coefficient $|S_{11}|$ are shown in solid and dashed traces, respectively. 22

2.9 **a)** Impedance and width profiles for the Dolph-Chevyshev taper design. **b)** Design of the taper for the sinuous antenna, the path of the taper is designed to follow the antenna's arms. **c)** Comparison of the theoretical analysis of the taper and EM simulations for the basic straight and final sinuous design. The resulting transmission coefficient S_{21} is shown in solid trace and reflection coefficient S_{11} in dashed traces for each case. 24

2.10 Tubular circuit topology implemented for the in-line band-defining filters. 25

2.11 **a)** Schematic of the inductive CPW line. **b)** Design layout design for the inductor, the dark gray sections represent the groundplane while the lighter gray areas represent the stepped-impedance transmission lines. **c)** Optimized length values for the inductors appearing in the band-pass filters for the 150 GHz and 220 GHz bands at their respective central frequencies. 26

2.12 **a)** Schematic of the capacitive π-network. **b)** Design layout of capacitive π-network, the dark gray sections represent the groundplane while the lighter gray areas represent the stepped-impedance transmission lines. **c)** Capacitor length values adjusted for the 150 GHz and 220 GHz bands at their respective central frequencies. 27

2.13 $|S_{21}|$ parameter of the 150 GHz (**a**) and 220 GHz (**b**) band-pass filters. The green trace represents the theoretical response of the filters, as calculated using discrete circuit components in LTSpice. The purple trace corresponds to the EM simulations performed with SONNET® after optimization. 27

2.14 Ladder-type circuit implemented in the physical realization of the 300 GHz low-pass filters. 28

2.15 Diplexer network design including low-pass filters for off-band resonance attenuation. The physical design and equivalent circuits are shown. . . . 28

2.16 Diplexer scattering parameters illustrating the response of the diplexer network. The scattering parameters of the diplexer are depicted in dashed traces, and the scattering parameters accounting for the inclusion of the low-pass filters is shown in solid traces. Additionally, the atmospheric opacity calculated for the conditions at the QUBIC site is displayed. . . . 29

2.17 Signal flow graph illustrating the proposed dual-band radiation coupling, depicting the connections between the millimeter-wave components involved in the pixel. 31

2.18 Optical efficiency results of the sinuous antenna pixel **(a)** and the log-spiral antenna pixel **(b)**. The analysis takes $\mathfrak{O}_{\text{eff}}(f)$ for the 150 GHz (green) and 220 GHz (blue) bands and compares it to the brick-wall-type ideal diplexer. The comparison, expressed as percentage for each case, represents the ratio between the intersecting area and the total target area for each band. The results are calculated for the case of no AR coatings and the three-layer AR coating developed for the SPT-3G focal plane [101]. 32

3.1 **a)** Thermal model of the MMB detector relating the thermal components described in the text. **b)** Electrical circuit analog used to describe the thermodynamic behavior of the detector. Noise sources representing thermodynamic energy fluctuations between different detector sub-systems are included in parallel to each thermal link. 39

3.2 Representation of an Au:Er or Ag:Er sample volume from one Monte Carlo iteration. The number of Er^{3+} ions determines the cubic fcc lattice size needed to simulate the desired erbium concentration. 43

3.3 Results of the Monte Carlo-based calculation of the specific heat (**a**) and magnetization (**b**) for an Au:Er sample with an Er concentration of $x_{Er} \approx$ 492 ppm, placed in a 10 mT magnetic field. The black solid line represents the mean values, while the soft light blue traces indicate the mean values over 10 iterations (thus 217 blue traces are visible in these plots). Magnetization curves plotted with a logarithmic temperature scale, providing uniform representation below 1 K; this representation is chosen since MMBs operate at higher temperatures than MMC detectors. 44

3.4 Scaling laws applied to simulations conducted with varying erbium concentrations. The results are adjusted to a final concentration of 300 ppm and correspond to an external magnetic field of 10 mT. 45

3.5 Results of our Monte-Carlo method based calculation of the specific heat (**a**) and magnetization (**b**) of a Au:Er sample with a concentration $x_{Er} \approx$ 300ppm biased with various magnetic fields. Solid lines represent the simulation results, and the data points are taken from measurements presented in [129]. 45

3.6 **a)** Meander-shaped pickup coil design used in the MMB. **b)** Side-view of the meander-shaped pickup coil with the paramagnetic sensor placed on top. **c)** Representation of the pickup coil coupled to the sensor in schematic circuits. **d)** Calculated magnetic field distribution when a field current of $I_{\text{field}} = 50\,\text{mA}$ flows through the inductor considering periodic boundary conditions. The meander-shaped pickup coil has a line width of $w = 2.5\,\mu\text{m}$ and a pitch of $p = 5\,\mu\text{m}$. 47

3.7 **a)** InductEx external field rejection simulation for the self-symmetric meander-shaped pickup coil. **b)** Simulation performed with a regular meander-shaped inductor, removing the redundant return line. 48

3.8 Schematic circuit of the MMB-based CMB detector pixel developed within this thesis. Incoming optical power (P_{opt}) is coupled by the radiation coupling circuit and guided towards a termination resistor. The resistor and the paramagnetic sensor, coupled to the pickup coil (L_{m}), constitute the MMB which is placed on a released dielectric membrane that provides a weak thermal coupling to the heat bath (low G_{bath}). The schematic also shows the bias circuit consisting of a load inductor (L_{load}) and the persistent current switch. The switch consists of a resistive heater placed on top of a Nb wire with inductance L_{sw}. The switch is operated by a current pulse delivered to the I_{H} leads. A current applied to leads $\pm I_{\text{F}}$ while the switch is operated will trap flux in the pickup coil, biasing the paramagnetic sensor. The current change produced in the pickup coil upon variation of the sensor magnetization is read out by a SQUID. There also exists a parasitic inductance (L_{stray}) in the connection to its input coil (L_{in}). 48

3.9 Schematic representation of the different steps during persistent current injection. **1)** Prior to the injection, the initial magnetic flux threading all closed superconducting loops is considered zero. **2)** A forward current I_{F} is applied to the circuit, and is distributed through each superconducting coil such that the total flux is kept constant. **3)** A current pulse is applied to the persistent current switch, opening all superconducting loops and allowing magnetic flux to enter the circuit. The red area represents a hotspot where the circuit presents non-zero resistance. **4)** The forward current I_{F} is turned off, and three persistent currents appear in the circuit, preserving the flux trapped during the injection. 50

3.10 **a)** Noise contribution diagram showcasing each noise source in the MMB. All these sources contribute to flux noise Φ_{N} threading the readout SQUID. At the input of the detector the photon noise equivalent power, NEP_{γ}, is introduced. **b)** All noise sources are referred to the input and regarded as a single intrinsic detector noise equivalent power ($\mathrm{NEP}_{\mathrm{det}}$). 51

3.11 Detailed view of the MMB detector. The coupled and filtered CMB signal is guided via microstrip transmission lines and fed to the termination resistor thermally anchored to the paramagnetic sensor. The sensor is magnetically coupled to the superconducting meander-shaped pickup coil that bias and readsout the temperature-dependent magnetization. These components are placed on a rectangular dielectric island, held in place by four dielectric legs. The length of the legs determines the effective heat conductance to the thermal bath (G_{bath}). The leg-isolated dielectric island is defined by the rectangular openings represented in green. 53

3.12 NEP and flux noise (Φ_N) of the different MMB noise contributions compared to the estimated background noise in the QUBIC technical demonstrator instrument. Dashed traces represent individual contributions to the MMB noise, highlighting their relative significance. 55

3.13 NEP_{γ} and $\mathrm{NEP}_{\mathrm{det}}$ for each optimization parameter. In the legend for each plot the detector response time (τ) is given for each parameter value in milliseconds. **a)** Leg length. **b)** Sensor thickness. **c)** Erbium concentration (x_{Er}). **d)** Bias field currents (I_{field}). The bath temperature is fixed at $T_{\mathrm{bath}} = 320\,\mathrm{mK}$. Each parameter is varied while keeping the others at their obtained optimal values indicated in each legend. 56

3.14 **a)** Detector noise equivalent power when lowering the bath temperature from 320 mK to 100 mK while keeping all other parameters constant relative to the estimated background NEP. The noise comparison in terms of (**a**) NEP and (**b**) flux noise (Φ_N) threading the readout SQUID are also presented at a fixed temperature of 100 mK representing individual contributions to the MMB noise in dashed traces. 58

3.15 **a)** MMB-TD prototype schematic diagram. **b)** Layout design of the MMB-TD prototype. Three currents are fed to this device (I_{F}) is the bias field current (I_{H}) drives the persistent current switch and a third current is driven to the termination resistor (I_{R}) in contact with the paramagnetic sensor to extract the MMB-TD response characteristics. The output signals ($\pm I_{\mathrm{SQ}}$) are measured with a SQUID connected to the output on the left via three connection pads for common-mode signal rejection. . . . 60

3.16 Design of the MMB-TD prototypes, the image includes a close-up view of a pair of fabricated MMB devices: One of them is released with 600 μm long legs, and the other is an non-released counterpart. 1) Pre-release dicing marks. 2) Connection pads to the readout SQUID ($\pm I_{\mathrm{SQ}}$). 3) Load Inductor. 4) Persistent current switch. 5) Released MMB. 6) Non-released MMB. 7) Persistent current switch pads (I_{H}). 8) Input signal pads (I_{R}). 9) Persistent current injection pads (I_{F}). 60

3.17 Microscope picture, layout design and zoomed-in view of a finished MMB detector. The island in the center holds the pickup coil, the paramagnetic sensor, and the termination resistor and four dielectric legs hold the island in place. Along the legs, the pickup coil lines carrying the persistent bias field current (I_{field}), one of the persistent current injection lines (I_{F}), and the termination resistor lines (I_{R}) are placed. 61

3.18 Microscope picture and layout design of the persistent current switch used to inject I_{field}. The connection of three lines connecting the pickup coil, the load inductor and the readout SQUID is placed directly underneath a resistor. A thin insulating layer separates the resistor from the superconducting line, and two additional lines are used to drive the switch pulse current (I_{H}). 61

4.1 Intrinsic stress ($\sigma(x)$) curves of Nb films obtained for multiple sputtering pressures using the method described in the text. Negative values correspond to compressive stress, while positive values indicate tensile stress. Stable values of $\sigma(x)$ are observed in the central region of each sample (between dashed black traces). 67

4.2 $I_{\mathrm{c}}(T)$ measurements of Nb films deposited with $P_{\mathrm{Ar}} = 3\,\mu$Bar in red and $P_{\mathrm{Ar}} = 11\,\mu$Bar in green. 70

4.3 **a)** Non-released meander-shaped pickup coil. **b)** Similar Nb pickup coil standing on a released dielectric membrane. 70

4.4 $I_{\mathrm{c}}(T)$ measurements comparing Nb straight lines with released and non-released meander-shaped pickup coils. 71

4.5 Colorized SEM picture of an FIB cut performed on one Nb/Nb via connection featuring the interface between both Nb layers. The two Nb layers showcase a subtle and almost undistinguishable black trace at the interface. A zoomed-in view of the area marks where the Nb/Nb interface should be. 73

4.6 **a)** Effect of the lift-off flaps at the edges of the via connections. For clarity, two SiO_2 depositions took place and the picture is showing only the top-most step of the Nb2 layer in the connection. **b)** FIB cut of the Nb/Al/Nb window-type Jossephson junction. 74
4.7 **a)** FIB cut on a persistent current switch. This image illustrates the fracture in the crystalline lattice of the second Nb layer (Nb2) when deposited on an uneven surface. **b)** Sketch offering an explanation for the formation of this fracture. During the sputtering deposition, the film is grown at different heights, and when the layer of the growing lower film encounters the already deposited first layers of the upper film, the Nb structures don't merge, producing an edge defect grain boundary. 75
4.8 **a)** Magnetic field distribution inside the sensor material using a non-planarized pickup coil. **b)** Magnetic field distribution using a planarized pickup coil. In these simulations the same geometric parameters are used, namely a pitch of $p = 5\,\mu$m and linewidth of $w = 2.5\,\mu$m, and thickness of $t = 250\,$nm. The sensor is $1\,\mu$m thick in both cases. Assuming the same circulating current (50 mA), the mean magnetic field in each case is also specified. 76
4.9 **a)** Self-planarization process involving anisotropic deposition of a silicon oxide insulating layer to fill the gaps between the meander-shaped pickup coils. **b)** Profile measurements illustrating the outcome of the process. The green trace represents the surface profile of the Nb structures without planarization, while the purple trace corresponds to a similar sample after undergoing the process. The height steps are significantly reduced, from 200 nm (Nb structures) to just 20 nm to 30 nm, indicating a much more planar surface. 77
4.10 **a)** Colorized SEM image of a cross-sectional cut performed with FIB, showing a pickup coil and sensor dummy. Nb lines are highlighted in green, the sensor dummy is colorized yellow, and the platinum ruler used for the FIB cut is highlighted in purple. **b)** High-resolution SEM image of the same structure, revealing artifacts at the edges of a pickup coil lines. 78
4.11 **a)** Anodization current and voltage as a function of time during the first 15 minutes of the process. **b)** Surface profile comparison between a planarized Nb structure before and after anodization. A thickness of 48.51 nm is attributed to the oxide coating. 79
4.12 On-state resistance of the Nb trace underneath the AuPd switch resistor as a function of I_F (**a**) and as a function of I_H (**b**). A horizontal dashed trace represents a resistance value of $0.2\,\Omega$ at which the switch is considered activated (on-state). The latching condition is portrayed on the left plot in which the product of I_F and the on-state resistance exceeds the latching power threshold. 80
4.13 Magnetization measurement of an Ag:Er pill fragment used for estimation of the Er concentration. A best-fit to the measurement yields a concentration of 5702.9 ppm. The best-fit curve is shown in green trace. 82

4.14 PTFE sample holder and etching system developed for testing crystal-oriented membrane release using KOH. **a)** Cross-sectional view of the sample holder, illustrating how the front side of the substrate is exposed to the etchant while the edges and backside are sealed with O-rings. Twelve nylon screws and nuts are used to press the caps together, ensuring uniform sealing pressure. **b)** Front view of the holder with a blank silicon substrate placed inside. **c)** Complete etching setup, including the PTFE container, thermometer, a pressure line for stirring the KOH solution, and a water-cooled glass condenser. **d)** and **e)** show the chip before and after the etching process, respectively. 85

4.15 KOH-based process. (1) Photolithography to define the shape of the membrane, (2) RIE etching exposes the silicon to be etched. (3) Removal of the photorresist. (4) The substrate placed in the PTFE sample holder is etched with the KOH solution. The process can be interrupted and resumed multiple times to periodically check if the structures are fully released. 85

4.16 **a)** Design layout to test the KOH-based release technique. 1) Spyder-type structures with legs at 45 degree angle of various lengths. 2) H-type structures 45 dgree legs of various lengths. 2) Cantilever structures for a qualitative stress determination of the released dielectric membrane. **b)** Pictures of the process steps results in a cantilever structure. **c)** Process step results in 45-degree angle h-shaped membrane. The numbers in the pictures correspond to the result of the process step in each case. 87

4.17 Stylus profiler measurement of an etched sample with the KOH solution. An $84\,\mu$m etched depth was measured and an $\approx 54.7^\circ$ angle was determined for the sidewall corresponding to the $\langle 111 \rangle$ crystal orientation expected in $\langle 100 \rangle$ crystal-oriented substrates used (in this depitcion x and y axes are not equally scaled, so the apparent angle looks different than in reality). 88

4.18 **a)** Phase diagram constructed from vapor pressure and triple point measurements of XeF_2 [167]. **b)** Measured pressure curves in the expansion chamber (violet trace) and process chamber (green) during the pulsed-controlled etching of silicon in the custom-built XeF_2 etching system developed. 90

4.19 **a)** Schematic design of the XeF_2 etching system. **b)** CAD model with the physical layout and placement of the system's components. 1) N_2 gas inlet. 2) Process chamber venting valve. 3) Expansion chamber venting valve. 4) XeF_2 gas valve. 5) Expansion chamber gas inlet valve. 6) XeF_2 reservoir. 7) Interconnect valve between the expansion and process chambers. 8) Expansion chamber. 9) Expansion chamber vacuum valve. 10) Process chamber. 11) Process chamber vacuum valve. 12) Mechanical vacuum pump. 91

4.20 Pictures of the finsihed XeF_2 etching system. **a)** Front-view (user side) of the machine. **b)** Back-view (service side) of the machine showing the electronic control system enclosed in a sealed backpack. **c)** Close-view of the main process chamber. 1) Main process chamber. 2) Pressure gauges. 3) Temperature control units. 4) Power, intialization and process-stop switches. 5) XeF_2 reservoir. 6) Main, control and heater circuit breakers. 7) PLC control unit. 8) Power supply. 9) Ethernet connection to user PC. 10) Safety magnetic latching contactor. 11) Process gas inlet to the process chamber. 12) Substrate plate standing below the lid showerhead and on top of the main vacuum outlet. 93

4.21 Front-side XeF_2 release process used in the development of the MMB-TD. **1)** Photolithography to define the shape of the membrane, **2)** RIE etching is used to etch the LSiN and thermal oxide layer exposing the silicon substrate. **3)** The BOSCH process is used to etch into the silicon substrate. **4)** The sample is placed in the XeF_2 etching system and etched with several etching cycles. The sample can be observed during the process to determine if the structures are fully released. **6)** Photorresist removal carried out in an O_2 plasma ashing system. 95

4.22 **a)** Layout design used for testing the XeF_2 etching system. 1) Spyder-type structures with legs at 45 degree angle of various lengths. 2) H-type structures 45 dgree legs of various lengths. 2) Cantilever structures for a qualitative stress determination of the released dielectric membrane. 4) Small footprint H-type structures with legs of various lengths. 5) Mesh structures often used for absorber-coupled detectors. **b)** Pictures of the results obtained on some of the tested structures after 15 XeF_2 etching pulses. **c)** Pictures of the results obtained after 25 XeF_2 etching pulses. . 96

4.23 SEM pictures of fully released silicon nitride structures of various shapes and sizes. **a)** H-shaped membranes of various leg lengths spanning from 600 μm to 1100 μm. **b)** Cantilever structures at 90-degree angles featuring an upward bending after the XeF_2-based release process. 97

4.24 **a)** Microscope pictures of the results obtained after each step in the release process during the MMB-TD fabrication. Each step is identified in the corresponding picture. **b)** Picture of a released and non-released MMB taken prior to their low-temperature characterization. 97

5.1 **a)** Illustration of the TransMIT PTC cryostat used for 4 K characterization of superconducting films and components. **b)** Illustration of the Bluefors $^3He/^4He$ dilution refrigerator utilized for characterization at milikelvin temperatures. 100

5.2 **a)** dc-SQUID I-V curve demonstrating its dependence on externally applied magnetic flux, highlighting the behavior at extrema values, $\Phi_{\max} = (n+1/2)\Phi_0$ in green and $\Phi_{\min} = n\Phi_0$ in purple traces. **b)** Voltage response at a constant current bias as a function of the applied magnetic flux, normalized to the magnetic flux quantum Φ_0. The flux-to-voltage gain (V_Φ) of the dc-SQUID corresponds to the slope presented at the working point (marked as a green star). 102

5.3 Two-stage SQUID-based amplifier schematic circuit consisting of the front-end dc-SQUID, the second stage dc-SQUID Array and a simplified schematic of the read-out electronics [185]. The amplifier can operate in AMP (open-loop) mode by bypassing the FLL integrator, or FLL (closed-loop) mode by using the feedback resistors. The feedback signal can be connected either to the front-end SQUID, the SQUID array or both with their respective feedback resistors R_{f} and R_{fX}. 104

5.4 Small-signal block diagram of the two-stage SQUID amplifier used to extract the frequency response. In this diagram the amplifier is configured to operate in FLL mode with the feedback signal connected to the front-end SQUID. A finite loop delay is introduced in the direct forward path and represents the signal lag introduced by the FLL electronics. 105

5.5 **a)** Schematic diagram of the dc-SQUID **b)** Microscope picture of a dc-SQUID designed and developed by IMS used as the front-end SQUID in this thesis for MMB-TD characterization. 107

5.6 **a)** Schematic diagram of a SQUID array. **b)** Microscope picture of the dc-SQUID arrays, designed and developed by IMS, used in this thesis. . . 107

5.7 Noise spectrum of the two-stage SQUID-based amplifier referred to the flux noise in the front-end SQUID. The spectrum was fitted to extract relevant amplifier parameters such as the amplifier bandwidth and overall noise peroformance (shown in light blue dashed trace). An additional low-frequency noise not originally considered in the noise model was observed and fitted with a low-pass first order function (yellow dashed trace) to extract its level and cut off frequency. 108

6.1 Cryogenic setup used for MMB characterization. **a)** The bonded chips are shown. **b)** Sample holder designed and built for this measurement. **c)** Setup installed in the mixing chamber flange of the LD250 refrigerator. 1) MMB-TD chip. 2) Released MMB. 3) Non-released MMB. 4) Front-end dc-SQUID chip. 5) Bias and excitation lines 6) CryoPhy® magnetic shield. 7) Aluminum housing. 8) Sample-holder body with connector PCB. 9) MMB-TD module installed. 10) Similar module containing dc-SQUID arrays required for two-stage SQUID amplification. 112

6.2 Schematic cross-section view of the MMB-TD sample holder. 1) Thermal anchor. 2) Connectors to SQUID arrays and current sources for biasing and excitation. 3) Forward current I_{F}, persistent current switch pulse I_{H} and excitation signal I_{R} wiring. 4) Plastic (ABS) thermal insulation between copper fingers. 5) Front-end SQUID finger. 6) Front-end SQUID chip. 7) MMB-TD chip. 8) MMB device finger. 9) Aluminum housing for magnetic screening. 10) Copper plate to thermalize the aluminum housing. 11) CryoPhy® magnetic shield. 112

6.3 Schematic circuit of an unknown inductance (L_{X}) connected to the front-end SQUID. The noise source arising from the normal conducting wire bonds is represented as a current source in parallel to its resistance R_{bond}. 114

6.4 Noise measurements taken at $T = 1.25\,\mathrm{K}$ to perform each inductance extraction step. The resulting output parameters R_{bond} and L_{X} were obtained by fitting the model described in Equation 6.3. The model fit for each case is plotted over the spectra in black dashed traces. 115

6.5 Persistent current injection stages observed with an oscilloscope. 1) Initial stage of the persistent current injection process. 2) A forward current $I_{\mathrm{F}} = 5\,\mathrm{mA}$ is applied to the circuit. 3) A current pulse (I_{H} pulse) is delivered to the switch, and the trapped flux cancels the flux introduced by I_{F}. 4) After removing I_{F}, the trapped flux remains in the circuit until a subsequent switch pulse is used to reset the detector. 116

6.6 MMB device appearance before and after a cooldown. Bulging of the Au:Er sensor is evident and hints to partial detachment of the sensor material from the released membrane. 117

6.7 Pictures of an MMB before and after thermal runaway breakdown. The Nb lines that carry the persistent current were found broken at a specific point. Additionally, the Au:Er sensor disappeared from above the pickup coil. 119

6.8 Device chip designed and produced to characterize the sensor material. a) Microscope picture and layout design. b) Schematic of the circuit, identifying all components involved. 120

6.9 Magnetization measurement setup. A periodic flux ramp signal is fed to the feedback coil of the front-end SQUID and monitored with an oscilloscope (green trace). The output signal from the SQUID is amplified using a single stage FLL amplifier formed by a SQUID array and the XXF-1 module (purple trace). A vertical cursor (shown in cyan) is positioned on one of the voltage peaks and used as a reference to follow the flux variations in the front-end SQUID as the temperature is swept. A picture of the experimental setup is also shown. 121

6.10 Results of the flux signal measurement for chip MT01. **a)** The flux offset is determined by fitting a straight line in the inverse temperature space corresponding to the almost Curie behavior of Au:Er above 100 mK. Data points in gray-shaded region do not follow this behavior and are thus ignored in the pre-calibration step. **b)** The pre-calibrated data is then fitted with the simulated flux signal with the erbium concentration as a free parameter. 122
6.11 Flux measurement performed in the modified MMC detector chips. **a)** With the Au:Er sensor material, yielding an erbium concentration of (977± 8) ppm. **b)** With an Ag:Er sensor material with an estimated erbium conceration of (448 ± 26) ppm. The increased uncertainty in the latter measurement is related to the lower signal amplitude and fewer effective data points available due to the lower amount of Φ_0 of flux variation in the SQUID. Both detectors with different sensor materials were correctly measured and fitted with the simulation scripts developed within this thesis. 123
6.12 Thermal calibration of the magnetization data. **a)** Actual sensor temperature T_S as a function of cryostat temperature, T_{MXC}. The previous magnetization fit is used to extract the T_S values. The plot also includes the thermal decoupling model applied to an FLL measurement performed on the same sample. **b)** Magnetization plot with calibrated temperatures below 60 mK. 124
6.13 Flux measurement of the MT02 device chip before and after being exposed to the O_2 plasma. Theoretical curves are built from the obtained best-fit erbium concentrations in each case. Three representative curves are shown for each measurement, the legend shows the forward current utilized for the injection in each case. 126
6.14 Flux measurement of the MT02 device chip before and after being exposed to the XeF_2 etching step for detector release, showing a subtle signal degradation compared to the baseline reference. 127

List of Tables

2.1 Refractive indices for the AR coatings with their respective thicknesses in brackets for ideal transmission and values using custom materials published for SPT-3G [101]. . . . 18
2.2 Element values calculated for the 5^{th}-order Chebyshev in-line band-defining filters. . . . 25
2.3 Calculated quality factors from the diplexer network scattering parameters. 30
2.4 Averaged optical efficiency results for each bolometer in both pixel designs 32
2.5 Optical loading characteristics of the QUBIC instrument used to determine the incoming optical power on the focal plane [68]. . . . 33
2.6 Estimated incoming optical power and photon noise equivalent power for both pixel designs within each observation band. The numbers are calculated using the optical efficiency accounting for the optimized three-layer AR coating and without any AR coating in brackets. . . . 34

3.1 Results of the external field rejection simulation comparing a self-symmetric with a regular meander. The self-symmetric design achieves a large external magnetic field rejection. . . . 47
3.2 Detector parameters and performance in the estimation of the noise contributions to achieve BLIP with MMB detectors installed in the focal plane of the QUBIC instrument. The estimated performance describes the average values corresponding to the range of expected incident power on the detector. . . . 54

4.1 Nb film intrinsic stress results obtained for varying sputtering pressure ($P = 60\,\text{W}$). . . . 67
4.2 Nb film intrinsic stress results obtained for varying sputtering power ($P_{\text{Ar}} = 3\,\mu\text{bar}$). . . . 68
4.3 Model fit results for the I_c measurements presented in Figure 4.4. . . . 71
4.4 Isolation tests results comparing two planarized samples with (V1) and without (V2) the anodization. Values indicated as OVLD were not measurable and mean the resistance is larger than $1\,\text{G}\Omega$, in those structures, insulation is considered succesful. . . . 79

5.1 Parameters of the front-end dc-SQUIDs and SQUID arrays used to characterize the MMB-TD prototypes. . . . 107

5.2 Amplifier bandwidth and noise performance parameters extracted from the noise spectrum measurement presented in Figure 5.7. 109

6.1 Simulated and/or measured inductance values of L_{stray}, L_{in}, L_{m} and L_{load} of the MMB-TD. 115
6.2 Design parameters and measured layer thicknesses of MT01 and MT02 chips used for characterization of the Au:Er sensor film. 120

List of Acronyms

ACTPol	Atacama Cosmology Telescope Polarimeter
AdvACT	Advanced Atacama Cosmology Telescope Polarimeter
AliCPT	Ali Cosmic Microwave Background Polarization Telescope
AR	Anti-Reflection 16
BICEP1	Background Imaging of Cosmic Extragalactic Polarization 1
BICEP2	Background Imaging of Cosmic Extragalactic Polarization 2
BICEP3	Background Imaging of Cosmic Extragalactic Polarization 3
BLIP	Background Limited Photometry 8
BOOMERANG	Balloon Observations of Millimetric Extragalactic Radiation and Geophysics
CAPMAP	Cosmic Anisotropy Polarization Mapper
CBI	Cosmic Background Imager
CLASS	Cosmology Large Angular Scale Surveyor
CMB	Cosmic Microwave Background 1
CMB-S4	Cosmic Microwave Background Stage 4
COBE	COsmic Background Explorer 1
DASI	Degree Angular Scale Interferometer
EM	Electromagnetic 11
ETF	Electro-Thermal Feedback 7
FIB	Focused Ion Beam 72
FIRAS	Far-Infrared Absolute Spectrophotometer 1
FLL	Flux-Locked Loop 102
ILC	Internal Linear Combination 2
IMS	Institute of Micro- and Nanoelectronic Systems 63
ITeDA	Instituto de Tecnologías en Detección y Astropartículas 63
KeckArray	Keck Array (successor to BICEP2)

LAMBDA	Legacy Archive for Microwave Background Data Analysis	
ΛCDM	Lambda Cold Dark Matter Model	2
LiteBIRD	Lite (Light) Satellite for the Studies of B-mode Polarization and Inflation from Cosmic Background Radiation Detection	
LSPE	Large-Scale Polarization Explorer	
MAXIPOL	Millimeter Anisotropy eXperiment IMaging POLarimeter	
MMB	Magnetic Microbolometer	7
MMB-TD	Magnetic Microbolometer Technical Demonstrator	59
MMC	Magnetic Microcalorimeter	7
PICO	Probe of Inflation and Cosmic Origins	
PIPER	Primordial Inflation Polarization Explorer	
PLANCK	Planck Satellite Mission	4
POLARBEAR	Polarization of Background Radiation	
POLARBEAR2	Polarization of Background Radiation 2	
PTC	Pulse-Tube Cryocooler	100
QUBIC	Q & U Bolometric Interferometer for Cosmology	1
QUaD	QUEST at DASI	
QUIET-Q	Q/U Imaging Experiment (Q-band)	
QUIET-W	Q/U Imaging Experiment (W-band)	
SimonsArray	Simons Array	
SPTPol	South Pole Telescope Polarimeter	
SQUID	Superconducting Quantum Interference Device	9
TDM	Time-Division Multiplexing	6
TES	Transition Edge Sensor	6
WMAP	Wilkinson Microwave Anisotropy Probe	1

List of Publications

- **“Suitability of magnetic microbolometers based on paramagnetic temperature sensors for CMB polarization measurements” Geria, J. M.**, Hampel, M. R., Kempf, S., Bonaparte, J. J. F., Ferreyro, L. P., Redondo, M. E. G., Almela, A, Salum, J. M., Müller, N. A., Bonilla Neira, J. D., Fuster, A. E., Platino, M. and Etchegoyen - A. - SPIE JATIS 2023 - https://doi.org/10.1117/1.JATIS.9.1.016002
- **Optimal demodulation domain for microwave SQUID multiplexers in presence of readout system noise** García Redondo, M. E., Müller, N. A., Salum, J. M., Ferreyro, L. P., Bonilla-Neira, J. D., **Geria, J. M.**, Bonaparte, J. J., Muscheid, T, Gartmann, R, Almela, A, Hampel, M. R., Fuster, A. E., Ardila-Perez, L. E., Wegner, M, Platino, M, Sander, O, Kempf, S. and Weber, M. - J Appl. Phys. 2024 - https://doi.org/10.1063/5.0222656
- **“An implementation of a channelizer based on a Goertzel Filter Bank for the read-out of cryogenic sensors"** L.P. Ferreyro, M. García Redondo, M.R. Hampel, A. Almela, A. Fuster, J. Salum, **J.M. Geria**, J. Bonaparte, J. Bonilla-Neira, N. Müller, N. Karcher, O. Sander, M. Platino, M. Weber and A. Etchegoyen - IOP JINST 2023 - https://doi.org/10.1088/1748-0221/18/06/P06009
- **“Aliasing Effect on Flux Ramp Demodulation: Nonlinearity in the Microwave Squid Multiplexer"** J. M. Salum, T. Muscheid, A. Fuster, M. E. Garcia Redondo, M. R. Hampel, L. P. Ferreyro, **J. M. Geria**, J. Bonilla-Neira, N. Müller, J. Bonaparte, A. Almela, L. E. Ardila-Perez, M. Platino, O. Sander and M. Weber - Springer J Low Temp. 2023 - https://doi.org/10.1007/s10909-023-02993-z
- **“Antenna-Coupled Magnetic Microbolometers for CMB Polarization Surveys" Juan Geria**, Alejandro Almela, Juan Bonaparte, Jesús Bonilla-Neira, Luciano Ferreyro, Alan Fuster, Manuel García Redondo, Matías Hampel, Nahuel Müller, Manuel Platino, Juan Salum, Sebastian Kempf, Marc Weber and Alberto Etchegoyen - Springer J Low Temp. 2024 - https://doi.org/10.1007/s10909-024-03217-8
- **“Spectral Engineering for Optimal Signal Performance in the Microwave SQUID Multiplexer"** J. M. Salum, M. E. García Redondo, L. P. Ferreyro, J. Bonilla-Neira, N. Müller, **J. M. Geria**, J. Bonaparte, T. Muscheid, R. Gartmann, A. Fuster, A. Almela, M. R. Hampel, L. E. Ardila-Perez, O. Sander, S. Kempf, M. Platino, M. Weber and A. Etchegoyen - Springer J Low Temp. 2024 -

https://doi.org/10.1007/s10909-024-03049-6

- **"Advances in the Goertzel Filter Bank Channelizer for Cryogenic Sensors Readout"** L. P. Ferreyro, M. E. García Redondo, J. M. Salum, T. Muscheid, M. Hampel, A. Almela, A. Fuster, **J. M. Geria**, J. Bonaparte, J. Bonilla-Neira, L. E. Ardila-Perez, R. Gartmann, N. Müller, M. Wegner, O. Sander, M. Platino, S. Kempf, A. Etchegoyen and M. Weber - Springer J Low Temp. 2024 - https://doi.org/10.1007/s10909-024-03204-z
- **"RFSoC Gen3-Based Software-Defined Radio Characterization for the Readout System of Low-Temperature Bolometers"** M. E. García Redondo, T. Muscheid, R. Gartmann, J. M. Salum, L. P. Ferreyro, N. A. Müller, J. D. Bonilla-Neira, **J. M. Geria**, J. J. Bonaparte, A. Almela, L. E. Ardila-Perez, M. R. Hampel, A. E. Fuster, M. Platino, O. Sander, M. Weber and A. Etchegoyen - Springer J Low Temp. 2024 - https://doi.org/10.1007/s10909-024-03079-0
- **"The Magnetic Microbolometer: A Proposal for QUBIC Next Gen"** Matías Hampel, Alejandro Almela, Juan Bonaparte, Jesús Bonilla Neira, Luciano Ferreyro, Alan Fuster, Manuel García Redondo, Robert Gartmann, **Juan Geria**, Nahuel Müller, Timo Muscheid, Juan Salum, Manuel Platino, Luis Ardila, Oliver Sander, Mathias Wegner, Sebastian Kempf, Marc Weber and Alberto Etchegoyen - Springer J Low Temp. 2024 - https://doi.org/10.1007/s10909-024-03203-0
- **"The Magnetic Microbolometer Detection Chain: A Proposed Detection System to Observe the B Modes of the Cosmic Microwave Background"** M. Platino, M. E. García Redondo, L. P. Ferreyro, J. M. Salum, N. A. Müller, J. D. Bonilla-Neira, T. Muscheid, R. Gartmann, **J. M. Geria**, J. J. Bonaparte, D. A. Almela, L. E. Ardila-Pérez, M. R. Hampel, A. E. Fuster, O. Sander, M. Weber and A. Etchegoyen - Springer J Low Temp. 2024 - https://doi.org/10.1007/s10909-024-03230-x
- **"Measuring the CMB primordial B-modes with Bolometric Interferometry: Status and future prospects of the QUBIC experiment"** A. Mennella*, P. Ade, A. Almela, G. Amico, L.H. Arnaldi, J. Aumont, S. Banfi, E.S. Battistelli, B. Bélier, L. Bergé, J.-Ph. Bernard, M. Bersanelli1, J. Bonaparte, J.D. Bonilla, E. Bunn, D. Buzi, F. Cacciotti, D. Camilieri, F. Cavaliere, P. Chanial, C. Chapron, L. Colombo, F. Columbro, A. Coppolecchia, M.B. Costanza, G. D'Alessandro, P. de Bernardis, G. De Gasperis, M. De Leo, M. De Petris, N. Del Castillo, S. Dheilly, A. Etchegoyen, S. Ferazzoli, L.P. Ferreyro, C. Franceschet, M.M. Gamboa Lerena, K. Ganga, B. García, M.E. García Redondo, D. Gayer, **J.M. Geria**, M. Gervasi, M. Giard, V. Gilles, M. Gómez Berisso, M. Gonzalez, M. Gradziel, L. Grandsire, J.-Ch. Hamilton, M.R. Hampel, G. Isopi, J. Kaplan, L. Lamagna, F. Lazarte, S. Loucatos, B. Maffei, A. Mancilla, S. Mandelli, E. Manzan, E. Marchitelli, S. Marnieros, W. Marty, S. Masi, A. May, J. Maya, M. McCulloch, L. Mele, D. Melo, N. Mirón-Granese, L. Montier, L. Mousset, N. Müller, F. Nati, C. O'Sullivan, A. Paiella, F. Pajot, S. Paradiso, E. Pascale, A. Passerini, A. Pelosi, M. Perciballi, F. Pezzotta, F. Piacentini, M. Piat, L. Piccirillo, G. Pisano, M. Platino, G. Polenta, D. Prêle, D. Rambaud, G. Ramos, E. Rasztocky, M. Régnier, C. Reyes, F.

Rodríguez, C.A. Rodríguez, G.E. Romero, J.M. Salum, A. Schillaci, C. Scóccola, G. Stankowiak, A. Tartari, J.-P. Thermeau, P. Timbie, M. Tomasi, S. Torchinsky, G. Tucker, C. Tucker, L. Vacher, F. Voisin, M. Wright, M. Zannoni and A. Zullo - EPJ Web Conf. 2024 - https://doi.org/10.1051/epjconf/202429300030

Bibliography

[1] A. A. Penzias and R. W. Wilson. "A measurement of excess antenna temperature at 4080 MHz." In "A Source Book in Astronomy and Astrophysics, 1900–1975," pp. 873–876. Harvard University Press, 1979.

[2] R. A. Alpher, H. Bethe, and G. Gamow. "The origin of chemical elements." *Physical Review*, vol. 73(7), p. 803, 1948.

[3] G. Gamow. "The evolution of the universe." *Nature*, vol. 162(4122), pp. 680–682, 1948.

[4] D. J. Fixsen, E. Cheng, J. Gales, J. C. Mather, R. Shafer, and E. Wright. "The cosmic microwave background spectrum from the full cobe* firas data set." *The Astrophysical Journal*, vol. 473(2), p. 576, 1996.

[5] G. Hinshaw, J. Weiland, R. Hill, N. Odegard, D. Larson, C. Bennett et al. "Five-year wilkinson microwave anisotropy probe* observations: data processing, sky maps, and basic results." *The Astrophysical Journal Supplement Series*, vol. 180(2), p. 225, 2009.

[6] D. Fixsen. "The temperature of the cosmic microwave background." *The Astrophysical Journal*, vol. 707(2), p. 916, 2009.

[7] C. L. Bennett, D. Larson, J. L. Weiland, N. Jarosik, G. Hinshaw, N. Odegard et al. "Nine-year Wilkinson Microwave Anisotropy Probe (WMAP) observations: final maps and results." *The Astrophysical Journal Supplement Series*, vol. 208(2), p. 20, 2013.

[8] P. Schneider. Extragalactic Astronomy and Cosmology. Springer Berlin Heidelberg, Berlin, Heidelberg, 2006. doi:10.1007/978-3-540-33175-9. URL http://dx.doi.org/10.1007/978-3-540-33175-9.

[9] S. Weinberg. Cosmology. OUP Oxford, 2008.

[10] A. Linde. Particle physics and inflationary cosmology, vol. 5. CRC press, 1990.

[11] E. Kolb. The early universe. CRC press, 2018.

[12] A. H. Guth. "Inflationary universe: A possible solution to the horizon and flatness problems." *Physical Review D*, vol. 23(2), p. 347, 1981.

[13] A. Kosowsky. "Cosmic microwave background polarization." *arXiv preprint astro-ph/9501045*, 1995.

[14] N. Aghanim, Y. Akrami, F. Arroja, M. Ashdown, J. Aumont, C. Baccigalupi et al. "Planck 2018 results-I. Overview and the cosmological legacy of Planck." *Astronomy & Astrophysics*, vol. 641, p. A1, 2020.

[15] D. N. Spergel and M. Zaldarriaga. "CMB polarization as a direct test of Inflation." *Physics Review Letter*. doi:10.1103/PhysRevLett.79.2180, 1997.

[16] U. Seljak and M. Zaldarriaga. "Signature of gravity waves in the polarization of the microwave background." *Physics Review Letter*, vol. 78(11), pp. 2054–2057. doi:10.1103/PhysRevLett.78.2054, 1997.

[17] A. Stebbins. "Weak lensing on the celestial sphere." *arXiv preprint astro-ph/9609149*, 1996.

[18] M. Kamionkowski, A. Kosowsky, and A. Stebbins. "Statistics of cosmic microwave background polarization." *Physical Review D*, vol. 55(12), p. 7368, 1997.

[19] G. Hinshaw, M. Nolta, C. Bennett, R. Bean, O. Doré, M. Greason et al. "Three-year wilkinson microwave anisotropy probe (wmap*) observations: Temperature analysis." *The Astrophysical Journal Supplement Series*, vol. 170(2), p. 288, 2007.

[20] L. Page, G. Hinshaw, E. Komatsu, M. Nolta, D. Spergel, C. Bennett et al. "Three-year Wilkinson microwave anisotropy probe (WMAP) observations: polarization analysis." *The Astrophysical Journal Supplement Series*, vol. 170(2), p. 335, 2007.

[21] N. Aghanim, Y. Akrami, M. Ashdown, J. Aumont, C. Baccigalupi, M. Ballardini et al. "Planck 2018 results-V. CMB power spectra and likelihoods." *Astronomy & Astrophysics*, vol. 641, p. A5, 2020.

[22] P. A. Ade, Z. Ahmed, R. Aikin, K. D. Alexander, D. Barkats, S. Benton et al. "BICEP2/Keck Array V: Measurements of B-mode polarization at degree angular scales and 150 GHz by the Keck Array." *The Astrophysical Journal*, vol. 811(2), p. 126, 2015.

[23] P. Collaborations, P. Ade, N. Aghanim, Z. Ahmed, R. Aikin, K. Alexander et al. "A joint analysis of bicep2/keck array and planck data." *arXiv preprint arXiv:1502.00612*, 2015.

[24] K. N. Abazajian, P. Adshead, Z. Ahmed, S. W. Allen, D. Alonso, K. S. Arnold et al. "CMB-S4 science book." *arXiv preprint arXiv:1610.02743*, 2016.

[25] Y. Akrami, M. Ashdown, J. Aumont, C. Baccigalupi, M. Ballardini, A. J. Banday et al. "Planck 2018 results-IV. Diffuse component separation." *Astronomy & Astrophysics*, vol. 641, p. A4, 2020.

[26] A. Lewis and A. Challinor. "Weak gravitational lensing of the CMB." *Physics Reports*, vol. 429(1), pp. 1–65, 2006.

[27] R. Adam, P. A. Ade, N. Aghanim, M. Alves, M. Arnaud, M. Ashdown et al. "Planck 2015 results-X. Diffuse component separation: Foreground maps." *Astronomy & Astrophysics*, vol. 594, p. A10, 2016.

[28] A. F. Ptak and T. M. Essinger-Hileman. "LAMBDA Education and Graphics.", 2021. URL https://lambda.gsfc.nasa.gov/education/lambda_graphics/cmb_power_spectra.html.

[29] S. K. Choi, M. Hasselfield, S.-P. P. Ho, B. Koopman, M. Lungu, M. H. Abitbol et al. "The Atacama Cosmology Telescope: a measurement of the Cosmic Microwave Background power spectra at 98 and 150 GHz." *Journal of Cosmology and Astroparticle Physics*, vol. 2020(12), p. 045, 2020.

[30] B. collaboration et al. "Degree-scale CMB polarization measurements from three years of BICEP1 data." *ApJ*, vol. 783, p. 67, 2014.

[31] B. collaboration et al. "BICEP2 I: Detection of B-mode polarization at degree angular scales." *arXiv preprint arXiv:1403.3985*.

[32] K. Array, B. Collaborations, P. Ade, Z. Ahmed, R. Aikin, K. Alexander et al. "BICEP2/Keck Array X: Constraints on Primordial Gravitational Waves using Planck, WMAP, and New BICEP2/Keck Observations through the 2015 Season." *arXiv preprint arXiv:1810.05216*, 2018.

[33] W. Jones, P. Ade, J. Bock, J. Bond, J. Borrill, A. Boscaleri et al. "A Measurement of the CMB (EE) Spectrum from the 2003 Flight of Boomerang." 2006.

[34] C. Bischoff, L. Hyatt, J. McMahon, G. Nixon, D. Samtleben, K. Smith et al. "New measurements of fine-scale CMB polarization power spectra from CAPMAP at both 40 and 90 GHz." *The Astrophysical Journal*, vol. 684(2), p. 771, 2008.

[35] J. L. Sievers, C. Achermann, J. Bond, L. Bronfman, R. Bustos, C. Contaldi et al. "Implications of the cosmic background imager polarization data." *The Astrophysical Journal*, vol. 660(2), p. 976, 2007.

[36] E. M. Leitch, J. Kovac, N. Halverson, J. Carlstrom, C. Pryke, and M. Smith. "Degree angular scale interferometer 3 year cosmic microwave background polarization results." *The Astrophysical Journal*, vol. 624(1), p. 10, 2005.

[37] J.-H. P. Wu, J. Zuntz, M. Abroe, P. A. Ade, J. Bock, J. Borrill et al. "MAXIPOL: data analysis and results." *The Astrophysical Journal*, vol. 665(1), p. 55, 2007.

[38] P. Ade, Y. Akiba, A. Anthony, K. Arnold, M. Atlas, D. Barron et al. "A measurement of the cosmic microwave background B-mode polarization power spectrum at sub-degree scales with POLARBEAR." *The Astrophysical Journal*, vol. 794(2), p. 171, 2014.

[39] Y. Akiba, A. Anthony, K. Arnold, M. Atlas, D. Barron, D. Boettger et al. "Erratum:"A Measurement of the Cosmic Microwave Background B-Mode Polarization Power Spectrum at Sub-degree Scales with POLARBEAR"(2014, ApJ, 794, 171)." *The Astrophysical Journal*, vol. 848(1), p. 73, 2017.

[40] M. Brown, P. Ade, J. Bock, M. Bowden, G. Cahill, P. Castro et al. "Improved measurements of the temperature and polarization of the cosmic microwave background from QUaD." *The Astrophysical Journal*, vol. 705(1), p. 978, 2009.

[41] C. Bischoff, A. Brizius, I. Buder, Y. Chinone, K. Cleary, R. Dumoulin et al. "First season quiet observations: measurements of cosmic microwave background polarization power spectra at 43 ghz in the multipole range $25 \ll \ell \ll 475$." *The Astrophysical Journal*, vol. 741(2), p. 111, 2011.

[42] D. Araujo, C. Bischoff, A. Brizius, I. Buder, Y. Chinone, K. Cleary et al. "Second season QUIET observations: Measurements of the cosmic microwave background polarization power spectrum at 95 GHz." *The Astrophysical Journal*, vol. 760(2), p. 145, 2012.

[43] J. Sayre, C. Reichardt, J. Henning, P. Ade, A. Anderson, J. Austermann et al. "Measurements of B-mode polarization of the cosmic microwave background from 500 square degrees of SPTpol data." *Physical Review D*, vol. 101(12), p. 122003, 2020.

[44] D. Larson, J. Dunkley, G. Hinshaw, E. Komatsu, M. Nolta, C. Bennett et al. "Seven-year wilkinson microwave anisotropy probe (WMAP*) observations: power spectra and WMAP-derived parameters." *The Astrophysical Journal Supplement Series*, vol. 192(2), p. 16, 2011.

[45] J.-C. Hamilton, L. Mousset, E. Battistelli, P. De Bernardis, M.-A. Bigot-Sazy, P. Chanial et al. "QUBIC I: Overview and science program." *Journal of Cosmology and Astroparticle Physics*, vol. 2022(04), p. 034, 2022.

[46] T. Essinger-Hileman, A. Ali, M. Amiri, J. W. Appel, D. Araujo, C. L. Bennett et al. "CLASS: the cosmology large angular scale surveyor." In "Millimeter, Submillimeter, and Far-Infrared Detectors and Instrumentation for Astronomy VII," vol. 9153, pp. 491–513. SPIE, 2014.

[47] D. Barron, P. Collaboration et al. "POLARBEAR2: A new multichroic receiver for precision measurements of cosmic microwave background polarization." In "American Astronomical Society Meeting Abstracts# 223," vol. 223, pp. 204–06. 2014.

[48] N. Stebor, P. Ade, Y. Akiba, C. Aleman, K. Arnold, C. Baccigalupi et al. "The Simons array CMB polarization experiment." In "Millimeter, Submillimeter, and Far-Infrared Detectors and Instrumentation for Astronomy VIII," vol. 9914, pp. 363–371. SPIE, 2016.

[49] A. Suzuki, P. Ade, Y. Akiba, C. Aleman, K. Arnold, C. Baccigalupi et al. "The polarbear-2 and the simons array experiments." *Journal of Low Temperature Physics*, vol. 184, pp. 805–810, 2016.

[50] S. Henderson, R. Allison, J. Austermann, T. Baildon, N. Battaglia, J. Beall et al. "Advanced ACTPol cryogenic detector arrays and readout." *Journal of Low Temperature Physics*, vol. 184, pp. 772–779, 2016.

[51] J. A. Grayson, P. Ade, Z. Ahmed, K. D. Alexander, M. Amiri, D. Barkats et al. "BICEP3 performance overview and planned Keck Array upgrade." In "Millimeter, Submillimeter, and Far-Infrared Detectors and Instrumentation for Astronomy VIII," vol. 9914, pp. 157–173. SPIE, 2016.

[52] H. Li, S.-Y. Li, Y. Liu, Y.-P. Li, Y. Cai, M. Li et al. "Probing primordial gravitational waves: Ali CMB polarization telescope." *National Science Review*, vol. 6(1), pp. 145–154, 2019.

[53] N. Galitzki, A. Ali, K. S. Arnold, P. C. Ashton, J. E. Austermann, C. Baccigalupi et al. "The Simons observatory: instrument overview." In "Millimeter, Submillimeter, and Far-Infrared Detectors and Instrumentation for Astronomy IX," vol. 10708, pp. 40–52. SPIE, 2018.

[54] J. Lazear, P. A. Ade, D. Benford, C. L. Bennett, D. T. Chuss, J. L. Dotson et al. "The primordial inflation polarization explorer (piper)." In "Millimeter, Submillimeter, and Far-Infrared Detectors and Instrumentation for Astronomy VII," vol. 9153, pp. 529–539. SPIE, 2014.

[55] G. Addamo, P. Ade, C. Baccigalupi, A. Baldini, P. Battaglia, E. Battistelli et al. "The large scale polarization explorer (LSPE) for CMB measurements: performance forecast." *Journal of Cosmology and Astroparticle Physics*, vol. 2021(08), p. 008, 2021.

[56] K. Abazajian, G. Addison, P. Adshead, Z. Ahmed, S. W. Allen, D. Alonso et al. "CMB-S4 science case, reference design, and project plan." *arXiv preprint arXiv:1907.04473*, 2019.

[57] L. Collaboration, E. Allys, K. Arnold, J. Aumont, R. Aurlien, S. Azzoni et al. "Probing cosmic inflation with the LiteBIRD cosmic microwave background polarization survey." *Progress of Theoretical and Experimental Physics*, vol. 2023(4), p. 042F01, 2023.

[58] K. Young, M. Alvarez, N. Battaglia, J. Bock, J. Borrill, D. Chuss et al. "Optical design of PICO: a concept for a space mission to probe inflation and cosmic origins." In "Space Telescopes and Instrumentation 2018: Optical, Infrared, and Millimeter Wave," vol. 10698, pp. 1242–1253. SPIE, 2018.

[59] G. Tucker, J. Kim, P. Timbie, S. Ali, L. Piccirillo, and C. Calderon. "Bolometric interferometry: the millimeter-wave bolometric interferometer." *New Astronomy Reviews*, vol. 47(11-12), pp. 1173–1176, 2003.

[60] F. Cavaliere, A. Mennella, M. Zannoni, P. Battaglia, E. Battistelli, P. De Bernardis et al. "QUBIC VII: The feedhorn-switch system of the technological demonstrator." *Journal of Cosmology and Astroparticle Physics*, vol. 2022(04), p. 040, 2022.

[61] M.-A. Bigot-Sazy, R. Charlassier, J.-C. Hamilton, J. Kaplan, and G. Zahariade. "Self-calibration: an efficient method to control systematic effects in bolometric interferometry." *Astronomy & Astrophysics*, vol. 550, p. A59, 2013.

[62] C. O'Sullivan, M. De Petris, G. Amico, E. Battistelli, P. De Bernardis, D. Burke et al. "QUBIC VIII: Optical design and performance." *Journal of Cosmology and Astroparticle Physics*, vol. 2022(04), p. 041, 2022.

[63] L. Mousset, M. G. Lerena, E. Battistelli, P. De Bernardis, P. Chanial, G. d'Alessandro et al. "QUBIC II: Spectral polarimetry with bolometric interferometry." *Journal of Cosmology and Astroparticle Physics*, vol. 2022(04), p. 035, 2022.

[64] P. Chanial, M. Regnier, J.-C. Hamilton, E. Bunn, V. Chabirand, A. Flood et al. "Spectral Imaging with QUBIC: building frequency maps from Time-Ordered-Data using Bolometric Interferometry." *arXiv preprint arXiv:2409.18698*, 2024.

[65] C. O'Sulivan, S. Scully, D. Gayer, M. Gradziel, J. Murphy, M. De Petris et al. "The QU Bolometric Interferometer for Cosmology (QUBIC)." In "36th ESA Antenna Workshop on Antennas and RF Systems for Space Science," ESA Publications Division c/o ESTEC, 2015.

[66] P. L. Richards. "Bolometers for infrared and millimeter waves." *Journal of Applied Physics*, vol. 76(1), pp. 1–24, 1994.

[67] J.-M. Lamarre. "Bolometers: the ultimate detectors for CMB measurements?" *Microwave Background Anisotropies*, p. 31, 1997.

[68] J. Aumont, S. Banfi, P. Battaglia, E. Battistelli, A. Bau, B. Bélier et al. "QUBIC technical design report." *arXiv preprint arXiv:1609.04372*, 2016.

[69] M. Piat, G. Stankowiak, E. Battistelli, P. De Bernardis, G. d'Alessandro, M. De Petris et al. "QUBIC IV: Performance of TES bolometers and readout electronics." *Journal of Cosmology and Astroparticle Physics*, vol. 2022(04), p. 037, 2022.

[70] D. Prêle, F. Voisin, M. Piat, T. Decourcelle, C. Perbost, C. Chapron et al. "A 128 multiplexing factor time-domain squid multiplexer." *Journal of Low Temperature Physics*, vol. 184, pp. 363–368, 2016.

[71] C. Hilsum. "Infrared absorption of thin metal films." *Journal of the Optical Society of America*, vol. 44(3), pp. 188–191, 1954.

[72] C. Perbost. Matrices de bolomètres supraconducteurs pour la mesure de la polarisation du fond diffus cosmologique: application à l'expérience QUBIC. Ph.D. thesis, Université de Paris 7-Denis Diderot, 2016.

[73] M. De Lucia, P. Dal Bo, E. Di Giorgi, T. Lari, C. Puglia, and F. Paolucci. "Transition edge sensors: Physics and applications." *Instruments*, vol. 8(4), p. 47, 2024.

[74] K. Irwin. "An application of electrothermal feedback for high resolution cryogenic particle detection." *Applied Physics Letters*, vol. 66(15), pp. 1998–2000, 1995.

[75] A. T. Lee, P. L. Richards, S. W. Nam, B. Cabrera, and K. D. Irwin. "A superconducting bolometer with strong electrothermal feedback." *Applied Physics Letters*, vol. 69(12), pp. 1801–1803, 1996.

[76] J. Bonetti, A. Turner, M. Kenyon, H. LeDuc, J. Brevik, A. Orlando et al. "Transition edge sensor focal plane arrays for the bicep2, keck, and spider cmb polarimeters." *IEEE transactions on applied superconductivity*, vol. 21(3), pp. 219–222, 2010.

[77] K. Arnold, P. A. Ade, A. Anthony, F. Aubin, D. Boettger, J. Borrill et al. "The POLARBEAR CMB polarization experiment." In "Millimeter, Submillimeter, and Far-Infrared Detectors and Instrumentation for Astronomy V," vol. 7741, pp. 404–414. SPIE, 2010.

[78] J. M. Geria, M. R. Hampel, S. Kempf, J. J. F. Bonaparte, L. P. Ferreyro, M. E. G. Redondo et al. "Suitability of magnetic microbolometers based on paramagnetic temperature sensors for CMB polarization measurements." *Journal of Astronomical Telescopes, Instruments, and Systems*, vol. 9(1), pp. 016002–016002, 2023.

[79] A. Fleischmann, C. Enss, and G. Seidel. "Metallic magnetic calorimeters." *Cryogenic particle detection*, pp. 151–216, 2005.

[80] S. Kempf, A. Fleischmann, L. Gastaldo, and C. Enss. "Physics and applications of metallic magnetic calorimeters." *Journal of Low Temperature Physics*, vol. 193, pp. 365–379, 2018.

[81] M. H. Abitbol, Z. Ahmed, D. Barron, R. B. Thakur, A. N. Bender, B. A. Benson et al. "CMB-S4 technology book." *arXiv preprint arXiv:1706.02464*, 2017.

[82] H. Jasik and R. Johnson. Antenna Engineering Handbook. Mcgraw-hill. URL https://books.google.de/books?id=zshJ0AEACAAJ.

[83] D. M. Pozar. Microwave engineering: theory and techniques. John wiley & sons, 2021.

[84] R. Chambers. "The anomalous skin effect." *Proceedings of the Royal Society of London. Series A. Mathematical and Physical Sciences*, vol. 215(1123), pp. 481–497, 1952.

[85] D. C. Mattis and J. Bardeen. "Theory of the anomalous skin effect in normal and superconducting metals." *Physical Review*, vol. 111(2), p. 412, 1958.

[86] A. Kerr. "Surface impedance of superconductors and normal conductors in EM simulators." *MMA Memo*, vol. 21(245), pp. 1–17, 1999.

[87] W. Zimmermann, E. Brandt, M. Bauer, E. Seider, and L. Genzel. "Optical conductivity of BCS superconductors with arbitrary purity." *Physica C: Superconductivity*, vol. 183(1-3), pp. 99–104, 1991.

[88] D. P. L. Aude. Modeling superconductors using surface impedance techniques. Ph.D. thesis, Massachusetts Institute of Technology, 2010.

[89] F. London and H. London. "The electromagnetic equations of the supraconductor." *Proceedings of the Royal Society of London. Series A-Mathematical and Physical Sciences*, vol. 149(866), pp. 71–88, 1935.

[90] A. D. O'Connell, M. Ansmann, R. C. Bialczak, M. Hofheinz, N. Katz, E. Lucero et al. "Microwave dielectric loss at single photon energies and millikelvin temperatures." *Applied Physics Letters*, vol. 92(11), 2008.

[91] C. A. Garcia, N. Bailey, C. Kirby, J. A. Strong, V. V. Talanov, A. Y. Herr et al. "Disentangling superconductor and dielectric microwave losses in submicrometer Nb/Si O 2 interconnects using a multimode microstrip resonator." *Physical Review Applied*, vol. 21(2), p. 024056, 2024.

[92] V. V. Talanov, D. Knee, D. Harms, K. Perkins, A. Urbanas, J. Egan et al. "Propagation of picosecond pulses on superconducting transmission line interconnects." *Superconductor Science and Technology*, vol. 35(5), p. 055011, 2022.

[93] R. O'Brient, J. Edwards, K. Arnold, G. Engargiola, W. Holzapfel, A. T. Lee et al. "Sinuous antennas for cosmic microwave background polarimetry." In "Millimeter and Submillimeter Detectors and Instrumentation for Astronomy IV," vol. 7020, pp. 404–414. SPIE, 2008.

[94] R. O'Brient, P. Ade, K. Arnold, J. Edwards, G. Engargiola, W. Holzapfel et al. "Sinuous-Antenna coupled TES bolometers for Cosmic Microwave Background Polarimetry." In "AIP Conference Proceedings," vol. 1185, pp. 502–505. American Institute of Physics, 2009.

[95] X. Yang, X. Liu, S. Yu, L. Gan, J. Zhou, and Y. Zeng. "Permittivity of undoped silicon in the millimeter wave range." *Electronics*, vol. 8(8), p. 886, 2019.

[96] J. M. Edwards, R. O'Brient, A. T. Lee, and G. M. Rebeiz. "Dual-polarized sinuous antennas on extended hemispherical silicon lenses." *IEEE Transactions on Antennas and Propagation*, vol. 60(9), pp. 4082–4091, 2012.

[97] D. F. Filipovic, S. S. Gearhart, and G. M. Rebeiz. "Double-slot antennas on extended hemispherical and elliptical silicon dielectric lenses." *IEEE Transactions on microwave theory and techniques*, vol. 41(10), pp. 1738–1749, 1993.

[98] B. Westbrook, C. Raum, S. Beckman, A. T. Lee, N. Farias, T. Sasse et al. "Detector fabrication development for the LiteBIRD satellite mission." In "Space Telescopes and Instrumentation 2020: Optical, Infrared, and Millimeter Wave," vol. 11443, pp. 915–936. SPIE, 2020.

[99] D. B. Judd. "Fresnel reflection of diffusely incident light." 1942.

[100] H. A. Macleod and H. A. Macleod. Thin-film optical filters. CRC press, 2010.

[101] A. Nadolski, A. Kofman, J. Vieira, P. Ade, Z. Ahmed, A. Anderson et al. "Broadband anti-reflective coatings for cosmic microwave background experiments." In "Millimeter, Submillimeter, and Far-Infrared Detectors and Instrumentation for Astronomy IX," vol. 10708, pp. 719–731. SPIE, 2018.

[102] B. A. Benson, P. Ade, Z. Ahmed, S. Allen, K. Arnold, J. Austermann et al. "SPT-3G: a next-generation cosmic microwave background polarization experiment on the South Pole telescope." In "Millimeter, Submillimeter, and Far-Infrared Detectors and Instrumentation for Astronomy VII," vol. 9153, pp. 552–572. SPIE, 2014.

[103] H. G. Booker. "Slot aerials and their relation to complementary wire aerials (Babinet's principle)." *Journal of the Institution of Electrical Engineers-Part IIIA: Radiolocation*, vol. 93(4), pp. 620–626, 1946.

[104] G. Deschamps. "Impedance properties of complementary multiterminal planar structures." *IRE Transactions on Antennas and Propagation*, vol. 7(5), pp. 371–378, 1959.

[105] D. P. Mcginnis and J. B. Beyer. "A broad-band microwave superconducting thin-film transformer." *IEEE transactions on microwave theory and techniques*, vol. 36(11), pp. 1521–1525, 1988.

[106] R. W. Klopfenstein. "A Transmission Line Taper of Improved Design." *Proceedings of the IRE*, vol. 44(1), pp. 31–35. doi:10.1109/JRPROC.1956.274847, 1956.

[107] R. M. Fano. "Theoretical limitations on the broadband matching of arbitrary impedances." *Journal of the Franklin Institute*, vol. 249(1), pp. 57–83, 1950.

[108] Z. Pourgholamhossein, G. Askari, H. M. Sadeghi, and M. Fadaei. "Analysis, design and simulation of a compact wide band VHF high power tubular band pass filter." *Progress In Electromagnetics Research*, vol. 967, 2014.

[109] S. Kumar, A. Vayonakis, H. G. LeDuc, P. K. Day, S. Golwala, and J. Zmuidzinas. "Millimeter-wave lumped element superconducting bandpass filters for multi-color imaging." *IEEE transactions on applied superconductivity*, vol. 19(3), pp. 924–929, 2009.

[110] G. De Lange, J. Kuipers, T. Klapwijk, R. Panhuyzen, H. Van De Stadt, and M. De Graauw. "Superconducting resonator circuits at frequencies above the gap frequency." *Journal of applied physics*, vol. 77(4), pp. 1795–1804, 1995.

[111] S. Paine. "The am atmospheric model." URL https://lweb.cfa.harvard.edu/~spaine/am/.

[112] K. Kurokawa. "Power waves and the scattering matrix." *IEEE transactions on microwave theory and techniques*, vol. 13(2), pp. 194–202, 2003.

[113] S. J. Mason. "Feedback theory-some properties of signal flow graphs." *Proceedings of the IRE*, vol. 41(9), pp. 1144–1156, 1953.

[114] J. Lamarre. "Photon noise in photometric instruments at far-infrared and submillimeter wavelengths." *Applied optics*, vol. 25(6), pp. 870–876, 1986.

[115] C. Enss and S. Hunklinger. Low-temperature physics. Springer Science & Business Media, 2005.

[116] J. Clarke and I. Braginski. "Alex, eds.,"The SQUID Handbook", Vol. 1.", 2004.

[117] E. Doebelin. System dynamics: modeling, analysis, simulation, design. CRC Press, 1998.

[118] D. Alpay and I. Gohberg. The state space method: generalizations and applications, vol. 161. Springer Science & Business Media, 2006.

[119] G. Wang, V. Yefremenko, V. Novosad, A. Datesman, J. Pearson, G. Shustakova et al. "Thermal properties of silicon nitride beams below 1 kelvin." In "AIP Conference Proceedings," vol. 1219, pp. 75–82. American Institute of Physics, 2010.

[120] C. Kittel and P. McEuen. Introduction to solid state physics. John Wiley & Sons, 2018.

[121] J. Korringa. "Nuclear magnetic relaxation and resonnance line shift in metals." *Physica*, vol. 16(7-8), pp. 601–610, 1950.

[122] M. Sjöstrand and G. Seidel. "Hyperfine resonance properties of Er 3+ in Au." *Physical review B*, vol. 11(9), p. 3292, 1975.

[123] K. Gschneidner and F. Calderwood. "The Ag- Er (Silver-Erbium) system." *Bulletin of Alloy Phase Diagrams*, vol. 6(1), pp. 17–19, 1985.

[124] G. Williams and L. Hirst. "Crystal-field effects in solid solutions of rare earths in noble metals." *Physical Review*, vol. 185(2), p. 407, 1969.

[125] R. Chui, R. Orbach, and B. Gehman. "Hyperfine splitting of a localized moment in a metal." *Physical Review B*, vol. 2(7), p. 2298, 1970.

[126] L. Tao, D. Davidov, R. Orbach, and E. Chock. "Hyperfine splitting of Er and Yb resonances in Au: A separation between the atomic and covalent contributions to the exchange integral." *Physical Review B*, vol. 4(1), p. 5, 1971.

[127] F. Pobell. "Solid Matter at Low Temperatures." In "Matter and Methods at Low Temperatures," pp. 30–63. Springer, 2007.

[128] M. A. Ruderman and C. Kittel. "Indirect exchange coupling of nuclear magnetic moments by conduction electrons." *Physical Review*, vol. 96(1), p. 99, 1954.

[129] A. Fleischmann, M. Link, T. Daniyarov, H. Rotzinger, C. Enss, and G. Seidel. "Metallic magnetic calorimeters (MMC): detectors for high-resolution X-ray spectroscopy." *Nuclear Instruments and Methods in Physics Research Section A: Accelerators, Spectrometers, Detectors and Associated Equipment*, vol. 520(1-3), pp. 27–31, 2004.

[130] J. Schönefeld. Entwicklung eines mikrostrukturierten magnetischen Tieftemperatur Kalorimeters zum hochauflösenden Nachweis von einzelnen Röntgenquanten. Ph.D. thesis.

[131] L. Isaacs. "Low-Temperature Specific Heat of Gold, Silver, and Copper." *The Journal of Chemical Physics*, vol. 43(1), pp. 307–308, 1965.

[132] J. Souletie and R. Tournier. "Specific heat and magnetization in dilute magnetic alloys." *Journal of Low Temperature Physics*, vol. 1, pp. 95–108, 1969.

[133] M. Herbst, A. Barth, A. Fleischmann, L. Gastaldo, D. Hengstler, N. Kovac et al. "Numerical calculation of the thermodynamic properties of silver erbium alloys for use in metallic magnetic calorimeters." *Journal of Low Temperature Physics*, vol. 209(5), pp. 1119–1127, 2022.

[134] J. C. Mather. "Bolometer noise: nonequilibrium theory." *Applied optics*, vol. 21(6), pp. 1125–1129, 1982.

[135] M. A. Herbst. High Resolution Magnetic Micro-calorimeters: Thermodynamics, Cooling Requirements, and Noise. Ph.D. thesis, 2023.

[136] S. Hanany, A. H. Jaffe, and E. Scannapieco. "The effect of the detector response time on bolometric cosmic microwave background anisotropy experiments." *Monthly Notices of the Royal Astronomical Society*, vol. 299(3), pp. 653–660, 1998.

[137] T. Imamura, T. Shiota, and S. Hasuo. "Fabrication of high quality Nb/AlO/sub x/-Al/Nb Josephson junctions. I. Sputtered Nb films for junction electrodes." *IEEE Transactions on applied superconductivity*, vol. 2(1), pp. 1–14, 2002.

[138] H. Gao, S. Wang, D. Xu, X. Wang, Q. Zhong, Y. Zhong et al. "Study of DC magnetron sputtered Nb films." *Crystals*, vol. 12(1), p. 31, 2021.

[139] E. Zikiy, I. Stepanov, S. Bukatin, D. Baklykov, M. Teleganov, E. Krivko et al. "Mutual control of critical temperature, RRR, stress, and surface quality for sputtered Nb films." *arXiv preprint arXiv:2502.03299*, 2025.

[140] C. Wu. "Intrinsic stress of magnetron-sputtered niobium films." *Thin Solid Films*, vol. 64(1), pp. 103–110, 1979.

[141] G. G. Stoney. "The tension of metallic films deposited by electrolysis." *Proceedings of the Royal Society of London. Series A, Containing Papers of a Mathematical and Physical Character*, vol. 82(553), pp. 172–175, 1909.

[142] M. Zecchino and T. Cunningham. "Thin film stress measurement using dektak stylus profilers." *Veeco Instruments Inc*, vol. 4, 2004.

[143] U. Pudasaini, G. Eremeev, and S. Cheban. "First Results From Nanoindentation of Vapor Diffused Nb3Sn Films on Nb." *arXiv preprint arXiv:2307.08757*, 2023.

[144] W. Skocpol, M. Beasley, and M. Tinkham. "Self-heating hotspots in superconducting thin-film microbridges." *Journal of Applied Physics*, vol. 45(9), pp. 4054–4066, 1974.

[145] S.-G. Jung, S. Seo, S. Lee, E. D. Bauer, H.-O. Lee, and T. Park. "A peak in the critical current for quantum critical superconductors." *Nature communications*, vol. 9(1), p. 434, 2018.

[146] K. Il'in, M. Siegel, A. Engel, H. Bartolf, A. Schilling, A. Semenov et al. "Current-induced critical state in NbN thin-film structures." *Journal of Low Temperature Physics*, vol. 151, pp. 585–590, 2008.

[147] M. J. Madou. Fundamentals of microfabrication: the science of miniaturization. CRC press, 2018.

[148] J. Choi, Y.-K. Kim, C.-D. Kim, S. Kim, and Y. Jo. "Enhancing the critical temperature of strained Niobium films." *Materials Research Express*, vol. 7(7), p. 076001, 2020.

[149] C. Koch and T. J. Rinke. Photolithography: Basics of Microstructuring. MicroChemicals GmbH, 2017.

[150] K. Hinode, T. Satoh, S. Nagasawa, Y. Kitagawa, and M. Hidaka. "Fabrication of reliable via conductors for niobium SFQ devices." *Physica C: Superconductivity and its applications*, vol. 426, pp. 1533–1540, 2005.

[151] D. Shi, J. He, Z. Zhou, and C. Huang. "Reactive ion etching of SiO2 and Mo sidewall profile process." In "Journal of Physics: Conference Series," vol. 2468, p. 012104. IOP Publishing, 2023.

[152] D. Zhao and X. Lu. "Chemical mechanical polishing: theory and experiment." *Friction*, vol. 1, pp. 306–326, 2013.

[153] A. Burck, S. Kempf, S. Schäfer, H. Rotzinger, M. Rodrigues, T. Wolf et al. "Microstructured magnetic calorimeter with meander-shaped pickup coil." *Journal of Low Temperature Physics*, vol. 151, pp. 337–344, 2008.

[154] A. A. Ramadan, R. D. Gould, and A. Ashour. "On the Van der Pauw method of resistivity measurements." *Thin solid films*, vol. 239(2), pp. 272–275, 1994.

[155] S. Mendoza-Acevedo, M. A. Reyes-Barranca, E. N. Vázquez-Acosta, J. A. Moreno-Cadenas, and J. L. González-Vidal. "Release Optimization of Suspended Membranes in MEMS." *Micromachining Techniques for Fabrication of Micro and Nano Structures*, pp. 183–204, 2012.

[156] R. E. Oosterbroek, J. W. Berenschot, H. V. Jansen, A. J. Nijdam, G. Pandraud, A. van den Berg et al. "Etching methodologies in< 111>-oriented silicon wafers." *Journal of microelectromechanical systems*, vol. 9(3), pp. 390–398, 2000.

[157] P. Pal and K. Sato. "Fabrication methods based on wet etching process for the realization of silicon MEMS structures with new shapes." *Microsystem technologies*, vol. 16, pp. 1165–1174, 2010.

[158] K. R. Williams and R. S. Muller. "Etch rates for micromachining processing." *Journal of Microelectromechanical systems*, vol. 5(4), pp. 256–269, 1996.

[159] D. Bodas, S. J. Patil, V. Krishnamurthy, and S. Gangal. "PMMA As an etch mask for silicon micromachining a feasibility study." *Journal of the Indian Institute of Science*, vol. 81(6), p. 645, 2001.

[160] J. Han, Y. J. Yin, D. Han, and L. Dong. "Improved PECVD SixNy film as a mask layer for deep wet etching of the silicon." *Materials Research Express*, vol. 4(9), p. 096301, 2017.

[161] J. Dalvi-Malhotra, X. Zhong, and C. Planje. "Photosensitive etch protection coating for silicon wet-etch applications." In "Reliability, Packaging, Testing, and Characterization of MEMS/MOEMS VII," vol. 6884, pp. 175–182. SPIE, 2008.

[162] R. A. Rahim, B. Bais, B. Y. Majlis, and G. Sugandi. "ProTEK PSB coating as an alternative polymeric protection mask for KOH bulk etching of silicon." *Microsystem technologies*, vol. 19, pp. 905–914, 2013.

[163] C. Posada, P. A. Ade, Z. Ahmed, A. Anderson, J. Austermann, J. Avva et al. "Fabrication of detector arrays for the SPT-3G receiver." *Journal of Low Temperature Physics*, vol. 193, pp. 703–711, 2018.

[164] D. E. Ibbotson, D. L. Flamm, J. A. Mucha, and V. M. Donnelly. "Comparison of XeF2 and F-atom reactions with Si and SiO2." *Applied Physics Letters*, vol. 44(12), pp. 1129–1131, 1984.

[165] D. Ibbotson, J. Mucha, D. Flamm, and J. Cook. "Plasmaless dry etching of silicon with fluorine-containing compounds." *Journal of applied physics*, vol. 56(10), pp. 2939–2942, 1984.

[166] M. Tramšek and B. Žemva. "Synthesis, Properties and Chemistry of Xenon(II) Fluoride." *Acta Chim. Slov*, vol. 53, pp. 105–116. doi:10.1002/chin.200721209, 05 2007.

[167] F. Schreiner, G. N. McDonald, and C. L. Chernick. "Vapor pressure and melting points of xenon difluoride and xenon tetrafluoride." *The Journal of Physical Chemistry*, vol. 72(4), pp. 1162–1166, 1968.

[168] H. F. Winters and F. Houle. "Gaseous products from the reaction of XeF2 with silicon." *Journal of Applied Physics*, vol. 54(3), pp. 1218–1223, 1983.

[169] F. I. Chang, R. Yeh, G. Lin, P. B. Chu, E. G. Hoffman, E. J. Kruglick et al. "Gas-phase silicon micromachining with xenon difluoride." In "Microelectronic structures and microelectromechanical devices for optical processing and multimedia applications," vol. 2641, pp. 117–128. SPIE, 1995.

[170] P. B. Chu, J. T. Chen, R. Yeh, G. Lin, J. C. Huang, B. A. Warneke et al. "Controlled pulse-etching with xenon difluoride." In "Proceedings of international solid state sensors and actuators conference (Transducers' 97)," vol. 1, pp. 665–668. IEEE, 1997.

[171] W. E. Gifford and R. Longsworth. "Pulse-tube refrigeration." 1964.

[172] E. Mikulin, A. Tarasov, and M. Shkrebyonock. "Low-temperature expansion pulse tubes." In "Advances in Cryogenic Engineering: Volume 29," pp. 629–637. Springer, 1984.

[173] Z. Shaowei, W. Peiyi, and C. Zhongqi. "Double inlet pulse tube refrigerators: an important improvement." *cryogenics*, vol. 30(6), pp. 514–520, 1990.

[174] H. London, G. Clarke, and E. Mendoza. "Osmotic pressure of He 3 in liquid He 4, with proposals for a refrigerator to work below 1 K." *Physical Review*, vol. 128(5), p. 1992, 1962.

[175] P. Das, R. B. de Ouboter, and K. Taconis. "A realization of a London-Clarke-Mendoza type refrigerator." In "Low Temperature Physics LT9: Proceedings of the IXth International Conference on Low Temperature Physics Columbus, Ohio, August 31–September 4, 1964," pp. 1253–1255. Springer, 1965.

[176] D. Cousins, S. N. Fisher, A. Guénault, R. Haley, I. Miller, G. Pickett et al. "An advanced dilution refrigerator designed for the new Lancaster microkelvin facility." *Journal of low temperature physics*, vol. 114, pp. 547–570, 1999.

[177] K. K. Likharev. Dynamics of Josephson junctions and circuits. Routledge, 2022.

[178] J. Clarke and A. I. Braginski. The SQUID handbook: Applications of SQUIDs and SQUID systems. John Wiley & Sons, 2006.

[179] C. D. Tesche and J. Clarke. "DC SQUID: Noise and optimization." *Journal of Low Temperature Physics*, vol. 29(3), pp. 301–331, 1977.

[180] J. Clarke and G. Hawkins. "Flicker (1 f) noise in Josephson tunnel junctions." *Physical Review B*, vol. 14(7), p. 2826, 1976.

[181] V. Foglietti, W. Gallagher, M. Ketchen, A. Kleinsasser, R. Koch, S. Raider et al. "Low-frequency noise in low 1/f noise dc SQUID's." *Applied physics letters*, vol. 49(20), pp. 1393–1395, 1986.

[182] S. Kempf, A. Ferring, and C. Enss. "Towards noise engineering: Recent insights in low-frequency excess flux noise of superconducting quantum devices." *Applied Physics Letters*, vol. 109(16), 2016.

[183] D. Drung. "Advanced SQUID read-out electronics." In "SQUID Sensors: Fundamentals, Fabrication and Applications," pp. 63–116. Springer, 1996.

[184] R. P. Welty and J. M. Martinis. "Two-stage integrated SQUID amplifier with series array output." *IEEE Transactions on Applied Superconductivity*, vol. 3(1), pp. 2605–2608, 2002.

[185] D. Drung. "High-performance DC SQUID read-out electronics." *Physica C: Superconductivity*, vol. 368(1-4), pp. 134–140, 2002.

[186] H. Padé. "Sur la représentation approchée d'une fonction par des fractions rationnelles." In "Annales scientifiques de l'Ecole normale supérieure," vol. 9, pp. 3–93. 1892.

[187] P. A. Holst. "Padé approximations and analog computer simulations of time delays." *Simulation*, vol. 12(6), pp. 277–290, 1969.

[188] F. Bauer. Rauscharme Stromsensor-dc-SQUIDs mit Impedanzanpassung für metallische magnetische Kalorimeter. Ph.D. thesis, Kirchhoff Institüt für Physik, Hedielberg Universität, 2022.

[189] D. Drung, C. Hinnrichs, and H.-J. Barthelmess. "Low-noise ultra-high-speed dc SQUID readout electronics." *Superconductor Science and Technology*, vol. 19(5), p. S235, 2006.